

ENHANCING SPECTRUM EFFICIENCY THROUGH HYBRID-DUPLEX SYSTEMS FOR AERONAUTICAL COMMUNICATIONS



Tan Zheng Hui Ernest

School of Computer Science and Engineering

A thesis submitted to the Nanyang Technological University
in partial fulfilment of the requirement for the degree of
Doctor of Philosophy (Ph.D)

2020

Statement of Originality

I hereby certify that the work embodied in this thesis is the result of original research, is free of plagiarised materials, and has not been submitted for a higher degree to any other University or Institution.

.....
06/12/2019.....

Date



.....
Tan Zheng Hui Ernest

Supervisor Declaration Statement

I have reviewed the content and presentation style of this thesis and declare it is free of plagiarism and of sufficient grammatical clarity to be examined. To the best of my knowledge, the research and writing are those of the candidate except as acknowledged in the Author Attribution Statement. I confirm that the investigations were conducted in accord with the ethics policies and integrity standards of Nanyang Technological University and that the research data are presented honestly and without prejudice.

.....06/12/2019.....

Date



A. S. Madhukumar

Authorship Attribution Statement

This thesis contains material from seven papers published in the following peer-reviewed journals in which I am listed as an author.

- Chapter 2 is published as **Tan Zheng Hui Ernest, A. S. Madhukumar, Rajendra Prasad Sirigina, and Anoop Kumar Krishna**, “Addressing Spectrum Efficiency Through Hybrid-Duplex UAV Communications: Challenges and Opportunities,” Submitted to Elsevier Vehicular Communications for possible publication.
- Chapter 3 is published as **Tan Zheng Hui Ernest, A. S. Madhukumar, Rajendra Prasad Sirigina, and Anoop Kumar Krishna**, “Outage Analysis and Finite SNR Diversity-Multiplexing Tradeoff of Hybrid-Duplex Systems for Aeronautical Communications,” **IEEE Transactions on Wireless Communications**, vol. 18, no. 4, pp. 2299–2313, April 2019.
- Chapter 4 is published as **Tan Zheng Hui Ernest, A. S. Madhukumar, Rajendra Prasad Sirigina, and Anoop Kumar Krishna**, “A Hybrid-Duplex System with Joint Detection for Interference-Limited UAV Communications,” **IEEE Transactions on Vehicular Technology**, vol. 68, no. 1, pp. 335–348, January 2019.
- Chapter 5 is published as **Tan Zheng Hui Ernest, A. S. Madhukumar, Rajendra Prasad Sirigina, and Anoop Kumar Krishna**, “A Power Series Approach for Hybrid-Duplex UAV Communication Systems Under Rician Shadowed Fading,” **IEEE Access**, vol. 7, pp. 76949–76966, June 2019.
- Chapter 6 is published as **Tan Zheng Hui Ernest, A. S. Madhukumar, Rajendra Prasad Sirigina, and Anoop Kumar Krishna**, “Hybrid-Duplex Communications for Multi-UAV Networks: An Outage Probability Analysis,” **IEEE Communications Letters**, vol. 23, no. 10, pp. 1831–1835, October 2019.

- Chapter 7 is published as **Tan Zheng Hui Ernest, A. S. Madhukumar, Rajendra Prasad Sirigina, and Anoop Kumar Krishna, “NOMA-Aided Multi-UAV Communications in Full-Duplex Heterogeneous Networks,” Submitted to IEEE Transactions on Communications for possible publication.**
- Chapter 8 is published as **Tan Zheng Hui Ernest, A. S. Madhukumar, Rajendra Prasad Sirigina, and Anoop Kumar Krishna, “NOMA-aided UAV Communications over Correlated Rician Shadowed Fading Channels,” Submitted to IEEE Transactions on Signal Processing for possible publication.**

The contributions of the co-authors are as follows:

- Prof. A.S. Madhukumar, Dr Rajendra Prasad Sirigina, and Dr Anoop Kumar Krishna provided the initial research directions.
- Prof. A.S. Madhukumar, Dr Rajendra Prasad Sirigina suggested the analytical frameworks that can be explored in the manuscripts.
- I derived all the associated mathematical equations for the analytical frameworks proposed in the manuscripts.
- I wrote the MATLAB and Mathematica codes to obtain the simulation results presented in the manuscripts.
- I analyzed and interpreted the simulation and numerical results, with assistance from Dr Rajendra Prasad Sirigina.
- I prepared all the manuscript drafts. The manuscripts were revised together with Prof. A.S. Madhukumar and Dr Rajendra Prasad Sirigina.

.....
06/12/2019
Date


.....
Tan Zheng Hui Ernest

Abstract

Spectrum scarcity is a significant challenge in aeronautical communications due to increasing demand for future wireless services in manned and unmanned aerial vehicle (UAV) networks. To this end, hybrid-duplex (HBD) systems are proposed as a pragmatic solution as it improves spectrum efficiency in aeronautical communications over various realistic environments.

Towards highlighting the feasibility of HBD aeronautical networks, this thesis first studies the outage probability and diversity gain of aeronautical networks with single uplink and downlink nodes for various interference management approaches. Then, the performance of HBD UAV networks is characterized in environments with fading and shadowing. Next, performance analysis is conducted for multi-UAV networks with an arbitrary number of uplink and downlink UAVs using stochastic geometry tools. Finally, we examine correlated non-orthogonal multiple access (NOMA) transmissions for multi-antenna receivers in UAV communication systems (UCSs). Through the various performance analysis, the benefits of HBD systems over half-duplex (HD) systems at low signal-to-noise ratio (SNR) regimes are highlighted. The major contributions of this thesis are further elaborated below.

Firstly, for aeronautical networks with single uplink and downlink nodes, we present new closed-form expressions for outage probability and finite SNR analysis. Through extensive analysis, we show that HBD systems attain lower outage probability and higher diversity gain over conventional HD systems at low SNR regimes. Furthermore, we identify ideal scenarios that enable HBD systems to outperform HD systems for various interference management strategies.

Secondly, for HBD UAV networks experiencing fading and shadowing, we derive new closed-form expressions for the probability density function (PDF), cumulative distribution function (CDF), and fractional moments under Rician shadowed fading. We

demonstrate that shadowing on the self-interference (SI) link has a negligible impact on the full-duplex (FD) ground station (GS), i.e., FD-GS. On the contrary, severe shadowing on the desired link leads to higher outage probability at the FD-GS, despite SI mitigation measures. At the downlink UAV, interference management through the joint detection approach is shown to be more robust to shadowing than the interference ignorant method.

Thirdly, for multi-UAV networks with an arbitrary number of uplink and downlink UAVs, we propose exact analytical frameworks that incorporate stochastic geometry tools, i.e., binomial point processes (BPPs), that accurately models the random location of UAVs. For FD heterogeneous networks (FD-HetNets) and HBD multi-UAV networks, we observe a lower outage probability, higher ergodic capacity, and greater number of deployed UAVs on the same spectrum, as compared to HD-based multi-UAV networks. Even with weaker SI suppression and strong oscillator phase noise at the FD-GS, FD-HetNets still attain higher ergodic sum capacity over the HD-HetNets.

Finally, for multi-antenna receivers in NOMA-aided UCSs, we present new closed-form expressions for the joint PDF and joint CDF under the bivariate Rician shadowed fading model. An analysis of the NOMA-aided UCS demonstrates that more UAVs can be deployed on the same spectrum, at similar outage probability, than orthogonal multiple access based (OMA-based) UCSs. Also, cross correlation is shown to affect the diversity gain of both NOMA and OMA transmissions only at low SNR regimes.

Therefore, the analysis conducted in this thesis demonstrates the feasibility and benefits of addressing spectrum scarcity in aeronautical communications through HBD systems.

Acknowledgments

It has been my utmost privilege to be given this opportunity to pursue a Ph.D degree. First, I would like to express my sincere gratitude to my supervisor, Prof. A. S. Madhukumar for his invaluable mentorship throughout my Ph.D candidature. The countless discussions that I have had with him have played a considerable role in orientating my research direction in the vast area of wireless communications. As a fair and honest critic of my work, Prof. Madhu has enabled me to have a better understanding of my research area through his insights and encouragement. His expectation of high standard and rigour has also been instrumental in raising the quality of my work.

Next, I would like to thank my co-supervisor, Dr Anoop Kumar Krishna, for his support of my Ph.D project. With his long experience and deep expertise in the industry, Dr Anoop's comments and suggestions have been crucial in improving the practical relevance of my work. I am also grateful for Dr Anoop's help in enabling me to have an enriching internship at Airbus Singapore Pte Ltd before the start of my candidature. The internship allowed me to experience upstream research and development, and also served as an introduction to my Ph.D topic.

I would also like to thank Dr Rajendra Prasad Sirigina for his significant role in imparting valuable knowledge to me, particularly in the first two years of my candidature. It was only through Dr Rajendra's guidance that I was able to grasp key mathematical concepts and techniques that were necessary for my work. I am also particularly grateful to Dr Rajendra for the advice and encouragement dispensed in the course of the review process for all my papers, and the help in critiquing my work, despite his busy schedule.

I want to extend my thanks to Airbus Singapore Pte Ltd and the Singapore Economic Development Board (EDB) for the support and funding of this Ph.D project, and also to Nanyang Technological University for the conducive environment in the School of Computer Science and Engineering.

Last, but not least, I would like to thank my parents and Li Ying for being my pillar of support throughout my Ph.D candidature. Their love, care, and encouragement have been the key to sustaining my mental strength throughout my intellectual pursuit these past four years.

Contents

Abstract	v
Acknowledgments	vii
List of Figures	xvii
List of Tables	xxii
List of Abbreviations	xxiv
List of Publications	xxvii
1 Introduction	1
1.1 Background	1
1.2 Improving Spectrum Efficiency with Hybrid-Duplex Communications	3
1.3 Thesis Motivation and Objective	4
1.4 Major Contributions	5
1.4.1 Chapter 3	6
1.4.2 Chapter 4	7
1.4.3 Chapter 5	7
1.4.4 Chapter 6	8
1.4.5 Chapter 7	8
1.4.6 Chapter 8	9
1.5 Thesis Organization	9
2 Addressing Spectrum Efficiency Through Hybrid-Duplex Communica-	
tions: A Literature Review	11
2.1 Introduction	11
2.2 UAV Channel Models	15

2.2.1	Stochastic Approach	15
2.2.2	Log Distance Approach	17
2.3	Self-Interference at FD Ground Stations	20
2.3.1	SI Mitigation Architectures	20
2.3.1.1	Passive Domain	21
2.3.1.2	Analog Domain	22
2.3.1.3	Digital Domain	23
2.3.1.4	Combination of Domains and Other Alternative Approaches	24
2.3.2	Modeling FD Transceiver Impairments in HBD UAV Communications	25
2.3.2.1	Phase Noise	25
2.3.2.2	Imperfect SI Channel Estimation	26
2.3.2.3	Quantization Noise	26
2.4	Inter-UAV Interference Management Strategies	27
2.4.1	Interference Management Strategies	27
2.4.1.1	Interference-Ignorant	28
2.4.1.2	Successive Interference Cancellation	29
2.4.1.3	Joint Detection	30
2.4.2	Performance Evaluation of the II, SIC, and JD Strategies for HBD UAV Communications	31
2.4.2.1	Outage Probability	32
2.4.2.2	Finite SNR Diversity Gain	35
2.5	Power-Domain Non-Orthogonal Multiple Access for HBD UAV Communications	37
2.5.1	Towards Multi-User HBD Communications	38
2.5.2	Brief Overview of NOMA	40
2.5.2.1	Code-Domain NOMA	40
2.5.2.2	Power-Domain NOMA	43
2.5.2.3	Relevance of Power-Domain NOMA in an HBD-UCS	43
2.6	Chapter Summary	45

3	Interference Management in Hybrid-Duplex Aeronautical Communication Systems	46
3.1	Introduction	46
3.1.1	Related Literature	47
3.1.2	Relevance to Related Literature	49
3.2	System Model	49
3.2.1	Ground Station	50
3.2.2	Air-Station 2	52
3.3	Calculation of Outage Probabilities	52
3.3.1	Hybrid-Duplex Outage Probability	53
3.3.1.1	Ground Station	53
3.3.1.2	Air-Station 2 (Interference Ignorant Detector)	54
3.3.1.3	Air-Station 2 (Successive Interference Cancellation Detector)	54
3.3.2	Half-Duplex Outage Probability	55
3.3.3	System Level Outage Probability	56
3.4	Finite SNR Analysis	56
3.4.1	Finite SNR Diversity Gain	57
3.4.2	Finite SNR DMT Parameters	57
3.4.3	Finite SNR Diversity Gain for HBD Systems	59
3.4.4	Finite SNR Diversity Gain for HD Systems	61
3.4.5	Finite SNR DMT Analysis for HBD Systems	62
3.4.6	Finite SNR DMT Analysis for HD Systems	63
3.4.7	System Level Finite SNR Diversity Gain and DMT	64
3.5	Numerical Results	64
3.5.1	Finite SNR Diversity Gain and Outage Analysis	65
3.5.1.1	Impact of Residual SI at GS	65
3.5.1.2	Impact of Interference at AS-2	66
3.5.1.3	Impact of Interference at System Level	68
3.5.2	Finite SNR DMT Analysis	70
3.5.2.1	Impact of Residual SI at GS	70

3.5.2.2	Impact of Interference at AS-2	71
3.5.2.3	Impact of Interference at System Level	72
3.6	Chapter Summary	73
4	Interference Management Through Joint Detection for Hybrid-Duplex UAV Communications	75
4.1	Introduction	75
4.2	System Model	77
4.2.1	Ground Station	78
4.2.2	Unmanned Aerial Vehicle 2	79
4.3	Outage Probability Derivations	80
4.3.1	Joint Detector at UAV-2	80
4.3.2	Benchmark Schemes and System Level Outage Probability	83
4.4	Finite SNR Analysis	84
4.4.1	Finite SNR Diversity Gain	84
4.4.2	Finite SNR DMT Parameters	85
4.4.3	Finite SNR Diversity Gain and DMT for HBD Systems	86
4.4.4	Benchmark Schemes and System Level Finite SNR Diversity Gain	89
4.5	Numerical and Simulation Results	90
4.5.1	Outage and Finite SNR Diversity Gain Analysis at UAV-2	90
4.5.2	Outage and Finite SNR Diversity Gain Analysis at the System Level	92
4.5.3	Finite SNR DMT Analysis at UAV-2 and System level	93
4.5.4	Finite SNR Multiplexing Gain Regions at UAV-2	95
4.6	Chapter Summary	97
5	Hybrid-Duplex UAV Communication in Rician Shadowed Fading Environments	99
5.1	Introduction	99
5.2	System Model	102
5.2.1	Ground Station	103

5.2.2	Unmanned Aerial Vehicle 2	104
5.3	Alternative Expressions for the Rician Shadowed Fading Model	105
5.3.1	Rician Shadowed Fading Model	106
5.3.2	Rician Fading Model	107
5.4	Outage Probability Derivations	109
5.4.1	Hybrid-Duplex Outage Probability	110
5.4.1.1	Ground Station	111
5.4.1.2	Unmanned Aerial Vehicle 2 (Interference Ignorant Detector)	113
5.4.1.3	Unmanned Aerial Vehicle 2 (Joint Detector)	115
5.4.2	Half-Duplex Outage Probability	117
5.5	Numerical Results	118
5.5.1	Impact of Shadowing at GS	119
5.5.2	Impact of inter-UAV interference and Shadowing at UAV-2	121
5.6	Chapter Summary	125
6	Towards Hybrid-Duplex Multi-UAV Networks	126
6.1	Introduction	126
6.2	System Model	127
6.3	Outage Probability	129
6.3.1	Hybrid-Duplex Outage Probability	130
6.3.1.1	Uplink UAV- <i>i</i>	130
6.3.1.2	Downlink UAV	131
6.3.2	Half-Duplex Outage Probability	132
6.4	Numerical Results	133
6.5	Chapter Summary	135
7	NOMA-Aided Multi-UAV Communications in Full-Duplex Heterogeneous Networks	137
7.1	Introduction	137
7.1.1	Related Literature	138
7.2	System Model	139
7.2.1	Distance Distribution of the UAVs and MBS	140

7.2.2	Instantaneous SINR at the FD-GS	141
7.2.3	Instantaneous SINR at Downlink UAV- <i>j</i>	143
7.3	Ergodic Capacity Derivations	144
7.3.1	Ergodic Capacity of the MBS in the NOMA-Aided FD-HetNet . .	144
7.3.2	Ergodic Capacity of UL UAV- <i>i</i> in the NOMA-Aided FD-HetNet .	146
7.3.3	Ergodic Capacity of DL UAV- <i>j</i> in the NOMA-Aided FD-HetNet .	147
7.3.4	Ergodic Capacity of the NOMA-aided HD-HetNet	149
7.3.5	Ergodic Capacity Gains of NOMA-aided FD-HetNets over HD-HetNets	150
7.4	Numerical Results	152
7.4.1	Ergodic Capacity at the FD-GS and DL UAVs	152
7.4.2	Impact of Height on Ergodic Sum Capacity	153
7.4.3	Impact of the Number of Deployed UAVs on Ergodic Sum Capacity	155
7.4.4	Impact of SI Cancellation, Phase Noise, and Residual Interference on Ergodic Sum Capacity	156
7.5	Chapter Summary	157
8	NOMA-aided UAV Communications over Bivariate Rician Shadowed Fading Channels	159
8.1	Introduction	159
8.2	System Model	160
8.2.1	Distribution of UAV Spatial Locations	161
8.2.2	Instantaneous SINR at Downlink UAV- <i>j</i>	162
8.3	Bivariate Rician Shadowed Fading Model	163
8.3.1	Derivation of the Joint PDF and Joint CDF	163
8.3.2	Truncation Analysis of the Joint PDF and Joint CDF	165
8.4	Outage Probability Derivations	168
8.4.1	Downlink NOMA Outage Probability	168
8.4.2	Downlink OMA Outage Probability	169
8.5	Finite SNR Diversity Gain Derivations	169
8.5.1	Downlink NOMA Finite SNR Diversity Gain	170

8.5.2	Downlink OMA Finite SNR Diversity Gain	171
8.6	Numerical Results	172
8.6.1	Joint PDF Validation and Truncation Analysis	172
8.6.2	Outage Probability and Finite SNR Diversity Gain Analysis . . .	174
8.7	Chapter Summary	177
9	Conclusions and Future Directions	178
9.1	Conclusions	178
9.2	Future Directions	180
9.2.1	Impact of UAV Flight Velocity	180
9.2.2	FD Transceivers for UAV Communications	180
9.2.3	Feasibility of Interference Forwarding in HBD UAV Communications	181
9.2.4	SIC-based Detection Complexity and Error Propagation in Power-Domain NOMA	182
9.2.5	User Pairing in Power-Domain NOMA	183
Appendices		187
A Mathematical Proofs in Chapter 3		187
A.1	Proof of Outage Probability with SIC detector at AS-2	187
A.2	Proof of Asymptotic Diversity Gain at the FD-enabled GS	189
A.3	Proof of Asymptotic Diversity Gain for the II and SIC detectors at AS-2	189
A.4	Proof of Asymptotic Diversity Gain at the GS and AS-2 in the HD-ACS	189
B Mathematical Proofs in Chapter 4		191
B.1	Proof of Outage Probability with Joint Detector at UAV-2	191
B.2	Proof of Convergence Radius for (4.9)	193
C Mathematical Proofs in Chapter 5		194
C.1	Proof for the PDF of $ h ^2$ in (5.9)	194
C.2	Proof of $\widehat{a}(n, \Omega, K, \gamma)$ in (5.12)	195
C.3	Proof for the l^{th} Moment of $ h' ^2$ in (5.15)	195
C.4	Proof of Convergence for (5.16)	196

C.5	Proof of Outage Probability at the GS over Rician Shadowed Fading and Rician Fading channels	196
C.6	Proof of Outage Probability for the Joint Detector at UAV-2 over Rician shadowed fading channels	197
C.6.1	Outage Probability Derivation	197
C.6.2	Convergence of (5.30)	199
C.7	Proof of Outage Probability Error Floor for the Joint Detector at UAV-2 over Rician Shadowed Fading and Rician Fading channels	200
D	Mathematical Proofs in Chapter 6	201
D.1	Proof of Outage Probability for the Outage Event \mathcal{O} at an Arbitrary Receiver	201
E	Mathematical Proofs in Chapter 7	202
E.1	Proof of Ergodic Capacity at the MBS in the FD-HetNet	202
E.2	Proof of Ergodic Capacity at DL UAV- j in the FD-HetNet	202
E.3	Proof of Ergodic Capacity Gain at the MBS, UL UAV- i , and DL UAV- j in the FD-HetNet over the HD-HetNet	204
F	Mathematical Proofs in Chapter 8	205
F.1	Proof for the Bivariate Rician Shadowed Joint PDF in (8.5)	205
F.2	Proof of Convergence Radius for (8.5)	206
F.3	Proof for the Bivariate Rician Shadowed Joint CDF in (8.6)	208
F.4	Proof for the Upper Bound of the Truncation Error in (8.5)	208
F.5	Proof for the Upper Bound of the Truncation Error in (8.6)	209
F.6	Proof of Outage Probability for NOMA at Downlink UAV- j	210
F.7	Proof of Asymptotic Diversity Gain for NOMA at Downlink UAV- j	211
References		212

List of Figures

2.1	An illustrated example of a MAV network and UAV network.	12
2.2	The organization of the chapter.	14
2.3	An overview of the topics in Section 2.2.	15
2.4	An overview of the topics in Section 2.3.	20
2.5	An example of SI mitigation in multi-antenna and single-antenna FD transceivers. For both configurations, SI mitigation through combinations of passive, analog, and digital domain techniques are possible.	21
2.6	An overview of the topics in Section 2.4.	27
2.7	An example of the types of interference management strategies that can be adopted for UAV-2 in the HBD-UCS.	28
2.8	The achievable instantaneous rate region of the II, SIC, and JD interference management approaches. The transmission rate of the FD-GS and UAV-1 are denoted as R_{GS}^{HBD} and R_1^{HBD} , respectively. The variables X_{gs} and Y_1 denote the SOI and interference at UAV-2, respectively.	33
2.9	An overview of the topics in Section 2.5.	38
2.10	An example of implementing SCMA in an HBD-UCS for 3 uplink UAVs (UAV-1, UAV-2, UAV-3) and 3 downlink UAVs (UAV-4, UAV-5, UAV-6) over 4 time-frequency resource blocks. The variable x_i represents the desired message of UAV- i	42
2.11	An example of implementing power-domain NOMA in an HBD-UCS for 3 uplink UAVs (UAV-1, UAV-2, UAV-3) and 3 downlink UAVs (UAV-4, UAV-5, UAV-6) over the same time-frequency resource block.	44
3.1	Air-Station 1 (AS-1) and Air-Station 2 (AS-2) operating in HD mode while communicating with the FD GS.	49

3.2	Outage probability and finite SNR diversity gain at GS (II detector) for phase noise strength $\gamma_\phi^2 = -130$ dBm.	66
3.3	Outage probability and finite SNR diversity gain at AS-2 (II and SIC detectors) for $\alpha_{g,2} = 1$, i.e., link between GS and AS-2 has same distance as the reference link ($d_{1,g}$).	67
3.4	System level outage probability and finite SNR diversity gain (II and SIC detectors) for $\alpha_{g,2} = 1, \alpha_{g,g} = 1, \gamma_\phi^2 = -130$ dBm, $\epsilon \in \{0.01, 0.001\}$	69
3.5	Finite SNR DMT for $\alpha_{g,2} = 1, \gamma_\phi^2 = -130$ dBm, $\Omega_X = 10$ dB.	71
3.6	System level finite SNR DMT (II and SIC detectors) for $\alpha_{g,2} = 1, \alpha_{g,g} = 1, \gamma_\phi^2 = -130$ dBm, $\Omega_X = 10$ dB.	72
4.1	Unmanned Aerial Vehicle 1 (UAV-1) and Unmanned Aerial Vehicle 2 (UAV-2) operating in HD mode while communicating with the FD GS.	77
4.2	The achievable instantaneous rate regions of the II, SIC and joint detectors (unshaded areas) at UAV-2 with respect to the transmission rates of the GS (R_{GS}^{HBD}) and UAV-1 (R_1^{HBD}). The shaded areas, O_{JD}^1 and O_{JD}^2 , respectively denote the outage region of the joint detector if SOI detection fails or if the sum rate constraint is not met.	80
4.3	Outage probability and finite SNR diversity gain at UAV-2 (II, SIC and joint detectors) for $\alpha_{g,2} = 1$	91
4.4	System level outage probability and finite SNR diversity gain (II, SIC and joint detectors) for $\alpha_{g,2} = 1, \alpha_{g,g} = 1, \gamma_\phi^2 = -130$ dBm and $\epsilon \in \{0.01, 0.001\}$	93
4.5	Finite SNR DMT at UAV-2 and system level (II, SIC and joint detectors) for $\alpha_{g,2} = 1, \alpha_{g,g} = 1, \gamma_\phi^2 = -130$ dBm and $\Omega_X = 10$ dB.	94
4.6	Achievable finite SNR diversity gain of the SIC detector and joint detector at UAV-2 for different multiplexing gains at UAV-1 ($r_{f,1}$) and the GS ($r_{f,gs}$) when $\alpha_{g,2} = 1, \alpha_{1,2} = 15$ and $\Omega_X = 10$ dB.	95
4.7	Overlapping finite SNR MGRs of the II, SIC and joint detectors at UAV-2 for $\alpha_{g,2} = 1, \alpha_{1,2} = \{0.1, 15\}$ and $\Omega_X = 10$ dB. (The MGR separation can be smoothen by plotting the regions with very high resolutions.)	96

5.1	Unmanned Aerial Vehicle 1 (UAV-1) and Unmanned Aerial Vehicle 2 (UAV-2) operating in HD mode while communicating with the FD GS over Rician shadowed fading channels.	102
5.2	Comparison between the exact PDF of $ h ^2$ and power series approximation equivalent for $\Omega = 1$ and $K_{tr} = 50$	106
5.3	Comparison between the exact PDF of $ h' ^2$ and power series approximation equivalent for $\Omega = 1$ and $K_{tr} = 50$	109
5.4	Comparison between the exact CDF of $ h' ^2$ and power series approximation equivalent for $\gamma = 0.5$ and $K_{tr} = 50$	110
5.5	Comparison between the exact fractional moment of $ h' ^2$ and power series approximation equivalent for $\Omega = 1$ and $K_{tr} = 50$	111
5.6	Outage probability at GS for $\alpha_{g,g} = 1$, $\epsilon = 0.01$, $\gamma_\phi^2 = -130\text{dBm}$, and $K_{X_1} = K_{Y_{si,1}} = 15$	118
5.7	Outage probability at GS (HBD vs HD) for $\alpha_{g,g} = 1$, $\epsilon = 0.01$, $\gamma_\phi^2 = -130\text{dBm}$, $K_{X_1} = K_{Y_{si,1}} = 15$, $m_{Y_{si,1}} = 10$	119
5.8	Impact of shadowing and Rician K factors on outage probability at GS for $\Omega_X = 5\text{dB}$, $\alpha_{g,g} = 1$, $\epsilon = 0.01$, $\gamma_\phi^2 = -130\text{dBm}$, $K_{Y_{si,1}} = 10$, $m_{Y_{si,1}} = 2$	120
5.9	Outage probability at UAV-2 for $\alpha_{g,2} = 1$, $K_{X_{gs}} = K_{Y_1} = 15$, $m_{Y_1} = 10$	121
5.10	Comparison between the II and joint detectors at UAV-2 for $\alpha_{g,2} = 1$, $K_{X_{gs}} = K_{Y_1} = 15$, $m_{X_{gs}} = m_{Y_1} = 10$	123
5.11	Impact of shadowing and Rician K factors on outage probability at UAV-2 for $\Omega_X = 5\text{dB}$, $\alpha_{g,2} = 1$, $\alpha_{1,2} = 0.5$, $K_{Y_1} = 10$, $m_{Y_1} = 10$	124
6.1	An illustration of the UL UAV spatial locations. The spatial location of DL UAV-1 is described in the same fashion.	127
6.2	Outage probability of the HBD-UCS.	133
6.3	Impact of height and minimum distance on the outage probability of the HBD-UCS at $P_t = 5 \text{ dB}$, $\beta = 1$, $\lambda_{g,1} = 0.1$, and $D_{alt}^{UL} = D_{alt,i}^{UL}$	135

7.1	The FD-HetNet for NOMA-aided multi-UAV communications is illustrated here. The FD-GS in the FD-HetNet enables HD uplink and downlink UAVs and the HD MBS to concurrently share the same spectrum for NOMA transmissions. Through the BPP, it is assumed that the spatial locations of the deployed UAVs and the MBS follow a uniform distribution around a disc, with origin O at the FD-GS and radius r_a	140
7.2	Ergodic capacity comparison at the FD-GS and DL UAVs in the NOMA-aided FD-HetNet for $N_U = N_D = 3$, $H_{min} = 0.1$ km, $\omega = 0.1$, $\gamma_\phi^2 = -130$ dBm, $\epsilon = 0.01$, and $\beta_{mbs,j} = \beta_{i,j} = (0.04)^3$	153
7.3	Impact of height on the ergodic sum capacity of the NOMA-aided FD-HetNet and HD-HetNet for $N_U = N_D = 3$, $\gamma_\phi^2 = -130$ dBm, $\epsilon = 0.01$, and $\beta_{mbs,j} = \beta_{i,j} = (0.04)^3$	154
7.4	Impact of the number of deployed UAVs on the ergodic sum capacity of the NOMA-aided FD-HetNet and HD-HetNet for $H_{min} = 0.1$ km, $\omega = 0.1$, $\gamma_\phi^2 = -130$ dBm, $\epsilon = 0.01$, and $\beta_{mbs,j} = \beta_{i,j} = (0.04)^3$	155
7.5	Impact of SI cancellation and phase noise on the ergodic sum capacity of the NOMA-aided FD-HetNet for $N_U = N_D = 3$, $H_{min} = 0.1$ km, $\omega = 0.1$, and $\beta_{mbs,j} = \beta_{i,j} = (0.04)^3$	156
7.6	Impact of SI cancellation, phase noise, and residual interference on the ergodic sum capacity gain of the NOMA-aided FD-HetNet for $N_U = N_D = 3$, $H_{min} = 0.1$ km, and $\omega = 0.1$	157
8.1	An illustration of the NOMA-aided UCS operating in a suburban environment. The GS employs downlink NOMA to transmit data to the UAVs equipped with two reception antennas. At the UAVs, selection combining is employed to recover the transmitted data from the GS.	161
8.2	Joint PDF comparison between the exact expression in (8.4) (denoted in red markers) and the closed-form expression in (8.5) for $m = 10$, $K_{tr,1} = 150$, and Rician K factor of 10 dB.	172
8.3	Impact of the Rician K factor, m , σ , and ρ on $\mathcal{T}_{\epsilon,upper}$ for $r_1 = r_2 = 1$ and Rician K factor of 10 dB.	173

8.4	Impact of ρ and γ on e_{upper} for $\gamma_1 = \gamma_2 = -10$ dB and Rician K factor of 7 dB.	174
8.5	Impact of minimum altitude h_{min} on NOMA outage probability.	175
8.6	Impact of cross correlation coefficient ρ on NOMA outage probability. . . .	175
8.7	Impact of cross correlation coefficient ρ on NOMA finite SNR diversity gain.	176

List of Tables

2.1	Summary of UAV Channel Modeling Considerations	19
2.2	Summary of Advantages and Disadvantages of the UAV Channel Modeling Approaches	19
2.3	Summary of Studies on SI Mitigation Architectures	23
2.4	Summary of Studies on Interference Management Strategies	30
2.5	Outage probability definitions of the II, SIC, and joint detectors at UAV-2.	34
2.6	References of finite SNR diversity gain and finite SNR DMT expressions for the II, SIC, and joint detectors at UAV-2.	37
2.7	Summary of Studies on NOMA Techniques	41
3.1	Summary of Important Notations	52
3.2	Simulation Parameters	65
4.1	Summary of Important Notations	79
4.2	References for the outage probability of the benchmark schemes	83
4.3	References for the finite SNR diversity gains of the benchmark schemes .	89
4.4	System Level HBD-UCS Performance Bottleneck for $\epsilon \in \{0.01, 0.001\}$. .	92
5.1	Summary of Important Notations	105
5.2	Summary of presented closed-form expressions for the Rician shadowed fading and Rician fading models	112
5.3	Error margin of the outage probability at GS.	119
5.4	Error margin of the outage probability at the ii and joint detectors for $\alpha_{1,2} = 0.5$	122
6.1	Summary of Important Notations	129

7.1	Summary of Important Notations	143
7.2	Simulation Parameters	152
8.1	Summary of Important Notations	163
8.2	Simulation Parameters	174

List of Abbreviations

A/A	Air-to-Air
A/G	Air-to-Ground
ACS	Aeronautical Communication System
ADC	Analog-to-Digital Converter
AS	Air-Station
AWGN	Additive White Gaussian Noise
Balun	Balanced/Unbalanced
BD	Backscatter Devices
BLOS	Beyond-Line-of-Sight
BPP	Binomial Point Process
CAAS	Civil Aviation Authority of Singapore
CDF	Cumulative Distribution Function
CDMA	Code-Division Multiple Access
CNPC	Control And Non-Payload Communications
CSI	Channel State Information
DAC	Digital-to-Analog Converter
DL	Downlink
DMT	Diversity-Multiplexing Trade-Off
EH	Energy Harvesting
EUROCONTROL	European Organization for the Safety of Air Navigation
FAA	Federal Aviation Administration
FCI	Future Communications Infrastructure
FD	Full-Duplex
FD-ABCN	FD Ambient Backscatter Communication Network
FD-AP	FD Access Point
FD-GS	FD Ground Station
FD-HetNet	FD Heterogeneous Network
FDMA	Frequency Division Multiple Access
FD-WPCN	FD Wireless Powered Communication Network
FSPL	Free Space Path Loss
GMSK	Gaussian Minimum Shift Keying
GS	Ground Station
HBD	Hybrid-Duplex

HBD-ACS	HBD Aeronautical Communication System
HBD-UCS	HBD UAV Communication System
HD	Half-Duplex
HD-HetNet	HD Heterogeneous Network
HD-UCS	HD UCS
HetNet	Heterogeneous Network
IF	Interference Forwarding
II	Interference Ignorant
IoT	Internet of Things
IQ	Inphase/Quadrature
ITU	International Telecommunication Union
ITU-R	ITU Radiocommunication Sector
JD	Joint Detection
LDACS	L-band Aeronautical Communication System
LDS	Low-Density Spreading
LNA	Low Noise Amplifier
LOS	Line-of-Sight
LTE	Long Term Evolution
LU	Legacy User
MAV	Manned Aerial Vehicle
MBS	Macro Base Station
MGF	Moment Generating Function
MGR	Multiplexing Gain Region
MIMO	Multiple Input Multiple Output
MUI	Multi-User Interference
NLOS	Non-Line-Of-Sight
NOMA	Non-Orthogonal Multiple Access
OFDM	Orthogonal Frequency Division Multiplexing
OFDMA	Orthogonal Frequency Division Multiple Access
OMA	Orthogonal Multiple Access
PDF	Probability Density Function
PER	Packet Error Rate
PPP	Poisson Point Process
QoS	Quality-of-Service
RF	Radio Frequency
RHS	Right Hand Side
RV	Random Variable
SCMA	Sparse Code Multiple Access
SD	Simultaneous Decoding
SESAR	Single European Sky ATM Research
SI	Self-Interference
SIC	Successive Interference Cancellation

SINR	Signal-to-Interference-Plus-Noise Ratio
SIR	Signal-to-Interference Ratio
SND	Simultaneous Non-Unique Decoding
SNR	Signal-to-Noise Ratio
SOI	Signal-of-Interest
SWAP	Size, Weight, and Power
TDMA	Time Division Multiple Access
UAV	Unmanned Aerial Vehicle
UCS	UAV Communication System
UL	Uplink
VDL	VHF Datalink
WLAN	Wireless Local Area Network

List of Publications

International Conferences

1. Tan Zheng Hui Ernest, A. S. Madhukumar, Rajendra Prasad Sirigina, and Anoop Kumar Krishna, “Mitigating Cellular Interference in Uplink UAV Communications,” Submitted to IEEE 92nd Veh. Technol. Conf. (VTC Fall) 2020 for possible publication.
2. Tan Zheng Hui Ernest, A. S. Madhukumar, Rajendra Prasad Sirigina, and Anoop Kumar Krishna, “Impact of Cellular Interference on Uplink UAV Communications,” in Proc. IEEE 91st Veh. Technol. Conf. (VTC Spring), Antwerp, Belgium, 2020
3. Tan Zheng Hui Ernest, A. S. Madhukumar, Rajendra Prasad Sirigina, and Anoop Kumar Krishna, “Capacity Characterization of Uplink NOMA in Multi-UAV Networks,” in Proc. IEEE 91st Veh. Technol. Conf. (VTC Spring), Antwerp, Belgium, 2020.
4. Tan Zheng Hui Ernest, A. S. Madhukumar, Rajendra Prasad Sirigina, and Anoop Kumar Krishna, “Downlink NOMA in Multi-UAV Networks over Bivariate Rician Shadowed Fading Channels,” in Proc. IEEE 90th Veh. Technol. Conf. (VTC Fall), Hawaii, USA, 2019.
5. Tan Zheng Hui Ernest, A. S. Madhukumar, Rajendra Prasad Sirigina, and Anoop Kumar Krishna, “An Outage Probability Analysis of Full-Duplex NOMA in UAV Communications,” in Proc. IEEE Wireless Commun. Netw. Conf. (WCNC), Marrakech, Morocco, 2019, pp. 1–5.

6. Tan Zheng Hui Ernest, A. S. Madhukumar, Rajendra Prasad Sirigina, and Anoop Kumar Krishna, “Hybrid-Duplex Systems for UAV Communications Under Rician Shadowed Fading,” in Proc. IEEE 88th Veh. Technol. Conf. (VTC Fall), Chicago, USA, 2018.
7. Tan Zheng Hui Ernest, A. S. Madhukumar, Rajendra Prasad Sirigina, and Anoop Kumar Krishna, “Hybrid-Duplex based Control and Non-Payload Communication Systems for UAVs: An Outage Analysis,” in Proc. IEEE/AIAA 37th Digit. Avionics Syst. Conf. (DASC), London, UK, 2018.
8. Tan Zheng Hui Ernest, Rajendra Prasad Sirigina, Anoop Kumar Krishna, and A. S. Madhukumar, “On the Performance Analysis of Hybrid-Duplex Systems for Aeronautical Communications,” in Proc. IEEE 87th Veh. Technol. Conf. (VTC Spring), Porto, Portugal, 2018.
9. Tan Zheng Hui Ernest, Anoop Kumar Krishna, A. S. Madhukumar, and Rajendra Prasad Sirigina, “On the Efficiency Improvements to Aeronautical Waveforms and Integrated Modular Avionics Systems,” in Proc. IEEE/AIAA 35th Digit. Avionics Syst. Conf. (DASC), 2016. IEEE, Sacramento, CA, USA, 2016, pp. 1–8.

International Journals

1. Tan Zheng Hui Ernest, A. S. Madhukumar, Rajendra Prasad Sirigina, and Anoop Kumar Krishna, “NOMA-Aided Multi-UAV Communications in Full-Duplex Heterogeneous Networks,” Submitted to IEEE Systems Journal for possible publication.
2. Tan Zheng Hui Ernest, A. S. Madhukumar, Rajendra Prasad Sirigina, and Anoop Kumar Krishna, “NOMA-aided UAV Communications over Correlated Rician Shadowed Fading Channels,” Submitted to IEEE Transactions on Signal Processing for possible publication.
3. Tan Zheng Hui Ernest, A. S. Madhukumar, Rajendra Prasad Sirigina, and Anoop Kumar Krishna, “Addressing Spectrum Efficiency Through Hybrid-Duplex UAV

Communications: Challenges and Opportunities,” Elsevier Vehicular Communications, vol. 24, August 2020.

4. Tan Zheng Hui Ernest, A. S. Madhukumar, Rajendra Prasad Sirigina, and Anoop Kumar Krishna, “Hybrid-Duplex Communications for Multi-UAV Networks: An Outage Probability Analysis,” IEEE Communications Letters, vol. 23, no. 10, pp. 1831–1835, October 2019.
5. Tan Zheng Hui Ernest, A. S. Madhukumar, Rajendra Prasad Sirigina, and Anoop Kumar Krishna, “A Power Series Approach for Hybrid-Duplex UAV Communication Systems under Rician Shadowed Fading,” IEEE Access, vol. 7, pp. 76949–76966, June 2019.
6. Tan Zheng Hui Ernest, A. S. Madhukumar, Rajendra Prasad Sirigina, and Anoop Kumar Krishna, “Outage Analysis and Finite SNR Diversity-Multiplexing Tradeoff of Hybrid-Duplex Systems for Aeronautical Communications,” IEEE Transactions on Wireless Communications, vol. 18, no. 4, pp. 2299–2313, April 2019.
7. Tan Zheng Hui Ernest, A. S. Madhukumar, Rajendra Prasad Sirigina, and Anoop Kumar Krishna, “A Hybrid-Duplex System with Joint Detection for Interference-Limited UAV Communications,” IEEE Transactions on Vehicular Technology, vol. 68, no. 1, pp. 335–348, January 2019.

Chapter 1

Introduction

1.1 Background

In future generations of communication networks, e.g., fifth generation (5G) networks, unmanned aerial vehicles (UAVs) are expected to play an increasingly important role in the delivery of next-generation services. Already, various types of use cases for multi-UAV networks are being actively investigated. For instance, the studies in [1] and [2] have discussed the possibility of UAVs being deployed as aerial base stations, while other studies have investigated the application of UAVs for geographical surveying [3], UAV-aided relaying [4], and vehicular communications [5, 6]. The application of multi-UAV networks has been attracting keen interest from both industry and academia. Compared to single-UAV networks, large-scale deployment of UAVs, i.e., multi-UAV networks, enables greater link redundancy [7], while overcoming potential weight and flying time restrictions of a single UAV [3].

Although multi-UAV networks can unlock many potential benefits for next-generation networks, supporting large-scale deployments of UAVs require readily available spectrum for UAV communications. Operations related to UAV control and non-payload communication (CNPC) links, for instance, have been allocated the L-band (0.9 - 1.2 GHz) and C-band (5.03 - 5.091 GHz) by the International Telecommunications Union (ITU) [8]. However, it is noted that the L-band spectrum is highly congested. Taking the USA as an example, the L-band is shared by terrestrial systems (0.9 - 0.96 GHz), aeronautical communication systems (0.96 - 1.164 GHz), and satellite communication systems (1.164 - 1.215 GHz), in addition to UAV CNPC systems [9].

In Singapore, CNPC and non-CNPC links for UAV operations can only operate in the 433.05 - 434.79 MHz band, 2.4 - 2.4835 GHz band, and the 5.725 - 5.850 GHz band [10]. Similar to the USA, the allocated bands for UAV communications are also congested. Maritime mobile systems, for instance, operate in the 433.05 - 434.79 MHz band, while systems with Bluetooth or wireless local area network (WLAN), i.e., WiFi, capabilities operate in the 2.4 - 2.4835 GHz band [11, 12]. It is also noted that WLAN devices also operate in the 5.725 - 5.850 GHz band [11, 12].

Given the highly congested spectrum that has been allocated for UAV communications, the potential benefits of multi-UAV networks may become negated. With limited availability of spectrum, large-scale deployment of UAVs in multi-UAV networks may not be possible. Furthermore, other wireless systems sharing the same band can cause unnecessary interference to multi-UAV networks, which in turn jeopardizes the reliability of UAV communications. Therefore, a lack of available spectrum to support UAV communications, is itself, one of the significant challenges that must be addressed in the near future.

Apart from UAV communications, spectrum scarcity is also a major challenge in manned aerial vehicle (MAV), i.e., civilian aircraft, communications. With the number of flights expected to increase worldwide drastically [13], demand for spectrum to support the wireless communications is also expected to swell. These demands stem not only from existing avionic systems but also from upcoming avionics systems and services in the near future. For instance, the newer generation of avionic systems can provide vital statistical information which can support real-time health monitoring services to reduce aircraft maintenance time and to meet safety requirements. The newer systems can also include the provision for next-generation in-flight entertainment services as well. As a consequence, further strain is placed on existing aeronautical communication links, which are already operating under bandwidth constraints in a congested aeronautical spectrum. Also, existing aeronautical communication links have also been noted to be inadequate in providing the needed capacity to handle the expected increases in data communications [14].

On this note, several initiatives are underway to identify candidate technologies that can enable the civilian aviation industry to address spectrum scarcity. Examples of

such initiatives include the Future Communications Infrastructure (FCI) program by the European Organization for the Safety of Air Navigation (EUROCONTROL) and the Federal Aviation Administration (FAA), and Single European Sky ATM Research (SESAR) supported by the European Commission [15].

Although new candidate technologies have been singled out for possible use in future aeronautical communications, the issue of spectrum scarcity continues to plague the civilian aviation industry.

1.2 Improving Spectrum Efficiency with Hybrid-Duplex Communications

With spectrum scarcity being a major challenge in both UAV and MAV communications, hybrid-duplex (HBD) systems can be investigated as a potential solution to improve spectrum efficiency in aeronautical communications.

In HBD systems, half-duplex (HD) uplink and downlink nodes communicate with full-duplex (FD) nodes on the same spectrum to improve spectrum efficiency. Taking UAV networks as an example, an HBD UAV communication system (UCS), i.e., HBD-UCS, can be studied as a viable means to overcome spectrum scarcity in UAV communications. Specifically, an HBD-UCS comprising uplink and downlink UAVs equipped with HD transceivers concurrently communicate with FD ground stations (GSs) in the multi-UAV network. In this way, an HBD-UCS effectively improves spectrum utilization by doing away with the need for separate uplink and downlink bands, i.e., uplink and downlink UAVs are assigned the same spectrum..

On the same note, it is worth pointing out that equipping UAVs with FD transceivers, i.e., FD-UCS with only FD-enabled nodes, can enable spectrum efficiency to be further boosted. Such a setup has been proposed in [16], where UAVs equipped with FD transceivers function as aerial base stations. However, constraints on the size, weight, and power (SWAP) of UAVs may result in FD transceivers that are either infeasible to design or non-compliant with regulatory requirements. Therefore, overcoming spectrum scarcity with an HBD-UCS allows HD transceivers on UAVs to be used, while allowing multi-UAV networks a smoother transition from HD-UCSs to HBD-UCSs.

Despite the associated advantages, self-interference (SI), stemming from FD transmissions at the GSs, and uplink interference at the downlink UAVs, i.e., inter-UAV interference, are the main impediments in HBD-UCSs [17–20]. Although SI can be suppressed, either in the passive domain by introducing path loss, or in the analog or digital domain via interference cancellation, residual SI is unavoidable. In particular, SI mitigation at FD-enabled GSs is imperfect due to non-ideal characteristics in practical FD transceivers, such as carrier phase noise and imperfect SI channel estimation [17–21]. Therefore, an essential step in enabling practical HBD-UCSs starts with SI mitigation architectures that minimize the effect of non-ideal characteristics in FD transceivers. Likewise, practical HBD-UCSs require effective strategies at the downlink UAVs to manage inter-UAV interference.

1.3 Thesis Motivation and Objective

In spite of the corresponding limitations associated with HBD systems, HBD-based aeronautical networks are still tenable if SI mitigation and inter-node interference, e.g., inter-UAV or inter-MAV interference, management strategies can be effectively implemented and is the motivation of this research. Therefore, the objective of this thesis is to demonstrate the feasibility of address spectrum scarcity for both UAVs and MAVs, e.g., civilian aircraft, through HBD communications. It should be emphasized that this thesis mainly focuses on enhancing spectrum efficiency for UAV communications. However, the resulting conclusions are also applicable to MAV communications as well.

To this end, it is crucial to show that HBD UAV and MAV communications can achieve superior performance over conventional HD systems. Hence, a performance analysis framework, based on power series approaches, is proposed for both HBD aeronautical communication systems (HBD-ACSs) and HBD-UCSs which focuses on the particular case of one uplink and one downlink node. The proposed analytical framework is applied to analyze the outage probability and finite signal-to-noise ratio (SNR) diversity gain of UAV and aeronautical communications for various small-scale fading channels, e.g., Rician fading, and interference management strategies. Next, stochastic geometry is incorporated into the proposed analytical framework to enable outage probability and diversity gain analysis of large-scale HBD multi-UAV networks. By considering stochastic

geometry, the spatial locations of UAVs can be randomly generated in order to accurately model large-scale UAV deployments. In turn, the outage probability and finite SNR analysis of interference management strategies becomes more robust as the random spatial location of the UAV is also considered. Apart from outage probability and diversity gain, a new analytical framework based on stochastic geometry is also proposed for the evaluation of ergodic capacities in large-scale HBD-based multi-UAV networks.

Through extensive analysis, it is shown that HBD-UCSs and HBD-ACSs achieve lower outage probability, higher diversity gain, and higher ergodic capacity when compared to conventional HD systems. For large-scale HBD-based multi-UAV networks, a higher number of UAVs can be supported on the same spectrum with superior performance over HD systems. Therefore, the feasibility and advantages of addressing spectrum scarcity through HBD communications are highlighted in this thesis for UAV and MAV networks.

1.4 Major Contributions

The major contributions of this thesis are summarized below.

- HBD systems are demonstrated to be a pragmatic solution towards addressing spectrum scarcity in aeronautical communications over various types of realistic environments.
- Through several proposed analytical frameworks, HBD systems are shown to achieve better performance over HD systems at low SNR regimes in terms of outage probability, finite SNR diversity gain, and finite SNR diversity-multiplexing trade-off (DMT) for the specific case of single uplink and downlink UAV/MAV in the network.
- Suitable interference scenarios in UAV and MAV networks that enable HBD systems to outperform HD systems are also identified for the interference-ignorant (II), successive interference cancellation (SIC), and joint detection (JD) interference management strategies.

- For multi-UAV networks with an arbitrary number of uplink and downlink UAVs, new analytical frameworks based on stochastic geometry are proposed for HBD-based UCSs and non-orthogonal multiple access aided (NOMA-aided) UCSs. Important performance matrices such as outage probability, finite SNR diversity gain, and ergodic capacity are evaluated for the proposed systems using this framework.
- Extensive analysis highlights the benefits and feasibility of HBD-based and NOMA-aided multi-UAV networks, and proves its performance is equivalent or superior to HD systems.

To further elaborate on the above points, the main contributions of each chapter are summarized below.

1.4.1 Chapter 3

- This chapter presents closed-form expressions for the outage probability, finite SNR diversity gain, and finite SNR DMT of an II detector and a two-stage SIC detector in a Rician fading environment.¹
- It is shown that the proposed HBD-ACS attains superior outage performance over existing HD-ACS at low SNRs. At high SNRs, however, the outage performance of the proposed HBD-ACS is eclipsed by HD-ACS as the former becomes interference-limited. Nonetheless, it is shown through numerical simulations that the HBD-ACS can meet typical Quality-of-Service (QoS) requirements, e.g., frame error rate $\leq 10^{-3}$, at high SNRs for a range of interference levels through II and SIC detectors.
- The desired and interfering signal levels are related through a scaling parameter. In contrast to the results in [22], it is shown that the asymptotic diversity gain of the SIC detector is zero for all interference levels.
- The HD-ACS is shown to achieve better diversity gain than the proposed HBD-ACS at low multiplexing gains. However, at high multiplexing gains, the HD-ACS achieves zero diversity gain while the proposed HBD-ACS achieves non-zero diversity gain.

¹Closed-form expressions are desirable as it allows for easy computation and it can also be used to reveal the relationship between the metric of interest and the modeled variables, e.g., relationship between outage probability and transmit power.

1.4.2 Chapter 4

- As II and SIC detectors are the focus of Chapter 3, this chapter focuses on the analysis of the joint detector. Specifically, a novel approach to obtain closed-form expressions for the outage probability and finite SNR diversity gain (for both fixed and variable transmission rates) of a joint detector over Rician fading channels is presented in this chapter.
- It is demonstrated that the outage probability and diversity gain of the joint detector is independent of the inter-UAV interference levels in moderate and high SNR regimes.
- At moderate and high SNR regimes, it is observed that the system level performance of the HBD-UCS with JD is suboptimal due to SI at the GS.
- It is shown that the diversity gain of the joint detector is independent of the data rate of the interfering signal when inter-UAV interference is sufficiently strong. In contrast, the SIC detector requires the data rate of the interfering signal from the HD UAV to be lower than the data rate of the signal-of-interest (SOI) from the FD-enabled GS to achieve non-zero diversity gain.
- Through multiplexing gain region (MGR) analysis, the JD-based HBD-UCS is shown to achieve superior finite SNR diversity gain, i.e., reliability, while supporting a wider range of QoS requirements than the II-based and the SIC-based HBD-UCS.

1.4.3 Chapter 5

- This chapter proposes a novel approach towards obtaining alternative power series representations of the probability density function (PDF), cumulative distribution function (CDF), and fractional moment for both the Rician fading and the Rician shadowed fading models. Different from the previous chapters, the analysis in the present chapter focuses on Rician shadowed fading channels which can occur in suburban environments.

- From the derived equations, closed-form outage probability expressions for the II and joint detectors using alternative power series expressions for the Rician shadowed fading and Rician fading models are obtained. To the best of our knowledge, the closed-form outage probability expressions and analysis are unavailable in the literature.
- Although counter-intuitive, it is shown that the impact of shadowing on the SI link at the FD-enabled GS is negligible. We also show that severe shadowing on the desired link with strong LOS component, as compared to weak LOS component, causes reduction in reliability even when SI mitigation measures are implemented.
- At UAV-2, the effect of severe shadowing on the desired link with strong LOS components is shown to be less severe for the joint detector than for the II detector.

1.4.4 Chapter 6

- Extending upon the common system model from prior chapters, an analytical framework based on stochastic geometry is proposed for outage probability analysis of multi-UAV networks with HBD UAV communications.
- It is demonstrated that the HBD-UCS concurrently supports more UAVs while achieving higher reliability than the HD UCS (HD-UCS). Specifically, at low transmit power regimes, it is shown that the HBD-UCS attains lower uplink and downlink outage probability than an HD-UCS, even as the UAV operating altitude is increased.

1.4.5 Chapter 7

- This chapter presents exact ergodic capacity expressions over Rician fading channels for NOMA-aided multi-UAV communications in FD heterogeneous networks (FD-HetNets) and HD heterogeneous networks (HD-HetNets) based on the stochastic geometry framework from the previous chapter.
- It is demonstrated that the FD-GS enables all nodes in the FD-HetNet to achieve higher ergodic capacity over HD-HetNets for NOMA-aided multi-UAV communications.

- With effective interference mitigation, it is shown that a higher number of uplink (UL) and downlink (DL) UAVs can be deployed in the FD-HetNet at lower altitudes while achieving higher ergodic sum capacity and ergodic capacity gains over HD-HetNets.
- The FD-HetNet is also shown to attain a higher ergodic sum capacity over the HD-HetNet despite lower levels of SI suppression and strong oscillator phase noise at the FD-GS.

1.4.6 Chapter 8

- A comprehensive performance analysis of a NOMA-aided UCS, comprising dual-antenna UAVs with selection combining, communicating over bivariate Rician shadowed fading channels is conducted in this chapter. Specifically, correlated channels are considered in this chapter, which was not considered in all prior chapters.
- New closed-form expressions are obtained for the joint PDF and joint CDF of the bivariate Rician shadowed fading model through a power series approach. From the obtained joint CDF expression, closed-form outage probability and finite SNR diversity gain expressions for NOMA-aided and orthogonal multiple access based (OMA-based) UCSs are presented within a stochastic geometry framework.
- Extensive analysis demonstrates that the NOMA-aided UCS can support a larger number of UAVs on the same spectrum than OMA-based systems while achieving highly similar outage probability. Furthermore, it is shown that cross correlation only affects the diversity gain of both NOMA and OMA transmissions at low SNR regimes.

1.5 Thesis Organization

The remaining part of this thesis is organized as follows. First, the state-of-the-art concerning UAV channel modeling, SI mitigation, modeling of FD transceiver impairments, interference management strategies, and NOMA techniques are discussed in Chapter 2. Next, outage probability and finite SNR analysis are evaluated for an HBD-ACS and

HBD UAV communications with JD in Chapter 3 and Chapter 4, respectively. Chapter 5 discusses the performance of HBD UAV communications with JD and II interference management strategies over Rician shadowed fading channels, while Chapter 6 presents an outage probability evaluation model based on stochastic geometry for HBD multi-UAV networks. The ergodic capacity of NOMA-aided FD-HetNets is evaluated in Chapter 7, while Chapter 8 analyzes the outage probability and finite SNR diversity gain of NOMA-aided UCSSs over correlated Rician shadowed fading channels. Finally, the thesis is concluded in Chapter 9, with discussions on relevant future directions.

Chapter 2

Addressing Spectrum Efficiency Through Hybrid-Duplex Communications: A Literature Review

2.1 Introduction

Spectrum scarcity is a major challenge in aeronautical networks. In UAV networks, spectrum scarcity can potentially lead to more sources of interference on the L-band and C-band, which have been allocated for CNPC links. Accordingly, the performance of UAV communications, e.g., reliability, may become degraded [23]. Likewise, spectrum scarcity in MAV networks can also lead to stronger interference experienced in MAV communications. As a consequence, interference-limited MAV communications may not be able to meet reliability and throughput requirements, e.g., bit error rate below 10^{-6} [24] or data rates of 1.37 Mbps [25].

As a first step towards addressing spectrum scarcity in aeronautical communications, it is crucial to note the similarities between UAVs and MAVs. In terms of operating altitudes, MAVs can be operated at an altitude between 3 km to 10 km [26] or even beyond 10 km [27]. In contrast, UAV operating altitudes vary between 300 m [28] to beyond 10 km [29]. MAVs can also fly at up to 900 km/h [26], while UAVs can maintain a flight speed between 57.6 km/h to 482 km/h [29]. Furthermore, MAVs and UAVs can be designed using multi-rotor or fixed-wing platforms [29].¹

¹The work in this chapter is derived from [30], which has been submitted for publication.

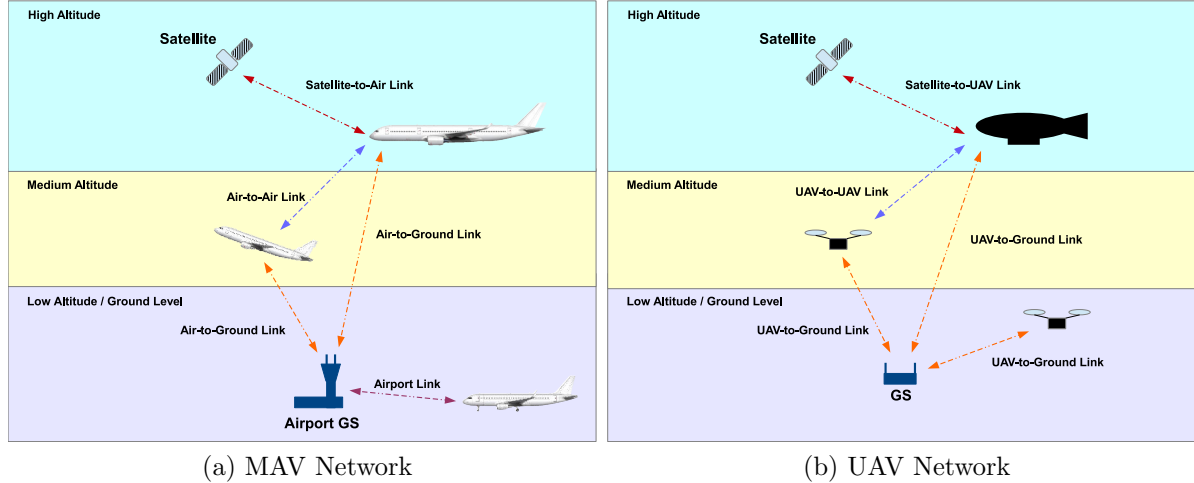


Fig. 2.1: An illustrated example of a MAV network and UAV network.

However, several differences are also noted between UAVs and MAVs. First, UAVs can be designed to be extremely lightweight, i.e., weighing less than 100 g [29]. UAVs also have limited range, flight time, and supported payload weight when compared to MAVs [29].

Nonetheless, when operated in a network, UAV and MAV networks are similar (Fig. 2.1). For instance, the multi-MAV network depicted in Fig. 2.1a shows an example of the airport link, Air-to-Ground, Air-to-Air, and Satellite-to-Air communications from ground level to a high altitude. Specifically, communications between the airport GS and the MAVs, i.e., aircraft, can occur at the ground level when the aircraft is stationary or moving on the tarmac [31]. At low to high altitude, MAVs can also communicate with the airport GS when en-route or arriving at the destination airport. MAVs can also communicate with other MAVs or satellite for navigational purposes.

Similarly, the multi-UAV network in Fig. 2.1b shows an example of UAV-to-Ground, UAV-to-UAV, and Satellite-to-UAV communications from ground level to a high altitude. In particular, communications between the GS or satellite and the UAVs can take place due to CNPC or non-CNPC transmissions. Depending on the type of application, UAVs can also transmit CNPC or non-CNPC data to other UAVs.

Given the similarities between UAV and MAV networks, the focus of this chapter will be on UAV communications. In particular, with considerable flight time, payload weight,

and range of MAVs, MAV networks can be viewed as a specific type of UAV network. Therefore, the work in this chapter is also applicable for MAV communications.

In the literature, UAVs have seen increased interest for various purposes, including the surveying of terrain [3], telecommunications relaying [4], and vehicular communications [5, 6]. In particular, the deployment of multi-UAV networks, i.e., swarms of UAVs, has received substantial interest from both industry and academia as a means towards addressing the limited payload and flight time of individual UAVs [3] and the lack of link redundancy in single-UAV networks [7]. Already, the deployment of multiple UAVs in the same network as flying base stations has been studied as a means to provide cellular service for ground users [2].

However, in light of the spectrum scarcity challenge and technical limitations associated with UAV communications, accurate and realistic modeling of an HBD-UCS is required before any potential solution can be explored. In the literature, extensive research has been carried out for various aspects of UAV communications. In [32], several aspects of UAV communications were surveyed, including the characterization of UAV network types, routing protocol requirements in multi-UAV networks, handoff schemes in multi-UAV networks, and energy efficiency algorithms in UAV communications at the physical, data link, and network layers. In [28], a survey discussing the delivery of Internet of Things (IoT) services with UAVs was noted. Specifically, the authors discussed several use cases and architectures for UAV-based IoT service delivery, UAV-related regulatory requirements, along with the associated technical challenges. In a survey paper presented by Hayat et al. [33], the characteristics, applications, and requirements of multi-UAV networks were discussed from a communications perspective. Several candidate technologies that can potentially support UAV communications were also surveyed, including Bluetooth and WiFi, along with open research problems and challenges. Apart from these survey papers, similar works that surveyed UAV communications for integrated satellite-aerial-terrestrial networks [27, 34], UAV-assisted wireless networks [35], UAV-based 5G and beyond networks [36], and UAV-assisted cellular networks [29] have been noted. Recent survey papers on channel modeling in UAV communications have also been seen [37, 38].

While the above survey papers have discussed many different aspects of UAV communications, the issue of spectrum scarcity has mainly been ignored. In this spirit, this

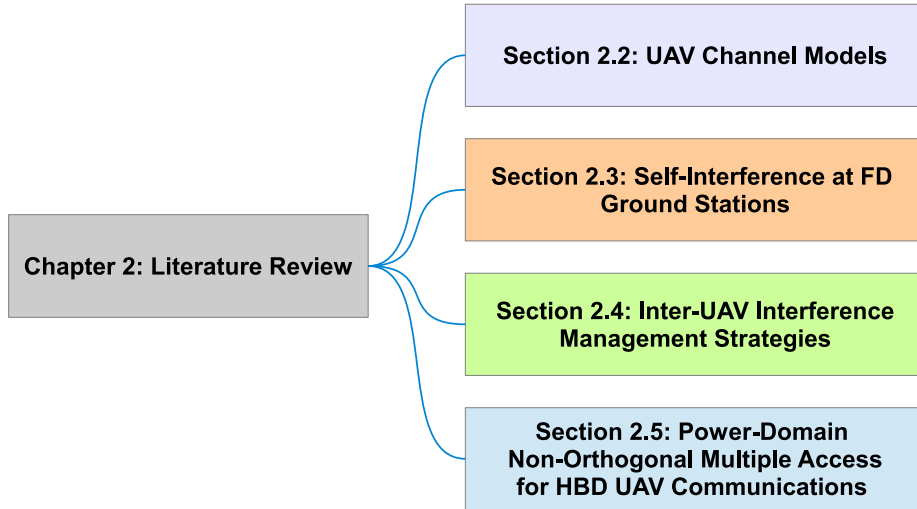


Fig. 2.2: The organization of the chapter.

chapter discusses the associated challenges and opportunities in HBD UAV communications. The focus here is on FD-based networks to improve spectrum efficiency in UAV communications.

The overall organization of this chapter is summarized in Fig. 2.2. In Section 2.2, the state-of-the-art related to UAV channel modeling is discussed, while Section 2.3 presents SI mitigation architectures that can be used in HBD-UCSs. The various types of FD transceiver imperfections, along with accurate modeling of the impairments, are also discussed in Section 2.3. Interference management strategies that can be adopted at the HD UAVs are discussed in Section 2.4. Specifically, the state-of-the-art and the advantages and disadvantages for different interference management strategies, and its practical implementation and performance evaluation when used in an HBD-UCS, are surveyed in Section 2.4. In Section 2.5, non-orthogonal multiple access (NOMA) methods are discussed to enable HBD-UCSs to support multi-UAV scenarios. Finally, the chapter is summarized in Section 2.6.

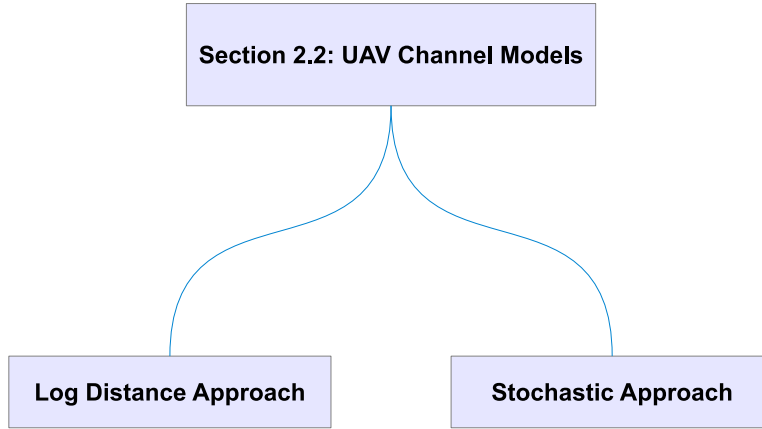


Fig. 2.3: An overview of the topics in Section 2.2.

2.2 UAV Channel Models

With UAVs operating in various types of environments, e.g., urban environments, and flight domains, e.g., en route, CNPC and non-CNPC transmissions can occur over line-of-sight (LOS), and beyond-line-of-sight (BLOS) links [39]. As a result, the experienced QoS levels in UAV communications can vary. In this context, accurate UAV channel modeling is a prerequisite towards any meaningful evaluation of HBD UAV communications. With no single validated and widely accepted UAV channel model in the literature [40], a review of UAV channel modeling is presented in this section (Fig. 2.3) and summarized in Tables 2.1 and 2.2.

2.2.1 Stochastic Approach

Summary 2.2.1 *The stochastic approach can be used to model UAV channels for specific scenarios/environments in the absence of available empirical data. However, the chosen statistical distribution of the UAV channel may not yield tractable expressions when computing performance metrics.*

The stochastic approach to UAV channel modeling considers the effects of small scale fading in the channel model, such as Rayleigh or Rician fading. In [41], the aeronautical channel model was characterized for MAVs, i.e., aircraft, over various flight domains. In particular, Haas [41] assumed that aeronautical communications took place over a

Rayleigh fading channel if the LOS path is blocked, e.g., when the aircraft is parked at the terminal. On the other hand, a Rician fading channel is assumed if a clear LOS path exists between the aircraft and the GS, e.g., when the aircraft is en route.

For UAV communications, recent studies on modeling the UAV channel through the stochastic approach have also made similar assumptions. For instance, the link between the GS and the UAV is modeled as a Rayleigh fading channel in [42–44]. Let $|h|^2$ be the squared channel gain for a UAV channel h . Then, the PDF of $|h|^2$ for an UAV channel under Rayleigh fading is [45, Table I]:

$$f_{|h|^2}(x) = \frac{1}{\Omega} \exp\left(-\frac{x}{\Omega}\right), \quad (2.1)$$

where Ω represents the average received power. While Rayleigh fading can be used to model the worst-case effects of the propagation environment [42] or UAV channels with blocked LOS links [43], such assumptions may not necessarily hold due to the operating altitude and terrain.

Measurement campaigns conducted for UAV communications over water [46], hilly terrains [47], and urban environments [8] have shown that the link between the GS and the UAV, i.e., A/G link, can be modeled as a Rician fading channel. More importantly, the empirical approach was undertaken in [8,46,47], which has yielded meaningful insights into the Rician K factor, path loss exponent, and delay spread that can be expected in the L-band and C-band. However, it must be pointed out that the measurement campaigns in [8, 46, 47] were conducted with a piloted aircraft. Therefore, the range of essential parameters for a UAV channel, e.g., Rician K factors, may differ from what was obtained from the empirical data due to differences in velocity and altitude between smaller sized UAVs and MAVs.

Nonetheless, the Rician fading assumption remains widely used in UAV channel modeling [48]. For a UAV channel under Rician fading, the PDF of $|h|^2$ is given as [45, Table I]:

$$f_{|h|^2}(x) = \frac{K+1}{\Omega} \exp\left(-K - \frac{K+1}{\Omega}x\right) I_0\left(2\sqrt{\frac{K(K+1)}{\Omega}}x\right), \quad (2.2)$$

where K , and $I_0(\cdot)$ are the Rician K factor and the modified zero order Bessel function of the first kind [49], respectively.

The expression in (2.2) has been used in [4, 50–52] to model the Rician fading UAV channel for A/G links. More interestingly, it was shown by Azari et al. [4] that the Rician K factor can be modeled as a function of the elevation angle θ (in radians), i.e., elevation-dependent, as:

$$K = A_1 \cdot \exp(A_2\theta), \quad (2.3)$$

where A_1 and A_2 are environment and frequency dependent constants, respectively. At higher altitudes, the likelihood of a direct LOS link (between a UAV and a GS) increases [53] due to less obstruction from buildings and terrain. Therefore, the UAV channel model in [4] is useful when taking the effect of LOS obstruction, i.e., non-line-of-sight (NLOS), into consideration. However, the main drawback is that the relationship between the Rician K factor and the elevation angle becomes environment-dependent [4].

Apart from A/G links, the Rician fading assumption has also been used to model the UAV-to-UAV channel in recent literature, e.g., in [54, 55]. The authors in [54] considered the impact of altitude on the Rician fading UAV-to-UAV channel and showed that the Rician K factor does not change significantly at high altitudes.

As seen from the earlier cited references in this subsection, the PDF expressions in (2.1) and (2.2) are widely used in the literature for UAV channel modeling. Moreover, PDF expressions enable a better understanding of how the propagation environment impacts UAV communications and also crucial in the computation of relevant performance metrics, e.g., outage probability. One disadvantage of the stochastic approach is the intractability of expressions when computing certain performance metrics owing to the complexity of PDF expressions. However, the stochastic approach enables UAV channel models to be approximated through PDF expressions, e.g., using (2.1) and (2.2), in the absence of readily available empirical data.

2.2.2 Log Distance Approach

Summary 2.2.2 *The log distance approach accurately models UAV channels when empirical data are readily available. However, such an approach is heavily dependent on the assumed operating environment. Thus, UAV channel models obtained through the log distance approach are environment-specific.*

The log distance approach involves modeling the UAV channel by quantifying path loss due to the transmission distance and propagation environment. Such an approach has been used by the International Telecommunication Union (ITU-R) [56], with free space path loss (FSPL) [57] being a common assumption in recent research.

In [58], FSPL was assumed for the UAV channel, where the path loss is a function of the elevation angle and transmission distance in the A/G link. Feng et al. [58] also modeled the effect of shadowing as a Normal distribution with zero mean and elevation-dependent standard deviation (σ) as:

$$\sigma = B_1(90 - \theta)^{B_2}, \quad (2.4)$$

where B_1 and B_2 are obtained through curve fitting for the environment of interest. In [59], FSPL was also assumed for the A/G link, with shadowing and scattering modeled as a Gaussian random variable (RV). Unfortunately, the effects of small scale fading are not considered in [58] and [59]. Thus, the analysis in [58, 59] cannot be readily applied for low altitude UAV channel models since small scale fading is likely to occur. In [2], the authors assumed FSPL for both LOS and NLOS links in the UAV channel model. The amount of FSPL is taken as a function of the ground receiver's location. Additionally, Mozaffari et al. [2] assumed the probability of the UAV channel encountering LOS and NLOS links to be elevation-dependent in the A/G link using the following relationship:

$$Pr(LOS) = b_1 \left(\frac{180}{\pi} \theta - 15 \right)^{b_2} \quad (2.5)$$

$$Pr(NLOS) = 1 - Pr(LOS), \quad (2.6)$$

where b_1 and b_2 are environment-dependent constants.

It must be pointed out that depending on the operating environment, the FSPL assumption might not always hold due to larger path loss exponents. To this end, recent works have adopted a general log distance approach to consider arbitrary path loss exponent values as follows:

$$L(d) = n \cdot 10 \log(d/d_0) + C + X, \quad (2.7)$$

where $L(d)$ is the path loss in dB from distance d in meters, $d_0 = 1$ is the reference distance, n is the path loss exponent, C is a constant dependent on antenna gain and path loss from distance d_0 , and X is a RV representing excess path loss.

Table 2.1: Summary of UAV Channel Modeling Considerations

Reference	Approach	Small Scale Fading Model	Shadowing Model	UAV Velocity Model	UAV Spatial Model
[2]	Log Distance	-	-	-	Gaussian
[4]	Stochastic	Rician	-	-	PPP
[42, 43]	Stochastic	Rayleigh	-	-	PPP
[44]	Stochastic	Rayleigh	-	-	-
[50, 51]	Stochastic	Rician	-	Constant	-
[52]	Stochastic	Rician Shadowed	Rician Shadowed	-	-
[54]	Stochastic	Rician	-	-	-
[55]	Stochastic	Rician	-	Constant	ST Mobility Model [60]
[58, 59]	Log Distance	-	Gaussian	-	-
[61, 62]	Log Distance	-	Gaussian	-	-
[63]	Log Distance	Rician, Rayleigh	Gaussian	Gaussian	Uniform
[64]	Log Distance	-	Log Normal	-	-

Table 2.2: Summary of Advantages and Disadvantages of the UAV Channel Modeling Approaches

Approach	Advantage	Disadvantage
Stochastic	Uses well-known statistical distributions to model the UAV channel.	Analysis may be intractable.
Log Distance	Accurately models UAV channels with empirical data.	Environment-specific.

In [61] and [62], path loss is modeled using (2.7) in the UAV channel model. Shadowing is also modeled in [61] by letting X be a zero mean Gaussian RV, with elevation-dependent standard deviation taken as:

$$\sigma = B_1\theta + B_2. \quad (2.8)$$

In [63], the authors modeled the UAV channel by combining the effect of path loss, gaseous absorption, shadowing, Doppler spread, and small scale fading. However, only arbitrary path loss exponents were considered for the NLOS link in the UAV channel model, with FSPL assumed for the LOS link. In [64], the log distance approach was assumed for an A/G UAV channel in a suburban environment. Sallouha et al. [64] also considered the impact of the elevation angle (θ) on the probability of LOS occurrence ($Pr(LOS)$) and the path loss exponent (n) through the following relationship:

$$Pr(LOS) \approx \frac{1}{1 + b_1 \exp(-b_2\theta)}, \quad (2.9)$$

$$n = (2 - B_3)Pr(LOS) + B_3, \quad (2.10)$$

where $B_3 \in [2.7, 3.5]$.

One disadvantage of the approach undertaken in [64], along with earlier cited references in this subsection, is that the resultant UAV channel model is highly dependent

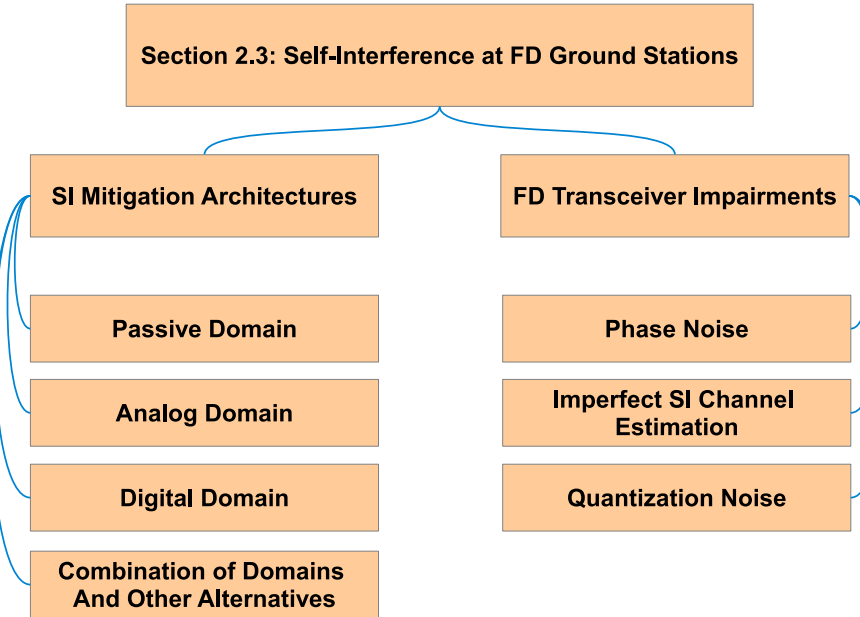


Fig. 2.4: An overview of the topics in Section 2.3.

on the operating environment. Thus, the insights gained from log distance-based UAV channel models in suburban environments may not necessarily apply for UAV channel models in other environments, e.g., over hilly terrains. Nevertheless, the log distance approach is still useful in modeling UAV channels for specific environments where empirical data can be readily obtained.

2.3 Self-Interference at FD Ground Stations

As GSs operate in FD mode in HBD UAV communications, SI at GSs must be modeled accurately to enable a meaningful performance analysis. To this end, a review of SI mitigation architectures and the impairments associated with FD transceivers are provided in this section (Fig. 2.4).

2.3.1 SI Mitigation Architectures

Summary 2.3.1 *SI mitigation architectures operate in the passive, analog, or digital domain. Architectures that involve combinations of different domains are also possible.*

However, SI cannot be completely removed due to FD transceiver impairments.

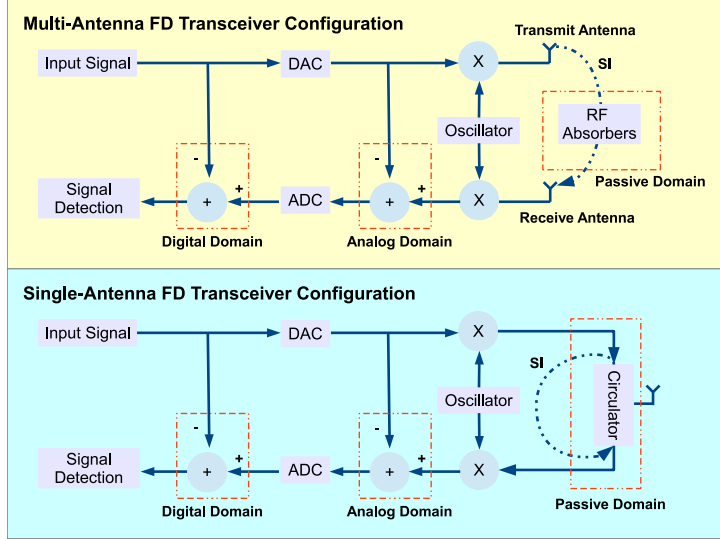


Fig. 2.5: An example of SI mitigation in multi-antenna and single-antenna FD transceivers. For both configurations, SI mitigation through combinations of passive, analog, and digital domain techniques are possible.

Mitigating SI in FD transceivers is a topic that has been widely investigated in the literature. In particular, a wide body of works has investigated SI mitigation architectures that operate in different signal domains. Alternative approaches, such as beamforming, have also been proposed. The principles and tradeoffs associated with the various architectures are presented below. A summary of studies on SI mitigation architectures is also provided in Table 2.3.

2.3.1.1 Passive Domain

SI mitigation architectures operating in the passive domain suppresses SI through the induction of pathloss. For multi-antenna FD transceivers, pathloss can be induced through antenna separation and placement of radio frequency (RF) absorbers [65]. The use of balanced/unbalanced (Balun) transformers has also been discussed [66]. On the other hand, circulators and duplexers are used to isolate the transmit and receive chains in single-antenna FD transceivers [67]. Specifically, a circulator restricts transmit chain signals from interfering with receive chain signals, e.g., Fig. 2.5, while a duplexer undergoes tuning to match the impedance of the antenna. In [68], an antenna patch for a

single-antenna FD transceiver configuration was designed to mitigate SI in the passive domain without the need for circulators and duplexers.

Although it has been shown that SI can be mitigated in the passive domain, there are still drawbacks associated with passive domain techniques. Multi-antenna FD transceivers suffer from a reduction in overall spectrum efficiency since antennas are dedicated to either transmit or receive signals [68]. For single-antenna FD transceivers, circulators may cause the overall size of the transceiver to be substantial due to the wavelength of the signal's frequency [67]. In contrast, duplexers can be smaller in size. However, frequent tuning is still required, thus reducing overall spectrum efficiency.

In the context of HBD UAV communications, passive domain techniques may be feasible in specific operating environments, e.g., FD-enabled GSs in urban environments. However, such techniques may not be cost-effective and suffer from limited SI mitigation capabilities [68]. Nonetheless, it must be noted that the size and power requirements for FD-enabled GSs may not be as stringent. Thus, the effectiveness of passive domain SI mitigation architecture can be further investigated for FD-enabled GSs in HBD UAV communications.

2.3.1.2 Analog Domain

For SI mitigation architectures operating in the analog domain, SI is mitigated before the receive chain signal enters the transceiver's analog-to-digital converter (ADC). In particular, the SI cancellation signal is first generated by taking a copy of the transmit chain signal at the output of the transceiver's digital-to-analog converter (DAC), e.g., Fig. 2.5. Such an approach enables the SI cancellation signal to retain the same transceiver impairments of the SI signal, such as oscillator phase noise. Thereafter, the SI cancellation signal is added to the incoming receive chain signal to remove SI. Examples of works that have investigated SI mitigation in the analog domain include [21, 69], and [70].

Although analog domain SI mitigation architectures have been widely studied, overcoming the associated limitations remains a challenge. The cost, size, and power consumption of the FD transceivers may increase when considering SI mitigation in the analog domain [71]. Furthermore, SI cancellation in the analog domain is limited by transceiver impairments, such as imperfect SI channel estimation and phase noise [21].

Table 2.3: Summary of Studies on SI Mitigation Architectures

Reference	Domain	SI Suppression	RF Chain Configuration	SI Channel Model
[17]	Analog, Digital	163 dB to 175 dB	Separate	Rician Fading
[18]	Analog, Digital	163 dB to 175 dB	Separate	Rician Fading
[19]	Analog, Digital	163 dB	Separate	Rician Fading
[20]	Analog, Digital	174 dB to 181 dB	Separate	Rician Fading
[21]	Analog, Digital	35 dB to 60 dB (Analog), 0 dB to 32 dB (Digital)	WARP [72], Vector Signal Generator [73]	Rayleigh Fading
[65]	Passive (Antenna Separation, RF Absorbers)	24.5 dB to 73.8 dB	Separate	Rician Fading, Rayleigh Fading
[66]	Passive (Balun)	40 dB to 52 dB	Separate	Rayleigh Fading
[67]	Passive (Circulators, Duplexers)	20 dB to 22 dB	Single	Non-linear
[68]	Passive (Single-Patch Antenna), Digital	56 dB to 60 dB (Passive) 14 dB to 35 dB (Digital) 84 dB to 88 dB (Total)	Single	Frequency-selective Rayleigh Fading
[69]	Analog, Digital	20 dB to 60 dB (Passive)	Separate	Rician Fading
[70]	Analog, Digital	60 dB to 110 dB (Total)	Separate	Multipath
[71]	Others (Advanced Sampling)	35 dB	Separate	Rician Fading
[74]	Digital	35 dB	Separate	Static Multipath
[75]	Digital	25 dB to 60 dB (Passive)	Separate	Rician Fading
[76]	Digital	20 dB to 60 dB	Separate	Rayleigh Fading
[77]	Analog, Digital	-	Separate	Rayleigh Fading
[78]	Others (Beamforming)	-	Separate	Multipath
[79]	Others (Beamforming)	-	Separate	Rayleigh Fading
[80]	Others (Beamforming)	-	Separate	Rayleigh Fading

Despite the limitations, implementing analog domain SI mitigation, in the context of HBD UAV communications, is an interesting research problem of practical significance. For instance, analog domain SI mitigation architectures at FD-enabled GSs can be investigated to understand potential cost and power requirements. Understanding such requirements will be beneficial towards an evaluation of development and operational feasibility for HBD UAV communications.

2.3.1.3 Digital Domain

For digital domain SI mitigation architectures, SI is mitigated after the receive chain signal exits the transceiver's ADC. Specifically, the SI cancellation signal is generated using a copy of the transmit chain signal at the input of the transceiver's ADC (Fig. 2.5). Similar to analog domain SI mitigation, the SI cancellation signal in the digital domain also retains the same transceiver impairments as the SI signal. SI is then mitigated by adding the SI cancellation signal to the receive chain signal at the output of the transceiver's ADC. Studies that have adopted such an approach include [21,68–70,74–76].

With extensive studies on digital domain SI mitigation architectures noted in the literature, some techniques have achieved substantial amounts of SI cancellation [71]. Nonetheless, there are several limitations associated with SI cancellation in the digital domain. Similar to analog domain techniques, digital domain SI cancellation is also limited by phase noise and imperfect SI channel estimation. In particular, the latter affects the quality of the SI cancellation signal since an imperfect SI channel estimate leads to inaccurate modeling of the actual SI signal [68]. In addition to phase noise and imperfect SI channel estimation, the dynamic range of the ADC is another key constraint in digital domain techniques. With a limited dynamic range, the input of the ADC is mostly dominated by the SI instead of the desired signal when the SI power is high [69, 74]. As a result, the desired signal becomes overwhelmed by quantization noise [71]. Other associated limitations include transceiver nonlinearities [75] and in-phase/quadrature (IQ) imbalance [76].

Addressing the limitations of digital domain SI mitigation remains an interesting research problem. These issues must be adequately investigated before the practical implementation of FD-enabled GSs in HBD UAV communications.

2.3.1.4 Combination of Domains and Other Alternative Approaches

Apart from focusing on SI mitigation techniques that operate in a specific domain, SI mitigation that involves the combination of techniques from different domains have been seen in the literature. For instance, Amjad et al. [68] combined passive suppression, through a proposed antenna design, with digital SI mitigation to achieve 88 dB of SI suppression.

Separately, other studies, e.g., [17–19, 21, 69, 77], have assumed a combination of analog and digital SI cancellation operating in cascade. Specifically, the SI signal undergoes SI mitigation in the analog domain first, before SI cancellation in the digital domain. To account for FD transceiver impairments, residual SI is considered in the signal models of [17–19, 21, 69, 76, 77]. The strength of the residual SI depends on a variety of factors, including the variance of the phase noise [17–19, 21, 69, 76], variance of the SI channel estimation error [17–19, 21, 69, 81], quantization noise [69], and transmit power [77].

Other than techniques that focus on SI cancellation, innovative solutions have also been pursued. Beamforming, for example, has been studied in [78–80] to suppress SI

while an advanced sampling technique that avoids sampling the SI signal was proposed in [71]. However, it remains to be seen if these techniques, e.g., beamforming or advanced sampling, can be realistically implemented owing to the associated computational complexity and hardware cost.

2.3.2 Modeling FD Transceiver Impairments in HBD UAV Communications

Summary 2.3.2 *Accurate modeling of FD transceiver impairments, e.g., phase noise, imperfect SI channel estimation errors, and quantization noise can be used to gauge the strength of residual SI in FD transceivers.*

As impairments are present in FD transceivers, realistic modeling of the imperfections is required to enable a sound analysis of HBD UAV communications. To this end, some of the impairments that are commonly found in the literature are discussed below.

2.3.2.1 Phase Noise

In FD transceivers, phase noise stems from the jitter present in the oscillator [21]. Depending on the FD transceiver design, the strength of the phase noise can differ. FD transceivers with shared oscillators are impaired from the same phase noise source on both the transmit and receive RF chains [76, 82]. In contrast, FD transceivers with separate oscillators for the transmit and receive RF chains are affected by two independent phase noise sources, thus leading to stronger phase noise [76].

To account for phase noise in FD transceivers, one can adopt the models in [17–19, 21]. Specifically, let the phase noise term be $\gamma_\phi w_\phi$, where w_ϕ is a Gaussian RV with zero mean and unit variance, and γ_ϕ be a scaling factor. The scaling factor depends on the oscillator of interest. For instance, the transceivers (transmit chain) used in [21, Appendix C] have variance (denoted as σ_ϕ in [21]) of $\gamma_\phi^2 = 0.717^\circ = 0.0125$ radians and $\gamma_\phi^2 = 0.066$. Furthermore, in [21, Appendix C], $\sigma_\phi = 2\pi f_c \Delta t_{RMS}$, where f_c is carrier frequency and Δt_{RMS} is the jitter in time. Thus, one can accurately model the strength of the phase noise based on the transceiver specifications such as the carrier frequency and jitter in time.

2.3.2.2 Imperfect SI Channel Estimation

In theory, SI can be eliminated if the full channel state information (CSI) of the SI channel is known. However, in practice, the SI channel is estimated using a training sequence [21, 75]. The inaccuracy of the SI channel estimation process invariably contributes to residual SI at the FD transceiver as the SI canceling signal is generated based on the estimated SI channel.

To model the imperfect SI channel estimation, one can adopt the model in [81]. In particular, let \tilde{h}_{si} be the error of the imperfect SI channel gain estimate, where $\tilde{h}_{si} = h_{si} - \hat{h}_{si}$, h_{si} is the SI channel gain, and \hat{h}_{si} is the imperfect estimation of h_{si} . Furthermore, let \tilde{h}_{si} be modeled as a zero mean, circularly symmetric complex Gaussian RV with variance ϵ to quantify the SI channel estimation error [81]. The variance ϵ of \tilde{h}_{si} represents the accuracy of the measured CSI for the SI channel. It is worth noting that the same approach has been seen in [83] for the modeling of residual interference in wireless networks. By modeling \tilde{h}_{si} as a Gaussian RV, the worst case residual SI can be accounted in the FD transceiver [81].

2.3.2.3 Quantization Noise

In FD transceivers, the quantization of the SI signal from the analog to the digital domain introduces noise to the overall SNR [69, 75]. When the SI signal is strong, the dynamic range of the ADC becomes increasingly occupied by the SI signal, thus reducing the dynamic range available for the desired signal [74]. In turn, the performance of the FD transceiver is limited by quantization noise, since the ADC operates with a small number of bits, which masks the weak desired signal at the ADC output [69, 71].

Quantization noise at an m -bit ADC can be modeled in terms of the low noise amplifier (LNA) as $\sigma_{ADC}^2 = \frac{1}{\alpha_{LNA} 12 \cdot 2^{2m-2}}$, where α_{LNA} denotes the LNA gain [69, 75]. Based on the definition of σ_{ADC}^2 , quantization noise can be effectively reduced by increasing the LNA gain (α_{LNA}) or the number of bits (m) [75]. However, having ADCs that can realistically operate with a large number of bits, e.g., $m > 16$, is still an open research problem.

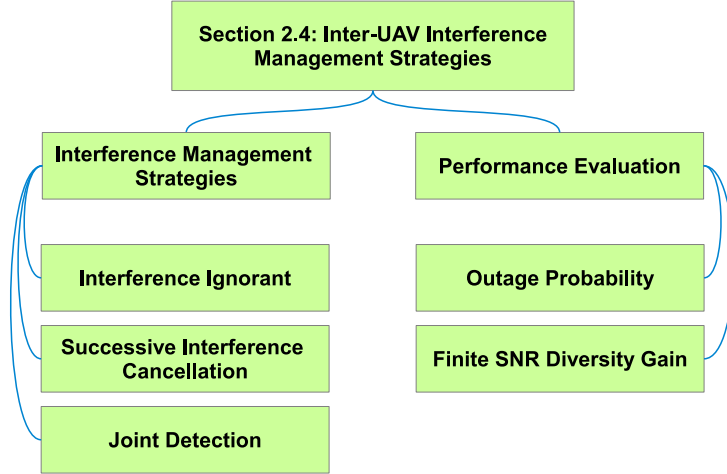


Fig. 2.6: An overview of the topics in Section 2.4.

2.4 Inter-UAV Interference Management Strategies

In HBD UAV communications, inter-UAV interference is experienced at the HD downlink UAVs due to simultaneous uplink and downlink transmissions. In this regard, a review of interference management techniques is presented in this section for HBD UAV communications. Thereafter, an overview of the performance analysis is presented for the discussed interference management techniques (Fig. 2.7) for the HBD-UCS. An overview of the topics in this section is provided in Fig. 2.6.

2.4.1 Interference Management Strategies

Summary 2.4.1 *The II and SIC strategies offer effective inter-UAV interference management under weak and strong interference, respectively. However, inter-UAV interference management with JD, based on simultaneous non-unique decoding, outperforms both II and SIC strategies.*

As mentioned earlier, inter-UAV interference in HBD UAV communications is caused by uplink and downlink transmissions occurring concurrently on the same spectrum. With inter-UAV interference management being an important aspect of realizing HBD UAV

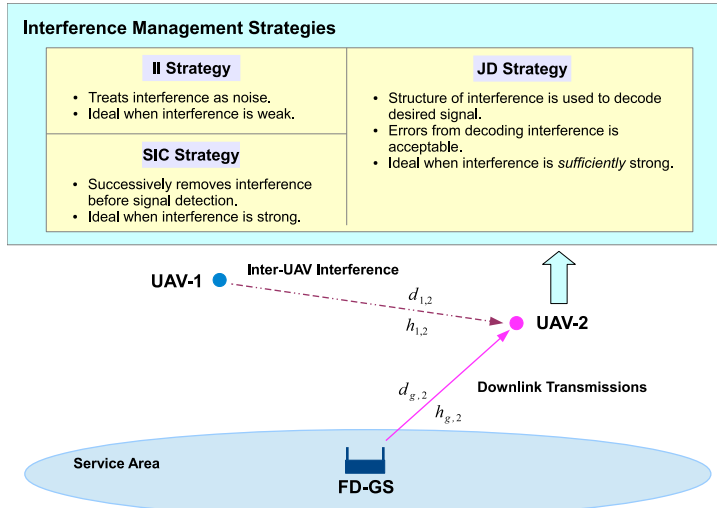


Fig. 2.7: An example of the types of interference management strategies that can be adopted for UAV-2 in the HBD-UCS.

communications, many interference management approaches have been investigated in the literature. Towards this endeavour, a review of interference management techniques for HBD UAV communications is presented below, with discussions focusing on the II, SIC, and JD approaches. A summary of studies on interference management strategies is also provided in Table 2.4.

2.4.1.1 Interference-Ignorant

The II approach is a simple interference management strategy that ignores interference by treating it as noise [17–19, 22, 84, 85]. In weak interference scenarios, the II approach is sum rate optimal [22]. However, under strong interference scenarios, the II approach is ineffective, particularly at high SNR regimes [17]. Furthermore, since information can be obtained from the received interfering signals, an opportunity to exploit the underlying structure of the interference for interference management is lost in the II approach [84].

Despite the limitations, the II approach has been analyzed for practical applications in wireless systems, e.g., in aeronautical communication systems [17] and cellular networks [85, 86]. For UAV communications, the II approach was investigated in [18, 19, 52] for an HBD-UCS as depicted in Fig. 2.7. Specifically, for the HBD-UCS in Fig. 2.7, the II detector at UAV-2 treats the signal from the FD-enabled GS ($x_{gs}[t]$) as the SOI while

treating the signal from UAV-1 ($x_1[t]$) as noise. Since the II approach is simple to implement, it can be used to provide effective interference management in an HBD-UCS for weak interference scenarios, as shown in [18, 52].

2.4.1.2 Successive Interference Cancellation

The SIC approach involves detecting and canceling the interference first, before the SOI is detected [17, 18, 20]. In particular, a SIC detector detects and removes the strongest interferer first, where the strongest interferer is defined either as the interferer with the highest average received power or the interfering node that is closest to the receiver [87]. Doing so enables the SIC detector to remove the interferer with the highest signal-to-interference-plus-noise ratio (SINR) from the received composite signal [87, 88]. The SIC process is repeated until interference from nearby interfering nodes within a cancellation region around the receiver is removed [87], or interference is wholly removed from the received composite signal [88]. For the former, the cancellation region describes a disk centered at the receiver, where a subset of the interfering nodes is located [87]. The radius of the cancellation region is then chosen such that the interference cancellation for a specific average number of interfering nodes can be performed.

Additionally, the considered SIC process can be either perfect or imperfect. The perfect SIC model assumes that interference from the prior SIC stages is entirely removed, e.g., in [17] and [87]. For the case of imperfect SIC, residual interference from previously canceled interfering signals is considered at each stage of the SIC process, e.g., in [20, 87]. Putting the practical relevance of the imperfect SIC model into perspective, the residual interference can be used to account for non-ideal transmission conditions such as channel estimation errors.

In the literature, the SIC approach has been shown to improve the performance of interference-limited systems, e.g., in terms of reliability or transmission rate, for both perfect SIC [17, 18, 87, 88] and imperfect SIC [20, 87]. Furthermore, it was shown in [87] that through the cancellation of the strongest interferer alone, significant performance improvements can be obtained. However, for the SIC process to work, the transmission rate of each interferer must be constrained to meet the SINR requirement such that the strongest interferer transmits with the lowest rate, and so on [88]. Therefore, enabling

Table 2.4: Summary of Studies on Interference Management Strategies

Reference	Approach	Channel Model	Performance Metric(s)
[17]	II, SIC	Rician Fading	Outage Probability, Finite SNR Diversity Gain, Finite SNR DMT
[18]	II, SIC, JD (SND)	Rician Fading	Outage Probability, Finite SNR Diversity Gain, Finite SNR DMT
[19]	II, JD (SND)	Rician Fading, Rician Shadowed Fading	Outage Probability
[20]	II, SIC	Rician Fading	Outage Probability
[52]	II	Rician Shadowed Fading	Outage Probability
[85]	II, JD (SND)	Rayleigh Fading	Diversity Gain Region
[86]	II	Rayleigh Fading, Squared K -distribution [91]	Outage Probability, Average Bit Error Probability
[87]	SIC	Path Loss	Outage Probability, Transmission Capacity
[88]	SIC	Rayleigh Fading	Throughput, CPU Run Time
[92]	JD (SD, SND)	-	Rate Region
[93]	II, JD (SD, SND)	Static AWGN	Rate Region, Throughput
[94]	JD (SD)	Path Loss	Capacity Region
[95]	JD (SND)	-	Rate Region
[96]	JD (SND)	Rayleigh Fading	Asymptotic DMT

the SIC detector to support a large number of interfering nodes requires trading away the overall achievable rate, i.e., a tradeoff between SIC capability and achievable rate [88].

Thus far, the SIC approach has attracted research interest, particularly in recent years, for various practical applications in wireless systems. For instance, the performance of SIC has been studied for cellular systems [22, 85, 89, 90]. Likewise, the feasibility of the SIC approach has been studied for UAV communications in [18, 20]. To illustrate, a two-stage SIC detector can be assumed for UAV-2 in Fig. 2.7. The SIC detector at UAV-2 detects and removes $x_1[t]$ from UAV-1, before detecting the SOI $x_{gs}[t]$ from the FD-enabled GS. As shown in [18], implementing SIC to manage inter-UAV interference enables the HBD-UCS to achieve better reliability over an equivalent HD-UCS in strong inter-UAV interference scenarios.

2.4.1.3 Joint Detection

The JD approach involves the joint detection of the SOI and interfering signals during the detection process. In the literature, multiple JD approaches have been studied. Of particular importance are two types of JD techniques, namely simultaneous decoding (SD) [92–94] and simultaneous non-unique decoding (SND) [92, 93, 95].² In SD, the receiver employs a strategy that utilizes the underlying structure of the interference to decode correctly, i.e., detect, both SOI and interference signal [92–95].

²In [92], SD and SND are referred as joint unique decoding and non-unique decoding, respectively.

In contrast, SND employs a strategy that is similar to SD, except that errors from decoding, i.e., detecting, the interfering signals are tolerated [92, 93, 95]. Thus, the SND strategy only focuses on the correct detection of the SOI transmitted over the interference channel. As it turns out, the SND strategy can attain the rate regions of the SD strategy and the II approach [93, 95]. As such, when compared to SD, SND attains better performance by simultaneously achieving the combined rate regions of the SD and the II approaches [93, 95], albeit at the cost of high complexity [18]. In light of the benefits brought on by the SND strategy, in the remainder of this section, discussions on JD will henceforth refer to the SND strategy.

It is noted that the JD approach, i.e., SND strategy, has been investigated for potential applications in practical wireless systems. For instance, a 2-user multiple input multiple output (MIMO) system was proposed in [96] that combines transmissions using interference alignment, i.e., beamforming, with receivers that adopt JD. For UAV communications, the feasibility of JD was studied in [18]. In particular, a joint detector employing the SND strategy can be equipped on UAV-2 for the HBD-UCS depicted in Fig. 2.7. Thereafter, the joint detector at UAV-2 jointly detects $x_{gs}[t]$ and $x_1[t]$ from the FD-enabled GS and UAV-1, respectively. Following the principles of the SND strategy, detection errors of the interfering signal $x_1[t]$ are tolerated by the joint detector at UAV-2, since the focus is on detecting the SOI $x_{gs}[t]$. Extensive performance analysis of a JD-based HBD-UCS in [18] has demonstrated that the JD approach outperforms the II and SIC approaches. In particular, the JD approach enables the HBD-UCS to achieve higher reliability than the II and SIC approaches while supporting a wider range of QoS requirements. Thus, JD is the most attractive interference management technique for HBD UAV communications when compared against the II, and SIC approaches.

2.4.2 Performance Evaluation of the II, SIC, and JD Strategies for HBD UAV Communications

Summary 2.4.2 *Outage probability and finite SNR diversity gain are useful tools in determining the effectiveness of the II, SIC, and JD approaches for inter-UAV interference management. In this aspect, JD attains lower outage probability and higher finite SNR diversity gain than the II and SIC approach.*

In this subsection, a review of the performance analysis of the II, SIC, and JD approaches is presented. To show the effectiveness of the considered interference management strategies for HBD UAV communications, the outage probability and finite SNR diversity gain of the II, SIC, and JD approaches are also discussed in the context of the HBD-UCS depicted in Fig. 2.7.

2.4.2.1 Outage Probability

One way to gauge the feasibility of the II, SIC, and JD approaches is to analyze the reliability of HBD UAV communications. In this sense, outage probability is a useful metric as it can be used to represent the packet error rate (*PER*) of the HBD-UCS for transmissions spanning over one fading block [17, 97], i.e., block fading assumption.

To obtain any meaningful analysis, closed-form outage probability expressions that can accurately reflect the communications environment, e.g., small-scale fading, receiver noise, and interference, are needed for the II, SIC, and JD approaches. For instance, closed-form outage probability expressions for the II detector are available for transmissions over Nakagami- m fading channels [98], and composite fading scenarios, where the SOI is transmitted over Rayleigh fading channels and interference is experienced over squared \mathcal{K} -distributed channels [86]. More recently, a unified moment-based approach was proposed by Rached et al. [45] that presents closed-form outage probability expressions for transmissions over various types of fading channels, including Rician fading channels that are encountered in UAV communications. Based on the work in [45], the II detector was subsequently analyzed for HBD-based aeronautical communication systems [17, 99] and HBD-UCSs over Rician fading channels [18–20, 52, 100] and Rician shadowed fading channels [19, 101].

Similarly, closed-form outage probability expressions for SIC detectors are available in [89] and [102]. In particular, the analysis in [89] and [102] assumes that the SOI is transmitted either over Nakagami- m , Rayleigh, or Rician fading channels while interference is experienced over Rayleigh fading channels. However, the resultant closed-form expressions presented in [89] and [102] are for partial SIC, where there is at least one remaining interferer once the SIC process ends. In [90], closed-form outage probability expressions were derived for a two-stage SIC detector that receives power-domain

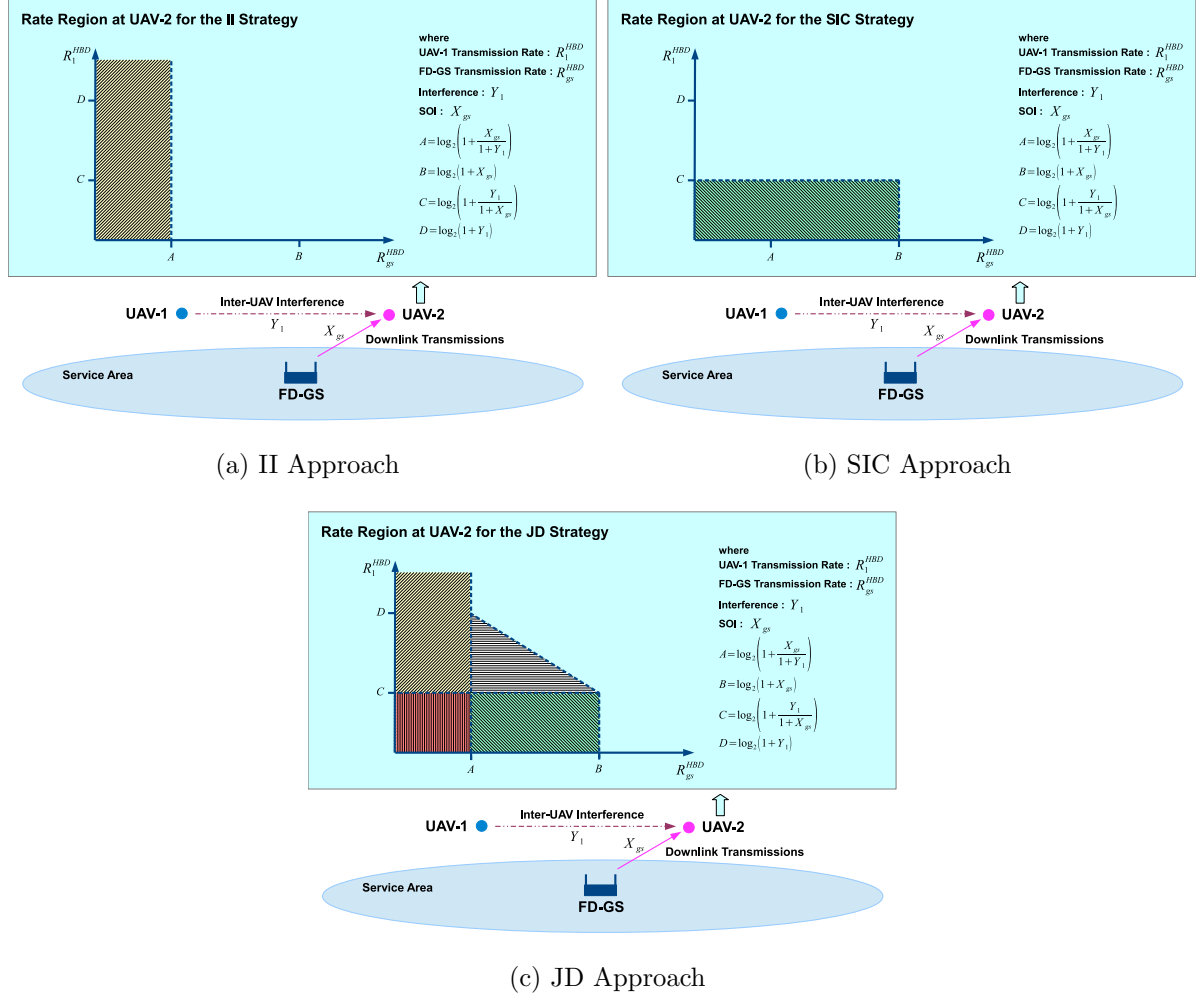


Fig. 2.8: The achievable instantaneous rate region of the II, SIC, and JD interference management approaches. The transmission rate of the FD-GS and UAV-1 are denoted as R_{gs}^{HBD} and R_1^{HBD} , respectively. The variables X_{gs} and Y_1 denote the SOI and interference at UAV-2, respectively.

Table 2.5: Outage probability definitions of the II, SIC, and joint detectors at UAV-2.

Protocol/Detector	Outage Notation	Outage Event Definitions	References
II Detector	$Pr(O_2^{HBD(II)})$	$O_2^{HBD(II)} = \left\{ h_{g,2}, h_{1,2} : R_{gs}^{HBD} \geq \log_2 \left(1 + \frac{X_{gs}}{Y_1+1} \right) \right\}$	[17, eq. (7)]
SIC Detector	$Pr(O_2^{HBD(SIC)})$	$O_2^{HBD(SIC)} = \left\{ h_{g,2}, h_{1,2} : R_1^{HBD} > \log_2 \left(1 + \frac{Y_1}{1+X_{gs}} \right) \right\}$ $\cup \left\{ h_{g,2}, h_{1,2} : R_1^{HBD} \leq \log_2 \left(1 + \frac{Y_1}{1+X_{gs}} \right), R_{gs}^{HBD} > \log_2 (1 + X_{gs}) \right\}$	[17, eq. (9)]
Joint Detector	$Pr(O_2^{HBD(JD)})$	$O_2^{HBD(JD)} = O_{JD}^1 \cup O_{JD}^2$ $O_{JD}^1 = \left\{ h_{g,2}, h_{1,2} : R_{gs}^{HBD} > \log_2 (1 + X_{gs}) \right\}$ $O_{JD}^2 = \left\{ h_{g,2}, h_{1,2} : R_1^{HBD} + R_{gs}^{HBD} > \log_2 \left(1 + X_{gs} + Y_1 \right), \log_2 \left(1 + \frac{X_{gs}}{1+Y_1} \right) \leq R_{gs}^{HBD} \leq \log_2 \left(1 + X_{gs} \right) \right\}$	[18, eq. (9)]
HD-UCS	$Pr(O_2^{HD})$	$O_2^{HD} = \left\{ h_{g,2} : R_{gs}^{HD} \geq \log_2 (1 + X_{gs}) \right\}$	[17, eq. (11)]

NOMA transmissions over Rayleigh fading channels. Apart from the studies mentioned above, closed-form outage probability expressions for a two-stage SIC detector was derived in [17] for an HBD aeronautical communication system, and also in [18, 100] for an HBD-UCS, where both the SOI and interference are transmitted over Rician fading channels.

For the case of the JD approach, closed-form outage probability expressions have been presented in [103] and [104] for receivers operating in a Rayleigh fading environment. In particular, the analysis in [103] and [104] was conducted for femtocell relay systems and cognitive radio systems, respectively, where the SND strategy was assumed at the relay node. In [18], closed-form outage probability expressions for JD in an HBD-UCS was derived over Rician fading channels, where it was shown that JD achieves near-optimal outage probability.

From the above discussions, the outage probability of the II, SIC, and JD approaches has been well analyzed for an HBD-UCS (Fig. 2.7), each with different advantages and limitations. To better illustrate this, the achievable instantaneous rate regions of the II, SIC and JD approaches at UAV-2 are depicted in Fig. 2.8 [18, Fig. 2], where X_{gs} and Y_1 denote the SOI from the FD-GS and interference from UAV-1, respectively. From Fig. 2.8, it is evident that JD achieves the largest achievable instantaneous rate region (Fig. 2.8c) compared to the II (Fig. 2.8a) and SIC (Fig. 2.8b) approaches at the cost of higher complexity costs [18]. Consequently, JD exhibits the smallest outage region when compared to the II and SIC detectors.

Based on the achievable instantaneous rate regions in Fig. 2.8 [18, Fig. 2], the resulting outage events, closed-form outage probability expressions, and the associated references are given in Table 2.5. The outage probability of the II, SIC, and joint detectors was analyzed in [18, Fig. 3], where it is noted that the JD approach attains ideal, i.e., interference-free, outage probability under sufficiently strong inter-UAV interference and is not interference-limited at high SNR regimes. In contrast, the II and SIC detectors only work well under weak and strong inter-UAV interference, respectively, and are interference-limited at high SNR regimes [18]. Thus, the effectiveness and suitability of adopting JD to manage inter-UAV interference are demonstrated.

2.4.2.2 Finite SNR Diversity Gain

Finite SNR diversity gain is another metric of interest which quantifies the outage probability decay of a given system operating at a particular SNR, with fixed transmission rate [105]. When variable transmission rates are considered, then one can also analyze the finite SNR DMT by varying the transmission rate, i.e., multiplexing gain, to gauge the finite SNR diversity gain [106]. In particular, for a wireless system with instantaneous channel gain \mathcal{H} , outage event $\mathcal{O} = \{\mathcal{H} < \gamma\}$, outage probability $Pr(\mathcal{O})$, transmission rate R , threshold $\gamma = 2^R - 1$, and normalized average received power Ω , the asymptotic SNR diversity gain d is [107]:

$$d = \lim_{\Omega \rightarrow \infty} \frac{\log_2(Pr(\mathcal{O}))}{\log_2(\Omega)}. \quad (2.11)$$

At finite SNR regimes, i.e., low-to-moderate SNRs, the finite SNR diversity gain d_f is [106, Eq. (5)]:

$$d_f = \frac{-\Omega}{Pr(\mathcal{O})} \frac{\partial}{\partial \Omega} Pr(\mathcal{O}), \quad (2.12)$$

where $\lim_{\Omega \rightarrow \infty} d_f = d$ [105, 108] and is consistent with (2.11) when evaluated at asymptotic SNR regimes [107]. Furthermore, when the transmission rate varies depending on Ω , i.e., variable transmission rate, the asymptotic SNR multiplexing gain r is modeled as [107]:

$$r = \lim_{\Omega \rightarrow \infty} \frac{R(\Omega)}{\log_2(\Omega)} \quad (2.13)$$

and, accordingly, the finite SNR multiplexing gain r_f is given as [106, Eq. (4)]:

$$r_f = \frac{R(\Omega)}{\log_2(1 + \Omega)} \quad (2.14)$$

Through finite SNR diversity gain and finite SNR DMT analysis, outage deviation behaviors, which will otherwise not be present at asymptotically high SNRs due to small-scale fading, are revealed [105]. In terms of practical relevance, finite SNR diversity gain analysis can be used to characterize the outage probability performance of wireless systems, which are typically designed to operate at low-to-moderate SNR ranges [17]. Furthermore, finite SNR diversity gain can be used to estimate the required SNR before a targeted rate of error decay is achieved [106], e.g., via turbo codes or low-density parity-check codes. Moreover, when outage probability is analyzed in conjunction with finite SNR diversity gain, one obtains the upper and lower limits of a system's bit error rate performance [17, 107, 109].

In the literature, several studies have analyzed finite SNR diversity gain over Nakagami- m fading channels [110] and Rayleigh fading channels [97, 111]. For Rician fading channels, Shin et al. [105] and Narasimhan [106] characterized the finite SNR diversity gain and finite SNR DMT for MIMO systems, where the impact of Rician K factors on outage behavior and finite SNR DMT was noted. The analysis of finite SNR diversity gain and finite SNR DMT has also been applied to several other wireless systems. In [108], finite SNR DMT analysis was analyzed for a network coded cooperative communication system. Despite the above studies, the literature discussing the application of finite SNR analysis in practical wireless systems is still limited, particularly for UAV communications. For instance, only the application of DMT analysis, i.e., diversity gain at asymptotic SNR regimes, for cellular systems was studied in [22, 85], where the SIC approach was considered. Likewise, in [96] where the II and the JD approach was considered, the authors focused only on DMT analysis.

To this end, closed-form expressions for the finite SNR diversity gain and finite SNR DMT of the II and SIC approaches were presented in [17] for aeronautical communication systems. Similarly, in [18], closed-form expressions were presented for the finite SNR diversity gain and finite SNR DMT of a joint detector at UAV-2. In both [17] and [18],

Table 2.6: References of finite SNR diversity gain and finite SNR DMT expressions for the II, SIC, and joint detectors at UAV-2.

Protocol/Detector	Finite SNR Diversity Gain Notation	Finite SNR DMT Notation	References (Diversity Gain)	References (DMT)
II Detector	$d_{f,2}^{HBD(II)}$	$d_{f,2}^{HBD(II)*}$	[17, eq. (21)]	[18, eq. (22)]
SIC Detector	$d_{f,2}^{HBD(SIC)}$	$d_{f,2}^{HBD(SIC)*}$	[17, eq. (22)]	[18, eq. (23)]
Joint Detector	$d_{f,2}^{HBD(JD)}$	$d_{f,2}^{HBD(JD)*}$	[18, eq. (18)]	[18, eq. (24)]
HD-UCS	$d_{f,2}^{HD}$	$d_{f,2}^{HD*}$	[17, eq. (25)]	[17, eq. (31)]

the resulting finite SNR analysis yielded closed-form expressions, which are summarized in Table 2.6.

From [18, Fig. 3] and [18, Fig. 5], it is noted that the II and SIC detectors achieve non-zero diversity gain at low SNR regimes under weak and strong inter-UAV interference, respectively. Also, at high SNR regimes, both the II and SIC detectors achieve zero diversity gain and are thus interference-limited. In contrast, the joint detector achieves ideal, i.e., interference-free, diversity gain when inter-UAV interference is sufficiently strong. Furthermore, the joint detector attains a diversity gain of one at high SNR regimes and is, therefore, not interference-limited. Through finite SNR analysis, the superiority of the JD approach for inter-UAV interference management over the II and SIC approaches is demonstrated. Furthermore, the use of finite SNR diversity gain as a useful tool to identify scenarios where the HBD-UCS becomes interference-limited is highlighted.

2.5 Power-Domain Non-Orthogonal Multiple Access for HBD UAV Communications

Discussions of the HBD-UCS has thus far been conducted under the assumption of one uplink UAV and one downlink UAV in the system model, e.g., Fig. 2.7. When an arbitrary number of uplink and downlink UAVs is considered in the system model, approaches that enable an accurate representation of UAV deployments and multi-UAV communications are needed. One such approach that can be considered is stochastic geometry. Specifically, stochastic geometry has been extensively employed in cellular networks, where the locations of base stations and user equipments are modeled as Poisson point processes (PPPs). However, in the context of multi-UAV networks, recent

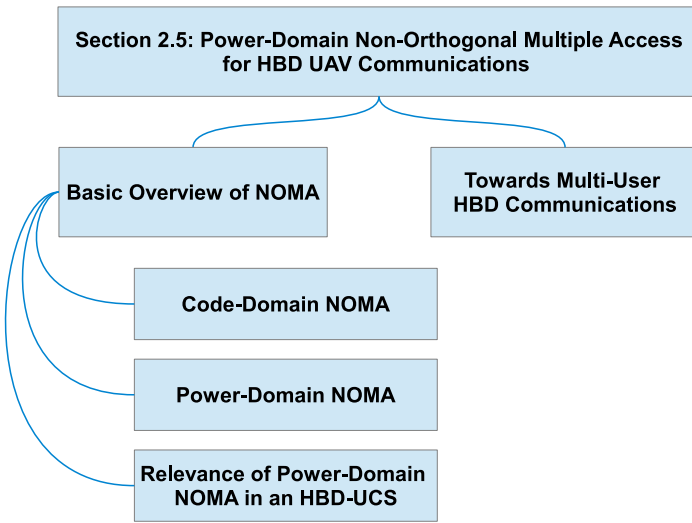


Fig. 2.9: An overview of the topics in Section 2.5.

works, e.g., [112] and [113] have shown binomial point processes (BPPs) to be more suitable due to the fixed number of deployed nodes in such networks.

Apart from UAV deployments, the detection of the desired messages at the UAVs and FD-enabled GS is also changed. In particular, to adhere to HBD transmission principles, the FD-enabled GS concurrently receives messages from all uplink UAVs while broadcasting messages to the downlink UAVs on the same spectrum. In this regard, discussions of multi-user HBD systems, preliminary NOMA concepts, and enabling methods to implement power-domain NOMA in an HBD-UCS are presented in the rest of this section. An overview of the topics in this section is provided in Fig. 2.9.

2.5.1 Towards Multi-User HBD Communications

Summary 2.5.1 While multi-user HBD communications can be implemented through FD systems based on TDMA, OFDMA, or CDMA, spectrum efficiency improvement is still limited due to constraints on the number of users sharing each time-frequency resources, interference, and computational complexity.

For the recovery of messages at the FD-enabled GS and downlink UAVs, groups of uplink and downlink UAVs can be scheduled to share the same time-frequency resource

blocks. Notably, in such multi-user FD-based systems, uplink and downlink nodes can be scheduled to share the same time-frequency resource block via time division multiple access (TDMA) or orthogonal frequency division multiple access (OFDMA) [114].

For sharing of time-frequency resource blocks in time domain, TDMA-based FD systems have been noted in energy harvesting (EH) communication systems such as FD wireless powered communication networks (FD-WPCNs) [115, 116] and FD ambient backscatter communication networks (FD-ABCNs) [117]. In FD-WPCNs, energy and information transmission co-occur over the same time slot and spectrum [115, 116]. For a frame with $K + 1$ time slots, frame duration T , and time slot duration $\tau_i T, i \in \{0, K\}$, an FD access point (FD-AP) transmits energy to all HD downlink EH users throughout the frame duration T . Also, TDMA is employed to receive information from EH users. Specifically, the FD-AP receives uplink data from the HD EH user- i at the i th time slot while concurrently transmitting energy over the same spectrum. For FD-ABCNs, an FD-AP transmits messages to a legacy user (LU) throughout the frame duration (T) [117]. Concurrently, at the HD EH backscatter devices (BD), the received ambient messages are modulated and reflected back to the FD-AP. Similar to FD-WPCNs, TDMA is employed to schedule the BD uplink transmissions [117]. Thus, BD- i transmits information to the FD-AP at the i th time slot while the FD-AP is simultaneously transmitting messages to the LU on the same spectrum. For the latter, OFMDA FD systems have been investigated in cellular systems to improve spectrum efficiency [118–121]. In such OFDMA cellular systems, each subcarrier supports one uplink user and one downlink user. Doing so allows an FD base station to transmit messages to the downlink user while concurrently receiving information from the uplink user. Apart from TDMA-based and OFDMA FD systems, multi-user FD-based systems can also enable the sharing of the same time-frequency resource block in code domain through code-division multiple access (CDMA) [122]. For instance, in [123], CDMA was employed as the multiple access scheme for a multi-user system with an FD relay.

Evidently, for TDMA-based and OFDMA FD systems, the improvement to spectrum efficiency is limited as only one pair of uplink and downlink user can utilize the same time-frequency resource block at any time instant. The limit of one uplink and downlink user pair per resource block stems from the need to avoid uplink interference at the downlink

user, e.g., at the EH user in FD-WPCN [116] and downlink user in OFDMA FD cellular systems [121]. For CDMA-based FD-systems, spectrum efficiency comes at the cost of SI, interference due to CDMA code correlation, and computational complexity. Yet, it is important to note that the recent advances in interference mitigation techniques, e.g., SIC, have demonstrated the feasibility of allowing more users to share the same time-frequency resource in FD systems.

Therefore, one may wish to consider employing power-domain NOMA for multi-UAV HBD-UCSs. Through power-domain NOMA, all communications between the FD-enabled GS and UAVs can occur concurrently on the same spectrum by employing some of the interference management techniques discussed earlier, e.g., SIC. We present further discussions on power-domain NOMA in the subsequent subsections.

2.5.2 Brief Overview of NOMA

Summary 2.5.2 *NOMA can be incorporated into multi-UAV HBD communications to enable the sharing of time-frequency resources between an arbitrary number of UAVs in code-domain or power-domain.*

Summary 2.5.3 *Although NOMA allows more UAVs to share the same time-frequency resource over OMA, spectrum efficiency for code-domain NOMA is attained at the expense of more signaling overheads and computational complexity. In contrast, power-domain NOMA can be feasibly adopted in multi-UAV networks through appropriate power allocation and interference management strategies.*

NOMA has been studied in the literature as a potential solution towards improving spectrum efficiency in 5G networks. Innovative NOMA techniques have been proposed to operate either in the power domain or in the code domain [124, 125]. To this end, a brief overview of code-domain and power-domain NOMA is presented below, with a summary of related studies on NOMA techniques given in Table 2.7.

2.5.2.1 Code-Domain NOMA

In code-domain NOMA, spreading sequences are employed to enable users in the network to share the same time-frequency resource. Although similar in principle to CDMA, the

Table 2.7: Summary of Studies on NOMA Techniques

Reference	NOMA Approach	Users Per NOMA Transmission	SIC Detection Order Criteria	Channel Model	Performance Metric(s)
[101]	Power-Domain	Two	Euclidean Distance	Rician Shadowed Fading	Outage Probability
[126]	Power-Domain	Two	Euclidean Distance	Rayleigh Fading	Ergodic Capacity, Outage Probability, Outage Capacity
[124]	Power-Domain	Two	Channel Gain	Rayleigh Fading	Outage Probability, Sum Rate
[125]	Power-Domain, Code-Domain	Two, Arbitrary	Channel Gain	-	Throughput, Block Error Rate, Bit Error Rate
[127]	Code-Domain	Arbitrary	-	Gaussian Channel	Bit Error Rate
[128]	Code-Domain	Arbitrary	-	-	Sum Rate, Complexity
[129]	Code-Domain	Arbitrary	-	Multipath	Bit Error Rate
[130]	Code-Domain	Arbitrary	-	Multipath, Hata	Bit Error Rate, Throughput, Fairness
[131]	Code-Domain	Arbitrary	-	-	Bit Error Rate
[132]	Code-Domain	Arbitrary	-	-	Bit Error Rate
[133]	Code-Domain	Arbitrary	-	AWGN	Bit Error Rate, Complexity
[134]	Power-Domain	Arbitrary	Euclidean Distance	Rayleigh Fading	Outage Probability, Fairness Rate, Min Transmit Power
[135]	Power-Domain	Arbitrary	Euclidean Distance	Rayleigh Fading	Conditional Success Probability
[136]	Power-Domain	Arbitrary (Two in simulations)	Euclidean Distance	Rayleigh Fading	Coverage Probability, Ergodic Capacity
[137]	Power-Domain	Two	Euclidean Distance	Rayleigh Fading	Ergodic Capacity
[138]	Power-Domain	Two	Channel Gain	Rayleigh Fading	Outage Probability, Ergodic Capacity
[139]	Power-Domain	Two (Arbitrary NOMA pairs)	Euclidean Distance	Rayleigh Fading	Outage Probability
[140]	Power-Domain	Two	Channel Gain	Rayleigh Fading	Probability of Low Sum Rate
[141]	Power-Domain	Two	Channel Gain	Rayleigh Fading	Average Throughput, Bit Error Rate
[142]	Power-Domain	Arbitrary	Channel Gain	Rayleigh Fading	Average SINR, Sum Rate, Utility
[143]	Code-Domain	Arbitrary	-	Rayleigh Fading, AWGN	Bit Error Rate

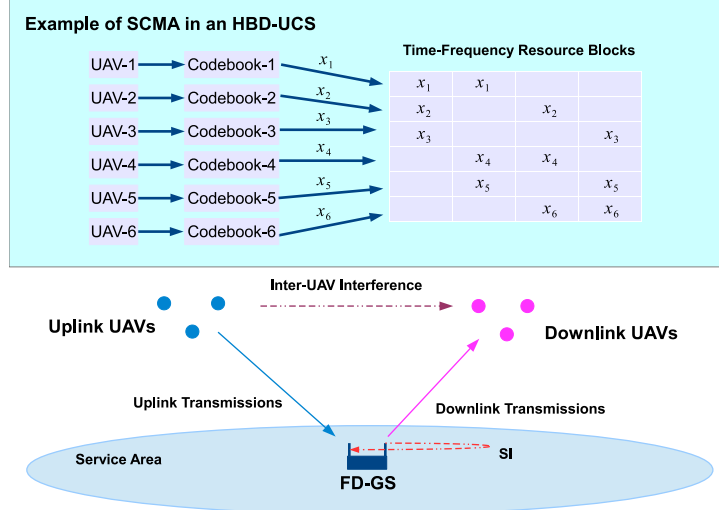


Fig. 2.10: An example of implementing SCMA in an HBD-UCS for 3 uplink UAVs (UAV-1, UAV-2, UAV-3) and 3 downlink UAVs (UAV-4, UAV-5, UAV-6) over 4 time-frequency resource blocks. The variable x_i represents the desired message of UAV- i .

main differentiating factor of code-domain NOMA lies in the fact that only sparse sequences or non-orthogonal low cross correlation sequences are employed to distinguish users [124,125]. Dominant techniques in code-domain NOMA include low-density spreading (LDS) CDMA, i.e., LDS-CDMA [124,125,127,128], LDS-based orthogonal frequency-division multiplexing (LDS-OFDM) [124,125,129,130], and sparse code multiple access (SCMA) [124,125,131–133]. In LDS-CDMA, the symbols of each user are mapped to an LDS sequence before transmission [125,127]. User detection is then performed on the received composite signal by employing the sum-product algorithm used in low-density parity-check decoding [127]. For LDS-OFDM, user symbols are mapped to LDS sequences before transmission over a set of subcarriers [124,125]. In contrast to LDS-CDMA and LDS-OFDM, SCMA employs bit-to-constellation mapping and spreading operations to generate unique codewords for each user [124,125,131]. An example of SCMA in an HBD-UCS is depicted in Fig. 2.10 for 3 uplink UAVs (UAV-1, UAV-2, UAV-3) and 3 downlink UAVs (UAV-4, UAV-5, UAV-6) over 4 time-frequency resource blocks. Specifically, the uplink UAVs employ codebook- i , $1 \leq i \leq 3$ to transmit the desired message x_i to the FD-GS. Simultaneously, the FD-GS employs codebook- j , $4 \leq j \leq 6$ to transmit the desired message x_j to the downlink UAVs. Thus, the desired messages of UAV-1, UAV-2,

and UAV-3 are multiplexed onto the same time-frequency resource block. Likewise, the desired messages of UAV-1, UAV-4, and UAV-5 are also multiplexed onto the same time-frequency resource block. Although promising, code-domain NOMA techniques achieve spectrum efficiency improvements at the cost of signaling cost and high complexity [125].

2.5.2.2 Power-Domain NOMA

Users in power-domain share the same time-frequency resource in power-domain through superposition coding [83, 101, 124–126, 134–141]. In particular, for uplink transmissions, users are distinguished through an unequal allocation of transmit powers before signal transmission in power-domain NOMA. Thereafter, all uplink users transmit the intended message to the receiver, e.g., base stations, effectively forming a multiple-access channel. Then, SIC detection is successively employed on the received composite signal to recover the desired messages from all users in the presence of multi-user interference (MUI) [87, 124, 126, 134, 135]. For downlink transmissions in power-domain NOMA, the transmitter, e.g., a base station, similarly distinguishes downlink users through an unequal allocation of transmit powers [124]. The transmitter then superimposes all intended messages into a composite signal before transmitting it to the downlink users, thus forming a broadcast channel. Under such a scenario, MUI is experienced by the downlink users. For downlink users experiencing strong MUI, SIC detection is successively employed until the desired message is recovered. On the other hand, II detection is employed at downlink users with weak MUI. For cases where MUI is neither weak nor strong, partial interference cancellation is employed to cancel MUI signals that are stronger than the desired message [124, 135].

2.5.2.3 Relevance of Power-Domain NOMA in an HBD-UCS

From the above discussions, transmit power allocation and SIC error propagation are some of the practical considerations of power-domain NOMA [124, 125]. However, power-domain NOMA enables the number of users sharing the same time-frequency resource to be easily scalable. Furthermore, compared to conventional OMA schemes, power-domain

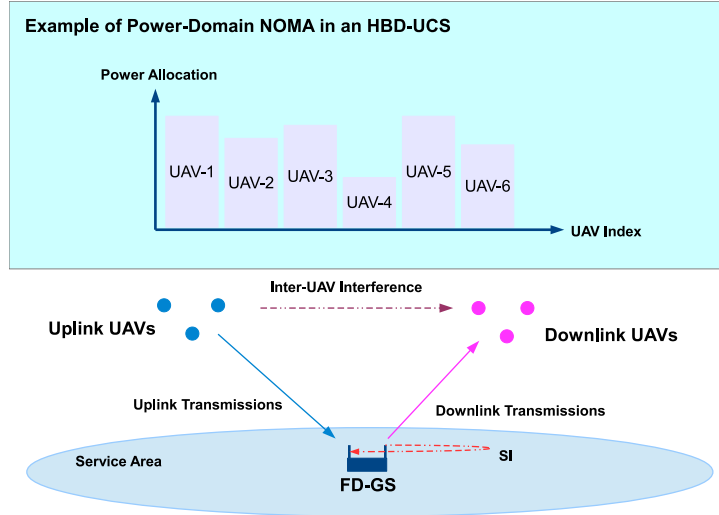


Fig. 2.11: An example of implementing power-domain NOMA in an HBD-UCS for 3 uplink UAVs (UAV-1, UAV-2, UAV-3) and 3 downlink UAVs (UAV-4, UAV-5, UAV-6) over the same time-frequency resource block.

NOMA can offer higher spectrum efficiency and is also capable of achieving the capacity region of broadcast channels [125].³

In the context of HBD UAV communications, power-domain NOMA is a suitable technique to enable multi-UAV deployment in HBD UAV communications. To illustrate this point, recall that the system model in Fig. 2.7 assumes only one uplink UAV and one downlink UAV concurrently communicating on the same spectrum. Such an assumption may not be realistic as arbitrary numbers of uplink and downlink UAVs can be simultaneously deployed in the HBD-UCS. To this end, the system model in Fig. 2.7 and the resultant signal models at the FD-enabled GS and downlink UAVs can be easily extended to account for arbitrary numbers of uplink and downlink UAVs, with an example illustrated in Fig. 2.11. However, doing so introduces MUI at both the FD-enabled GS and downlink UAVs, and uplink interference, i.e., inter-UAV interference, at the downlink UAVs [101]. Thus, a multi-UAV deployment scenario naturally raises questions on how the detection process at the FD-enabled GS and downlink UAVs can be conducted in the presence of MUI and uplink interference. In this aspect, power-domain NOMA

³We refer to frequency division multiple access (FDMA), TDMA, and CDMA as conventional OMA schemes in this survey.

can be employed in an HBD-UCS for multi-UAV deployment scenarios. For instance, at the FD-enabled GS, SIC detection can be employed to recover messages from the uplink UAVs in the presence of MUI. For the downlink UAVs, SIC and II detection can be employed to recover the desired message from the FD-enabled GS while mitigating MUI and inter-UAV interference from the uplink UAVs.

With the above reasons in mind, the feasibility of power-domain NOMA for HBD UAV communications will be studied in the later part of this thesis.

2.6 Chapter Summary

In this chapter, we reviewed vital enabling techniques in realizing HBD UAV communications to improve spectrum efficiency. First, a review of recent advances in UAV channel modeling for HBD UAV communications was presented, where it was shown that UAV channels can be modeled using common fading models such as Rician fading. The types of SI mitigation architectures that can be implemented at FD-enabled GSs were also surveyed. It was also noted that phase noise, SI channel estimation errors, and quantization noise are the main sources of residual SI for FD transceivers. For the HD UAVs, a survey of interference management techniques, which focuses on II, SIC, and JD strategies, was conducted to address inter-UAV interference. Apart from discussing the state-of-the-art, the performance of II, SIC, and JD approaches were discussed in terms of outage probability and finite SNR diversity gain. For multi-UAV HBD-UCSs, an overview of NOMA techniques was discussed to support multi-UAV deployment. The suitability of power-domain NOMA for multi-UAV networks highlighted, although the feasibility of power-domain NOMA for multi-UAV networks remains an open research problem.

Chapter 3

Interference Management in Hybrid-Duplex Aeronautical Communication Systems

3.1 Introduction

Thus far, the lack of spectrum has been discussed in the context of UAV communications. However, spectrum scarcity is also present in aeronautical communications involving manned aerial vehicles. In particular, between 2012 and 2032, air travel within the Pacific South East Asia region is projected to record a compounded annual growth rate of 5.3% [144]. This air travel growth trend exposes existing aeronautical communication systems (ACSs) to considerable strain due to demand for data communications from legacy, current, and future generation of avionics systems. Consequently, this places an additional strain upon existing Air-to-Ground (A/G) and Air-to-Air (A/A) aeronautical communication links on the congested aeronautical spectrum. With existing ACSs being unable to deliver the needed data capacity [14], various communication technologies have been proposed to improve the capabilities of existing A/G and A/A links [14, 145]. However, these solutions do not directly address the issue of spectrum utilization.¹

In this spirit, an HBD ACS, comprising HD air-stations (ASs) operating existing avionics systems with FD GSs, can be an alternative solution to the shortage of available spectrum currently faced by the aviation community. Changes to existing/legacy HD avionics systems currently on board aircrafts can be kept to a minimum in HBD-ACS,

¹The work in this chapter has been published in [17].

thus enabling HBD-ACS to be less disruptive to adopt. Wireless communication systems that have adopted the HBD paradigm include cognitive radio systems [146] and cellular systems [147–149]. With FD nodes experiencing SI, adopting effective SI mitigation strategies for HBD-ACSs enables spectrum scarcity to be addressed in the aviation industry. In particular, multiple aircrafts and ground stations can communicate on the same aeronautical spectrum, providing motivation for this chapter.

3.1.1 Related Literature

Apart from SI at FD nodes, HD nodes in HBD systems also experience interference due to transmissions from other HD and FD nodes. In the literature, multiple interference management approaches have been presented. However, this chapter focuses on two widely known approaches where interference is either ignored, i.e., II detector, or successively canceled, i.e., SIC detector.

To quantify the effectiveness of the II and SIC detectors, many related works in literature have attempted to determine the closed-form outage probabilities of these detectors under various fading models. Having a closed-form outage probability expression enables a system’s packet error rate, i.e., link availability, to be analyzed if the transmitted signals span over one fading block [97]. For the II detector, closed-form outage expressions for Nakagami- m fading [98] and composite fading consisting of exponentially distributed SOI and squared \mathcal{K} -distributed interfering signals [86] have been noted. However, [98] and [86] are only applicable to specific fading environments and may not be applicable for all aeronautical scenarios where Rician fading is experienced. To this end, a recent paper by Rached et al. [45] presented generalized outage probability expressions that apply to a wide variety of fading scenarios, including Rician fading.

For SIC detectors, multiple works on outage analysis have been noted. For instance, the outage probability of SIC has been investigated by Hasna et al. [89] and Romero-Jerez and Goldsmith [102], but these studies only considered partial SIC where at least one interfering signal remains after interference cancellation. A closed-form outage expression for SIC was presented by Weber et al. [87] for nodes distributed via a Poisson point process. However, the work in [87] did not consider fading and receiver noise in the signal model. Thus, the closed-form expressions are not directly applicable for aeronautical

communications. In a recent paper by Zhang et al. [90], outage probability expressions for a two-stage SIC detector were presented. Yet, the outage expressions are specific for Rayleigh fading scenarios and are not applicable to Rician fading scenarios that are common in aeronautical communications. From the mentioned studies, hitherto closed-form outage probability expressions for SIC detectors in Rician fading aeronautical scenarios remain an open problem.

Apart from outage probability, both finite SNR diversity gain and finite SNR DMT are metrics that can be used to measure the effectiveness of II or SIC detectors in fixed and variable transmission rate systems, respectively. In particular, both finite SNR diversity gain and finite SNR DMT quantify the slope of outage probability curves at a particular SNR [105], with the latter considering multiplexing gain [106]. Finite SNR analysis can reveal outage deviation behaviors, which are not present at asymptotically high SNRs due to fading statistics [105]. From a practical perspective, analyzing outage probability decay rates, i.e., finite SNR diversity gain, provides an accurate picture of a system's outage performance since wireless communication systems are typically designed to operate at low-to-moderate SNR ranges. It has also been pointed out by Narasimhan [106] that finite SNR diversity gain analysis can be used to estimate the SNR needed to achieve a particular rate of error decay, that can be done through turbo codes or low-density parity-check codes. More crucially, outage probability and diversity gain can be used to gauge the upper and lower limits of a system's bit error rate performance [107, 109].

Finite SNR analysis for Nakagami- m [110] and Rayleigh fading [97, 111] scenarios have also been studied. However, the conclusions drawn in these studies are specific to Nakagami- m and Rayleigh fading and are not fully applicable for ACSs since Rician fading scenarios, typically encountered in aeronautical communications, are not considered. Studies on finite SNR analysis for Rician fading channels have been seen. The impact of Rician K factors on outage behavior and finite SNR DMT for MIMO systems was investigated by Narasimhan [106] and Shin et al. [105]. A recent paper by Heidarpour et al. [108] saw finite SNR DMT analysis being applied to analyze the performance of a network coded cooperative communication system. Despite the noted studies, there is still room for further work on finite SNR DMT analysis for HBD-ACS.

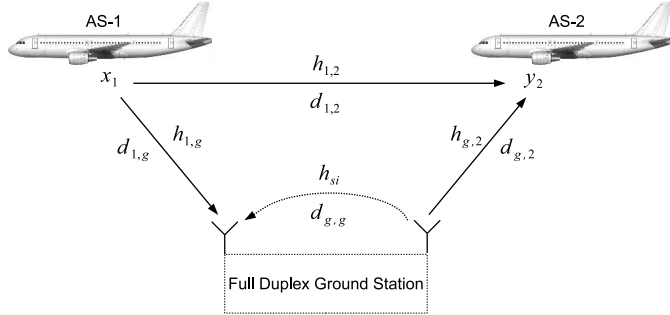


Fig. 3.1: Air-Station 1 (AS-1) and Air-Station 2 (AS-2) operating in HD mode while communicating with the FD GS.

3.1.2 Relevance to Related Literature

In this research, full interference cancellation is assumed for the two-stage SIC detector. This is unlike in [89] and [102] where only partial SIC is assumed. In addition, the impact of interference on the proposed HBD-ACS is analyzed from the outage probability and finite SNR DMT perspective, which was not covered in [45, 87, 90, 98, 146, 149]. In contrast to [105], [106] and [108], this work extends upon the outage and finite SNR DMT analysis framework to jointly identify interference scenarios for the proposed single-input-single-output equivalent HBD-ACS.

3.2 System Model

In this chapter, A/G communications involving an FD-enabled GS node with two HD ASs in an A/G link is studied (Fig. 3.1).² Specifically, a scenario with Air-Station 1 (AS-1) transmitting signals to the GS while Air-Station 2 (AS-2) is receiving signals from the GS is assumed. For the HD transceivers at AS-1 and AS-2, a single-antenna configuration with separate transmit and receive radio frequency chains is assumed. In contrast, the

²The present chapter can be extended to consider an arbitrary number of uplink and downlink nodes. To enable the modeling and analysis of such multi-node networks, the signal model at the GS and also at the nodes will need to be modified. Furthermore, stochastic geometry tools, i.e., the BPP model, will need to be employed to accurately model the deployment of the nodes. These issues are addressed in Chapter 6, where new signal models that consider the BPP model are proposed for an HBD multi-UAV network.

FD transceiver at the GS is assumed to be configured with one transmit antenna and one receive antenna through separate radio frequency chains. Due to the fact that the GS node is FD-capable, the HD AS-1 and HD AS-2 simultaneously transmits and receives, respectively, signals on the same aeronautical spectrum (e.g. VHF, L-band) as the GS. Therefore, AS-1 interferes with communications at AS-2 when the latter receives signals from the GS.

The current research assumes an SI mitigation architecture with a shared local oscillator at the FD-enabled GS. Such a setup enables lower levels of phase noise to be experienced [82], [76]. As such, we only consider residual SI at the FD-enabled GS as a result of imperfect SI channel estimation and phase noise [21]. Furthermore, the SI link (h_{si}) is modeled as a Rician fading channel to account for passive and active SI mitigation [75].³ Thus, an II detector is considered at the FD-enabled GS since signal detection is performed in the presence of residual SI.

Rician faded aeronautical communications channels in an en route scenario are assumed to provide a realistic evaluation of the HBD-ACS [8, 41, 55]. Following the work in [41] and [55], the link between AS-1 and AS-2 is also modeled as a Rician fading channel. Accordingly, we assume that the ASs are communicating with the GS at cruising altitude, with the signal model based on [21]. Also, the effect of Doppler shift is assumed to be compensated in this work [150].⁴ A summary of important notations is given in Table 3.1.

3.2.1 Ground Station

Let $x_1[t]$ and $x_{gs}[t]$ be the signals transmitted by AS-1 and GS, respectively, and $h_{1,g}[t]$ be the channel from AS-1 to GS. Additionally, let $x_{si}[t]$ be the SI signal at GS and let h_{si} be the SI channel gain. From the perspective of GS, $x_{si}[t] = x_{gs}[t]$. The received signal at GS can be written as

$$y_{gs}[t] = \sqrt{\Omega_X} h_{1,g}[t] x_1[t] + \sqrt{\Omega_X \alpha_{g,g}} \cdot |\tilde{h}_{si}| x_{si}[t] + \sqrt{\Omega_X \alpha_{g,g}} |h_{si}| \gamma_\phi w_\phi[t] + w_g[t] \quad (3.1)$$

³Depending on the degree of passive and active SI mitigation, the resultant SI channel (h_{si}) can be a Rician or Rayleigh fading channel [75]. Thus, modeling h_{si} as a Rician fading channel enables the degree of passive and active SI mitigation to be defined through the Rician K factor.

⁴It is useful to note that Doppler shift is not a performance limitation in the upcoming L-band digital aeronautical communication systems (LDACS) standard [151].

where \tilde{h}_{si} is the error of the imperfect SI channel gain estimate, defined as $\tilde{h}_{si} = h_{si} - \hat{h}_{si}$, and \hat{h}_{si} is the imperfect estimation of the SI channel gain. In addition, let \tilde{h}_{si} be modeled as a zero mean, circularly symmetric complex Gaussian RV with variance ϵ to quantify the SI channel estimation error [81]. Modeling \tilde{h}_{si} as a zero mean Gaussian RV with variance ϵ enables the system to model the worst case residual SI [81]. Also, let $w_g[t]$ be the GS additive white Gaussian noise (AWGN) with zero mean and variance σ_g^2 , and let the phase noise term $w_\phi[t]$ follow a Gaussian distribution with zero mean and unit variance, scaled by the scaling factor γ_ϕ [21].⁵

Let Ω_X be the average received signal power of the SOI. The average received signal power is defined based on the free space path loss model [152, Eq. (2.7)] and it is defined as

$$\Omega_X \propto \frac{P_t}{\left(\frac{4\pi \cdot 10^9}{3 \cdot 10^8}\right)^2 \cdot f_c^2 \cdot d_{1,g}^2 \cdot \sigma_g^2}, \quad (3.2)$$

where P_t , d , and f_c are the transmit power (Watts), distance (km), and carrier frequency (MHz), respectively. The received signal power levels are normalized with the receiver noise variance (σ_g^2). The channel between AS-1 and GS is selected as the reference link and the average received signal power in the other links are expressed relative to the reference link via the multiplicative factor $\alpha_{i,j}$, defined as

$$\alpha_{i,j} = \left(\frac{d_{1,g}}{d_{i,j}} \right)^n, i \in \{g, 1\}, j \in \{g, 2\}, i \neq j. \quad (3.3)$$

The variable $\alpha_{g,g}$ is treated as a scaling factor for the average residual SI power at GS. From (3.2) and (3.3), the average received power of the residual SI at GS can be expressed as $\Omega_X \alpha_{g,g}$, where it is assumed that the residual SI scaled by $\alpha_{g,g}$ is below the saturation level of the FD transceiver.

From [81], the overall level of SI suppression, i.e., combination of passive suppression with analog and digital SI cancellation, can be calculated as $\frac{1}{\alpha_{g,g} \epsilon \sigma_g^2}$.

⁵The scaling factor γ_ϕ models the jitter present in oscillators due to hardware imperfections [21]

Table 3.1: Summary of Important Notations

Notations	Description
Ω_X	Average received power
$a_{i,j}, i \in \{g, 1\}, j \in \{g, 2\}, i \neq j$	Strength of interference between i and j
ϵ	SI channel estimation error at the FD-enabled GS
γ_ϕ^2	Strength of phase noise at the FD- enabled GS oscillator
σ_g^2	Strength of AWGN at the FD-enabled GS
σ_2^2	Strength of AWGN at the AS-2

3.2.2 Air-Station 2

Let $h_{g,2}[t]$ be the channel between GS and AS-2, $h_{1,2}[t]$ be the channel between AS-1 and AS-2, and $w_2[t]$ be the AWGN at AS-2 with zero mean and variance σ_2^2 . From the perspective of AS-2, $x_{gs}[t]$ and $x_1[t]$ are the SOI and interfering signal, respectively. The received signal at AS-2 can be expressed as

$$y_2[t] = \sqrt{\Omega_X \alpha_{g,2}} h_{g,2}[t] x_{gs}[t] + \sqrt{\Omega_X \alpha_{1,2}} h_{1,2}[t] x_1[t] + w_2[t], \quad (3.4)$$

where $\Omega_X \alpha_{g,2}$ and $\Omega_X \alpha_{1,2}$ indicate the average received signal powers of the SOI and interfering signal, respectively.

To handle the interference at AS-2, two approaches are studied. The first approach assumes an II detector at AS-2. The II detector treats $x_1[t]$ as noise. Therefore, interference is effectively ignored. The second approach assumes a SIC detector at AS-2. The two-stage SIC detector first tries to detect and cancel $x_1[t]$ before proceeding to detect $x_{gs}[t]$ [153].

3.3 Calculation of Outage Probabilities

To begin the outage analysis at GS and AS-2, we first define the HBD transmission rates of AS-1 and GS as R_1^{HBD} and R_{gs}^{HBD} , respectively, and the sum rate of the HBD system as $R_{sum}^{HBD} = R_1^{HBD} + R_{gs}^{HBD}$. Similarly, the HD transmission rates of AS-1 and GS are defined as R_1^{HD} and R_{gs}^{HD} , respectively, and the sum rate of the HD system is defined as $R_{sum}^{HD} = R_1^{HD} + R_{gs}^{HD}$. For fair comparison between HBD and HD systems, $R_i^{HBD} = \frac{1}{2}R_i^{HD}$ for $i \in \{1, gs\}$ [154–156]. The respective HBD and HD outage probabilities at GS and AS-2 are defined in the following subsections.

3.3.1 Hybrid-Duplex Outage Probability

The FD-enabled GS receives $x_1[t]$ while simultaneously transmitting $x_{gs}[t]$ in the same time slot. The simultaneous transmission and reception of signals result in strong SI at GS. Let $X_1 = \Omega_X |h_{1,g}|^2$ be the instantaneous received signal power of the SOI at GS, modeled as a non-centered chi-squared distributed RV with Rician K factor K_{X_1} . Let $Y_{si,1} = \Omega_X \alpha_{g,g} \gamma_\phi^2 |h_{si}|^2$ and $Y_{si,2} = \Omega_X \alpha_{g,g} |\tilde{h}_{si}|^2$ be the instantaneous received signal power corresponding to SI components. In particular, $Y_{si,1}$ is modeled as a non-centered chi-squared distributed RV with Rician K factor $K_{Y_{si,1}}$ and $Y_{si,2}$ is modeled as an exponentially distributed RV.

Concurrently, AS-2 also experiences interference from AS-1. Let $X_{gs} = \Omega_X \alpha_{g,2} |h_{g,2}|^2$ and $Y_1 = \Omega_X \alpha_{1,2} |h_{1,2}|^2$ be the instantaneous received signal power of the SOI and interference at AS-2, respectively, where X_{gs} and Y_1 are independent non-centered chi-squared distributed RV with respective Rician K factors $K_{X_{gs}}$ and K_{Y_1} , respectively. Additionally, let $\alpha(q, \Omega, K, \gamma)$ be defined as

$$\alpha(q, \Omega, K, \gamma) \equiv (-1)^q \exp(-K) \frac{L_q^{(0)}(K)}{(1+q)!} \left(\frac{(1+K)}{\Omega} \gamma \right)^{q+1}, \quad (3.5)$$

where q , Ω , K and γ represent an arbitrary non-negative integer, average received power of the signal, Rician K factor, and threshold, respectively. The function $L_q^{(0)}(\bullet)$ represents the q -th degree, zero-order Laguerre polynomials [157] while $\alpha(q, \Omega, K, \gamma)$ in (3.5) represents the Rician power CDF expansion due to Rician faded signal parameters.

3.3.1.1 Ground Station

At GS, let the HBD threshold be $\gamma_{th,gs}^{HBD} = 2^{R_1^{HBD}} - 1$, with HBD outage event $\mathcal{O}_{gs}^{HBD} = \left\{ h_{1,g}, h_{si} : R_1^{HBD} \geq \log_2 \left(1 + \frac{X_1}{Y_{si,1} + Y_{si,2} + 1} \right) \right\}$. By substituting $X_1, Y_{si,1}$ and $Y_{si,2}$ into [45, Eq. (12)], the closed-form outage probability at GS can be expressed as

$$Pr(\mathcal{O}_{gs}^{HBD}) = \sum_{q \geq 0} \sum_{l_1+l_2+l_3=q+1} \alpha(q, \Omega_X, K_{X_1}, \gamma_{th,gs}^{HBD}) \frac{(q+1)!}{l_1! \cdot l_2! \cdot l_3!} E\{Y_{si,1}^{l_1}\} E\{Y_{si,2}^{l_2}\}, \quad (3.6)$$

where $\alpha(q, \Omega_X, K_{X_1}, \gamma_{th,gs}^{HBD})$ is the Rician SOI power CDF expansion at GS, as defined in (3.5). In addition, $E\{Y_{si,1}^{l_1}\}$ and $E\{Y_{si,2}^{l_2}\}$ are the l_1^{th} and l_2^{th} moments of $Y_{si,1}$ and $Y_{si,2}$,

respectively. From [45, Table II], $E\{Y_{si,1}^{l_1}\} = \Gamma(1 + l_1) \left(\frac{\alpha_{g,g}\gamma_\phi^2}{1+K_{Y_{si,1}}}\right)^{l_1} {}_1F_1(-l_1, 1; -K_{Y_{si,1}})(\Omega_X)^{l_1}$ and $E\{Y_{si,2}^{l_2}\} = \Gamma(1 + l_2)(\alpha_{g,g}\epsilon)^{l_2}(\Omega_X)^{l_2}$. The function ${}_1F_1(\bullet)$ represents the confluent Hypergeometric function [49, Eq. (9.210.1)] and summation on the right hand side (RHS) of (3.6) is convergent if $\gamma_{th,gs}^{HBD} \leq \frac{\Omega_X}{3(1+K_{X_1})(\Omega_X\alpha_{g,g}\epsilon)}$ [45, Eq. (14)]. In (3.6), $E\{Y_{si,1}^{l_1}\}$ and $E\{Y_{si,2}^{l_2}\}$ quantifies the strength of residual SI due to phase noise and SI channel estimation errors, respectively. We do not expect $\alpha_{g,g}$ to approach infinity as the distance on the SI link ($d_{g,g}$) cannot be zero. However, it is possible for the average received SI power to be strong if $d_{g,g}$ is short. From $E\{Y_{si,1}^{l_1}\}$ and $E\{Y_{si,2}^{l_2}\}$, the impact of residual SI is diminished as $\alpha_{g,g} \rightarrow 0$ and hence, proper SI mitigation strategies is crucial at the FD-enabled GS.

3.3.1.2 Air-Station 2 (Interference Ignorant Detector)

At AS-2, let the HBD threshold be $\gamma_{th,2}^{HBD} = 2^{R_{gs}^{HBD}} - 1$ and the HBD outage event be $O_2^{HBD(II)} = \left\{h_{g,2}, h_{1,2} : R_{gs}^{HBD} \geq \log_2 \left(1 + \frac{X_{gs}}{Y_1+1}\right)\right\}$. By substituting X_{gs} and Y_1 into [45, Eq. (12)], the closed-form outage probability at AS-2 can be expressed as

$$Pr(O_2^{HBD(II)}) = \sum_{q \geq 0} \sum_{l=0}^{q+1} \alpha(q, \Omega_X \alpha_{g,2}, K_{X_{gs}}, \gamma_{th,2}^{HBD}) \binom{q+1}{l} E\{Y_1^l\}, \quad (3.7)$$

where $\alpha(q, \Omega_X \alpha_{g,2}, K_{X_{gs}}, \gamma_{th,2}^{HBD})$ is the Rician SOI power CDF expansion at AS-2, as defined in (3.5), and $E\{Y_1^l\}$ is the l^{th} moment of the interfering signal from AS-1. From [45, Table II], $E\{Y_1^l\} = \Gamma(1 + l) \left[\frac{\alpha_{1,2}}{1+K_{Y_1}}\right]^l {}_1F_1(-l, 1; -K_{Y_1})(\Omega_X)^l$ and the RHS of (3.7) is convergent if $\gamma_{th,2}^{HBD} \leq \frac{\Omega_X \alpha_{g,2}(1+K_{Y_1})}{2(1+K_{X_{gs}})\Omega_X \alpha_{1,2}}$ [45, Eq. (14)]. In (3.7), $E\{Y_1^l\}$ quantifies the strength of the interference from AS-1 through moment parameters of Y_1 .

To investigate the impact of inter-AS interference, we evaluate $\lim_{\alpha_{1,2} \rightarrow L} E\{Y_1^l\}$ for $L \in \{0, \infty\}$. Although $\alpha_{1,2}$ does not reach infinity in practice, large values of $\alpha_{1,2}$ are possible when $d_{1,2}$ is small and vice-versa. Evaluating $\lim_{\alpha_{1,2} \rightarrow L} E\{Y_1^l\}$ for $L \in \{0, \infty\}$ shows that the impact of inter-AS interference reduces as $\alpha_{1,2} \rightarrow 0$, and increases as $\alpha_{1,2} \rightarrow \infty$. Thus, the II detector operates effectively in low interference scenarios such as over remote airspace where inter-AS distance is long.

3.3.1.3 Air-Station 2 (Successive Interference Cancellation Detector)

In the case of SIC, if the first stage is unable to detect the interfering signal or if the SOI cannot be detected at the second stage, then outage occurs. Therefore, the HBD outage

event at AS-2 is defined as

$$\begin{aligned} O_2^{HBD(SIC)} &= \left\{ h_{g,2}, h_{1,2} : R_1^{HBD} > \log_2 \left(1 + \frac{Y_1}{1 + X_{gs}} \right) \right\} \\ &\cup \left\{ h_{g,2}, h_{1,2} : R_1^{HBD} \leq \log_2 \left(1 + \frac{Y_1}{1 + X_{gs}} \right), R_{gs}^{HBD} > \log_2 (1 + X_{gs}) \right\}. \end{aligned} \quad (3.8)$$

Theorem 3.1 *The closed-form expression for outage probability with SIC detector at AS-2 is*

$$\begin{aligned} Pr(O_2^{HBD(SIC)}) &= \sum_{q \geq 0} \sum_{l=0}^{q+1} \alpha(q, \Omega_X \alpha_{1,2}, K_{Y_1}, \gamma_{th,gs}^{HBD}) \binom{q+1}{l} E\{X_{gs}^l\} \\ &+ 1 - Q_1 \left(\sqrt{2K_{X_{gs}}}, \sqrt{\frac{2(K_{X_{gs}} + 1)\gamma_{th,2}^{HBD}}{\Omega_X \alpha_{g,2}}} \right) \\ &- \sum_{n \geq 0} \sum_{i=0}^n \sum_{j=0}^{i+1} \alpha(i, \Omega_X \alpha_{1,2}, K_{Y_1}, \gamma_{th,gs}^{HBD}) \alpha(n-i, \Omega_X \alpha_{g,2}, K_{X_{gs}}, 1) \binom{i+1}{j} \frac{(\gamma_{th,2}^{HBD})^{j+n-i+1}}{j+n-i+1} \end{aligned} \quad (3.9)$$

where $Q_1(\cdot, \cdot)$ is the Marcum Q function [157], [158, Eq. (4.33)] and $E\{X_{gs}^l\} = \Gamma(1 + l) \left(\frac{\Omega_X \alpha_{g,2}}{1 + K_{X_{gs}}} \right)^l {}_1F_1(-l, 1; -K_{X_{gs}})$ [45, Table II].

Proof: The proof can be found in Appendix A.1.

The first term in (3.9) is the outage probability due to detecting interference from AS-1. The second term in (3.9) is the outage probability due to SOI detection after interference cancellation. From $\alpha(q, \Omega_X \alpha_{1,2}, K_{Y_1}, \gamma_{th,2}^{HBD})$ in (3.9), it is evident that the SIC detector works effectively in high interference scenarios, such as in congested airspace where inter-AS distance is short, since the effect of interference at the SOI detection stage is diminished when $\alpha_{1,2}$ is large. The closed-form expressions in (3.6), (3.7) and (3.9) can shed insights into the impact of residual SI at GS and interference from AS-1 at AS-2. Further discussions on outage performance with respect to the level of interference are presented in Section 3.5.

3.3.2 Half-Duplex Outage Probability

When the GS is operating in HD mode, AS-2 does not experience interference from AS-1. Let the HD threshold at GS and AS-2 be defined as $\gamma_{th,gs}^{HD} = 2^{2R_1^{HBD}} - 1$ and

$\gamma_{th,2}^{HD} = 2^{2R_{gs}^{HBD}} - 1$, respectively. Then, the HD outage probabilities at GS and AS-2 are given in (3.10) and (3.11), respectively [45, Table I].

$$Pr(O_{gs}^{HD}) = \sum_{m \geq 0} \alpha(m, \Omega_X, K_{X_1}, \gamma_{th,gs}^{HD}), \quad (3.10)$$

$$Pr(O_2^{HD}) = \sum_{m \geq 0} \alpha(m, \Omega_X \alpha_{g,2}, K_{X_{gs}}, \gamma_{th,2}^{HD}). \quad (3.11)$$

The outage probability expressions in (3.10) and (3.11) can be used as a benchmark comparison against HBD mode at GS and AS-2, respectively, which is presented in Section 3.5.

3.3.3 System Level Outage Probability

For the proposed multi-user system, the overall system level outage probability is used as a performance metric to compare HBD and HD protocols. For $\beta \in \{HBD(II), HBD(SIC)\}$, the system level outage probability is defined as $P_{out,system}^{\beta} = \max(Pr(O_{gs}^{HBD}), Pr(O_2^{\beta}))$ and $P_{out,system}^{HD} = \max(Pr(O_{gs}^{HD}), Pr(O_2^{HD}))$. The system level outage probability provides the worst case system level outage behavior for the II and SIC detectors and allows the identification of performance bottlenecks in HBD-ACS. Having knowledge of the performance bottleneck in the HBD-UCS enables interference management to be more effective. For instance, if the link between the FD-enables GS and AS-2 has the highest outage probability, then the design requirements of the SI mitigation architecture at the FD-enabled GS can be less stringent which can lead to hardware with lower cost or power requirements.

3.4 Finite SNR Analysis

In the following subsections, the mathematical preliminaries and derivations related to finite SNR diversity gain are presented for both fixed and variable transmission rates, with detailed derivation omitted for brevity. As it will be shown, finite SNR analysis is an effective tool in evaluating the performance of the II and SIC detectors in an interference-limited environment.

3.4.1 Finite SNR Diversity Gain

For a system with outage event \mathcal{O} , outage probability $Pr(\mathcal{O})$, transmission rate R , threshold γ , and average received power Ω with unit noise variance, the diversity gain d at high SNR is given by Zheng and Tse [107] as

$$d = \lim_{\Omega \rightarrow \infty} \frac{\log_2(Pr(\mathcal{O}))}{\log_2(\Omega)}. \quad (3.12)$$

The diversity gain definition in (3.12) is for systems that operate at high SNR ranges. The finite SNR diversity gain d_f , which quantifies the decay rate of the outage probability at low-to-moderate SNRs, is given as [106, Eq. (5)]

$$d_f = \frac{-\Omega}{Pr(\mathcal{O})} \frac{\partial}{\partial \Omega} Pr(\mathcal{O}). \quad (3.13)$$

It has since been shown by Shin et al. [105] and Heidarpour et al. [108] that $\lim_{\Omega \rightarrow \infty} d_f = d$. Therefore, (3.13) is consistent with the asymptotic diversity definitions in [107] at high SNR. Practical wireless systems typically operate at the low-to-moderate SNR range [106]. The outage behavior of these systems may also be different at high and moderate SNRs. Therefore, there is motivation to quantify diversity gains at finite SNRs since (3.12) does not accurately reflect outage behaviors at low-to-moderate SNRs [105].

3.4.2 Finite SNR DMT Parameters

For a system which varies its transmission rate with respect to Ω , i.e., variable transmission rate, the high SNR multiplexing gain r is given by Zheng and Tse [107] as

$$r = \lim_{\Omega \rightarrow \infty} \frac{R(\Omega)}{\log_2(\Omega)} \quad (3.14)$$

and the finite SNR multiplexing gain r_f for such systems is [106, Eq. (4)]

$$r_f = \frac{R(\Omega)}{\log_2(1 + \Omega)}. \quad (3.15)$$

It has similarly been shown by Shin et al. [105] and Heidarpour et al. [108] that $\lim_{\Omega \rightarrow \infty} r_f = r$, with $Pr(\mathcal{O})$ computed with respect to the threshold $\gamma = (1 + \Omega)^{r_f} - 1$.

The finite SNR diversity gain for such a variable transmission rate system (denoted as d_f^*) can be obtained from (3.13) as [105, Eq. (36)]

$$d_f^* = \frac{-\Omega}{Pr(O)} \lim_{\Delta(\Omega) \rightarrow 0} \left[\frac{Pr(\widehat{O}) - Pr(O)}{\Delta(\Omega)} \right], \quad (3.16)$$

where $\Delta(\Omega) = \widehat{\Omega} - \Omega$, $\widehat{\Omega} > \Omega$ and \widehat{O} is the outage event with respect to $R(\Omega + \Delta(\Omega))$. Furthermore, $Pr(\widehat{O})$ is the outage probability with average received power $\widehat{\Omega} = \Omega + \Delta(\Omega)$, threshold $\widehat{\gamma} = [1 + \Omega + \Delta(\Omega)]^{r_f} - 1$ and $Pr(\widehat{O}) = Pr(O)$ when $\Delta(\Omega) = 0$. Applying L'Hospital's rule in (3.16) by differentiating with respect to $\Delta(\Omega)$ and setting $\Delta(\Omega) = 0$ yields

$$d_f^* = \left. \frac{-\Omega}{Pr(O)} \frac{\partial}{\partial \Delta(\Omega)} Pr(\widehat{O}) \right|_{\Delta(\Omega)=0}. \quad (3.17)$$

Let Z be a RV with normalized n^{th} moment defined as $M\{Z^n\} = \frac{E\{Z^n\}}{(\Omega)^n}$ and let function $g(i, j, \Omega, r_f)$ be

$$g(i, j, \Omega, r_f) = ([1 + \Omega]^{r_f} - 1)^i (\Omega)^j \left[\left([1 + \Omega]^{r_f} - 1 \right) \frac{j}{\Omega} + (i+1)(r_f)(1 + \Omega)^{r_f-1} \right], \quad (3.18)$$

where i and j are integers. The function $M\{Z^n\}$ represents the normalized n^{th} moment of an interfering signal while the function $g(i, j, \Omega, r_f)$ reflects the outage probability decay rate of a variable transmission rate scheme due to average received power (Ω) and finite SNR multiplexing gain (r_f).

Although [105, Eq. (36)] and [106, Eq. (5)] evaluate finite SNR diversity gains using different approaches, the principles underlying them are the same since the latter is an extension of the former. To this end, (3.17) can be used to evaluate d_f^* for adaptive systems, with r_f indicating the sensitivity of the rate adaptation scheme [106]. It is also of interest to analyze d_f^* as it can lead to better code designs that improve transmission rates at the expense of reliability for adaptive systems and vice-versa.

3.4.3 Finite SNR Diversity Gain for HBD Systems

Let the finite SNR HBD diversity gain at GS and AS-2 be defined as $d_{f,gs}^{HBD}$ and $d_{f,2}^{HBD,i}, i \in \{II, SIC\}$, respectively. Additionally, let R_1 and R_{gs} be fixed constants with average received power $\Omega = \Omega_X$. Then, the finite SNR diversity gain at GS and AS-2 are presented in the following propositions.

Proposition 3.1 *The finite SNR diversity gain at the FD-enabled GS is*

$$d_{f,gs}^{HBD} = \frac{-\Omega_X}{Pr(O_{gs}^{HBD})} \sum_{q \geq 0} \sum_{l_1+l_2+l_3=q+1} \alpha(q, 1, K_{X_1}, \gamma_{th,gs}^{HBD}) \\ \times \frac{(q+1)!(l_1+l_2-q-1)}{l_1! \cdot l_2! \cdot l_3!} M\{Y_{si,1}^{l_1}\} M\{Y_{si,2}^{l_2}\} (\Omega_X)^{l_1+l_2-q-2} \quad (3.19)$$

Proof: The finite SNR diversity gain at GS can be obtained by substituting (3.6) into (3.13).

At low-to-moderate Ω_X , the outage behavior at GS can be analyzed from (3.19). In particular, (3.19) allows observation of subtle changes in outage behavior due to the scaling factor associated with the SI strength ($\alpha_{g,g}$) and SI channel estimation error (ϵ) that is not present at high Ω_X . In addition, the asymptotic behavior of $d_{f,gs}^{HBD}$ can be obtained from (3.19) as shown in the following corollary.

Corollary 3.1 *The asymptotic behavior of $d_{f,gs}^{HBD}$ is given by*

$$\lim_{\Omega_X \rightarrow \infty} \frac{-\Omega_X}{Pr(O_{gs}^{HBD})} \frac{\partial}{\partial \Omega_X} Pr(O_{gs}^{HBD}) = 0. \quad (3.20)$$

Proof: The proof is given in Appendix A.2.

From (3.20), $d_{f,gs}^{HBD} \rightarrow 0$ as $\Omega_X \rightarrow \infty$ because increasing Ω_X also causes residual SI to be stronger, hence there is no improvement in the overall SINR. Also, (3.20) suggests that the tolerance for residual SI in HBD-ACS is progressively diminished as Ω_X is increased since $d_{f,gs}^{HBD} \rightarrow 0$ corresponds to negligible improvements in outage probability at GS.

Proposition 3.2 *The finite SNR diversity gain at AS-2 with the II ($d_{f,2}^{HBD(II)}$) and SIC detectors ($d_{f,2}^{HBD(SIC)}$) are*

$$d_{f,2}^{HBD(II)} = \frac{-\Omega_X}{Pr(O_2^{HBD(II)})} \sum_{q \geq 0} \sum_{l=0}^{q+1} \alpha(q, \alpha_{g,2}, K_{X_{gs}}, \gamma_{th,2}^{HBD}) \\ \times \binom{q+1}{l} M\{Y_1^l\} (l-q-1) (\Omega_X)^{l-q-2} \quad (3.21)$$

$$d_{f,2}^{HBD(SIC)} = \frac{-\Omega_X}{Pr(O_2^{HBD(SIC)})} \left[\sum_{q \geq 0} \sum_{l=0}^{q+1} \alpha(q, \alpha_{1,2}, K_{Y_1}, \gamma_{th,gs}^{HBD}) \\ \times \binom{q+1}{l} M\{X_{gs}^l\} (l-q-1) (\Omega_X)^{l-q-2} \right. \\ + \sum_{m \geq 0} \alpha(m, \alpha_{g,2}, K_{X_{gs}}, \gamma_{th,2}^{HBD}) (-m-1) (\Omega_X)^{-m-2} \\ - \sum_{n \geq 0} \sum_{i=0}^n \sum_{j=0}^{i+1} \alpha(i, \alpha_{1,2}, K_{Y_1}, \gamma_{th,gs}^{HBD}) \alpha(n-i, \alpha_{g,2}, K_{X_{gs}}, 1) \\ \left. \times \binom{i+1}{j} \frac{(\gamma_{th,2}^{HBD})^{j+n-i+1}}{j+n-i+1} (-n-2) (\Omega_X)^{-n-3} \right] \quad (3.22)$$

Proof: At AS-2, $d_{f,2}^{HBD(i)}, i \in \{II, SIC\}$ can be obtained for the II and SIC by respectively substituting (3.7) and (3.9) into (3.13).

The outage behavior at AS-2 can be analyzed from (3.21) and (3.22) at low-to-moderate Ω_X . In particular, (3.21) and (3.22) enables the observation of subtle changes in outage behavior for both II and SIC detectors, which are not present at high Ω_X , as inter-aircraft interference varies. Extending upon (3.21) and (3.22), the asymptotic behavior of $d_{f,2}^{HBD(i)}, i \in \{II, SIC\}$ can be obtained as follows.

Corollary 3.2 *The asymptotic behavior of $d_{f,2}^{HBD(i)}, i \in \{II, SIC\}$ is given by*

$$\lim_{\Omega_X \rightarrow \infty} \frac{-\Omega_X}{Pr(O_2^{HBD,i})} \frac{\partial}{\partial \Omega_X} Pr(O_2^{HBD,i}) = 0. \quad (3.23)$$

Proof: The proof is given in Appendix A.3.

Remark 3.1 *In [84] and [22], the average received signal powers of the desired ($\Omega_x \alpha_{g,2}$) and interfering ($\Omega_x \alpha_{1,2}$) links are related through an exponent, where a large exponent*

corresponds to very strong interference. At high SNRs, the SIC-based receiver is shown to achieve full diversity under very strong interference levels. In contrast, this work demonstrates that the SIC detector achieves zero diversity gain at high SNRs when the desired and interfering signal levels are related through a scaling parameter.

In the presence of interference at AS-2, (3.23) shows that improvements to outage probability at AS-2 progressively diminishes since $d_{f,2}^{HBD(i)} \rightarrow 0$ as $\Omega_X \rightarrow \infty$ for $i \in \{II, SIC\}$. For the II detector, increasing Ω_X results in strong interference. As a consequence, there is no improvement to the overall SINR. Hence, the II detector is unsuitable in strong interference environments. Similarly, for the SIC detector, increasing Ω_X causes $x_{gs}[t]$ to be stronger, making the detection and subtraction of $x_1[t]$ increasingly challenging at stage 1 of the SIC detector. Hence, $\alpha_{1,2}$ must either increase (for the II detector) or decrease (for the SIC detector) at high Ω_X for HBD-ACS to see meaningful improvements in outage probability.

3.4.4 Finite SNR Diversity Gain for HD Systems

Let the finite SNR diversity gain at GS and AS-2 be defined as $d_{f,i}^{HD}, i \in \{gs, 2\}$, respectively, with R_1 and R_{gs} assumed to be constants with average received power $\Omega = \Omega_X$. Then, the finite SNR diversity gain at GS and AS-2 are presented in the following proposition.

Proposition 3.3 *The finite SNR diversity gain at GS and AS-2 operating in HD mode are given in (3.24) and (3.25), respectively.*

$$d_{f,gs}^{HD} = \frac{-\Omega_X}{Pr(O_{gs}^{HD})} \sum_{m \geq 0} \alpha(m, 1, K_{X_1}, \gamma_{th,gs}^{HD}) (-m - 1) (\Omega_X)^{-m-2} \quad (3.24)$$

$$d_{f,2}^{HD} = \frac{-\Omega_X}{Pr(O_2^{HD})} \sum_{m \geq 0} \alpha(m, \alpha_{g,2}, K_{X_{gs}}, \gamma_{th,2}^{HD}) (-m - 1) (\Omega_X)^{-m-2} \quad (3.25)$$

Proof: The expressions in (3.24) and (3.25) can be obtained by respectively substituting (3.10) and (3.11) into (3.13).

The HD outage behavior at GS and AS-2 can be analyzed from (3.24) and (3.25), respectively, and it enables the observation of changes in outage probability decay rate that is not visible at high Ω_X . As $\Omega_X \rightarrow \infty$, (3.24) and (3.25) can be evaluated to determine the asymptotic diversity gain as follows.

Corollary 3.3 *The asymptotic behavior of $d_{f,i}^{HD}, i \in \{gs, 2\}$ is*

$$\lim_{\Omega_X \rightarrow \infty} d_{f,i}^{HD} = 1. \quad (3.26)$$

Proof: The proof is provided in Appendix A.4.

From (A.5), $d_{f,i}^{HD} \rightarrow 1$ as $\Omega_X \rightarrow \infty$ for $i \in \{gs, 2\}$ and it indicates that the HD system achieves full diversity in the absence of interference at high Ω_X , which is consistent with [105, Fig. 3].

3.4.5 Finite SNR DMT Analysis for HBD Systems

Let the finite SNR diversity gain at GS for a HBD system be defined as $d_{f,gs}^{HBD*}$, with variable transmission rate $R_1^{HBD}(\Omega_X) = r_f \log_2(1 + \Omega_X)$ and threshold $\gamma_{th,gs}^{HBD} = [1 + \Omega_X]^{r_f} - 1$. Similarly, let the finite SNR diversity gain at AS-2 for a HBD system be denoted as $d_{f,2}^{HBD(i)*}, i \in \{II, SIC\}$, with variable transmission rate $R_{gs}^{HBD}(\Omega_X) = r_f \log_2(1 + \Omega_X)$ and threshold $\gamma_{th,2}^{HBD} = [1 + \Omega_X]^{r_f} - 1$. The finite SNR diversity gains at GS and AS-2 are presented in the following propositions.

Proposition 3.4 *At GS, the finite SNR diversity gain is given as*

$$d_{f,gs}^{HBD*} = \frac{-\Omega_X}{Pr(O_{gs}^{HBD})} \sum_{q \geq 0} \sum_{l_1+l_2+l_3=q+1} \alpha(q, 1, K_{X_1}, 1) \times \frac{(q+1)!}{l_1! \cdot l_2! \cdot l_3!} M\{Y_{si,1}^{l_1}\} M\{Y_{si,2}^{l_2}\} g(q, l_1 + l_2 - q - 1, \Omega_X, r_f). \quad (3.27)$$

Proof: Let $\Omega = \Omega_X$, $\widehat{\Omega} = \widehat{\Omega}_X$ and $\gamma = \gamma_{th,gs}^{HBD} = [1 + \Omega_X]^{r_f} - 1$ and $O = O_{gs}^{HBD}$. Then, $d_{f,gs}^{HBD*}$ can be obtained through algebraic manipulations by substituting (3.6) into (3.17).

Proposition 3.5 At AS-2, the finite SNR diversity gain with II and SIC detectors are

$$d_{f,2}^{HBD(II)*} = \frac{-\Omega_X}{Pr(O_2^{HBD(II)})} \sum_{q \geq 0} \sum_{l=0}^{q+1} \alpha(q, \alpha_{g,2}, K_{X_{gs}}, 1) \times \binom{q+1}{l} M\{Y_1^l\} g(q, l-q-1, \Omega_X, r_f), \quad (3.28)$$

$$\begin{aligned} d_{f,2}^{HBD(SIC)*} = & \frac{-\Omega_X}{Pr(O_2^{HBD(SIC)})} \left[\sum_{q \geq 0} \sum_{l=0}^{q+1} \alpha(q, \alpha_{1,2}, K_{Y_1}, 1) \right. \\ & \times \binom{q+1}{l} M\{X_{gs}^l\} g(q, l-q-1, \Omega_X, r_f) \\ & + \sum_{m \geq 0} \alpha(m, \alpha_{g,2}, K_{X_{gs}}, 1) g(m, -m-1, \Omega_X, r_f) \\ & - \sum_{n \geq 0} \sum_{i=0}^n \sum_{j=0}^{i+1} \alpha(i, \alpha_{1,2}, K_{Y_1}, 1) \alpha(n-i, \alpha_{g,2}, K_{X_{gs}}, 1) \\ & \left. \times \frac{\binom{i+1}{j}}{j+n-i+1} g(j+n+1, -n-2, \Omega_X, r_f) \right]. \end{aligned} \quad (3.29)$$

Proof: Let $\Omega = \Omega_X$, $\widehat{\Omega} = \widehat{\Omega}_X$ and $\gamma = \gamma_{th,2}^{HBD} = [1 + \Omega_X]^{r_f} - 1$ and $O = O_2^{HBD,i}, i \in \{II, SIC\}$. Then, similar to (3.27), $d_{f,2}^{HBD(II)*}$ and $d_{f,2}^{HBD(SIC)*}$ can be obtained through algebraic manipulations by respectively substituting (3.7) and (3.9) into (3.17).

In the presence of interference at GS and AS-2, DMT at low-to-moderate Ω_X can be analyzed from (3.27), (3.28) and (3.29). It reveals the interference scenarios in which the II or SIC detectors achieves better diversity gain than HD systems.

3.4.6 Finite SNR DMT Analysis for HD Systems

Let the finite SNR HD diversity gain at GS be defined as $d_{f,gs}^{HD*}$. To ensure fair comparison, we let the variable HD data rate be twice the variable HBD data rate. Let $R_1^{HD}(\Omega_X) = 2r_f \log_2(1 + \Omega_X)$ be the variable transmission rate at AS-1 with threshold $\gamma_{th,gs}^{HD} = [1 + \Omega_X]^{2r_f} - 1$. Similarly at AS-2, let the finite SNR HD diversity gain at AS-2 be defined as $d_{f,2}^{HD*}$ with variable transmission rate $R_{gs}^{HD}(\Omega_X) = 2r_f \log_2(1 + \Omega_X)$ and threshold $\gamma_{th,2}^{HD} = [1 + \Omega_X]^{2r_f} - 1$. The closed-form expressions for the finite SNR diversity gains at GS and AS-2 are presented in the following proposition.

Proposition 3.6 *For a variable transmission rate scheme, the finite SNR diversity gain at GS and AS-2 are given in (3.30) and (3.31), respectively.*

$$d_{f,gs}^{HD*} = \frac{-\Omega_X}{Pr(O_{gs}^{HD})} \sum_{m \geq 0} \alpha(m, 1, K_{X_1}, 1) g(m, -m - 1, \Omega_X, 2r_f), \quad (3.30)$$

$$d_{f,2}^{HD*} = \frac{-\Omega_X}{Pr(O_2^{HD})} \sum_{m \geq 0} \alpha(m, \alpha_{g,2}, K_{X_{gs}}, 1) g(m, -m - 1, \Omega_X, 2r_f). \quad (3.31)$$

Proof: The expressions in (3.30) and (3.31) can be obtained through algebraic manipulations by respectively substituting (3.10) and (3.11) into (3.17).

In the absence of interference, (3.30) and (3.31) can be used to evaluate the DMT at GS and AS-2, providing a benchmark that can be used in evaluating the performance of the II and SIC detectors in HBD systems.

3.4.7 System Level Finite SNR Diversity Gain and DMT

The system level finite SNR diversity gain and DMT for the multi-user system in Fig. 3.1 will be used as a metric to compare HBD and HD systems. For fixed transmission rate schemes, the HBD and HD system level finite SNR diversity gain are defined as $d_{f,system}^{\beta} = \min(d_{f,gs}^{HBD}, d_{f,2}^{\beta})$ and $d_{f,system}^{HD} = \min(d_{f,gs}^{HD}, d_{f,2}^{HD})$, respectively. Similarly, for variable transmission rate schemes, the HBD and HD system level finite SNR DMT are defined as $d_{f,system}^{\beta*} = \min(d_{f,gs}^{HBD*}, d_{f,2}^{\beta*})$ and $d_{f,system}^{HD*} = \min(d_{f,gs}^{HD*}, d_{f,2}^{HD*})$, respectively. Quantifying the finite SNR diversity gain and DMT provides insights into the degree of improvements in outage performance at the system level, which will be further discussed in Section 3.5.

3.5 Numerical Results

In this section, numerical results pertaining to the outage probabilities and finite SNR diversity gains at GS, AS-2 and system level are discussed, with the simulation parameters provided in Table 3.2. Monte Carlo simulations are conducted with 10^9 samples using MATLAB to verify the accuracy of the outage probability computations. Likewise, the

Table 3.2: Simulation Parameters

Parameter(s)	Value(s)
Rician K Factors	15 [8]
Noise Variance	$\sigma_g^2 = \sigma_2^2 = -115$ dBm [159]
Sum Rate	$R_{sum}^{HD} = R_{sum}^{HBD} = 1$
Phase Noise	$\gamma_\phi^2 = -130$ dBm, normalized by $\sigma_g^2 = -115$ dBm in the simulations
SI Suppression Level	163 dB to 175 dB for $\alpha_{g,g} = \{1, 1.5\}$ and $\epsilon = \{0.01, 0.001\}$
Average Received Power	$0 \text{ dB} \leq \Omega_X \leq 30 \text{ dB}$

numerical results are also computed using MATLAB.⁶ ⁷ ⁸

3.5.1 Finite SNR Diversity Gain and Outage Analysis

3.5.1.1 Impact of Residual SI at GS

Observation 3.5.1.1 *The FD-enabled GS has near-ideal outage probability and diversity gain at very low SNR, and is interference-limited at high SNR.*

The HBD outage probability at GS is shown in Fig. 3.2a. The ideal HBD and the HD outage probability are also plotted in Fig. 3.2a as a benchmark comparison. From Fig. 3.2a, it can be seen that $Pr(O_{gs}^{HBD})$ is close to the ideal HBD case, i.e., no interference, at low-to-moderate average received power (Ω_X) and vice-versa. As expected, $Pr(O_{gs}^{HBD})$ is higher as SI channel estimation error (ϵ) is increased. In addition, increasing the strength of the residual SI ($\alpha_{g,g}$) degrades the outage performance more than that obtained with the increase in ϵ since a larger $\alpha_{g,g}$ corresponds to a higher average residual SI power, with phase noise (γ_ϕ^2) scaled accordingly. In fact, $Pr(O_{gs}^{HBD})$ approaches the ideal HBD case when $\alpha_{g,g} = 1, \epsilon = 0.001$ at low Ω_X in Fig. 3.2a. Hence, sufficient SI mitigation is needed in order for the FD-enabled GS to outperform the HD-enabled GS.

⁶Assuming a noise figure of 6 dB, $\sigma_g^2 = \sigma_2^2 = -115$ dBm results in an effective bandwidth of 200kHz. Such a bandwidth falls within the range of existing VHF datalink (VDL) standards (25kHz) [160, Table 3.16], and the upcoming orthogonal frequency-division multiplexing (OFDM)-based L-band digital aeronautical communication systems-1 (LDACS-1) standard [151, 161] and Gaussian minimum shift keying (GMSK)-based LDACS-2 standard (500kHz) [151].

⁷It is worth noting that the normalized phase noise strength falls within the range of phase noise seen in Appendix C of [21].

⁸In this work, we consider $0 \text{ dBm} \leq P_t \leq 36.4 \text{ dBm}$. Taking the GMSK-based LDACS-2 as an example [151], with 200kHz of bandwidth, noise figure of 6 dB, and carrier frequency $f_c = 968\text{MHz}$, a transmit power of $P_t = 26.4$ dBm is obtained for $d_{1,g} = 9.2\text{km}$ [8], $\alpha_{1,2} = 0.5$, $d_{1,2} = 4.6\text{km}$ [162], and $\Omega_X = 30$ dB. When $d_{1,g} = 29\text{km}$ [8], $\alpha_{1,2} = 5$, $d_{1,2} = 145\text{km}$ [162], and $\Omega_X = 30$ dB, $P_t = 36.4$ dBm is obtained. The obtained values of P_t is comparable to [151], where a transmit power of $P_t = 41$ dBm was used in the performance analysis of LDACS-2.

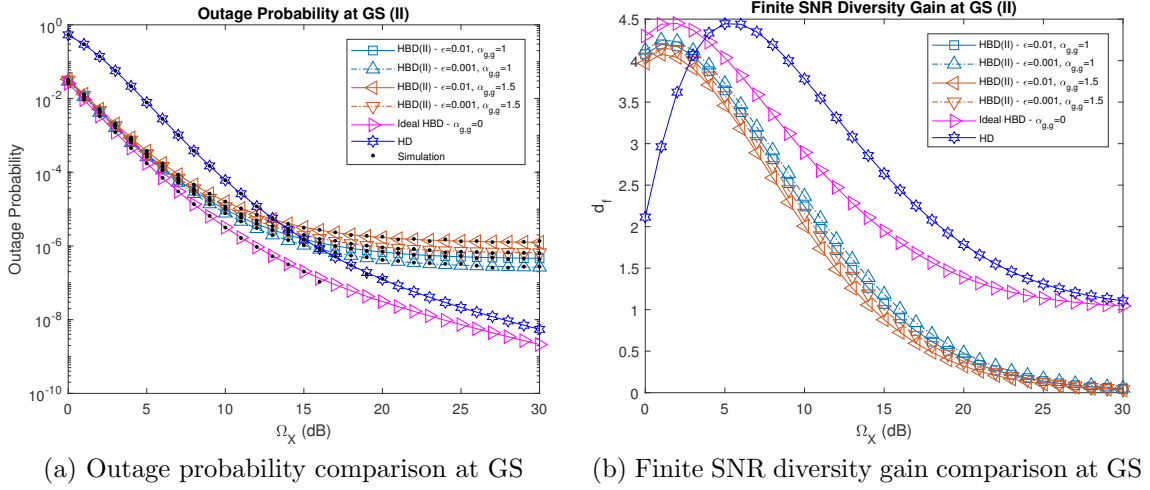


Fig. 3.2: Outage probability and finite SNR diversity gain at GS (II detector) for phase noise strength $\gamma_\phi^2 = -130$ dBm.

The finite SNR diversity gain at GS is shown in Fig. 3.2b, where it can be seen that $d_{f,g,s}^{HBD}$ peaks at $\Omega_X = 2$ dB while $d_{f,g,s}^{HD}$ peaks at $\Omega_X = 6$ dB.⁹ Additionally, (3.20) and (3.26) are also confirmed in Fig. 3.2b as $\Omega_X \rightarrow \infty$ and is also corroborated in Fig. 3.2a, where the slope of the outage probability curves become constant as $\Omega_X \rightarrow \infty$. In other words, the FD-enabled GS becomes interference-limited at high Ω_X . Interestingly, in the absence of interference at the FD-enabled GS, $d_{f,g,s}^{HBD} \rightarrow 1$ as $\Omega_X \rightarrow \infty$ since only SNR needs to be considered at GS. From Fig. 3.2, residual SI is the performance limiting factor for the FD-enabled GS. Therefore, it is important to sufficiently mitigate SI at each of the cascaded stages in Fig. 3.1 in order to keep the strength of the residual SI low in practical realizations of the FD-enabled GS.

3.5.1.2 Impact of Interference at AS-2

Observation 3.5.1.2 *The II and SIC detectors achieve lower outage probability and higher diversity gain than HD-mode at low SNR regimes and are interference-limited at*

⁹Higher diversity gain does not mean lower outage probability and vice-versa. To get a parametric representation for outage probability from diversity gain and SNR, the array gain, coding gain, or SNR offset, needs to be factored as shown in [163] and the references therein. Similar analysis is needed from the interference-limited receiver's perspective to quantify the SNR offsets for different protocols at a given interference level, and it is left as a future extension of the current chapter.

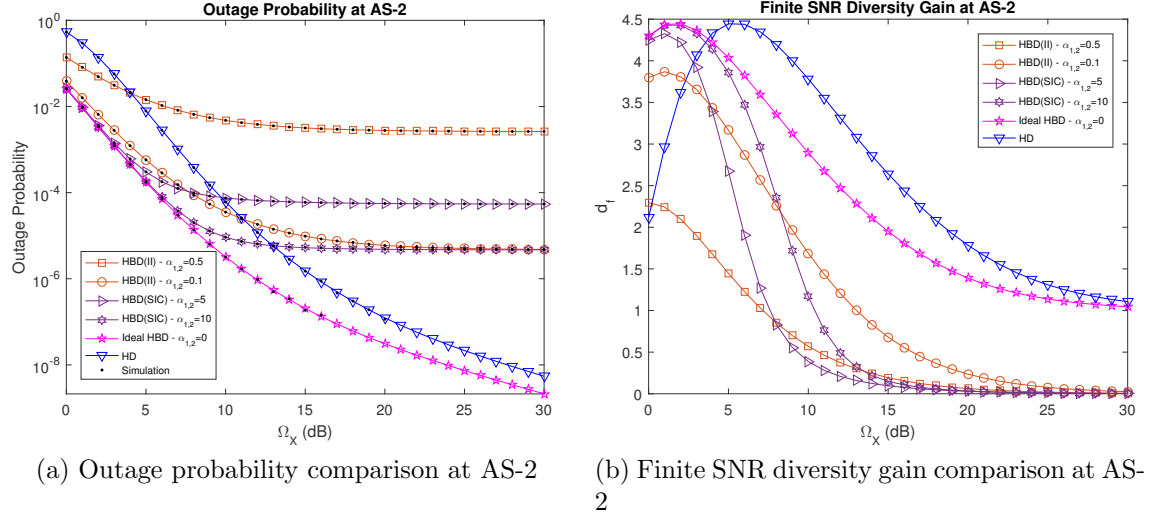


Fig. 3.3: Outage probability and finite SNR diversity gain at AS-2 (II and SIC detectors) for $\alpha_{g,2} = 1$, i.e., link between GS and AS-2 has same distance as the reference link ($d_{1,g}$).

high SNR regimes. For the SIC detector, strong interference at low SNR regime enables easy removal of the interfering signal.

The HBD outage probabilities at AS-2 for both II and SIC detectors are shown in Fig. 3.3a. It can be seen that the II detector at AS-2 outperforms the HD mode at low-to-moderate Ω_X when inter-AS interference ($\alpha_{1,2}$) is weak. The trend in Fig. 3.3a also suggests that the further reduction in $\alpha_{1,2}$ will enable the II detector at AS-2 to attain the ideal HBD outage performance for moderate Ω_X , which is expected since $\alpha_{1,2} \rightarrow 0$ corresponds to diminishing levels of interference at AS-2.

The SIC detector performs better than the HD mode at the low-to-moderate Ω_X when interference is strong, e.g., $\alpha_{1,2} = 10$, since stage 1 of the SIC detector is more likely to detect and subtract $x_1[t]$. The resultant signal at stage 2 of the SIC detector is thus almost interference-free. As $\alpha_{1,2}$ increases, the SIC detector performance approaches that of the ideal HBD case due to the near perfect cancellation of interference in the first stage. When $\Omega_X > 10$ dB for $\alpha_{1,2} \in \{5, 10\}$, an error floor is present which verifies Corollary 3.2. Similar error floor observations are also made for the II detector and it indicates that the II and SIC detectors become interference-limited at high Ω_X . From a practical perspective, the trend in Fig. 3.3a shows that the II detector is well suited for

en route scenarios with less congested flight routes such as those over sparsely populated or oceanic regions since the II detector experiences weak interference due to path loss as a result of large inter-aircraft or aircraft to GS distance. On the other hand, the SIC detector is suitable for use in congested airspace scenarios such as the landing or even continental en route scenarios as interference from nearby aircrafts can be effectively removed. Although HD-ACS has superior outage performance compared to the II and SIC detectors at high Ω_X , the interference-limited HBD detectors can meet typical QoS requirements, e.g., frame error rate $\leq 10^{-3}$.

The finite SNR diversity gains, $d_{f,2}^{HBD(II)}$ and $d_{f,2}^{HBD(SIC)}$, at AS-2 are shown in Fig. 3.3b. A trend similar to what was seen in Fig. 3.2b can be found in Fig. 3.3b, with $d_{f,2}^{HBD(II)}$ and $d_{f,2}^{HBD(SIC)}$ peaking at $\Omega_X = 2$ dB, and $d_{f,2}^{HD}$ peaking at $\Omega_X = 6$ dB. As expected, reducing $\alpha_{1,2}$ causes $d_{f,2}^{HBD(II)}$ to perform close to the ideal HBD case at low Ω_X . Fig. 3.3b also confirms (3.23) for both the II and SIC detectors. It is clear that the SIC detector can attain an outage probability decay rate that is similar to the ideal HBD case when $\Omega_X \leq 5$ dB. Further increasing $\alpha_{1,2}$ will enable $d_{f,2}^{HBD(SIC)}$ to be almost identical to the ideal HBD case at $\Omega_X \leq 5$ dB since the system becomes noise-limited rather than interference-limited. The trends in Fig. 3.3b are also reflected in Fig. 3.3a since the slope of the outage probability curves behave as indicated in (3.23) and (3.26) as $\Omega_X \rightarrow \infty$.

3.5.1.3 Impact of Interference at System Level

Observation 3.5.1.3 *The system level performance of the HBD-ACS is constrained by inter-AS interference. When the II detector is considered, weak inter-AS interference enables near-ideal system level performance. Likewise for the SIC detector when strong inter-AS interference is present. If the SI suppression level is lower, then it is possible for the GS to be the bottleneck.*

Fig. 3.4a and Fig. 3.4b respectively shows the outage probability and finite SNR diversity gain at the system level. Through numerical analysis, we observed that $P_{out,system}^{HBD(II)}$ is dominated by the II detector at AS-2 for $\alpha_{1,2} \in \{0.1, 0.5\}$ and $0 \text{ dB} \leq \Omega_X \leq 30 \text{ dB}$, i.e., $Pr(O_{gs}^{HBD}) < Pr(O_2^{HBD(II)})$ because inter-AS interference at AS-2 is stronger than

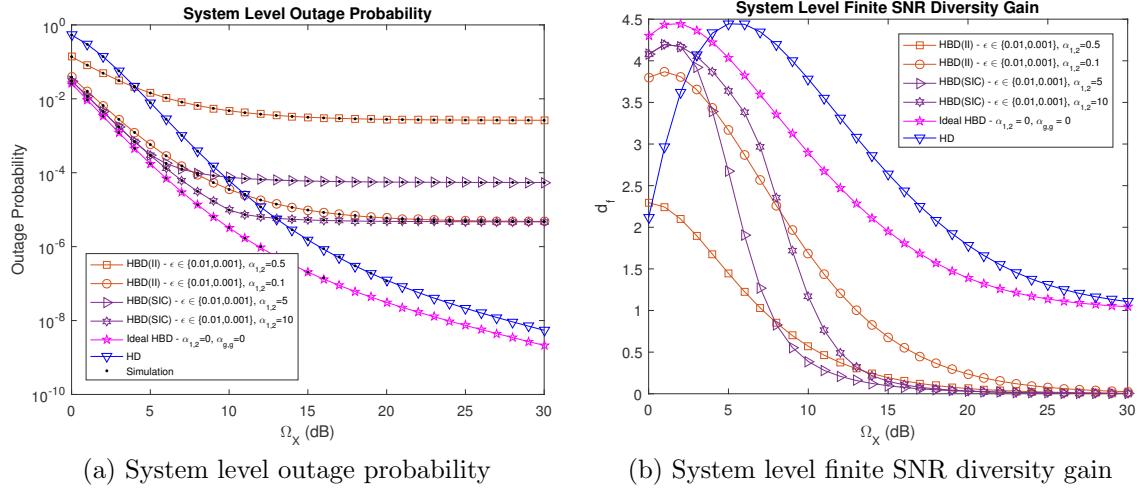


Fig. 3.4: System level outage probability and finite SNR diversity gain (II and SIC detectors) for $\alpha_{g,2} = 1, \alpha_{g,g} = 1, \gamma_\phi^2 = -130$ dBm, $\epsilon \in \{0.01, 0.001\}$.

the residual SI experienced at GS. Thus, although not shown in the figure, increasing $\alpha_{g,g}$ or ϵ does not affect $P_{out,system}^{HBD(II)}$ unless inter-AS interference is decreased. It can also be observed from Fig. 3.4a that $P_{out,system}^{HBD(II)} \leq P_{out,system}^{HD}$ when $\Omega_X \leq 4$ dB, $\alpha_{1,2} = 0.5$. When $\alpha_{1,2} = 0.1$, $P_{out,system}^{HBD(II)} \leq P_{out,system}^{HD}$ for $\Omega_X \leq 11$ dB. In fact, $P_{out,system}^{HBD(II)}$ approaches that of the ideal HBD case when $\alpha_{1,2}$ is decreased due to the near absence of inter-AS interference at the II detector and it also explains the trend seen in Fig. 3.4b where it can be seen that $d_{f,system}^{HBD(II)}$ approaches that of the ideal HBD case when $\alpha_{1,2}$ is decreased. In other words, the decay of $P_{out,system}^{HBD(II)}$ approaches that of the ideal HBD case when inter-AS interference weakens, as reflected in Fig. 3.4b, for $\Omega_X \leq 5$ dB. Therefore, when an II detector is used at AS-2, the inter-AS interference is the limiting factor for both $P_{out,system}^{HBD(II)}$ and $d_{f,system}^{HBD(II)}$.

When AS-2 adopts an SIC detector, $P_{out,system}^{HBD(SIC)}$ is dominated by GS when $\Omega_X \leq 4$ dB and $\alpha_{1,2} = 5$. Similar trends for the SIC detector are also seen in Fig. 3.4b for $\Omega_X \leq 5$ dB. When $\Omega_X > 4$ dB, $P_{out,system}^{HBD(SIC)}$ is dominated by AS-2 and it can be explained from the perspective of the two-stage SIC detector at AS-2. When $\alpha_{1,2} = 5$, $x_1[t]$ is five times stronger than the SOI from GS ($x_{gs}[t]$). In addition, at stage 1 of the SIC detector, noise power (σ_2^2) is stronger than $x_{gs}[t]$ when $\Omega_X \leq 4$ dB. Thus, the SIC detector is more likely to detect and cancel $x_1[t]$ which results in $Pr(O_{gs}^{HBD}) > Pr(O_2^{HBD(SIC)})$ due

to residual SI at GS. When $\Omega_X > 4$ dB, σ_2^2 will be weaker than $x_{gs}[t]$ at stage 1 of the SIC detector. Consequently, the SIC detector is less likely to detect and cancel $x_1[t]$, leading to $Pr(O_{gs}^{HBD}) < Pr(O_2^{HBD(SIC)})$. When $\alpha_{1,2} = 10$, $P_{out,system}^{HBD(SIC)}$ is dominated by GS for $\Omega_X \leq 10$ dB due to stronger interference at AS-2, with $P_{out,system}^{HBD(SIC)}$ close to that of the ideal HBD case. Further increasing $\alpha_{1,2}$ enables $P_{out,system}^{HBD(SIC)}$ to reach near-ideal HBD performance for a wider Ω_X range due to the increased likelihood of successfully detecting and canceling $x_1[t]$, thus explaining the trend in Fig. 3.4b. Hence, the strength of the interference from AS-1 ($\alpha_{1,2}$) is the main limiting factor for both $P_{out,system}^{HBD(SIC)}$ and $d_{f,system}^{HBD(SIC)}$ when a SIC detector is used at AS-2.

From Fig. 3.4a and Fig. 3.4b, the outage and finite SNR diversity gain analysis has highlighted the feasibility of HBD-ACS over legacy HD-ACS in weak and strong interference scenarios through the II and SIC detectors, respectively. For instance, weak and strong interference scenarios could involve en route flights over sparsely and densely populated airspace, respectively. From the perspective of implementing an actual HBD system, the proposed HBD-ACS has better reliability over HD-ACS while providing more throughput than legacy HD systems.

3.5.2 Finite SNR DMT Analysis

3.5.2.1 Impact of Residual SI at GS

Observation 3.5.2.1 *The FD-enabled GS achieves non-zero diversity gain for a larger range of multiplexing gains compared to the HD GS.*

Fig. 3.5a shows the finite SNR diversity gain at GS, where it is evident that the stronger residual SI due to SI channel estimation error (ϵ) or phase noise (γ_ϕ^2) reduces $d_{f,gs}^{HBD*}$. Increasing the strength of the residual SI ($\alpha_{g,g}$) affects $d_{f,gs}^{HBD*}$ more than increasing the SI channel estimation error (ϵ) since the effect of phase noise (γ_ϕ^2) on the residual SI is amplified. From the outage probability perspective, increasing residual SI results in a slower decay rate of the outage probability, which lowers $d_{f,gs}^{HBD*}$. However, it does not imply that outage probability is better when a higher maximum value for $d_{f,gs}^{HBD*}$ is attained. Nonetheless, the range of r_f for which $d_{f,gs}^{HBD*} \geq d_{f,gs}^{HD*}$ increases when the strength of the residual SI ($\alpha_{g,g}$) decreases and vice versa. Therefore, FD-enabled GS

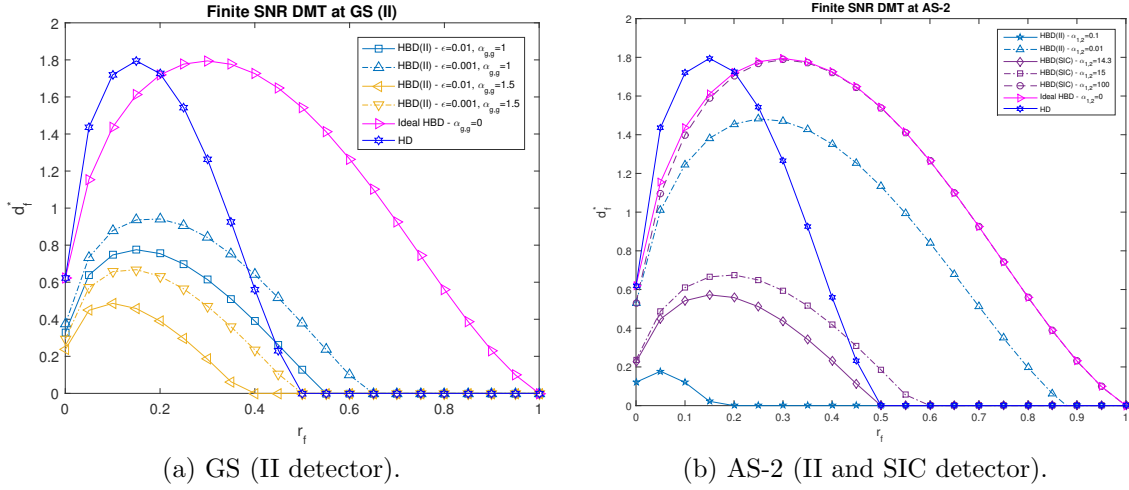


Fig. 3.5: Finite SNR DMT for $\alpha_{g,2} = 1, \gamma_\phi^2 = -130$ dBm, $\Omega_X = 10$ dB.

can experience improved DMT as residual SI decreases, which is evident in Fig. 3.5a for $\alpha_{g,g} = 1$. Although $d_{f,gs}^{HBD*}$ is limited by residual SI, the importance of proper SI mitigation is again emphasized since it is still feasible for GS to be FD-enabled if operating at a higher r_f is the objective of an ACS.

3.5.2.2 Impact of Interference at AS-2

Observation 3.5.2.2 At low multiplexing gains, the II and SIC detectors have lower finite SNR diversity gain. In contrast, at high multiplexing gains, the II and SIC detectors achieve near-ideal finite SNR diversity gain under weak and strong inter-AS interference, respectively.

Fig. 3.5b shows the finite SNR diversity gain at AS-2. The trends seen in Fig. 3.5b are similar to what was seen in [106, Fig. 4], with lower $d_{f,2}^{HBD(i)*}, i \in \{II, SIC\}$ and $d_{f,2}^{HD*}$ observed as $r_f \rightarrow 0$. It has been pointed out by Narasimhan [106] and Shin et al. [105] that Rician fading outage probability curves are influenced by Rician K factors. In particular, increasing the Rician K factor causes the slope of outage probability curves to become steeper [105, Fig. 2]. From a finite SNR DMT perspective, $r_f \rightarrow 0$ causes $K_{X_{gs}}$ to have less impact on the outage performance at AS-2.

On the other hand, Fig. 3.5b also suggests that the II and SIC detectors are able to provide better reliability at higher multiplexing gains compare to HD systems. At high

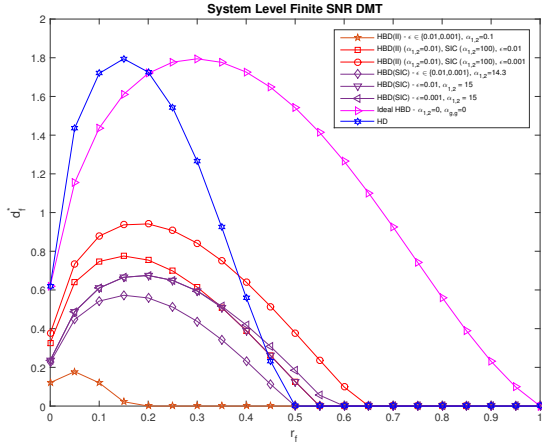


Fig. 3.6: System level finite SNR DMT (II and SIC detectors) for $\alpha_{g,2} = 1$, $\alpha_{g,g} = 1$, $\gamma_\phi^2 = -130$ dBm, $\Omega_X = 10$ dB.

multiplexing gains, if the inter-AS interference reduces, then $d_{f,2}^{HBD(II)*} \geq d_{f,2}^{HD*}$. On the other hand, at low multiplexing gains, $d_{f,2}^{HBD(II)*} < d_{f,2}^{HD*}$ even at low inter-AS interference. In fact, $d_{f,2}^{HBD(II)*}$ approaches that of the ideal HBD case as $\alpha_{1,2} \rightarrow 0$ since the signal at the II detector is almost interference-free. As a consequence, the resultant outage probability decay rate becomes similar to that of the ideal HBD case. When the SIC detector is adopted at AS-2, $d_{f,2}^{HBD(SIC)*} \geq d_{f,2}^{HD*}$ as inter-AS interference increases (for example, refer to $d_{f,2}^{HBD(SIC)*}$ at $\alpha_{1,2} = 14.3$ in Fig. 3.5b). As $\alpha_{1,2} \rightarrow \infty$, it becomes easier to detect and remove $x_1[t]$ at the two-stage SIC detector. When coupled with the lower threshold requirement of the SIC detector, as compared to HD systems, the SIC detector can potentially achieve superior diversity gains over HD systems in strong interference scenarios. Moreover, at large values of $\alpha_{1,2}$, if the multiplexing gain is high, the achievable $d_{f,2}^{HBD(SIC)*}$ matches the ideal HBD case. As shown in Fig. 3.5b, at low multiplexing gain, the achievable $d_{f,2}^{HBD(SIC)*}$ is close to that of the ideal HBD case. Therefore, the II and SIC detectors provides better reliability at higher multiplexing gains compared to HD-ACS in the presence of weak and strong interference, respectively. However, at low multiplexing gains, HD-ACS exhibited better reliability than the II and SIC detectors.

3.5.2.3 Impact of Interference at System Level

Observation 3.5.2.3 At high multiplexing gains, the HBD-ACS achieves better finite SNR diversity gain at the system level than the HD-ACS and is also constrained by inter-

AS interference and residual SI.

Fig. 3.6 shows the system level finite SNR diversity gain for HBD-ACS ($d_{f,system}^{\beta*}$) and HD-ACS ($d_{f,system}^{HD*}$) for $\beta \in \{HBD(II), HBD(SIC)\}$. From Fig. 3.6, it is evident that $d_{f,system}^{HBD(II)*} > d_{f,system}^{HD*}$ and $d_{f,system}^{HBD(SIC)*} > d_{f,system}^{HD*}$ as r_f increases, and it enables an HBD-ACS to provide better reliability at higher multiplexing gain than HD-ACS since HBD-ACS requires a lower operating threshold than existing HD-ACS at both GS and AS-2. However, the degree of improvement that HBD-ACS has over HD-ACS is constrained by the strength of interference experienced at GS and AS-2 in the HBD-ACS.

When the II detector is adopted at AS-2 for weak interference scenarios, $d_{f,gs}^{HBD*} > d_{f,2}^{HBD(II)*}$ for $\alpha_{1,2} = 0.1$. Reducing the strength of the inter-AS interference ($\alpha_{1,2} = 0.01$) causes $d_{f,2}^{HBD(II)*} > d_{f,gs}^{HBD*}$, with lower SI channel estimation error (ϵ) corresponding to higher $d_{f,system}^{HBD(II)*}$. In the presence of strong interference at AS-2 ($\alpha_{1,2} = 100$), adopting the SIC detector at AS-2 results in $d_{f,2}^{HBD(SIC)*} > d_{f,gs}^{HBD*}$. However, when interference from AS-1 is not as strong, e.g., $\alpha_{1,2} \in \{14.3, 15\}$, then $d_{f,gs}^{HBD*} > d_{f,2}^{HBD(SIC)*}$. From Fig. 3.6, the reliability of the HBD-ACS depends on the inter-AS interference at AS-2 for both II and SIC detectors and residual SI at GS. Furthermore, it is possible for the proposed HBD-ACS to attain finite SNR DMT curves that are identical to the ideal HBD case at sufficiently low residual SI.

From Fig. 3.6, the trends show that the proposed HBD-ACS is a viable alternative to legacy HD-ACS in weak and strong interference scenarios. In particular, the proposed HBD-ACS can operate at a higher multiplexing gain than legacy HD-ACS, thus offering better throughput and reliability compared to the latter.

3.6 Chapter Summary

An HBD-ACS consisting of an FD-enabled GS and two HD ASs simultaneously communicating on the same spectrum is proposed to improve spectrum utilization. To investigate the impact of interference on the proposed HBD-ACS, closed-form outage probability and finite SNR diversity gain expressions are presented in this chapter for a SIC detector over Rician fading aeronautical channels. Through outage and finite SNR diversity gain analysis, it is established that residual SI is the main limiting factor at the FD-enabled

GS. Therefore, the need for sufficient SI mitigation must be properly addressed in a HBD-ACS. At AS-2, inter-AS interference is the main limiting factor for both II and SIC detectors. At the system level, the proposed HBD-ACS is found to be very suitable for weak and strong interference scenarios for the II and SIC detectors, respectively. The proposed HBD-ACS is also able to achieve superior outage performance and better diversity gains at low-to-moderate SNRs compared to existing HD-ACS for both weak and strong interference scenarios. Finite SNR DMT analysis has also revealed that HBD-ACS can achieve interference-free diversity gain if residual SI is sufficiently suppressed, enabling HBD-ACS to be more reliable than HD-ACS at higher multiplexing gains while operating at low SNR ranges.

As this chapter focuses on HBD systems in aeronautical communications for weak and strong interference scenarios, the JD approach is investigated in the next chapter for moderate interference environments in UAV communications.

Chapter 4

Interference Management Through Joint Detection for Hybrid-Duplex UAV Communications

4.1 Introduction

In Chapter 3, HBD-ACSs are studied as a potential solution to address spectrum scarcity in MAV communications as a result of air traffic growth in the near future. Apart from MAV communications, air traffic growth for UAVs is also expected to grow rapidly in the years to come. Despite the potential benefits of multi-UAV networks, many challenges remain. One notable instance is the allocation of L-band and C-band spectrum by the ITU for UAV communications, e.g., for CNPC applications [8]. However, there is limited available spectrum for UAV communications as many other systems, e.g., aeronautical communication systems, also operate on L-band and C-band [8]. Therefore, spectrum scarcity in UAV communications is an issue that must be addressed in due time.

To this end, an HBD-UCS has been studied as a viable alternative to improve spectrum utilization with minimal disruptions [52]. With suitable SI mitigation architectures, HBD systems enable HD and FD-enabled nodes to operate concurrently on the same spectrum, leading to improved spectrum utilization. While opting for an FD-UCS, i.e., UAVs and GSs operating in FD mode, results in better spectrum utilization over the HBD paradigm, constraints imposed on the size, weight, and power requirements of UAVs may cause FD transceiver designs to be infeasible.¹ Therefore, opting for an

¹The work in this chapter has been published in [18].

HBD-UCS allows spectrum utilization to be addressed while retaining existing HD-UCS, with related applications seen in aeronautical communication systems [17, 99].

Apart from SI, inter-UAV interference is also present at the HD UAVs in the HBD-UCS. Regarding this, interference management strategies, such as the II, SIC, or the JD strategies, can be adopted to mitigate inter-UAV interference. The II approach regards interference as noise and is optimal in weak interference scenarios [164, 165] while the SIC approach, which first removes interference before detecting the SOI, is effective in strong interference scenarios [87, 88]. On the other hand, the JD approach jointly decodes the SOI and interference at the receiver, and is optimal when strong interference is present albeit at the cost of high computational complexity [94, 166]. In [99] and [17], outage probability analysis of HBD aeronautical communication systems showed that the II and the SIC strategies are interference-limited at high SNR regimes and are effective in weak and strong interference scenarios, respectively. However, in the context of UAV communications, suitable interference management strategies to handle the different levels of inter-UAV interference in multi-UAV systems have still yet not been identified.

Another issue in HBD-UCS is the need to concurrently meet QoS requirements for both CNPC links and non-CNPC links as a result of simultaneous communications over a common spectrum ². To safely operate multi-UAV systems, CNPC links have high reliability and low data rate requirements [48]. On the other hand, non-CNPC links, i.e., data links, have higher data rate requirements than CNPC links, which is dependent on the task at hand [48]. As the QoS requirements of both CNPC and non-CNPC links must be concurrently satisfied in the HBD-UCS, the extent of reliability tradeoffs for higher transmission rates in the presence of inter-UAV interference is not yet known. More importantly, it still remains to be seen if the HBD-UCS can better meet the necessary QoS requirements compared to existing HD-UCS.

To this end, the finite SNR diversity gain and finite SNR DMT of the HBD-UCS can be analyzed. The finite SNR diversity gain and finite SNR DMT describe outage probability decay rate (reliability) at a particular SNR [105], with multiplexing gain

²To enable the sharing of the spectrum for CNPC and non-CNPC links with a joint detector, the block length of the codes used, e.g., LDPC codes, should be the same [167].

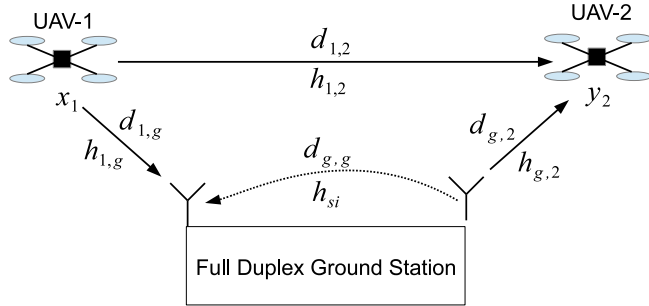


Fig. 4.1: Unmanned Aerial Vehicle 1 (UAV-1) and Unmanned Aerial Vehicle 2 (UAV-2) operating in HD mode while communicating with the FD GS.

(data rate) considered in the latter [106]. Such analysis reveals the outage probability behavior of the HBD-UCS at low SNR regimes, which is lost at asymptotic SNRs [105]. A corresponding MGR of the HBD-UCS can also be determined [168] to identify the multiplexing gains of the interfering and desired transmitters that achieves non-zero diversity gains. Through diversity gain and MGR analysis, the supported QoS range of the HBD-UCS, along with the necessary conditions to achieve non-zero diversity gains, e.g., inter-UAV interference levels and data rates, for various interference management strategies can be identified.

4.2 System Model

Fig. 4.1 shows the proposed HBD-UCS for UAV communications in a suburban environment between an FD-enabled GS node and two HD UAVs.³ In particular, Unmanned Aerial Vehicle 1 (UAV-1) transmits non-CNPC data to the GS while Unmanned Aerial Vehicle 2 (UAV-2) concurrently receives CNPC data from the GS on the same spectrum, e.g., L-band. Two antennas, one for transmission and another for reception of signals, with a shared local oscillator are assumed at the FD-enabled GS. Also, the Doppler

³The present chapter can be extended to consider an arbitrary number of uplink and downlink UAVs. To enable the modeling and analysis of such a multi-UAV network, the signal model at the GS and downlink UAVs will need to be modified. Furthermore, stochastic geometry tools, i.e., the BPP model, will need to be employed to accurately model UAV deployment. These issues are addressed in Chapter 6, where new signal models that considers the BPP model are proposed for an HBD multi-UAV network.

effect as a result of UAV mobility is assumed to be compensated. Clearly, spectrum utilization is improved at the expense of introducing SI and inter-UAV interference at the FD-enabled GS and UAV-2, respectively. To enable realistic modeling of the suburban environment, Rician fading is assumed on all UAV communication channels [8]. Additionally, the SI signal is assumed to undergo passive SI mitigation before active SI mitigation at the FD-enabled GS. Thus, we consider only residual SI at the FD-enabled GS, with the SI link (h_{si}) modeled as a Rician fading channel to account for passive and active SI mitigation [75]. A summary of important notations is also given in Table 4.1.

4.2.1 Ground Station

At the FD-enabled GS, let $x_{gs}[t]$ and $x_1[t]$ be the transmitted signals from GS and UAV-1, respectively, where the SOI and the SI signal are $x_1[t]$ and $x_{si}[t] = x_{gs}[t]$, respectively. Additionally, let $h_{1,g}[t]$ be the channel between UAV-1 and GS, and h_{si} be the SI channel gain. Then, the received signal at GS can be written as [21]:

$$y_{gs}[t] = \sqrt{\Omega_X} h_{1,g}[t] x_1[t] + \sqrt{\Omega_X \alpha_{g,g}} |h_{si}| \gamma_\phi w_\phi[t] + \sqrt{\Omega_X \alpha_{g,g}} |\tilde{h}_{si}| x_{si}[t] + w_g[t], \quad (4.1)$$

where \tilde{h}_{si} is the error of the imperfect SI channel gain estimate, defined as $\tilde{h}_{si} = h_{si} - \hat{h}_{si}$, and \hat{h}_{si} is the imperfect estimation of the SI channel gain. To model the worst case residual SI, the channel estimation error (\tilde{h}_{si}) is modeled as a circularly symmetric zero-mean complex Gaussian random variable RV with variance ϵ [81].

Additionally, let the AWGN at GS be $w_g[t]$, with zero-mean and variance σ_g^2 , and let the phase noise term $w_\phi[t]$ follow a Gaussian distribution with zero-mean and unit variance, scaled by the strength of the phase noise γ_ϕ ⁴ [21].

Let the average received signal power of the SOI, normalized with the GS receiver noise variance (σ_g^2), be Ω_X , which is related to the transmit power P_t (Watts) and distance $d_{1,g}$ (km) as:

$$\Omega_X \propto \frac{P_t}{(d_{1,g})^n \sigma_g^2}, \quad (4.2)$$

⁴The scaling factor γ_ϕ models the jitter present in oscillators due to hardware imperfections [21]

Table 4.1: Summary of Important Notations

Notations	Description
Ω_X	Average received power
$\alpha_{i,j}, i \in \{g, 1\}, j \in \{g, 2\}, i \neq j$	Strength of interference between i and j
ϵ	SI channel estimation error at the FD-enabled GS
γ_ϕ^2	Strength of phase noise at the FD- enabled GS oscillator
σ_g^2	Strength of AWGN at the FD-enabled GS
σ_2^2	Strength of AWGN at the UAV-2

where n is the pathloss exponent. We select the channel between UAV-1 and GS as the reference link, with the average received signal power in the other links expressed relative to the reference link to represent the inter-UAV interference level $\alpha_{i,j}$ as follows:

$$\alpha_{i,j} = \left(\frac{d_{1,g}}{d_{i,j}} \right)^n, i \in \{g, 1\}, j \in \{g, 2\}. \quad (4.3)$$

From (4.2) and (4.3), the average received SI power at GS can be expressed as $\Omega_X \alpha_{g,g}$.

4.2.2 Unmanned Aerial Vehicle 2

The SOI and the interfering signal at UAV-2 are $x_{gs}[t]$ and $x_1[t]$, respectively. Let $h_{g,2}[t]$ be the channel between GS and UAV-2, and let $h_{1,2}[t]$ be the channel between UAV-1 and UAV-2. Let $w_2[t]$ be the AWGN at UAV-2 with zero-mean and variance σ_2^2 . Then, the received signal at UAV-2 can be expressed as:

$$y_2[t] = \sqrt{\Omega_X \alpha_{g,2}} h_{g,2}[t] x_{gs}[t] + \sqrt{\Omega_X \alpha_{1,2}} h_{1,2}[t] x_1[t] + w_2[t], \quad (4.4)$$

where $\Omega_X \alpha_{g,2}$ and $\Omega_X \alpha_{1,2}$ indicate the average received signal powers of the SOI and interfering signal, respectively.

As interference is present at UAV-2, we consider three approaches to handle the interference. The first approach is to assume an II detector at UAV-2 by treating $x_1[t]$ as noise, thus effectively ignoring interference. The second approach assumes a two-stage SIC detector at UAV-2 where $x_1[t]$ is detected and removed before $x_{gs}[t]$ is detected [153]. The final approach assumes a joint detector where both $x_{gs}[t]$ and $x_1[t]$ are jointly detected [169].

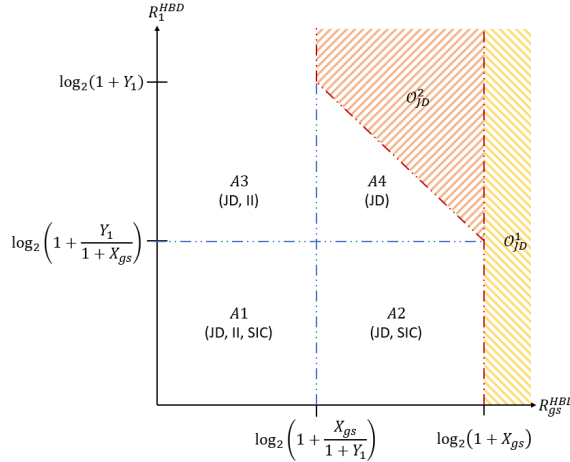


Fig. 4.2: The achievable instantaneous rate regions of the II, SIC and joint detectors (unshaded areas) at UAV-2 with respect to the transmission rates of the GS (R_{GS}^{HBD}) and UAV-1 (R_1^{HBD}). The shaded areas, O_{JD}^1 and O_{JD}^2 , respectively denote the outage region of the joint detector if SOI detection fails or if the sum rate constraint is not met.

4.3 Outage Probability Derivations

In this section, we derive the closed-form outage probability expression for the joint detector at UAV-2. As inter-UAV interference increases, we show that the outage probability of the joint detector approaches that of an interference-free UAV-2. We also define the system level outage probability, along with references for benchmark schemes, to identify bottlenecks in the proposed HBD-UCS system.

4.3.1 Joint Detector at UAV-2

Let R_1^i and R_{gs}^i be the transmission rates of UAV-1 and GS, respectively, where $i \in \{HBD, HD\}$, and $R_{sum}^i = R_1^i + R_{gs}^i$ be the sum rate of the system. To maintain the same sum rate, the transmission rate of HD systems must be twice that of HBD systems as spectrum is shared between nodes in the former [75, 154]. Thus, let $R_j^{HBD} = \frac{1}{2}R_j^{HD}$ for $j \in \{1, gs\}$ to maintain a fair comparison between HBD-UCS and HD-UCS.

At UAV-2, let the instantaneous received signal power of the SOI and the inter-UAV interference be $X_{gs} = \Omega_X \alpha_{g,2} |h_{g,2}|^2$ and $Y_1 = \Omega_X \alpha_{1,2} |h_{1,2}|^2$, respectively, where X_{gs} and Y_1 are independent non-centered Chi-squared distributed RV with respective Rician K factors $K_{X_{gs}}$ and K_{Y_1} .

To mitigate inter-UAV interference, the joint detector at UAV-2 simultaneously detects both SOI and interference from GS and UAV-1, respectively. The resultant instantaneous achievable rate region of the joint detector ($A1$ to $A4$), along with the II detector ($A1$ and $A3$) and the SIC detector ($A1$ and $A2$), are illustrated in Fig. 4.2. Based on the instantaneous achievable rate region, the HBD outage event of the joint detector at UAV-2 is defined as:

$$O_2^{HBD(JD)} = O_{JD}^1 \cup O_{JD}^2 \quad (4.5)$$

$$\text{where } O_{JD}^1 = \left\{ h_{g,2}, h_{1,2} : R_{gs}^{HBD} > \log_2 \left(1 + X_{gs} \right) \right\}, \quad (4.6)$$

$$O_{JD}^2 = \left\{ h_{g,2}, h_{1,2} : R_1^{HBD} + R_{gs}^{HBD} > \log_2 \left(1 + X_{gs} + Y_1 \right), \right. \\ \left. \log_2 \left(1 + \frac{X_{gs}}{1 + Y_1} \right) \leq R_{gs}^{HBD} \leq \log_2 \left(1 + X_{gs} \right) \right\}. \quad (4.7)$$

Remark 4.1 *The joint detector outage event ($O_2^{HBD(JD)}$) occurs if SOI detection fails (O_{JD}^1) or if the sum rate constraint is not met (O_{JD}^2). Evidently, meeting the sum rate constraint (O_{JD}^2) enables the joint detector to attain a larger rate region than the II and the SIC detectors at the cost of complex hardware [166, 169].*

In a two-user multiple access channel, the joint detector simultaneously decodes the two user's data streams as the SOIs. An outage event occurs if either of the streams cannot be decoded [153]. In contrast, only the signal from the FD-enabled GS is treated as the SOI while the signal from UAV-2 is treated as interference in this chapter. Therefore, the joint detector tries to decode only the SOI, while utilizing the structure of the interfering signal. Consequently, the interfering signal can be transmitted at a higher rate than the capacity of the interfering link [170].

The advantages of the joint detector in this chapter is evident in Fig. 4.2. In particular, (4.6) and (4.7) are obtained using the above principles. A similar decoding algorithm for an interference-limited receiver in a two-user interference channel is also investigated in [93, 95], where similar achievable instantaneous rate regions were obtained. For the II and SIC detectors, the respective achievable instantaneous rate regions are obtained using the outage events definition in [17]. Together, the achievable instantaneous rate regions in Fig. 4.2 form the basis for Remark 4.1.

Next, let $\bar{\alpha}(q, \Omega, K, \gamma)$ be the CDF expansion of a Rician fading channel, which is defined as:

$$\bar{\alpha}(q, \Omega, K, \gamma) = (-1)^q \exp(-K) \frac{L_q^{(0)}(K)}{(1+q)!} \left(\frac{(1+K)}{\Omega} \gamma \right)^{q+1}, \quad (4.8)$$

where q , Ω , K and γ represents an arbitrary non-negative integer, average received power of a Rician signal, Rician K factor and threshold, respectively, and $L_q^{(0)}(\bullet)$ represents the q -th degree, zero-order Laguerre polynomials [157]. Then, the closed-form outage probability expression for the joint detector is presented in the following theorem.

Theorem 4.1 *The closed-form expression for the outage probability with joint detector at UAV-2 is:*

$$\begin{aligned} \Pr(O_2^{HBD(JD)}) \approx & 1 - Q_1 \left(\sqrt{2K_{X_{gs}}}, \sqrt{\frac{2(K_{X_{gs}} + 1)\gamma_{th,2}^{HBD}}{\Omega_X \alpha_{g,2}}} \right) \\ & + \sum_{n=0}^{K_{tr}} \sum_{i=0}^n \sum_{j=0}^{i+1} \bar{\alpha}(i, \Omega_X \alpha_{1,2}, K_{Y_1}, 1) \bar{\alpha}(n-i, \Omega_X \alpha_{g,2}, K_{X_{gs}}, 1) \binom{i+1}{j} \\ & \times (-1)^{i+1} G_1(i, j, b_2, \gamma_{th,2}^{HBD}) \frac{G_2(j+n-i+1, b_1, \gamma_{th,2}^{HBD})}{j+n-i+1}, \end{aligned} \quad (4.9)$$

where K_{tr} is the truncation order, $\gamma_{th,2}^{HBD} = 2^{R_{gs}^{HBD}} - 1$ is the threshold, $b_1 = 2^{R_1^{HBD}} (2^{R_{gs}^{HBD}} - 1)$, $b_2 = 2^{R_1^{HBD} + R_{gs}^{HBD}} - 1$, $G_1(i, j, b_2, \gamma_{th,2}^{HBD}) = (-b_2)^{i+1-j} - (-\gamma_{th,2}^{HBD})^{-j}$, $G_2(j+n-i+1, b_1, \gamma_{th,2}^{HBD}) = (b_1)^{j+n-i+1} - (\gamma_{th,2}^{HBD})^{j+n-i+1}$ and $Q_1(\cdot, \cdot)$ is the Marcum Q function [157]

Proof: The proof can be found in Appendix B.1.

Remark 4.2 *The first two terms on the RHS of (4.9) are due to the outage event O_{JD}^1 . These two terms also correspond to the outage probability of an interference-free UAV-2. The third term on the RHS of (4.9) is due to the outage event O_{JD}^2 , where the functions $\bar{\alpha}(i, \Omega_X \alpha_{1,2}, K_{Y_1}, 1)$ and $\bar{\alpha}(n-i, \Omega_X \alpha_{g,2}, K_{X_{gs}}, 1)$ are due to the inter-UAV interference and SOI, respectively. From (4.9), it is evident that failure to either detect the SOI or meet the sum rate constraint contributes to outage probability.*

The expression in (4.9) is only valid if the power series in the second term on the RHS converges, which is proven in the following theorem.

Table 4.2: References for the outage probability of the benchmark schemes

Protocol/Detector	Notation	Reference
II Detector at GS	$Pr(\bar{O}_{gs}^{HBD})$	[17, eq. (6)]
II Detector at UAV-2	$Pr(O_2^{HBD(II)})$	[17, eq. (8)]
SIC Detector at UAV-2	$Pr(O_2^{HBD(SIC)})$	[17, eq. (10)]
HD-UCS at GS	$Pr(O_{gs}^{HD})$	[17, eq. (12)]
HD-UCS at UAV-2	$Pr(O_2^{HD})$	[17, eq. (13)]

Theorem 4.2 *The power series in (4.9) has a convergence radius of ∞ .*

Proof: The proof can be found in Appendix B.2.

It should be noted that the differentiation of a convergent power series, e.g., (B.8), is also valid within the convergence radius [49, 171], which is useful for deriving expressions related to finite SNR analysis in the next section.

It is known that the joint detector is effective when strong interference is encountered [94, 165, 166, 169]. To investigate the effect of strong inter-UAV interference, we evaluate the limit of $\bar{\alpha}(i, \Omega_X \alpha_{1,2}, K_{Y_1}, 1)$ with respect to $\alpha_{1,2}$. In particular, we evaluate the limit for the extreme case of very strong inter-UAV interference ($\alpha_{1,2} \rightarrow \infty$), using the same approach in [17, eq.(11)]. From (4.8) and (4.9), it can be seen that the outage probability with joint detector approaches that of an interference-free UAV-2 as $\alpha_{1,2} \rightarrow \infty$. Hence, the joint detector is suitable for strong interference scenarios since the detection of the SOI becomes easier. Although the SIC is also known to perform well at very strong inter-UAV interference levels, the joint detector still outperforms the SIC detector at high SNRs, as will be shown in Section 4.5. More importantly, (4.9) also suggests the possibility of the joint detector attaining near-genie-aided (near perfect), i.e., interference-free, outage performance when interference is sufficiently strong.

4.3.2 Benchmark Schemes and System Level Outage Probability

In this chapter, the II detector, SIC detector, and the HD-UCS are also considered at UAV-2. These schemes are treated as benchmark schemes as the associated outage probability expressions are already available in the literature, with the references provided in Table 4.2. At the GS, residual SI is present and thus, the GS effectively adopts an II detector. The outage probability expression for the GS is also available in the literature and is similarly provided in Table 4.2.

To compare the overall performance of the HBD-UCS against the HD-UCS at the system level, we define the HBD and HD system level outage probability as:

$$P_{out,system}^{\beta} = \max \{Pr(O_{gs}^{HBD}), Pr(O_2^{\beta})\}, \quad (4.10)$$

$$P_{out,system}^{HD} = \max \{Pr(O_{gs}^{HD}), Pr(O_2^{HD})\} \quad (4.11)$$

where $\beta \in \{HBD(II), HBD(SIC), HBD(JD)\}$. The defined HBD system level outage probability enables the identification of performance bottleneck in the proposed HBD-UCS.

4.4 Finite SNR Analysis

In this section, the necessary mathematical analysis and closed-form expressions for finite SNR diversity gains are presented for both fixed and variable transmission rate systems, with detailed derivations omitted for brevity.

4.4.1 Finite SNR Diversity Gain

The asymptotic diversity gain of a system, given by Zheng and Tse [107, eq. (3)], quantifies the outage probability decay rate at high SNR. However, the definition in [107, eq. (3)] may not be accurate at low to moderate SNR ranges [105].

To this end, finite SNR diversity gain definitions for low to moderate SNR ranges have been presented by Narasimhan [106, eq. (5)] and Shin et al. [105]. Let O , $Pr(O)$, R , γ and Ω be the outage event, outage probability, transmission rate, threshold and average received power with unit noise variance, respectively. Then, the finite SNR diversity gain (d_f) of a given system is [106, eq. (5)]:

$$d_f = \frac{-\Omega}{Pr(O)} \frac{\partial}{\partial \Omega} Pr(O). \quad (4.12)$$

At high SNR, (4.12) is consistent with the asymptotic diversity gain definition given by Zheng and Tse [107], as proven by Shin et al. [105] and Heidarpour et al. [108]. Moreover, (4.12) enables system designers to investigate the impact of residual SI and inter-UAV interference in HBD-UCS and to quantify potential outage performance improvements through code designs for the II, SIC and joint detectors at typical operating SNR ranges.

4.4.2 Finite SNR DMT Parameters

For variable transmission rate systems, i.e., adaptive rate systems, the finite SNR multiplexing gain r_f is defined as [106, eq. (4)]:

$$r_f = \frac{R(\Omega)}{\log_2(1 + \Omega)}. \quad (4.13)$$

In variable transmission rate systems, $Pr(O)$ is computed with respect to $\gamma = (1 + \Omega)^{r_f} - 1$. The finite SNR multiplexing gain indicates the sensitivity of γ when Ω changes, and similar to (4.12), (4.13) has also been proven by Shin et al. [105] and Heidarpour et al. [108] to be consistent with asymptotic multiplexing gain in [107, eq. (3)].

Let $\Delta(\Omega) = \widehat{\Omega} - \Omega$ where $\widehat{\Omega} > \Omega$. Then, extending upon (4.12), the finite SNR diversity gain for variable transmission rate systems (denoted as d_f^*) is [105, eq. (36)]:

$$d_f^* = \frac{-\Omega}{Pr(O)} \lim_{\Delta(\Omega) \rightarrow 0} \left[\frac{Pr(\widehat{O}) - Pr(O)}{\Delta(\Omega)} \right] \quad (4.14)$$

$$= \frac{-\Omega}{Pr(O)} \frac{\partial}{\partial \Delta(\Omega)} Pr(\widehat{O}) \Big|_{\Delta(\Omega)=0}, \quad (4.15)$$

where (4.15) is obtained from (4.14) by applying L'hopital's rule with respect to $\Delta(\Omega)$, \widehat{O} is the outage event with respect to $R(\Omega + \Delta(\Omega))$ and $Pr(\widehat{O})$ is the outage probability with average received power $\widehat{\Omega} = \Omega + \Delta(\Omega)$, threshold $\widehat{\gamma} = [1 + \Omega + \Delta(\Omega)]^{r_f} - 1$ and $Pr(\widehat{O}) = Pr(O)$ when $\Delta(\Omega) = 0$. Furthermore, although not explicitly shown in (4.15), we define d_f^* to be non-negative, i.e., $d_f^* = \max \left\{ 0, \frac{-\Omega}{Pr(O)} \frac{\partial}{\partial \Delta(\Omega)} Pr(\widehat{O}) \Big|_{\Delta(\Omega)=0} \right\}$, as it is a measure of the negative slope of the outage probability curve [106].

Let the normalized n^{th} moment of a RV Z be:

$$M\{Z^n\} = \frac{E\{Z^n\}}{(\Omega)^n} \quad (4.16)$$

and let function $g(i, j, \Omega, r_f)$ be:

$$g(i, j, \Omega, r_f) = ([1 + \Omega]^{r_f} - 1)^i (\Omega)^j \left[([1 + \Omega]^{r_f} - 1) \frac{j}{\Omega} + (i + 1)(r_f)(1 + \Omega)^{r_f - 1} \right], \quad (4.17)$$

where i and j are integers. The function $g(i, j, \Omega, r_f)$ reflects the outage probability decay rate of a variable transmission rate scheme due to average received power (Ω) and finite SNR multiplexing gain (r_f) [17].

It should be noted that the resultant finite SNR diversity gain expression in (4.15) is based on [105, eq. (36)] and [106, eq. (5)]. Although [105, eq. (36)] and [106, eq. (5)] evaluated finite SNR diversity gain through different approaches and definitions, the former is based on the latter. Hence, (4.15) shows that both works are unified under the same principles. Similar to (4.12), the impact of residual SI and inter-UAV interference in adaptive HBD-UCS can be analyzed through (4.15).

4.4.3 Finite SNR Diversity Gain and DMT for HBD Systems

For the joint detector, the finite SNR diversity gain ($d_{f,2}^{HBD(JD)}$) is given in the following proposition.

Proposition 4.1 *The finite SNR diversity gain at UAV-2 for the joint detector is:*

$$d_{f,2}^{HBD(JD)} \approx \frac{-\Omega_X}{Pr(O_2^{HBD(JD)})} \left[\sum_{m=0}^{K_{tr}} \bar{\alpha}(m, \alpha_{g,2}, K_{X_{gs}}, \gamma_{th,2}^{HBD}) \right. \\ \times (-m-1)(\Omega_X)^{-m-2} + \sum_{n=0}^{K_{tr}} \sum_{i=0}^n \sum_{j=0}^{i+1} \bar{\alpha}(i, \alpha_{1,2}, K_{Y_1}, 1) \\ \times \bar{\alpha}(n-i, \alpha_{g,2}, K_{X_{gs}}, 1) \binom{i+1}{j} (-1)^{i+1} G_1(i, j, b_2, \gamma_{th,2}^{HBD}) \\ \times \left. \frac{G_2(j+n-i+1, b_1, \gamma_{th,2}^{HBD})}{j+n-i+1} (-n-2)(\Omega_X)^{-n-3} \right]. \quad (4.18)$$

Proof: At UAV-2, $d_{f,2}^{HBD(JD)}$ can be obtained from (4.9) and (4.12).

The expression in (4.18) is accurate even at low to moderate Ω_X , and it is useful in evaluating the impact of inter-UAV interference on outage probability decay trends.⁵ To uncover the asymptotic outage behavior for the joint detector, we evaluate (4.18) at high Ω_X , as shown in the following corollary.

Corollary 4.1 *At UAV-2, the joint detector achieves full diversity at high SNR regimes.*

Proof: *To prove Corollary 4.1, we have to show that*

$$\lim_{\Omega_X \rightarrow \infty} \frac{-\Omega_X}{Pr(O_2^{HBD(JD)})} \frac{\partial}{\partial \Omega_X} Pr(O_2^{HBD(JD)}) = 1. \quad (4.19)$$

⁵To analytically gauge the accuracy of the new power series expressions presented in this Chapter, one will need to conduct a truncation analysis. Work in this direction is left as an open research challenge which can be addressed in future studies.

By simplifying (4.18) and evaluating the limits with respect to Ω_X leads to the following expression:

$$\lim_{\Omega_X \rightarrow \infty} d_{f,2}^{HBD(JD)} \approx \lim_{\Omega_X \rightarrow \infty} \frac{-1}{\Omega_X \cdot Pr(O_2^{HBD(JD)})} \left[\sum_{m=0}^{K_{tr}} \bar{\alpha}(m, \alpha_{g,2}, K_{X_{gs}}, \gamma_{th,2}^{HBD})(-m-1)(\Omega_X)^{-m} \right. \\ + \sum_{n=0}^{K_{tr}} \sum_{i=0}^n \sum_{j=0}^{i+1} \bar{\alpha}(i, \alpha_{1,2}, K_{Y_1}, 1) \bar{\alpha}(n-i, \alpha_{g,2}, K_{X_{gs}}, 1) \binom{i+1}{j} \\ \times G_1(i, j, b_2, \gamma_{th,2}^{HBD}) \frac{G_2(j+n-i+1, b_1, \gamma_{th,2}^{HBD})(-n-2)}{(-1)^{-i-1}(j+n-i+1)(\Omega_X)^{n+1}} \left. \right]. \quad (4.20)$$

For the first term in the numerator of (4.20), $\lim_{\Omega_X \rightarrow \infty} (\Omega_X)^{-m} = 0$ when $m > 0$ and $\lim_{\Omega_X \rightarrow \infty} (\Omega_X)^{-m} = 1$ when $m = 0$. Likewise for the second term in the numerator, $\lim_{\Omega_X \rightarrow \infty} (\Omega_X)^{-n-1} = 0$ for $n \geq 0$. Therefore, we only consider $m = 0$ when evaluating the limit in the numerator. Repeating the same steps for the denominator in (4.20) leads to (4.19)

From (4.19), the joint detector's diversity gain is better than the II and SIC detectors, as shown in [17, eq. (28)], and is equivalent to an HD-UCS [17, eq. (31)].

For the GS and UAV-2 operating under a variable rate transmission scheme, let the variable transmission rate of UAV-1 and GS be $R_1^{HBD}(\Omega_X) = r_{f,1} \log_2(1 + \Omega_X)$ and $R_{gs}^{HBD}(\Omega_X) = r_{f,gs} \log_2(1 + \Omega_X)$, respectively. Also, let the threshold at GS and UAV-2 be $\gamma_{th,gs}^{HBD} = [1 + \Omega_X]^{r_{f,1}} - 1$ and $\gamma_{th,2}^{HBD} = [1 + \Omega_X]^{r_{f,gs}} - 1$, respectively. Then, the variable rate finite SNR diversity gain expressions are presented in the following propositions.

Proposition 4.2 At GS, the variable rate finite SNR diversity gain is:

$$d_{f,gs}^{HBD*} \approx \frac{-\Omega_X}{Pr(O_{gs}^{HBD})} \sum_{q=0}^{K_{tr}} \sum_{l_1+l_2+l_3=q+1} \bar{\alpha}(q, 1, K_{X_1}, 1) \frac{(q+1)!}{l_1! \cdot l_2! \cdot l_3!} \\ \times M\{Y_{si,1}^{l_1}\} M\{Y_{si,2}^{l_2}\} g(q, l_1 + l_2 - q - 1, \Omega_X, r_{f,1}). \quad (4.21)$$

Proof: Let $\Omega = \Omega_X$, $\widehat{\Omega} = \widehat{\Omega}_X$ and $\gamma = \gamma_{th,gs}^{HBD} = [1 + \Omega_X]^{r_{f,1}} - 1$ and $O = O_{gs}^{HBD}$. Then, $d_{f,gs}^{HBD*}$ can be obtained through algebraic manipulations by substituting [17, eq. (6)] into (4.15).

$$d_{f,2}^{HBD(II)*} \approx \frac{-\Omega_X}{Pr(O_2^{HBD(II)})} \sum_{q=0}^{K_{tr}} \sum_{l=0}^{q+1} \bar{\alpha}(q, \alpha_{g,2}, K_{X_{gs}}, 1) \times \binom{q+1}{l} M\{Y_1^l\} g(q, l-q-1, \Omega_X, r_{f,gs}). \quad (4.22)$$

$$d_{f,2}^{HBD(SIC)*} \approx \frac{-\Omega_X}{Pr(O_2^{HBD(SIC)})} \left[\sum_{q=0}^{K_{tr}} \sum_{l=0}^{q+1} \bar{\alpha}(q, \alpha_{1,2}, K_{Y_1}, 1) \binom{q+1}{l} M\{X_{gs}^l\} g(q, l-q-1, \Omega_X, r_{f,1}) + \sum_{m=0}^{K_{tr}} \bar{\alpha}(m, \alpha_{g,2}, K_{X_{gs}}, 1) g(m, -m-1, \Omega_X, r_{f,gs}) - \sum_{n=0}^{K_{tr}} \sum_{i=0}^n \sum_{j=0}^{i+1} \bar{\alpha}(i, \alpha_{1,2}, K_{Y_1}, 1) \times \bar{\alpha}(n-i, \alpha_{g,2}, K_{X_{gs}}, 1) \frac{\binom{i+1}{j}}{j+n-i+1} g(j+n+1, -n-2, \Omega_X, r_{f,1}) \right]. \quad (4.23)$$

$$d_{f,2}^{HBD(JD)*} \approx \frac{-\Omega_X}{Pr(O_2^{HBD(JD)})} \left[\sum_{m=0}^{K_{tr}} \bar{\alpha}(m, \alpha_{g,2}, K_{X_{gs}}, 1) g(m, -m-1, \Omega_X, r_{f,gs}) + \sum_{n=0}^{K_{tr}} \sum_{i=0}^n \sum_{j=0}^{i+1} \bar{\alpha}(i, \alpha_{1,2}, K_{Y_1}, 1) \bar{\alpha}(n-i, \alpha_{g,2}, K_{X_{gs}}, 1) \binom{i+1}{j} \frac{(-1)^{i+1}}{j+n-i+1} \times \left(G_1(i, j, b_2, \gamma_{th,2}^{HBD}) G_2(j+n-i+1, b_1, \gamma_{th,2}^{HBD}) \frac{-n-2}{(\Omega_X)^{n+3}} + (\Omega_X)^{-n-2} \left[G_1(i, j, b_2, \gamma_{th,2}^{HBD}) G'_2(j+n-i+1, b_1, \gamma_{th,2}^{HBD}) + G_2(j+n-i+1, b_1, \gamma_{th,2}^{HBD}) G'_1(i, j, b_2, \gamma_{th,2}^{HBD}) \right] \right) \right]. \quad (4.24)$$

Proposition 4.3 At UAV-2, the variable rate finite SNR diversity gain with the II and the SIC detectors are given in (4.22) and (4.23), respectively.

Proof: Let $\Omega = \Omega_X$, $\widehat{\Omega} = \widehat{\Omega}_X$ and $\gamma = \gamma_{th,2}^{HBD} = [1 + \Omega_X]^{r_{f,gs}} - 1$ and $O = O_2^{HBD,i}, i \in \{II, SIC\}$. Then, $d_{f,2}^{HBD(II)*}$ and $d_{f,2}^{HBD(SIC)*}$ can be obtained through algebraic manipulations by respectively substituting [17, eq. (8)] and [17, eq. (10)] into (4.15).

Proposition 4.4 At UAV-2, the variable rate finite SNR diversity gain for the joint

Table 4.3: References for the finite SNR diversity gains of the benchmark schemes

Protocol/Detector	Notation	Reference
II Detector at GS	$d_{f,gs}^{HBD}$	[17, eq. (24)]
II Detector at UAV-2	$d_{f,2}^{HBD(II)}$	[17, eq. (26)]
SIC Detector at UAV-2	$d_{f,2}^{HBD(SIC)}$	[17, eq. (27)]
HD-UCS at GS	$d_{f,gs}^{HD}$	[17, eq. (29)]
HD-UCS at UAV-2	$d_{f,2}^{HD}$	[17, eq. (30)]

detector is given in (4.24), where:

$$\begin{aligned}
 G'_1(i, j, b_2, \gamma_{th,2}^{HBD}) &= (i+1-j)(-b_2)^{i-j}(-(r_{f,1} + r_{f,gs})) \\
 &\quad \times (1 + \Omega_X)^{(r_{f,1} + r_{f,gs})-1} - \frac{j(r_{f,gs})(1 + \Omega_X)^{r_{f,gs}-1}}{(-\gamma_{th,2}^{HBD})^{j+1}} \\
 G'_2(j+n-i+1, b_1, \gamma_{th,2}^{HBD}) &= (j+n-i+1)(b_1)^{j+n-i} \\
 &\quad \times [(r_{f,1} + r_{f,gs})(1 + \Omega_X)^{r_{f,1}+r_{f,gs}-1} - r_{f,1}(1 + \Omega_X)^{r_{f,1}-1}] \\
 &\quad - (j+n-i+1)(\gamma_{th,2}^{HBD})^{j+n-i}(r_{f,gs}(1 + \Omega_X)^{r_{f,gs}-1})
 \end{aligned}$$

It should be pointed out that $G'_1(i, j, b_2, \gamma_{th,2}^{HBD})$ and $G'_2(j+n-i+1, b_1, \gamma_{th,2}^{HBD})$ are the derivative of $G_1(i, j, b_2, \gamma_{th,2}^{HBD})$ and $G_2(j+n-i+1, b_1, \gamma_{th,2}^{HBD})$, respectively.

Proof: Let $b_1 = (1 + \Omega_X)^{r_{f,1}+r_{f,gs}} - (1 + \Omega_X)^{r_{f,1}}$, $b_2 = (1 + \Omega_X)^{r_{f,1}+r_{f,gs}} - 1$, $\Omega = \Omega_X$, $\widehat{\Omega} = \widehat{\Omega}_X$ and $\gamma = \gamma_{th,2}^{HBD} = [1 + \Omega_X]^{r_{f,gs}} - 1$ and $O = O_2^{HBD(JD)}$. Then, following a similar approach in [17, eq. (35)], $d_{f,2}^{HBD(JD)*}$ is obtained from (4.15).

The finite SNR diversity gain presented earlier enables system designers to quantify the degree of improvement obtainable through an increase in SNR, thus identifying suitable detectors for various inter-UAV interference scenarios.

4.4.4 Benchmark Schemes and System Level Finite SNR Diversity Gain

Similar to Section 4.3.2, the diversity gains of the benchmark schemes at the GS and at UAV-2 are available in the literature, with the references provided in Table 4.3. The system level diversity gains are defined as:

$$d_{f,system}^{\beta} = \min \{d_{f,gs}^{HBD}, d_{f,2}^{\beta}\}, \quad (4.25)$$

$$d_{f,system}^{HD} = \min \{d_{f,gs}^{HD}, d_{f,2}^{HD}\}, \quad (4.26)$$

$$d_{f,system}^{\beta*} = \min \{d_{f,gs}^{HBD*}, d_{f,2}^{\beta*}\}, \quad (4.27)$$

$$d_{f,system}^{HD*} = \min \{d_{f,gs}^{HD*}, d_{f,2}^{HD*}\}, \quad (4.28)$$

where $\beta \in \{HBD(II), HBD(SIC), HBD(JD)\}$. Quantifying the system level diversity gains allows for the identification of supported QoS requirements for the discussed detectors under various inter-UAV interference scenarios, which is discussed in Section 4.5.

4.5 Numerical and Simulation Results

In this section, we present the numerical and simulation results of the outage probabilities and finite SNR diversity gains at UAV-2 and at system level. Monte Carlo simulations, conducted with 10^9 samples, are also presented to verify the accuracy of the outage probability computations of the various detectors. The Rician K factors, i.e., $K_{X_1} K_{Y_{si,1}}$, $K_{X_{gs}}$, K_{Y_1} , are fixed at 15. The noise variance at GS (σ_g^2) and UAV-2 (σ_2^2) are fixed at $-115dBm$, with HD sum rate (R_{sum}^{HD}) and HBD sum rate (R_{sum}^{HBD}) set to 1, i.e., $R_{sum}^{HD} = R_{sum}^{HBD} = 1$.

4.5.1 Outage and Finite SNR Diversity Gain Analysis at UAV-2

Observation 4.5.1.1 *The joint detector achieves genie-aided outage performance when inter-UAV interference is sufficiently strong and is not interference-limited at high SNR regimes.*

The outage probabilities and diversity gains of the II, SIC, and the joint detectors are plotted in Fig. 4.3. As a comparison, the outage probability and diversity gain of the HD-UCS are also included. From Fig. 4.3a, it is observed for all inter-UAV interference levels that the joint detector achieves genie-aided outage probability at moderate and high SNR regimes. However, at very low SNR regimes, a slight performance degradation is observed for the joint detector due to weak inter-UAV interference. Additionally, it is observed that both the II and the SIC detectors are interference-limited at high SNR regimes, unlike the joint detector. Such a behavior is reflected in the intersection of the HBD-UCS outage probability with the HD-UCS in Fig. 4.3a. Nonetheless, the SIC detector attains lower outage probability than the II detector under strong inter-UAV interference, e.g., $\alpha_{1,2} = 5$. Similarly, the II detector attains lower outage probability than the SIC detector under weak inter-UAV interference, e.g., $\alpha_{1,2} = 0.5$.

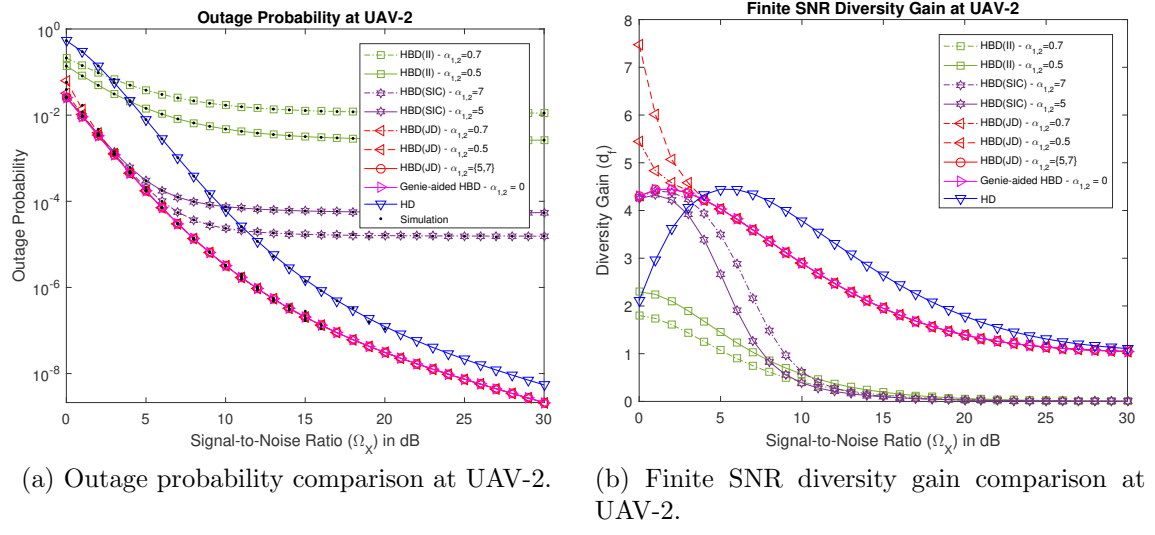


Fig. 4.3: Outage probability and finite SNR diversity gain at UAV-2 (II, SIC and joint detectors) for $\alpha_{g,2} = 1$.

In Fig. 4.3b, the diversity gain expressions of the II, SIC and the joint detectors are validated. As finite SNR diversity gain quantifies the decay of outage probability curves, it can be observed that the diversity gain of the various detectors corresponds to the steepness of the associated outage probability curves in Fig. 4.3a. Furthermore, the diversity gain of the joint detector indicates that outage probability can be further improved when Ω_X is increased. It is also shown that the joint detector attains genie-aided diversity gains as $\Omega_X \rightarrow \infty$, validating Corollary 4.1.

When compared against the HD-UCS, the joint detector achieves much better finite SNR diversity gains at low SNR regimes. However, at moderate SNR regimes, the absence of inter-UAV interference causes the HD-UCS to achieve better diversity gains than the joint detector and the genie-aided HBD-UCS. In particular, the effect of inter-UAV interference on the joint detector's finite SNR diversity gain is reflected in the second term of (4.18). In the case of HD-UCS, the inter-UAV interference term is absent, thus enabling better diversity gain than the joint detector. Finally, the HD-UCS, joint detector and the genie-aided HBD-UCS achieves the same diversity gains at asymptotic SNR regimes. In contrast, the diversity gain of the II and the SIC detectors approaches 0 as $\Omega_X \rightarrow \infty$ since both detectors are interference-limited at high SNR regimes. Similar to Fig. 4.3a, the intersection in Fig. 4.3b indicates the SNR where the decay rate of the HD-UCS is

Table 4.4: System Level HBD-UCS Performance Bottleneck for $\epsilon \in \{0.01, 0.001\}$

Mode	$\alpha_{1,2}$	$Pr(O_{gs}) \leq Pr(O_2)$	$Pr(O_{gs}) > Pr(O_2)$
HBD(II)	$\alpha_{1,2} \in \{0.5, 0.7\}$	$0dB \leq \Omega_X \leq 30dB$	-
HBD(SIC)	$\alpha_{1,2} = 5$	$4dB < \Omega_X \leq 30dB$	$0dB \leq \Omega_X \leq 4dB$
HBD(SIC)	$\alpha_{1,2} = 7$	$7dB < \Omega_X \leq 30dB$	$0dB \leq \Omega_X \leq 7dB$
HBD(JD)	$\alpha_{1,2} \in \{0.5, 0.7\}$	$0dB \leq \Omega_X < 2dB$	$2dB \leq \Omega_X \leq 30dB$
HBD(JD)	$\alpha_{1,2} \in \{5, 7\}$	-	$0dB \leq \Omega_X \leq 30dB$

greater than the HBD-UCS. However, it must be noted that a large diversity gain is not an indication of better performance in absolute terms. Instead, it only shows how fast outage probability is decaying as SNR is increasing.

Observation 4.5.1.2 *The impact of moderate inter-UAV interference on the joint detector is negligible, with lower outage probability observed than the II and the SIC detectors.*

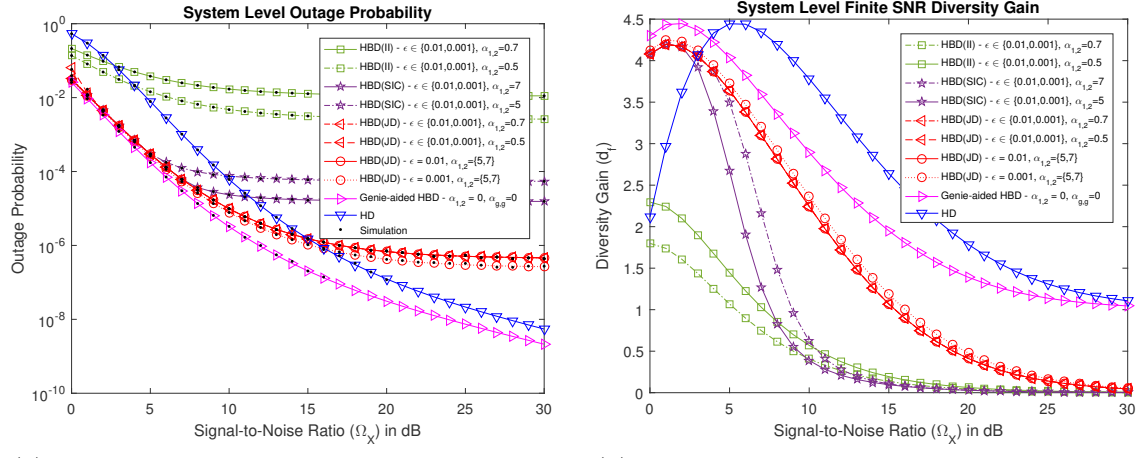
It can be observed in Fig. 4.3a that the SIC detector attains lower outage probability as inter-UAV interference ($\alpha_{1,2}$) is increased. Likewise, the II detector attains lower outage probability as $\alpha_{1,2}$ is decreased. On the contrary, the joint detector is observed to be unaffected by inter-UAV interference and maintains a lower outage probability than the II and the SIC detectors.

From Fig. 4.3, the II and the SIC detectors are suitable for weak and strong inter-UAV interference scenarios, respectively. Furthermore, the joint detector attains, either genie-aided or near-genie-aided, outage performance over the II and the SIC detectors in weak, moderate and strong interference scenarios. Therefore, the proposed HBD-UCS with joint detector can achieve superior reliability and is suitable across weak, moderate, and strong inter-UAV interference scenarios.

4.5.2 Outage and Finite SNR Diversity Gain Analysis at the System Level

Observation 4.5.2.1 *At the system level, the HBD-UCS with JD achieves near-genie-aided performance at low SNR regimes. In contrast, SI causes the HBD-UCS with JD to be suboptimal at moderate and high SNR regimes.*

The system level outage probability and diversity gain are plotted in Fig. 4.4 for the HBD-UCS and the HD-UCS. When the II detector is used, the system level performance



(a) System level outage probability comparison. (b) System level finite SNR diversity gain comparison.

Fig. 4.4: System level outage probability and finite SNR diversity gain (II, SIC and joint detectors) for $\alpha_{g,2} = 1$, $\alpha_{g,g} = 1$, $\gamma_\phi^2 = -130\text{dBm}$ and $\epsilon \in \{0.01, 0.001\}$.

(outage probability and diversity gain) of the HBD-UCS is constrained by inter-UAV interference. For the SIC detector, the system level performance of the HBD-UCS at low SNR regime is noise-limited. Residual SI is also treated as noise at the FD-enabled GS. Therefore, the GS is the bottleneck at low SNR regimes. When SNR is high, the system level performance is constrained by the inter-UAV interference at UAV-2. For JD, the system level performance of the HBD-UCS is observed to be constrained by residual SI under strong inter-UAV interference ($\alpha_{1,2} \in \{5, 7\}$). For weak inter-UAV interference, e.g., $\alpha_{1,2} \in \{0.5, 0.7\}$, system level performance is only constrained by $\alpha_{1,2}$ at very low SNR regimes.

When compared against the II and the SIC detectors, the joint detector enables the HBD-UCS to achieve near-genie-aided system level performance at low SNR regimes under weak, moderate and strong inter-UAV interference levels. However, the advantages of the joint detector comes at the cost of higher computational complexity. These observations are validated through numerical simulations and tabulated in Table 4.4.

4.5.3 Finite SNR DMT Analysis at UAV-2 and System level

For variable transmission rate schemes, finite SNR DMT curves at UAV-2 are presented in Fig. 4.5a. At the system level, the HBD finite SNR DMT is plotted in Fig. 4.5b.

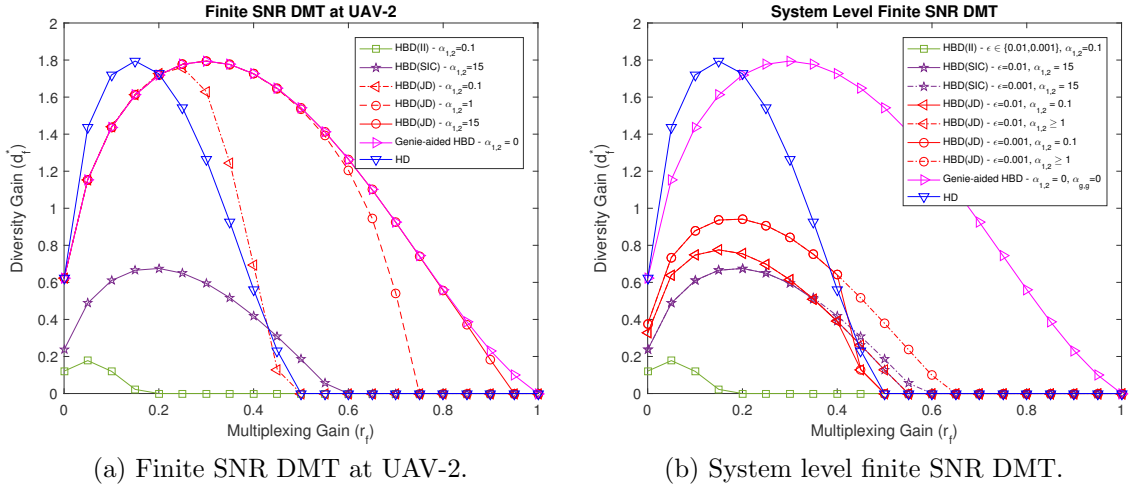


Fig. 4.5: Finite SNR DMT at UAV-2 and system level (II, SIC and joint detectors) for $\alpha_{g,2} = 1$, $\alpha_{g,g} = 1$, $\gamma_\phi^2 = -130\text{dBm}$ and $\Omega_X = 10\text{dB}$.

Observation 4.5.3.1 As inter-UAV interference increases, the joint detector attains better diversity gain at higher multiplexing gains than the II detector, SIC detector, and HD-UCS at both UAV-2 and system level.

In Fig. 4.5a, it is shown that the joint detector at UAV-2 attains genie-aided finite SNR diversity gains at low multiplexing gains. At high multiplexing gains, the joint detector attains near-genie-aided finite SNR diversity gains as inter-UAV interference increases. On the other hand, the II and the SIC detectors at UAV-2 are observed to attain lower finite SNR diversity gains than the HD-UCS at low multiplexing gains. Furthermore, only the SIC detector showed better finite SNR diversity gains than the HD-UCS at moderate multiplexing gains, e.g., $0.45 \leq r_f \leq 0.6$. Finally, it is observed that the HD-UCS achieves non-zero diversity gain only up to $r_f = 0.5$ while the joint detector achieves non-zero diversity gains up to twice that of the HD-UCS.

At the system level (Fig. 4.5b), the finite SNR diversity gain is constrained by residual SI at the FD-enabled GS due to imperfect SI channel estimation (ϵ) for the II, SIC, and the joint detectors. Only the SIC and the joint detectors exhibited better finite SNR diversity gains than the HD-UCS as inter-UAV interference increases for $0.45 \leq r_f \leq 0.65$.

From Fig. 4.5, the joint detector enables HBD-UCS to achieve better reliability in multi-UAV networks while attaining higher throughput than existing HD-UCS.

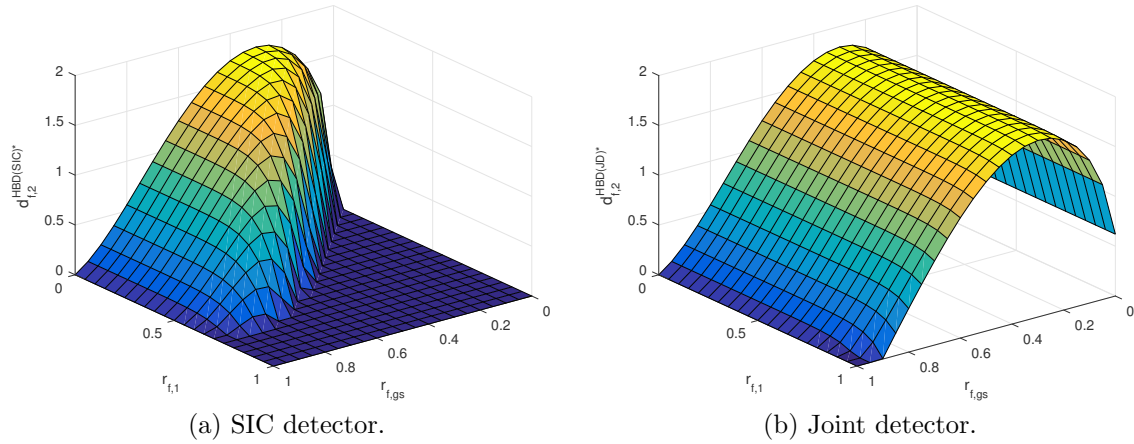


Fig. 4.6: Achievable finite SNR diversity gain of the SIC detector and joint detector at UAV-2 for different multiplexing gains at UAV-1 ($r_{f,1}$) and the GS ($r_{f,gs}$) when $\alpha_{g,2} = 1$, $\alpha_{1,2} = 15$ and $\Omega_X = 10dB$.

4.5.4 Finite SNR Multiplexing Gain Regions at UAV-2

So far, we have assumed that the multiplexing gains of the FD-enabled GS and UAV-1 are the same, i.e., $r_{f,1} = r_{f,gs} = r_f$. In contrast, we assume different multiplexing gains for UAV-1 and the GS in the subsequent analysis. The achievable finite SNR diversity gains for the SIC detector ($d_{f,2}^{HBD(SIC)*}$) and the joint detector ($d_{f,2}^{HBD(JD)*}$) are plotted in Fig. 4.6a and Fig. 4.6b, respectively. We omit plotting the achievable finite SNR diversity gain of the II detector ($d_{f,2}^{HBD(II)*}$) as the expression is independent of the multiplexing gain of the interference ($r_{f,1}$).

Observation 4.5.4.1 *The SIC detector achieves non-zero diversity gain when the multiplexing gain of the SOI is larger than the multiplexing gain of the interferer. On the contrary, the achievable diversity gain of the joint detector is independent of the multiplexing gain of the interferer.*

From Fig. 4.6, it is observed that the SIC detector achieves non-zero diversity gain when the multiplexing gain of the SOI is larger than the multiplexing gain of the interferer. As noted in [106], the multiplexing gain of a variable transmission rate scheme determines the impact of Rician K factors on outage decay. In particular, a higher multiplexing gain elicits a stronger influencing effect of the Rician K factor on outage decay

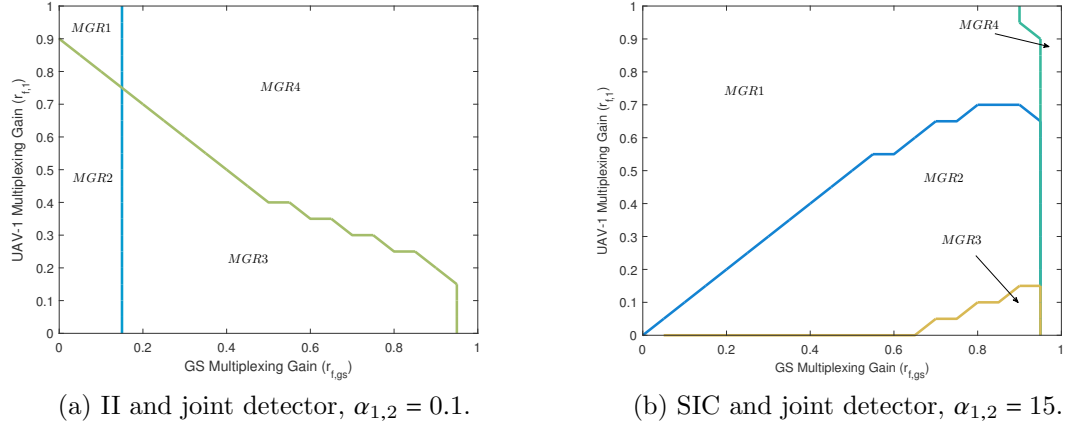


Fig. 4.7: Overlapping finite SNR MGRs of the II, SIC and joint detectors at UAV-2 for $\alpha_{g,2} = 1$, $\alpha_{1,2} = \{0.1, 15\}$ and $\Omega_X = 10dB$. (The MGR separation can be smoothen by plotting the regions with very high resolutions.)

and vice versa. The same principle also explains the trend seen in Fig. 4.6a for the SIC detector. As $r_{f,1}$ increases, the Rician K factor corresponding to the interfering link (K_{Y_1}) starts to affect the overall outage decay of the SIC detector. Therefore, $r_{f,gs}$ must also increase , i.e., $0 < r_{f,1} < r_{f,gs} < 1$ to offset the influence of K_{Y_1} on the overall outage decay with the Rician K factor corresponding to the SOI link ($K_{X_{gs}}$).

On the contrary, Fig. 4.6b shows that the achievable diversity gain of the joint detector is independent of the multiplexing gain of the interferer. Therefore, non-zero $d_{f,2}^{HBD(JD)*}$ can be obtained for a wider range of $r_{f,1}$ and $r_{f,gs}$ values compared to the SIC detector. In strong inter-UAV interference scenarios, the joint detector enables the proposed HBD-UCS to accommodate a wider range of data rate requirements compared to the SIC detector. For instance, video streaming capabilities can be deployed on UAV-1 while still meeting the QoS requirements of CNPC links at the FD-enabled GS, even when inter-UAV interference is strong. Hence JD-based HBD-UCS deployment in UAV networks is attractive when the high data rate requirements are met, albeit at the cost of higher computational complexity compared to SIC-based HBD-UCS⁶.

⁶The complexity of the joint detector depends on the particular encoding scheme (e.g., Low-density parity-check or turbo codes) and decoding scheme (e.g., bipartite graph-based or trellis-based decoders), interested readers can refer to [166] for more details

Observation 4.5.4.2 *The joint detector achieves non-zero diversity gain over a larger multiplexing gain region than the II and the SIC detectors under equivalent inter-UAV interference levels.*

In Fig. 4.7a, the MGRs of the joint detector and II detector are shown for $\alpha_{1,2} = 0.1$. In particular, the joint detector achieves non-zero $d_{f,2}^{HBD(JD)*}$ in regions *MGR2* and *MGR3* while the II detector achieves non-zero $d_{f,2}^{HBD(II)*}$ in regions *MGR1* and *MGR2*. In *MGR4*, both the joint detector and II detector achieve zero finite SNR diversity gains. Evidently, the joint detector achieves non-zero finite SNR diversity gains over a larger MGR region than the II detector, with $d_{f,2}^{HBD(JD)*} > d_{f,2}^{HBD(II)*}$ in *MGR2*.

In Fig. 4.7b, the MGRs of the joint detector and SIC detector are shown for $\alpha_{1,2} = 15$. The joint detector achieves non-zero $d_{f,2}^{HBD(JD)*}$ in regions *MGR1*, *MGR2* and *MGR3*. The SIC detector achieves non-zero $d_{f,2}^{HBD(SIC)*}$ in regions *MGR2* and *MGR3*. In *MGR4*, both the joint detector and SIC detector achieve zero finite SNR diversity gains.

From Fig. 4.7b, it can be observed that the joint detector achieves non-zero finite SNR diversity gains over a larger MGR region than the SIC detector. Furthermore, $d_{f,2}^{HBD(JD)*} > d_{f,2}^{HBD(SIC)*}$ in *MGR2*. However, $d_{f,2}^{HBD(JD)*} = d_{f,2}^{HBD(II)*}$ in *MGR3* when $r_{f,gs}$ is high and $r_{f,1}$ is low since the SIC detector is more likely to detect and remove $x_1[t]$. As inter-UAV interference increases, the joint detector can achieve non-zero diversity gain over a large MGR. In other words, the interfering signal can be transmitted at higher data rates as inter-UAV interference increases.

The trends in Fig. 4.6 and Fig. 4.7 show that the joint detector enables the proposed HBD-UCS to achieve higher reliability than the II and SIC detectors while meeting a wider range of QoS requirements. Therefore, the JD-based HBD-UCS is more flexible in responding to changing QoS requirements and exhibits better reliability over II-based and SIC-based HBD-UCS in multi-UAV networks.

4.6 Chapter Summary

An HBD-UCS with JD is proposed in this chapter as a step towards addressing spectrum scarcity in UAV communications. An innovative approach to deriving closed-form outage probability and finite SNR diversity gain expressions over Rician fading channels is also

presented. Through a comprehensive performance analysis, suitable detectors for various inter-UAV interference scenarios are identified. The degree of performance improvements offered by the joint detector over the II and the SIC detectors are also highlighted. It is also observed that the SIC detector achieves non-zero diversity gain when the interfering signal from UAV-1 is transmitted at a lower data rate than the SOI from the FD-enabled GS. However, when inter-UAV interference is sufficiently strong, the joint detector is observed to be independent of the data rate of the interfering signal. An analysis of the MGR for the II, SIC, and the joint detectors is also conducted, where it is shown that the JD-based HBD-UCS can support a wide range of data rate requirements while achieving superior reliability over the II-based and SIC-based HBD-UCS.

While II-based, SIC-based, and JD-based HBD-UCSs has been shown to be highly effective for UAV communications over Rician fading channels, the performance of joint detection over channels experiencing joint fading and shadowing is unclear. Thus, in the next chapter, the performance of the HBD-UCS is evaluated in a Rician shadowed fading environment to understand the effects of fading and shadowing on UAV communications.

Chapter 5

Hybrid-Duplex UAV Communication in Rician Shadowed Fading Environments

5.1 Introduction

In Chapter 4, the performance of II-based, SIC-based, and JD-based HBD-UCSs operating in Rician fading environments was studied as a potential solution to address spectrum scarcity in UAV communications. Although Rician fading channels are commonly encountered in UAV communications, transmissions in practice are also impaired by the combined effect of fading and shadowing [40, 172], especially in urban environments [59].¹

To begin modeling a realistic UAV communication channel, it is first noted that channel measurement campaigns for UAV-to-ground links showed a close match between the measurement data and the Rician fading model [47]. For UAV-to-UAV links, i.e., inter-UAV channels, measurement campaigns in [54] have also demonstrated the Rician fading channel as a suitable model for inter-UAV links. The authors in [55] similarly employ the Rician fading model for inter-UAV links to account for the availability of LOS links, scattering, and reflection from the environment. Nonetheless, despite several recent works on UAV channel modeling, e.g., [173–176], channel models that jointly account for fading and shadowing have not been investigated extensively. In particular, the Rician fading model may not be accurate in a suburban environment as it does not account for shadowing due to terrain or buildings [40, 59, 172]. In the empirical data

¹The work in this chapter has been published in [19].

of [47], where the characterization of UAV communication channels in hilly terrain was studied, Rician shadowed fading, i.e., LOS blockage, was observed. However, due to the limited dynamic range of the transceiver used during the measurement campaign, the authors in [47] omitted measurement data containing LOS shadowing.

In light of the above limitations, the Rician shadowed fading model presented in [52] is a suitable choice for UAV channel modeling. Through the Rician shadowed fading model, Rician fading or Rayleigh fading UAV channels [100] can be modeled as special cases. It is worth noting that the Rician shadowed fading model is one of several shadowed fading, i.e., composite fading, models available in the literature. Such composite fading models combine shadowing, i.e., large-scale fading, with small-scale fading, e.g., $\kappa - \mu$ or Rician fading². Also, fluctuations caused by shadowing are modeled using Gaussian, lognormal, gamma, or inverse Gaussian distributions [59, 177].³ For the Rician shadowed fading model, one can employ the $\kappa - \mu$ shadowed fading model, where the non-centered Chi-squared and Nakagami- m distributions are assumed for the multipath and LOS components, respectively [177–180]. In particular, the non-centered Chi-squared distribution accounts for both the LOS and NLOS components encountered over the UAV channel, while the degree of LOS shadowing is modeled through the Nakagami- m distribution. Thus, using the Rician shadowed fading model, the severity of LOS shadowing and the ratio of the LOS-to-NLOS components can be accurately captured through the Nakagami- m shaping parameter and the Rician K factor, respectively. Furthermore, in contrast to the $\kappa - \mu$ shadowed fading model which considers LOS and NLOS shadowing for more than one multipath cluster, only one multipath cluster with LOS shadowing is considered for the Rician shadowed fading model. On top of the Rician shadowed fading model, it was shown by Paris [178] that the $\kappa - \mu$ shadowed fading model includes the one-sided Gaussian, Rayleigh, $\kappa - \mu$, and Rician fading models as special cases, obtainable through the substitution of appropriate shaping parameters. However,

²Small-scale fading occurs when the received signal power undergoes variations due to LOS or NLOS components, multipath clustering with circularly symmetric or elliptical scattering, and power imbalance between the in-phase and quadrature signal components [177]. Depending on the type of environment, different kinds of small-scale fading can occur. For instance, Rician fading is commonly encountered in UAV communications [8], [47], which can be modeled using the non-centered Chi-squared distribution.

³Shadowing occurs when a communication link is obstructed by buildings or terrain [40, 59, 172, 177], causing the total received signal power to fluctuate randomly [177]. The resultant fluctuations can be modeled using the Gaussian, lognormal, gamma, or inverse Gaussian distributions [59, 177].

the relevant statistics from [177] and [178] are represented in the form of complicated functions, such as the confluent hypergeometric function [49] and the Gauss hypergeometric function [181], which may not yield tractable solutions. Hence, one can adopt the Rician shadowed fading model presented in [52]. In particular, the work in [52] presented power series expressions for statistics in the Rician shadowed fading model. While the closed-form expressions in [52] enables tractable mathematical analysis, the generality of the Rician shadowed fading model using the power series approach, i.e., to obtain the Rician fading model, remains an open research problem which will be investigated in this chapter.

Although UAV communications in the presence of shadowing has been studied in the literature, e.g., [61, 62, 182], these works have not considered Rician shadowed fading or Rician fading and are only valid for interference-free scenarios. For interference management strategies, the II approach has already been investigated from the outage probability perspective for aeronautical communications over Rician fading channels [17, 99], and for UAV communications over Rician fading channels [100] and Rician shadowed fading channels [52]. In particular, the work in [52] presented new power series expressions for statistics associated with the Rician shadowed fading model. Thereafter, closed-form outage probability expressions for the II detector involving SINRs of the form $\frac{Z_0}{1+Z_1}$, where Z_0 and Z_1 denote the desired and interfering signals, respectively, were derived for the Rician shadowed fading model through a power series approach. Thus, through the power series approach in [52], one can easily obtain closed-form outage probability expressions for the II detector over Rician shadowed fading channels. In contrast, one may have to resort to numerical methods to evaluate the outage probability of the II detector using the statistics presented in [183, eq. (3)], [177, eq. (12)], and [178, eq. (4)]. For the JD strategy, closed-form outage probability expressions are only available for Rician fading channels, e.g., [18]. Therefore, the outage probability analysis of UAV communications for JD over Rician shadowed fading channels through closed-form expressions remains an open problem.

To this end, we extend the Rician shadowed fading model in [52] to include the Rician fading model as a special case. It is worth mentioning that closed-form power series expressions for the Rician fading model are already available in [45, Table I and Table II].

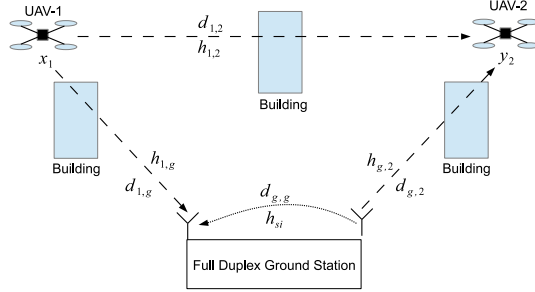


Fig. 5.1: Unmanned Aerial Vehicle 1 (UAV-1) and Unmanned Aerial Vehicle 2 (UAV-2) operating in HD mode while communicating with the FD GS over Rician shadowed fading channels.

However, we present alternative power series representations for the Rician fading model using the Rician shadowed fading model in this chapter. We demonstrate that the Rician shadowed fading model in this chapter unifies Rician shadowed fading, Rician fading, and Rayleigh fading under the same power series-based model. Through the newly obtained closed-form expressions for the Rician shadowed fading model, we conduct an outage probability analysis of HBD UAV communications for multi-UAV networks in both Rician shadowed fading and Rician fading environments. Specifically, the outage probability analysis takes into consideration the effects of inter-UAV interference, SI, fading, and shadowing for the II and JD interference management approaches. Additionally, it is worth noting that this chapter is an extension of the work in [52], where the UAV-to-GS and the SI links are modeled as Rician fading channels. The current chapter models the UAV channels and SI channel using the Rician shadowed fading model. As such, the system model and the subsequent analysis in [52] can be obtained in this chapter as specific cases, thus illustrating the generality of the employed Rician shadowed fading model in this chapter.

5.2 System Model

The multi-UAV HBD-UCS operating in a suburban environment is shown in Fig. 5.1. In particular, it is assumed that the HD UAV-1 is simultaneously transmitting data to the FD-enabled GS while the HD UAV-2 is receiving control information on the same channel

(Fig. 5.1). Such an arrangement enables the HBD-UCS to utilize spectrum efficiently, which is a challenge in UAV communications [8]. Another major issue in multi-UAV networks is the interference present in the HBD-UCS [28]. In Fig. 5.1, signals from Unmanned Aerial Vehicle 1 (UAV-1) are transmitted to both GS and Unmanned Aerial Vehicle 2 (UAV-2) as the SOI and interference, respectively. Simultaneously at the FD-enabled GS, signals are transmitted to UAV-2. Consequently, inter-UAV interference and SI are experienced at UAV-2 and the FD-enabled GS, respectively.

In a suburban environment, it is likely that LOS components to be obstructed by buildings [40, 59, 172]. As such, Rician shadowed fading [177] is assumed on all UAV links ($h_{1,g}$, $h_{g,2}$, $h_{1,2}$) to adequately model the suburban UAV communication channels. As in [18], UAV mobility is assumed to be compensated in this chapter. For SI channel modeling at the FD-enabled GS, recent literature have assumed the Rayleigh fading model [147, 184, 185] or the Rician fading model [75]. However, in this chapter, the SI link (h_{si}) at the FD-enabled GS is modeled as a Rician shadowed fading channel. Such an assumption enables the analysis to consider the effects of passive SI suppression through shadowing experienced on the SI channel. Additionally, Rayleigh fading can be obtained through the Rician shadowed fading model as a special case by letting the Rician K factor be zero. Also, it is assumed that the SI signal undergoes active SI mitigation after passive SI suppression at the FD-enabled GS. Thus, only residual SI is considered at the GS. A summary of important notations is also given in Table 5.1.

5.2.1 Ground Station

At the GS, let the SOI transmitted from UAV-1 be $x_1[t]$, the signal transmitted from GS be $x_{gs}[t]$, and the SI be $x_{si}[t]$, where $x_{si}[t] = x_{gs}[t]$. Also, let $h_{1,g}[t]$, h_{si} , and $\tilde{h}_{si} = h_{si} - \hat{h}_{si}$ be the channel between UAV-1 and GS, the SI channel gain, and the SI channel gain estimate error, respectively, where \hat{h}_{si} is the imperfect estimation of the SI channel gain. Then, the received signal at GS can be written as [21]:

$$y_{gs}[t] = \sqrt{\Omega_X} h_{1,g}[t] x_1[t] + \sqrt{\Omega_X \alpha_{g,g}} |h_{si}| \gamma_\phi w_\phi[t] + \sqrt{\Omega_X \alpha_{g,g}} \cdot |\tilde{h}_{si}| x_{si}[t] + w_g[t] \quad (5.1)$$

where $w_g[t]$ is the AWGN at GS with zero-mean and variance σ_g^2 , and $w_\phi[t]$ is the Gaussian distributed phase noise term with zero-mean and unit variance, scaled by phase

noise strength γ_ϕ [21]⁴. The imperfect SI channel estimate (\tilde{h}_{si}) is modeled as a circularly symmetric zero-mean complex Gaussian random variable RV with variance ϵ to model the worst case residual SI [81].

Using the free space path loss model, the average received signal power of the SOI (Ω_X), normalized by σ_g^2 , is defined as:

$$\Omega_X \propto \frac{P_t}{(d_{1,g})^n \sigma_g^2}, \quad (5.2)$$

where P_t and $d_{1,g}$ are the transmit power (Watts) and distance (km), respectively. It should be pointed out that equal transmit power P_t is assumed for the HBD-UCS and $h_{1,g}[t]$ is chosen as the reference link in this chapter. Thus, the average received signal power in the other links are expressed relative to $h_{1,g}[t]$, using the multiplicative factor ($\alpha_{i,j}$) defined as:

$$\alpha_{i,j} = \left(\frac{d_{1,g}}{d_{i,j}} \right)^n, i \in \{g, 1\}, j \in \{g, 2\}, i \neq j. \quad (5.3)$$

For $i = j = g$, $\alpha_{g,g}$ is treated as a scaling variable for the average residual SI power at the GS. Together with $\alpha_{g,g}$, σ_g^2 , and ϵ , the amount of SI suppression is quantified as $\frac{1}{\alpha_{g,g}\epsilon\sigma_g^2}$ [17, 81].

5.2.2 Unmanned Aerial Vehicle 2

At UAV-2, let the SOI transmitted from GS be $x_{gs}[t]$, and the inter-UAV interference from UAV-1 be $x_1[t]$. Also, let $h_{g,2}[t]$ and $h_{1,2}[t]$ be the channels between GS and UAV-2, and UAV-1 and UAV-2, respectively. Then, the received signal at UAV-2 can be expressed as:

$$y_2[t] = \sqrt{\Omega_X \alpha_{g,2}} h_{g,2}[t] x_{gs}[t] + \sqrt{\Omega_X \alpha_{1,2}} h_{1,2}[t] x_1[t] + w_2[t], \quad (5.4)$$

where $w_2[t]$ is the AWGN at UAV-2 with zero-mean and variance σ_2^2 . Additionally, $\Omega_X \alpha_{g,2}$ and $\Omega_X \alpha_{1,2}$ respectively indicate the average received signal powers of the SOI and interfering signal. Due to the presence of interference at both the FD-enabled GS and UAV-2, II and JD interference management approaches are considered in this chapter.

⁴The scaling factor γ_ϕ models the jitter present in oscillators due to hardware imperfections [21]

Table 5.1: Summary of Important Notations

Notations	Description
Ω_X	Average received power
$\alpha_{i,j}, i \in \{g, 1\}, j \in \{g, 2\}, i \neq j$	Strength of interference between i and j
ϵ	SI channel estimation error at the FD-enabled GS
γ_ϕ^2	Strength of phase noise at the FD- enabled GS oscillator
σ_g^2	Strength of AWGN at the FD-enabled GS
σ_2^2	Strength of AWGN at the UAV-2

5.3 Alternative Expressions for the Rician Shadowed Fading Model

The $\kappa - \mu$ shadowed fading model has κ , μ and m as shaping parameters [177]. Specifically, κ represents the ratio between the total powers of the dominant component to the scattered component while μ denotes the number of multipath clusters. The variable m denotes the shadowing severity, obtained through the Nakagami-m distribution [177].

For a Rician shadowed fading channel h , the channel gain $|h|^2$ is obtained by setting $\mu = 1$ and letting κ be the Rician K factor [177, 178], i.e., $\kappa = K$, as follows [177, eq. (8)]:

$$|h|^2 = [X + \xi p]^2 + Y^2, \quad (5.5)$$

where $p = \sqrt{\frac{K}{1+K}}$, X and Y are mutually independent Gaussian RVs with

$$E\{X\} = E\{Y\} = 0, E\{X^2\} = E\{Y^2\} = \sigma^2, \quad (5.6)$$

and ξ is a Nakagami-m RV with $E\{\xi^2\} = 1$. The term $[X + \xi p]^2$ represents the dominant component and it contains both scattering and LOS components that are subjected to shadowing, while Y^2 represents the non-dominant component and it contains only the scattered component [55]. Additionally, under the obtained Rician shadowed fading model, LOS shadowing is modeled using ξ , with m indicating the severity of the shadowing [177]. From (5.5), the PDF of $|h|^2$, i.e., Rician shadowed fading PDF, can be obtained from [177, Table I] as:

$$f_{|h|^2}(x) = \frac{m^m(1+K)}{\Omega(K+m)^m} \exp\left(-\frac{(1+K)x}{\Omega}\right) {}_1F_1\left(m; 1; \frac{K(1+K)}{(K+m)\Omega}x\right), \quad (5.7)$$

where Ω and ${}_1F_1(\bullet)$ are the average received power and the confluent Hypergeometric function [49], respectively.

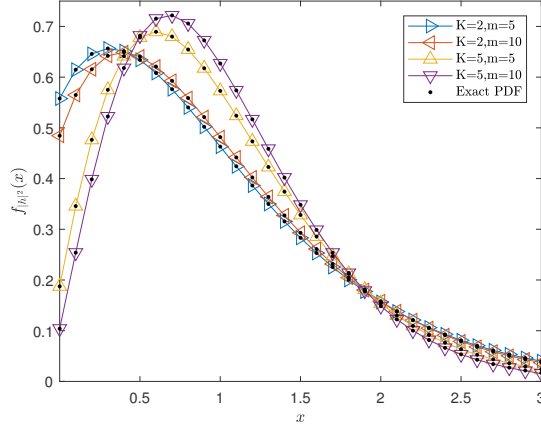


Fig. 5.2: Comparison between the exact PDF of $|h|^2$ and power series approximation equivalent for $\Omega = 1$ and $K_{tr} = 50$.

As complicated functions are employed in the above PDF expression, an outage probability analysis of the HBD-UCS may lead to intractable expressions. Separately, it should be noted that the $\kappa - \mu$ shadowed fading model includes the Rician fading and the Rician shadowed fading models as specific cases as it is possible to obtain the Rician fading model from [177, Table I]. However, in its current form, important performance metrics, e.g., outage probability or finite SNR diversity gain, are not easily obtainable from (5.7). Therefore, we present alternative closed-form expressions for the Rician shadowed fading and the Rician fading models in the subsequent sections based on the work in [52].

5.3.1 Rician Shadowed Fading Model

Let $\bar{a}(n, \Omega, K, m, \gamma)$ be defined as:

$$\bar{a}(n, \Omega, K, m, \gamma) = \sum_{i=0}^n (-1)^{n-i} \left(\frac{m}{K+m} \right)^m \frac{(m)_i}{\Gamma^2(i+1)} \left(\frac{K}{K+m} \right)^i \left(\frac{1+K}{\Omega} \right)^{n+1} \frac{\gamma^{n+1}}{(n-i)!(n+1)}. \quad (5.8)$$

Then, alternative power series representations of the Rician shadowed fading PDF and the corresponding CDF are presented as follows.

Theorem 5.1 *The PDF of $|h|^2$ can be represented as the following power series:*

$$f_{|h|^2}(x) \approx \sum_{n=0}^{K_{tr}} \bar{a}(n, \Omega, K, m, 1)(n+1)x^n, \quad (5.9)$$

where K_{tr} denotes the truncation order.

Proof: The proof can be found in [52] and is reproduced in Appendix C.1.

Theorem 5.2 *The CDF of $|h|^2$ can be expressed as the following power series:*

$$F_{|h|^2}(\gamma) = \int_0^\gamma f_{|h|^2}(x)dx \approx \sum_{n=0}^{K_{tr}} \bar{a}(n, \Omega, K, m, \gamma). \quad (5.10)$$

Proof: The CDF is obtained by interchanging the summation and integration, i.e., term-wise integration [49].

Theorem 5.3 *The l^{th} moment of $|h|^2$ is given as [177, eq. (10)]:*

$$E\{(|h|^2)^l\} = \left(\frac{\Omega}{1+K}\right)^l \Gamma(1+l) \left(\frac{m}{K+m}\right)^{m-1-l} {}_2F_1\left(1-m, 1+l; 1; \frac{-K}{m}\right), \quad (5.11)$$

where ${}_2F_1(\bullet)$ is the Gauss hypergeometric function [181].

Fig. 5.2 shows the power series representation of $f_{|h|^2}(x)$, computed from (5.9), with the exact PDF in (5.7) plotted for comparison. It can be seen that (5.9) provides a close fit to the exact PDF at the cost of computation time, which increases as $m \rightarrow \infty$.⁵ Additionally, although not plotted in Fig. 5.2, one obtains the Rician fading PDF by letting $m \rightarrow \infty$.

The closed-form expressions of the PDF, CDF and fractional moments of $|h|^2$, given in (5.9), (5.10), and (5.11), respectively, are useful in evaluating performance metrics, such as outage probability, in shadowing environments. Furthermore, the new power series expressions for the PDF, CDF and fractional moments are, to the best of our knowledge, not available in the literature.

5.3.2 Rician Fading Model

To understand the impact of shadowing, (5.8) and (5.11) can be evaluated for large values of m . In particular, one obtains the Rician fading channel h' from the Rician shadowed fading channel h as $m \rightarrow \infty$. In the following Corollaries, new closed-form expressions for Rician fading models are presented.

⁵To analytically gauge the accuracy of the new power series expressions, one will need to conduct a truncation analysis. Work in this direction is left as an open research challenge which can be addressed in future studies.

Corollary 5.1 As $m \rightarrow \infty$, (5.8) can be expressed as:

$$\widehat{a}(n, \Omega, K, \gamma) = \sum_{i=0}^n \frac{(-1)^{n-i} K^i}{\Gamma^2(i+1)} \left(\frac{1+K}{\Omega} \right)^{n+1} \frac{\exp(-K)\gamma^{n+1}}{(n-i)!(n+1)}. \quad (5.12)$$

Proof: The proof can be found in Appendix C.2.

Remark 5.1 Although not shown in Corollary 5.1, it should be noted that the value in $\widehat{a}(n, \Omega, K, \gamma)$ in (5.12) reduces as $K \rightarrow \infty$.

Corollary 5.2 The PDF ($f_{|h'|^2}(\bullet)$) and CDF ($F_{|h'|^2}(\bullet)$) of the Rician fading channel h' can be represented as the following power series:

$$f_{|h'|^2}(x) \approx \sum_{n=0}^{K_{tr}} \widehat{a}(n, \Omega, K, 1)(n+1)x^n, \quad (5.13)$$

$$F_{|h'|^2}(\gamma) \approx \sum_{n=0}^{K_{tr}} \widehat{a}(n, \Omega, K, \gamma), \quad (5.14)$$

where $\widehat{a}(n, \Omega, K, \gamma)$ is given in (5.12).

Proof: From (5.12), algebraic manipulation yields the power series expression of $f_{|h'|^2}(\bullet)$ and $F_{|h'|^2}(\bullet)$ in (5.13) and (5.14), respectively.

Corollary 5.3 The closed-form expression for the l^{th} moment of $|h'|^2$ is:

$$E\{|h'|^2\} = \lim_{m \rightarrow \infty} E\{(|h|^2)^l\} \approx \left(\frac{\Omega}{1+K} \right)^l \Gamma(1+l) \sum_{n=0}^{K_{tr}} \frac{(-l)_n}{n!(1)_n} (-K)^n. \quad (5.15)$$

Proof: The proof can be found in Appendix C.3.

The Rician fading PDF in (5.13) is plotted in Fig. 5.3 and compared against the exact Rician fading PDF $f_{|h'|^2}(x) = \frac{K+1}{\Omega} \exp(-K - \frac{K+1}{\Omega}x) I_0\left(2\sqrt{\frac{K(K+1)}{\Omega}}x\right)$, where $I_0(\cdot)$ is the modified Bessel function of the first kind with zero order [49]. It can be observed that (5.13) provides a close fit to the exact PDF in Fig. 5.3.

The Rician fading CDF $F_{|h'|^2}(\gamma)$ in (5.14) is plotted in Fig. 5.4. When compared against the numerical integration of $f_{|h'|^2}(x)$ and the exact CDF, $F_{|h'|^2}(\gamma) = 1 - Q_1\left(\sqrt{2K}, \sqrt{\frac{2(K+1)\gamma}{\Omega}}\right)$ where $Q_1(\cdot, \cdot)$ is the Marcum Q function [45], a close fit is also

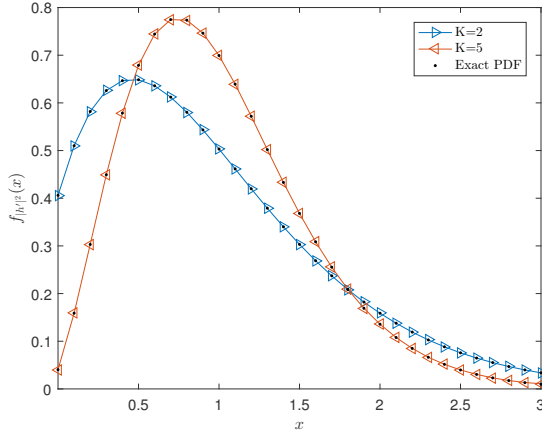


Fig. 5.3: Comparison between the exact PDF of $|h'|^2$ and power series approximation equivalent for $\Omega = 1$ and $K_{tr} = 50$.

observed. Similar observations are also made in Fig. 5.5 when (5.15) is compared against $E\{(|h'|^2)^l\} = \Gamma(1+l) \left[\frac{\Omega}{1+K}\right]^l {}_1F_1(-l, 1; -K)$ [45, Table II].

Evidently, (5.8) and (5.11) become independent of m as $m \rightarrow \infty$. More importantly, Corollaries 5.1 and 5.3 show that the computed values of (5.8) and (5.11) decreases and increases, respectively, based on the Rician K factor as $m \rightarrow \infty$. The presented power series representations of the Rician shadowed fading and Rician fading models in this section are summarized in Table 5.2⁶. Together, these observations and expressions are essential in evaluating the outage probability of the HBD-UCS, which is discussed in Section 5.4.

5.4 Outage Probability Derivations

In this section, closed-form outage probability expressions are derived for the HBD-UCS. The transmission rates of UAV-1 and GS are defined as R_1^{HBD} and R_{gs}^{HBD} , respectively, with HBD system sum rate defined as $R_{sum}^{HBD} = R_1^{HBD} + R_{gs}^{HBD}$. Similarly for HD transmission, the transmission rates of UAV-1 and GS are defined as R_1^{HD} and R_{gs}^{HD} , respectively, with HD system sum rate $R_{sum}^{HD} = R_1^{HD} + R_{gs}^{HD}$. To maintain a fair comparison between

⁶The functions $\gamma(\cdot, \cdot)$, $I_0(\cdot)$, $Q_1(\cdot, \cdot)$, and ${}_1F_1(\bullet)$ represent the lowercase incomplete gamma function [177], the modified Bessel function of the first kind with zero order [49], the Marcum Q function [45], and the confluent Hypergeometric function [49], respectively. The fractional moment of $|h|^2$, i.e., $E\{(|h|^2)^j\}$ is given in (5.11) while $\bar{a}(n, \Omega, K, m, 1)$ and $\hat{a}(n, \Omega, K, \gamma)$ are given in (5.8) and (5.12), respectively.

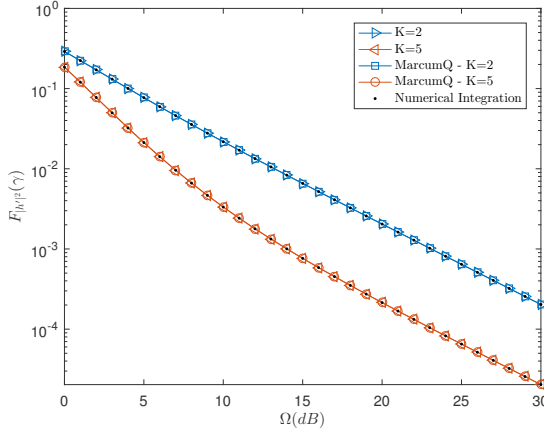


Fig. 5.4: Comparison between the exact CDF of $|h'|^2$ and power series approximation equivalent for $\gamma = 0.5$ and $K_{tr} = 50$.

HBD and HD systems, we let $R_i^{HBD} = \frac{1}{2}R_i^{HD}$ for $i \in \{1, gs\}$ [156]. Based on these definitions, the HBD and HD outage probabilities at GS and UAV-2 are defined in the following subsections.

5.4.1 Hybrid-Duplex Outage Probability

Starting with the FD-enabled GS, strong SI is experienced due to the simultaneous transmission and reception of $x_{gs}[t]$ and $x_1[t]$, respectively. Let the instantaneous received signal power of the SOI at GS be $X_1 = \Omega_X|h_{1,g}|^2$, modeled as a Rician shadowed distributed RV with Rician K factor K_{X_1} and shadowing severity parameter m_{X_1} . Also, let the instantaneous received signal power of the SI components be $Y_{si,1} = \Omega_X\alpha_{g,g}\gamma_\phi^2|h_{si}|^2$ and $Y_{si,2} = \Omega_X\alpha_{g,g}\epsilon|\tilde{h}_{si}|^2$. The RVs, $Y_{si,1}$ and $Y_{si,2}$, are modeled as a Rician shadowed distributed RV with Rician K factor $K_{Y_{si,1}}$ and shadowing parameter $m_{Y_{si,1}}$, and an exponentially distributed RV, respectively.

At UAV-2, let the instantaneous received signal power of the SOI and interference be $X_{gs} = \Omega_X\alpha_{g,2}|h_{g,2}|^2$ and $Y_1 = \Omega_X\alpha_{1,2}|h_{1,2}|^2$, respectively. Both X_{gs} and Y_1 are respectively modeled as independent Rician shadowed distributed RVs, with Rician K factors $K_{X_{gs}}$ and K_{Y_1} , and shadowing severity parameters $m_{X_{gs}}$ and m_{Y_1} .

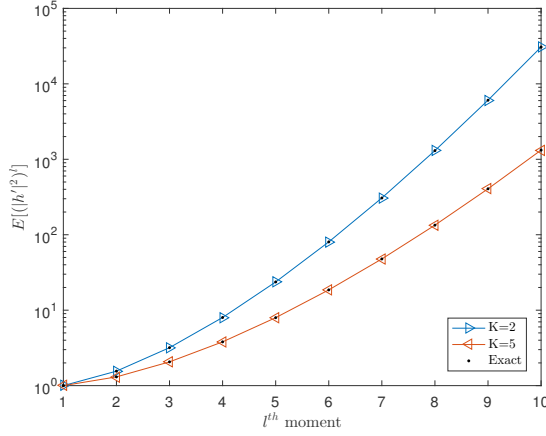


Fig. 5.5: Comparison between the exact fractional moment of $|h'|^2$ and power series approximation equivalent for $\Omega = 1$ and $K_{tr} = 50$.

5.4.1.1 Ground Station

At the FD-enabled GS, SI mitigation is imperfect due to phase noise and SI channel estimation error. As a result, residual SI is experienced at the GS. Thus, an II detector is assumed at the GS, which treats residual SI ($Y_{si,1}, Y_{si,2}$) as noise when detecting the SOI (X_1). Let the outage event, outage probability, and the HBD threshold at the FD-enabled GS be $\mathcal{O}_{gs}^{HBD} = \left\{ h_{1,g}, h_{si}, \tilde{h}_{si} : R_1^{HBD} \geq \log_2 \left(1 + \frac{X_1}{Y_{si,1} + Y_{si,2} + 1} \right) \right\}$, $Pr(\mathcal{O}_{gs}^{HBD})$, and $\gamma_{th,gs}^{HBD} = 2^{R_1^{HBD}} - 1$, respectively.

Theorem 5.4 *The closed-form outage probability at GS over Rician shadowed fading channels is:*

$$Pr(\mathcal{O}_{gs}^{HBD}) \approx \sum_{n=0}^{K_{tr}} \sum_{l_1+l_2+l_3=n+1} \bar{a}(n, \Omega_X, K_{X_1}, m_{X_1}, \gamma_{th,gs}^{HBD}) \frac{(n+1)!}{l_1! \cdot l_2! \cdot l_3!} E\{Y_{si,1}^{l_1}\} E\{Y_{si,2}^{l_2}\}, \quad (5.16)$$

where

$$\begin{aligned} E\{Y_{si,1}^{l_1}\} &= \Gamma(1+l_1) \left(\frac{\alpha_{g,g} \gamma_\phi^2}{1 + K_{Y_{si,1}}} \right)^{l_1} \left(\frac{m_{Y_{si,1}}}{K_{Y_{si,1}} + m_{Y_{si,1}}} \right)^{m_{Y_{si,1}}-1-l_1} \\ &\quad \times {}_2F_1 \left(1 - m_{Y_{si,1}}, 1 + l_1; 1; \frac{-K_{Y_{si,1}}}{m_{Y_{si,1}}} \right) (\Omega_X)^{l_1}, \end{aligned} \quad (5.17)$$

$$E\{Y_{si,2}^{l_2}\} = \Gamma(1+l_2) (\alpha_{g,g} \epsilon)^{l_2} (\Omega_X)^{l_2}. \quad (5.18)$$

Table 5.2: Summary of presented closed-form expressions for the Rician shadowed fading and Rician fading models

Fading Model	PDF Expression	Comment
Rician shadowed	$f_{ h ^2}(x) \approx \sum_{n=0}^{K_{tr}} \bar{a}(n, \Omega, K, m, 1)(n+1)x^n$	Current Work
	$f_{ h ^2}(x) = \frac{m^m(1+K)}{\Omega(K+m)^m} \exp\left(\frac{-(1+K)x}{\Omega}\right) {}_1F_1\left(m; 1; \frac{K(1+K)x}{(K+m)\Omega}\right)$	[177]
	$f_{ h ^2}(x) = \sum_{n=0}^{\infty} \sum_{i=0}^n \sum_{j=0}^n \frac{(-1)^{i+j}}{\Gamma[i+1]j!} \binom{n}{i} \binom{n}{n-j} E\{(h ^2)^j\} x^i \exp(-x)$	[177]
Rician	$f_{ h' ^2}(x) \approx \sum_{n=0}^{K_{tr}} \hat{a}(n, \Omega, K, 1)(n+1)x^n$	Current Work
	$f_{ h' ^2}(x) = \frac{K+1}{\Omega} \exp\left(-K - \frac{K+1}{\Omega}x\right) I_0\left(2\sqrt{\frac{K(K+1)}{\Omega}}x\right)$	[45]
Fading Model	CDF Expression	Comment
Rician shadowed	$F_{ h ^2}(\gamma) \approx \sum_{n=0}^{K_{tr}} \bar{a}(n, \Omega, K, m, \gamma)$	Current Work
	$F_{ h ^2}(x) = \sum_{n=0}^{\infty} \sum_{i=0}^n \sum_{j=0}^n \frac{(-1)^{i+j}}{\Gamma(i+2)j!} \binom{n}{i} \binom{n}{n-j} E\{(h ^2)^j\} x^{i+1} + \gamma(1, x)$	[177]
Rician	$F_{ h' ^2}(\gamma) \approx \sum_{n=0}^{K_{tr}} \hat{a}(n, \Omega, K, \gamma)$	Current Work
	$F_{ h' ^2}(\gamma) = 1 - Q_1\left(\sqrt{2K}, \sqrt{\frac{2(K+1)\gamma}{\Omega}}\right)$	[45]
Fading Model	Fractional Moments Expression	Comment
Rician	$E\{(h' ^2)^l\} \approx \left(\frac{\Omega}{1+K}\right)^l \Gamma(1+l) \sum_{n=0}^{K_{tr}} \frac{(-l)_n}{n!(1)_n} (-K)^n$	Current Work
	$E\{(h' ^2)^l\} = \Gamma(1+l) \left[\frac{\Omega}{1+K}\right]^l {}_1F_1(-l, 1; -K)$	[45]

Proof: The outage probability at GS can be obtained as $Pr(O_{gs}^{HBD}) = E\left\{F_{X_1}\left(\gamma_{th,gs}^{HBD}(1+Y_{si,1}+Y_{si,2})\right)\right\}$, where $F_{X_1}(\bullet)$ is the CDF of X_1 obtained from (5.10). The final expression for $Pr(O_{gs}^{HBD})$ can be calculated from [45, eq. (8)], with the proof of convergence given in Appendix C.4.

As shadowing is considered at the GS, the impact of shadowing on the SI link due to passive SI suppression can be investigated using (5.16). Furthermore, for the case of Rician fading channels, we present an alternative outage probability expression from (5.16) in the following Corollary.

Corollary 5.4 *The closed-form outage probability at GS over Rician fading channels is:*

$$Pr(O_{gs}^{HBD*}) \approx \sum_{n=0}^{K_{tr}} \sum_{l_1+l_2+l_3=n+1} \hat{a}(n, \Omega_X, K_{X_1}, \gamma_{th,gs}^{HBD}) \frac{(n+1)!}{l_1! \cdot l_2! \cdot l_3!} E\{Y_{si,1}^{l_1*}\} E\{Y_{si,2}^{l_2}\}, \quad (5.19)$$

where $Y_{si,1}^{l_1*}$ is a RV defined using the Rician fading model and

$$E\{Y_{si,1}^{l_1*}\} = \Gamma(1+l_1) \left(\frac{\alpha_{g,g} \gamma_{\phi}^2 \Omega_X}{1+K_{Y_{si,1}}} \right)^{l_1} \sum_{i=0}^{K_{tr}} \frac{(-l_1)_i}{i!(1)_i} (-K_{Y_{si,1}})^i. \quad (5.20)$$

Proof: Replacing $\bar{a}(n, \Omega_X, K_{X_1}, m_{X_1}, \gamma_{th,gs}^{HBD})$ in (5.16) with (5.12) and applying (5.15) to evaluate $E\{Y_{si,1}^{l_1*}\}$ yields (5.19). Additionally, it can be shown that (5.19) converges absolutely by following the same steps in Appendix C.4.

The closed-form expression in Corollary 5.4 is used as a benchmark to evaluate the reliability of the GS over Rician fading channels. From [17], it is known that the FD-enabled GS becomes interference-limited at high SNR regimes. Thus, in the following Corollary, the asymptotic outage probability of the FD-enabled GS over Rician shadowed fading channels and Rician fading channels is presented.

Corollary 5.5 *The closed-form asymptotic outage probability expressions at the GS over Rician shadowed fading channels ($Pr(O_{gs,\infty}^{HBD})$) and Rician fading channels ($Pr(O_{gs,\infty}^{HBD*})$) are:*

$$Pr(O_{gs,\infty}^{HBD}) \approx \sum_{n=0}^{K_{tr}} \sum_{l_1+l_2=n+1} \bar{a}(n, 1, K_{X_1}, m_{X_1}, \gamma_{th,gs}^{HBD}) \frac{(n+1)!}{l_1! \cdot l_2!} M\{Y_{si,1}^{l_1}\} M\{Y_{si,2}^{l_2}\}, \quad (5.21)$$

$$Pr(O_{gs,\infty}^{HBD*}) \approx \sum_{n=0}^{K_{tr}} \sum_{l_1+l_2=n+1} \hat{a}(n, 1, K_{X_1}, \gamma_{th,gs}^{HBD}) \frac{(n+1)!}{l_1! \cdot l_2!} M\{Y_{si,1}^{l_1*}\} M\{Y_{si,2}^{l_2}\}, \quad (5.22)$$

where $M\{Z^l\} = E\{Z^l\}/(\Omega_X)^l$ is the normalized l^{th} moment of RV Z [17].

Proof: The proof is given in Appendix C.5.

As the FD-enabled GS is interference-limited [17], Corollary 5.5 can be used to obtain the outage probability error floor, which is useful in determining how SI and shadowing affects reliability. Further discussion on the outage probability at GS are presented in Section 5.5.

5.4.1.2 Unmanned Aerial Vehicle 2 (Interference Ignorant Detector)

At UAV-2, inter-UAV interference (Y_1) is treated as noise when the II detector is detecting the SOI (X_{gs}). Let the outage event, outage probability, and the HBD threshold at UAV-2 be $O_2^{HBD(II)} = \left\{ h_{g,2}, h_{1,2} : R_{gs}^{HBD} \geq \log_2 \left(1 + \frac{X_{gs}}{Y_1 + 1} \right) \right\}$, $Pr(O_2^{HBD(II)})$, and $\gamma_{th,2}^{HBD} = 2^{R_{gs}^{HBD}} - 1$, respectively.

Theorem 5.5 *The closed-form outage probability expression with II detector at UAV-2 over Rician shadowed fading channels is:*

$$Pr(O_2^{HBD(II)}) \approx \sum_{n=0}^{K_{tr}} \sum_{j=0}^{n+1} \bar{a}(n, \Omega_X \alpha_{g,2}, K_{X_{gs}}, m_{X_{gs}}, \gamma_{th,2}^{HBD}) \binom{n+1}{j} E\{Y_1^j\}, \quad (5.23)$$

where $E\{Y_1^j\} = \left(\frac{\Omega_X \alpha_{1,2}}{1+K_{Y_1}}\right)^j \Gamma(1+j) \left(\frac{m_{Y_1}}{K_{Y_1} + m_{Y_1}}\right)^{m_{Y_1}-1-j} {}_2F_1\left(1-m_{Y_1}, 1+j; 1; \frac{-K_{Y_1}}{m_{Y_1}}\right)$.

Proof: The closed-form outage probability expression at UAV-2 can be obtained as $Pr(O_2^{HBD(II)}) = E\{F_{X_{gs}}(\gamma_{th,2}^{HBD}(1+Y_1))\}$, where $F_{X_{gs}}(\bullet)$ is the CDF of X_{gs} from (5.10). The final expression for $Pr(O_2^{HBD(II)})$ is calculated from [45, eq. (8)]. Separately, it can be shown that (5.23) converges absolutely by repeating the same approach in Appendix C.4.

For the case of Rician fading channels, an alternative outage probability expression from (5.23) is presented in the following Corollary.

Corollary 5.6 *The closed-form outage probability expression with II detector at UAV-2 over Rician fading channels is:*

$$Pr(O_2^{HBD(II)*}) \approx \sum_{n=0}^{K_{tr}} \sum_{j=0}^{n+1} \hat{a}(n, \Omega_X \alpha_{g,2}, K_{X_{gs}}, \gamma_{th,2}^{HBD}) \binom{n+1}{j} E\{Y_1^{j*}\}, \quad (5.24)$$

where Y_1^{j*} is a RV defined using the Rician fading model and $E\{Y_1^{j*}\} = \left(\frac{\Omega_X \alpha_{1,2}}{1+K_{Y_1}}\right)^j \Gamma(1+j) \sum_{i=0}^{K_{tr}} \frac{(-j)_i}{i!(1)_i} (-K_{Y_1})^i$.

Proof: Substituting $\bar{a}(n, \Omega_X \alpha_{g,2}, K_{X_{gs}}, m_{X_{gs}}, \gamma_{th,2}^{HBD})$ in (5.23) with (5.12) yields (5.24). Similarly, applying (5.15) yields the closed-form expression for $E\{Y_1^{j*}\}$. Similar to (5.23), (5.24) is shown to be absolutely convergent by repeating the same approach in Appendix C.4.

As the II detector is interference-limited at high SNR regimes [17], characterizing the asymptotic outage probability will provide useful insights into how inter-UAV interference affects the error floor. In the following Corollary, the asymptotic outage probability of the II detector is presented for Rician shadowed fading channels and Rician fading channels.

Corollary 5.7 *The closed-form asymptotic outage probability expressions for the II detector at UAV-2 over Rician shadowed fading channels ($\Pr(\mathcal{O}_{2,\infty}^{HBD(II)})$) and Rician fading channels ($\Pr(\mathcal{O}_{2,\infty}^{HBD(II)*})$) are:*

$$\Pr(\mathcal{O}_{2,\infty}^{HBD(II)}) \approx \sum_{n=0}^{K_{tr}} \bar{a}(n, \alpha_{g,2}, K_{X_{gs}}, m_{X_{gs}}, \gamma_{th,2}^{HBD}) M\{Y_1^{n+1}\}, \quad (5.25)$$

$$\Pr(\mathcal{O}_{2,\infty}^{HBD(II)*}) \approx \sum_{n=0}^{K_{tr}} \hat{a}(n, \alpha_{g,2}, K_{X_{gs}}, \gamma_{th,2}^{HBD}) M\{Y_1^{n+1*}\}. \quad (5.26)$$

Proof: Corollary 5.7 is obtained using the same steps provided in Appendix C.5.

With shadowing experienced on both the SOI link ($h_{g,2}$) and the interfering link ($h_{1,2}$), the impact of shadowing on the II detector can be investigated from (5.23). In addition, the II detector works well in weak interference scenarios [17]. Thus, it is of practical significance to understand the impact of inter-UAV interference and shadowing on outage probability, which is presented in Section 5.5.

5.4.1.3 Unmanned Aerial Vehicle 2 (Joint Detector)

The joint detector jointly estimates both the SOI (X_{gs}) and the inter-UAV interference signal (Y_1), with GS and UAV-1 transmitting under a sum rate constraint. In particular, the joint detector treats the GS signal X_{gs} as the SOI and the UAV-1 signal Y_1 as interference. As such, the joint detector decodes the SOI with the knowledge of interfering signal's structure. Such an arrangement enables UAV-1 to transmit at a higher rate than the capacity of the interfering link [170], with similar decoding algorithms investigated for interference-limited receivers in two-user interference channels [93, 95].

The outage event for the joint detector $\mathcal{O}_2^{HBD(JD)}$ can be defined as [18]:

$$\mathcal{O}_2^{HBD(JD)} = \mathcal{O}_{JD}^1 \cup \mathcal{O}_{JD}^2, \quad (5.27)$$

$$\text{where } \mathcal{O}_{JD}^1 = \left\{ h_{g,2}, h_{1,2} : R_{gs}^{HBD} > \log_2 \left(1 + X_{gs} \right) \right\}, \quad (5.28)$$

$$\begin{aligned} \mathcal{O}_{JD}^2 &= \left\{ h_{g,2}, h_{1,2} : R_1^{HBD} + R_{gs}^{HBD} > \log_2 \left(1 + X_{gs} + Y_1 \right), \right. \\ &\quad \left. \log_2 \left(1 + \frac{X_{gs}}{1 + Y_1} \right) \leq R_{gs}^{HBD} \leq \log_2 \left(1 + X_{gs} \right) \right\}. \end{aligned} \quad (5.29)$$

The outage event ($O_2^{HBD(JD)}$) occurs if SOI detection fails (O_{JD}^1) or if the sum rate constraint is not met (O_{JD}^2).

Theorem 5.6 *The closed-form expression for the outage probability with the joint detector at UAV-2 over Rician shadowed fading channels is:*

$$\begin{aligned} \Pr(O_2^{HBD(JD)}) &\approx \sum_{n=0}^{K_{tr}} \bar{a}(n, \Omega_X \alpha_{g,2}, K_{X_{gs}}, m_{X_{gs}}, \gamma_{th,2}^{HBD}) \\ &+ \left(\sum_{n=0}^{K_{tr}} \sum_{q=0}^n \sum_{k=0}^{q+1} \bar{a}(q, \Omega_X \alpha_{1,2}, K_{Y_1}, m_{Y_1}, 1) \bar{a}(n-q, \Omega_X \alpha_{g,2}, K_{X_{gs}}, m_{X_{gs}}, 1) \right. \\ &\quad \times (n+1) \binom{q+1}{k} (-1)^{q+1} G_1(q, k, b_2, \gamma_{th,2}^{HBD}) \frac{G_2(k+n-q+1, b_1, \gamma_{th,2}^{HBD})}{k+n-q+1} \Bigg) \end{aligned} \quad (5.30)$$

where $b_1 = 2^{R_1^{HBD}} (2^{R_{gs}^{HBD}} - 1)$, $b_2 = 2^{R_1^{HBD} + R_{gs}^{HBD}} - 1$, $G_1(q, k, b_2, \gamma_{th,2}^{HBD}) = (-b_2)^{q+1-k} - (-\gamma_{th,2}^{HBD})^{-k}$, $G_2(k+n-q+1, b_1, \gamma_{th,2}^{HBD}) = (b_1)^{k+n-q+1} - (\gamma_{th,2}^{HBD})^{k+n-q+1}$.

Proof: The proof pertaining to the derivation of the outage probability expression and its convergence can be found in Appendix C.6.

For the case of Rician fading, an alternative outage probability expression using (5.30) is presented in the following Corollary.

Corollary 5.8 *The closed-form outage probability expression with the joint detector at UAV-2 over Rician fading channels is:*

$$\begin{aligned} \Pr(O_2^{HBD(JD)*}) &\approx \sum_{n=0}^{K_{tr}} \hat{a}(n, \Omega_X \alpha_{g,2}, K_{X_{gs}}, \gamma_{th,2}^{HBD}) \\ &+ \left(\sum_{n=0}^{K_{tr}} \sum_{q=0}^n \sum_{k=0}^{q+1} \hat{a}(q, \Omega_X \alpha_{1,2}, K_{Y_1}, 1) \hat{a}(n-q, \Omega_X \alpha_{g,2}, K_{X_{gs}}, 1) \right. \\ &\quad \times (n+1) \binom{q+1}{k} (-1)^{q+1} G_1(q, k, b_2, \gamma_{th,2}^{HBD}) \frac{G_2(k+n-q, b_1, \gamma_{th,2}^{HBD})}{k+n-q+1} \Bigg) \end{aligned} \quad (5.31)$$

Proof: Equation (5.31) is obtained using the same approach in Corollary 5.6. Furthermore, it can be demonstrated that (5.31) converges absolutely by adopting the same technique used in Appendix C.6.

At high SNR regimes, the joint detector has been shown to exhibit interference-free performance [18]. As it will be demonstrated in the next Corollary, the joint detector achieves zero outage probability at asymptotic SNR regimes over Rician shadowed fading channels and Rician fading channels.

Corollary 5.9 *The joint detector attains zero outage probability over Rician shadowed fading channels and Rician fading channels at asymptotic SNR regimes.*

Proof: The proof is provided in Appendix C.7.

The joint detector works well when the SOI and the interfering signal are sufficiently strong [165], with Corollary 5.1 suggesting that a lower $\Pr(O_2^{HBD(JD)})$ is attained when $K_{X_{gs}}$, K_{Y_1} , $m_{X_{gs}}$, and m_{Y_1} are high. To this end, the combined impact of inter-UAV interference and shadowing on the joint detector can be analyzed from (5.30), which is discussed in detail in Section 5.5.

5.4.2 Half-Duplex Outage Probability

When operating in HD mode, interference is non-existent at both GS and UAV-2. Let the HD threshold at GS and UAV-2 be $\gamma_{th,gs}^{HD} = 2^{2R_1^{HBD}} - 1$ and $\gamma_{th,2}^{HD} = 2^{2R_{gs}^{HBD}} - 1$, respectively. Then, the HD outage probability at GS ($\Pr(O_{gs}^{HD})$) and UAV-2 ($\Pr(O_2^{HD})$) over Rician shadowed fading channels is obtained from (5.10) as:

$$\Pr(O_{gs}^{HD}) \approx \sum_{n=0}^{K_{tr}} \bar{a}(n, \Omega_X, K_{X_1}, m_{X_1}, \gamma_{th,gs}^{HD}). \quad (5.32)$$

$$\Pr(O_2^{HD}) \approx \sum_{n=0}^{K_{tr}} \bar{a}(n, \Omega_X \alpha_{g,2}, K_{X_{gs}}, m_{X_{gs}}, \gamma_{th,2}^{HD}). \quad (5.33)$$

Adopting the same technique to derive Corollary 5.6 yields the following closed-form outage probability expressions over Rician fading channels:

$$\Pr(O_{gs}^{HD*}) \approx \sum_{n=0}^{K_{tr}} \hat{a}(n, \Omega_X, K_{X_1}, \gamma_{th,gs}^{HD}). \quad (5.34)$$

$$\Pr(O_2^{HD*}) \approx \sum_{n=0}^{K_{tr}} \hat{a}(n, \Omega_X \alpha_{g,2}, K_{X_{gs}}, \gamma_{th,2}^{HD}). \quad (5.35)$$

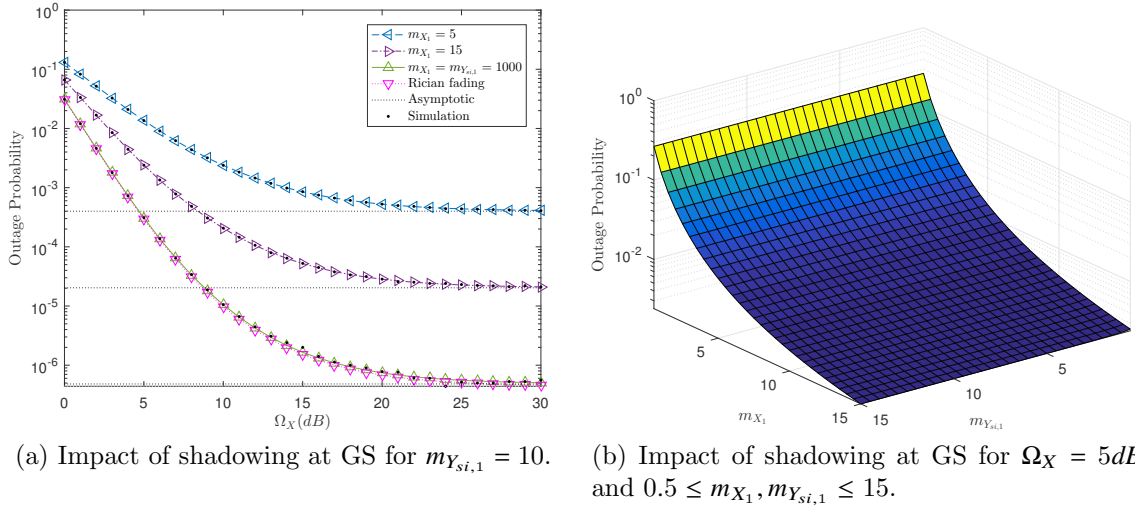


Fig. 5.6: Outage probability at GS for $\alpha_{g,g} = 1$, $\epsilon = 0.01$, $\gamma_\phi^2 = -130\text{dBm}$, and $K_{X_1} = K_{Y_{si,1}} = 15$.

Finally, it should be noted that by repeating the steps in Appendix C.6, it can be shown that the HD outage probability expressions converge absolutely. Separately, operating the GS and UAV-2 in HD mode results in interference-free transmissions. As such, by utilizing the same approach in Appendix C.7, it can be shown that both the GS and UAV-2 achieves zero outage probability over Rician shadowed fading channels and Rician fading channels at asymptotic SNR regimes.

The HD outage probability expressions provide benchmark comparison against the HBD mode of operation at GS and UAV-2, which is discussed in Section 5.5.

5.5 Numerical Results

Numerical results pertaining to the outage probability at UAV-2 and at the GS are presented in this section, along with Monte Carlo simulations conducted with 10^7 samples. The Monte Carlo simulations are conducted in MATLAB, using the *random* and *rand* functions. To maintain a fair comparison between the HBD-UCS and HD-UCS, we let $R_{sum}^{HD} = R_{sum}^{HBD} = 1$, with $\sigma_g^2 = \sigma_2^2 = -115\text{dBm}$.

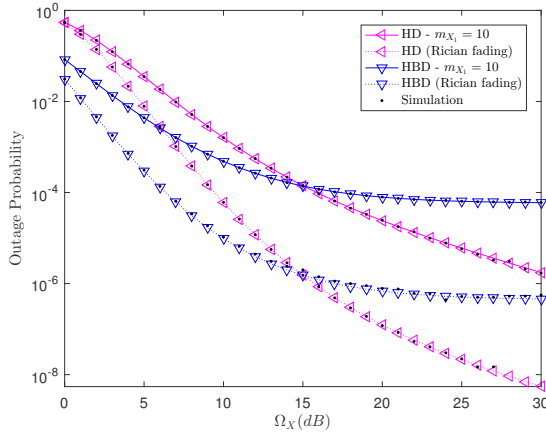


Fig. 5.7: Outage probability at GS (HBD vs HD) for $\alpha_{g,g} = 1$, $\epsilon = 0.01$, $\gamma_\phi^2 = -130\text{dBm}$, $K_{X_1} = K_{Y_{si,1}} = 15$, $m_{Y_{si,1}} = 10$.

Table 5.3: Error margin of the outage probability at GS.

	$\Omega_X = 5 \text{ dB}$	$\Omega_X = 15 \text{ dB}$	$\Omega_X = 30 \text{ dB}$
$m_{X_1} = 5$	4.68×10^{-5}	2.74×10^{-5}	1.14×10^{-5}
$m_{X_1} = 15$	1.34×10^{-6}	8.59×10^{-6}	8.51×10^{-6}
$m_{X_1} = m_{Y_{si,1}} = 1000$	1.98×10^{-6}	-	-
Rician fading	1.25×10^{-5}	-	-

5.5.1 Impact of Shadowing at GS

Observation 5.5.1.1 *Shadowing on the SI link has negligible impact on outage probability at the GS.*

The HBD outage probability at GS ($\Pr(O_{gs}^{HBD})$), given in (5.16), is shown in Fig. 5.6a for $m_{X_1} \in \{5, 15, 1000\}$. For the case of Rician fading channels, $\Pr(O_{gs}^{HBD})$ is plotted using (5.19) which matches with that using (5.16) for $m_{X_1} = m_{Y_{si,1}} = 1000$. Likewise, $\Pr(O_{gs}^{HBD})$ is plotted using (5.34) for the case of Rician fading channels. The error margins of the outage probability at GS are shown in Table 5.3.

From Fig. 5.6a, it can be seen that the outage probability drops more steeply as m_{X_1} increases due to less shadowing on the desired link ($h_{1,g}$) than the SI link (h_{si}). In Fig. 5.6b, it is observed that shadowing on the SI link ($m_{Y_{si,1}}$) has negligible impact on the outage probability, especially when $m_{Y_{si,1}}$ is large. From Corollary 5.3, it is shown that the fractional moment of a Rician shadowed RV is independent of m as $m \rightarrow \infty$.

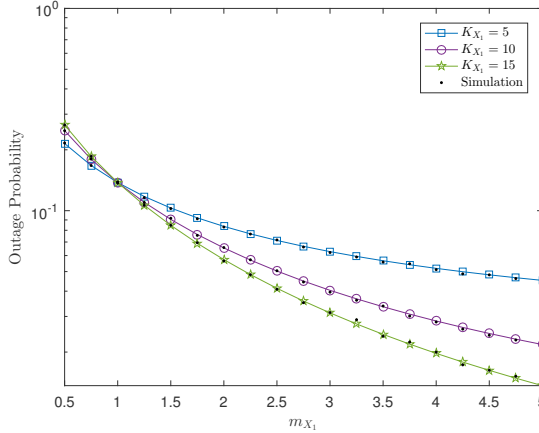


Fig. 5.8: Impact of shadowing and Rician K factors on outage probability at GS for $\Omega_X = 5\text{dB}$, $\alpha_{g,g} = 1$, $\epsilon = 0.01$, $\gamma_\phi^2 = -130\text{dBm}$, $K_{Y_{si,1}} = 10$, $m_{Y_{si,1}} = 2$.

Therefore, the outage probability at the GS is independent of $m_{Y_{si,1}}$ as $m_{Y_{si,1}} \rightarrow \infty$. The trend in Fig. 5.6b shows that having higher amounts of passive SI mitigation, i.e., smaller $m_{Y_{si,1}}$, will not further reduce outage probability at the FD-enabled GS. As SI is first mitigated at the passive SI suppression stage, residual SI is further mitigated at the active SI mitigation stage. Thus, large amounts of passive SI suppression results in less amounts of SI being mitigated at the active SI mitigation stage and vice-versa. A similar trend has also been seen in [21, Fig. 9], where higher amounts of passive SI mitigation did not result in higher SI cancellation.

Observation 5.5.1.2 *The FD-enabled GS is more reliable than the HD-GS at low SNR regimes, even in the presence of shadowing.*

In Fig. 5.7, the HBD outage probability ($Pr(O_{gs}^{HBD})$) and HD outage probability ($Pr(O_{gs}^{HD})$) at GS are plotted, with the latter obtained from (5.32). It can be seen in Fig. 5.7 that even in the presence of shadowing, the FD-enabled GS achieves lower outage probability at low SNR regimes than the HD-enabled GS. The FD-enabled GS also achieves better reliability in a shadowing environment than the HD-GS operating in a non-shadowing environment at low SNR regimes.

Observation 5.5.1.3 *When severe shadowing is experienced with strong LOS component at the FD-enabled GS, reliability is diminished even when SI mitigation measures are implemented.*

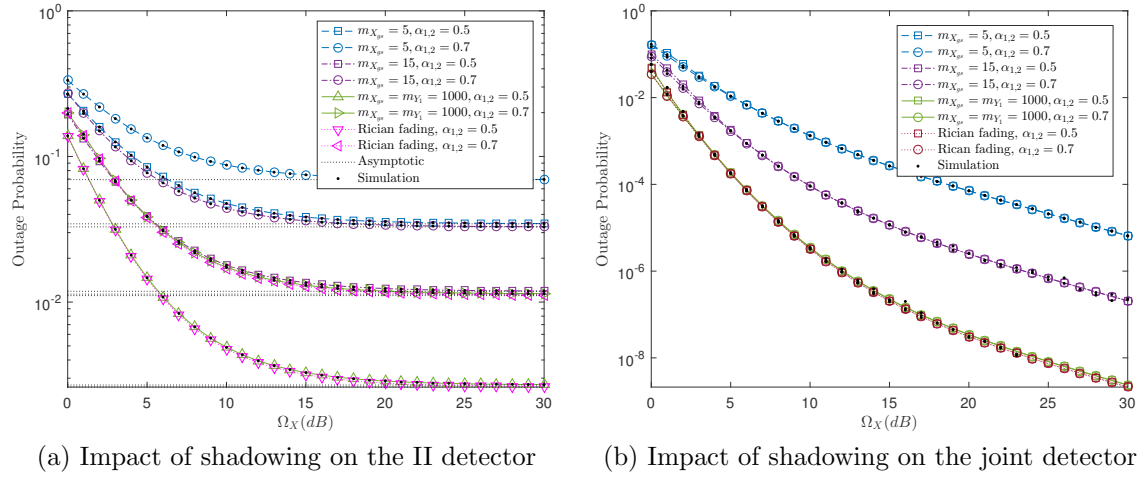


Fig. 5.9: Outage probability at UAV-2 for $\alpha_{g,2} = 1$, $K_{X_{gs}} = K_{Y_1} = 15$, $m_{Y_1} = 10$.

In Fig 5.8, the impact of shadowing and Rician K factors on $Pr(O_{gs}^{HBD})$, from (5.16), is analyzed. Interestingly, it can be seen that $Pr(O_{gs}^{HBD})$ is high when the Rician K factor is high and $m_{x_1} < 1$. Similar trends in [186, Fig. 9] have also been observed. A large Rician K factor implies that the average received power of the scattered component is low. When m is small, e.g., $m_{x_1} < 1$, severe shadowing on the LOS component is experienced. Under such circumstances, a large Rician K factor causes overall average received power to be lower than when Rician K factor is small. Also, from Corollaries 5.1 and 5.3, the Rician K factor has a positive influence on the outage probability when m is large. Therefore, the opposite is also true, i.e., a small m causes the Rician K factor to negatively impact the outage probability. Thus, the reliability of the FD-enabled GS diminishes more as the Rician K factor increases while the LOS component of the desired link ($h_{1,g}$) is obstructed, e.g., by buildings, despite the implementation of SI mitigation measures. To overcome the effect of shadowing on the desired link, relaying strategies can be considered.

5.5.2 Impact of inter-UAV interference and Shadowing at UAV-2

Observation 5.5.2.1 Severe shadowing on the desired link has the equivalent impact of higher inter-UAV interference at the II detector, which results in diminished reliability.

Table 5.4: Error margin of the outage probability at the ii and joint detectors for $\alpha_{1,2} = 0.5$.

	$\Omega_X = 5 \text{ dB}$	$\Omega_X = 15 \text{ dB}$	$\Omega_X = 30 \text{ dB}$
$m_{X_{gs}} = 5 \text{ (II)}$	2.3×10^{-5}	7.45×10^{-6}	5.35×10^{-5}
$m_{X_{gs}} = 15 \text{ (II)}$	3.6×10^{-6}	3.34×10^{-5}	2.6×10^{-5}
$m_{X_{gs}} = m_{Y_1} = 1000 \text{ (II)}$	6.91×10^{-5}	9.67×10^{-6}	8.4×10^{-6}
Rician fading (II)	3.8×10^{-4}	1.47×10^{-4}	9.46×10^{-5}
$m_{X_{gs}} = 5 \text{ (JD)}$	3.03×10^{-4}	2.79×10^{-5}	-
$m_{X_{gs}} = 15 \text{ (JD)}$	5.34×10^{-5}	8.1×10^{-7}	-
$m_{X_{gs}} = m_{Y_1} = 1000 \text{ (JD)}$	1.17×10^{-6}	-	-
Rician fading (JD)	5.23×10^{-6}	-	-

The HBD outage probability for the II detector ($Pr(O_2^{HBD(II)})$) at UAV-2, computed from (5.23), is plotted in Fig. 5.9a for $m_{X_{gs}} \in \{5, 15, 1000\}$ and $\alpha_{1,2} \in \{0.5, 0.7\}$. Also, $Pr(O_2^{HBD(II)})$ is plotted in Fig. 5.9a for the II detector over Rician fading channels using (5.24), where it is seen to be matching with (5.23) for $m_{X_{gs}} = m_{Y_1} = 1000$ and $\alpha_{1,2} \in \{0.5, 0.7\}$. For HD-UCS, $Pr(O_2^{HD})$ is plotted using (5.35). The error margins of the outage probability at UAV-2 are shown in Table 5.4.

In Fig. 5.9a, similar observations seen in Fig. 5.6a are noted. Specifically, a lower $Pr(O_2^{HBD(II)})$ is attained when the desired link ($h_{g,2}$) experiences less severe shadowing than the interfering link ($h_{1,2}$), i.e., $m_{X_{gs}} > m_{Y_1}$. Also, for $m_{X_{gs}} = 5$ and $\alpha_{1,2} = 0.5$, $Pr(O_2^{HBD(II)})$ is similar to that obtained for $m_{X_{gs}} = 15$ and $\alpha_{1,2} = 0.7$. Similar observations are also made for the case of $m_{X_{gs}} = 15$ and $\alpha_{1,2} = 0.5$, and $m_{X_{gs}} = 1000$ and $\alpha_{1,2} = 0.7$. Therefore, severe shadowing on the desired link has the equivalent effect of higher inter-UAV interference levels on the received signal at the II detector. From Fig. 5.9a, it is apparent that both shadowing on the desired link and inter-UAV interference causes the II detector to have diminished reliability. Thus, deploying the II detector-based HBD-UCS for multi-UAV networks in urban environments results in diminished reliability. Such a limitation inadvertently places constraints on the overall QoS requirements for the multi-UAV network.

Observation 5.5.2.2 *Shadowing and inter-UAV interference reduces the outage probability decay rate of the joint detector at low SNR regimes.*

The HBD outage probability for the joint detector ($Pr(O_2^{HBD(JD)})$) at UAV-2, computed from (5.30), is plotted in Fig. 5.9b for $m_{X_{gs}} \in \{5, 15\}$ and $\alpha_{1,2} \in \{0.5, 0.7\}$. For

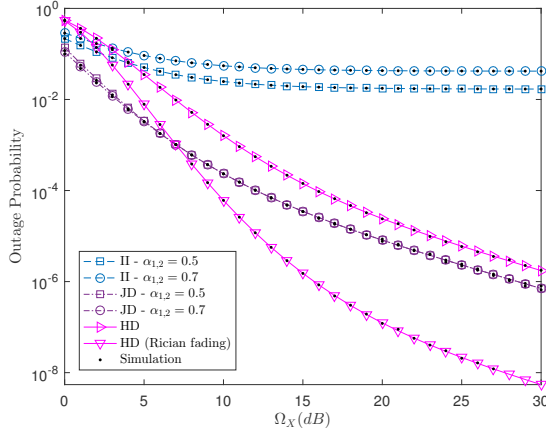


Fig. 5.10: Comparison between the II and joint detectors at UAV-2 for $\alpha_{g,2} = 1$, $K_{X_{gs}} = K_{Y_1} = 15$, $m_{X_{gs}} = m_{Y_1} = 10$.

reference, $Pr(O_2^{HBD(JD)})$ is plotted in Fig. 5.9b over Rician fading channels using (5.31) to reflect the outage probability at the joint detector in the absence of shadowing.

From Fig. 5.9b, the effect of shadowing on the joint detector is more pronounced than inter-UAV interference, especially at moderate and high SNR regimes. Since the joint detector works well in the presence of strong interference [94, 165, 166, 169], it is not interference-limited at high SNR regimes. Instead, the combined effect of shadowing and inter-UAV interference reduces the outage probability decay rate at low SNR regimes. When $m_{X_{gs}} = 15$ and $\alpha_{1,2} \in \{0.5, 0.7\}$, $Pr(O_2^{HBD(JD)})$ decays more steeply, as compared to setting $m_{X_{gs}} = 5$ and $\alpha_{1,2} \in \{0.5, 0.7\}$. Thus, the joint detector exhibits higher reliability when $\alpha_{1,2} \rightarrow \infty$ and $m_{X_{gs}} > m_{Y_1}$. In contrast to the II detector, multi-UAV networks with joint detector-based HBD-UCS can achieve higher reliability, especially in urban environments.

Observation 5.5.2.3 *In the presence of inter-UAV interference and shadowing, the joint detector exhibits lower outage probability than the II detector and the HD-UCS at low SNR regimes.*

In Fig. 5.10, the HBD outage probability of the II detector ($Pr(O_2^{HBD(II)})$) and the joint detector ($Pr(O_2^{HBD(JD)})$) are plotted. In addition, the HD-UCS outage probability at UAV-2 ($Pr(O_2^{HD})$) is also plotted using (5.33). As reference, $Pr(O_2^{HD})$ in the absence of shadowing is provided using (5.14) by substituting $\Omega = \Omega_X \alpha_{g,2}$, $K = K_{X_{gs}}$, and $\gamma = \gamma_{th,2}^{HD}$.

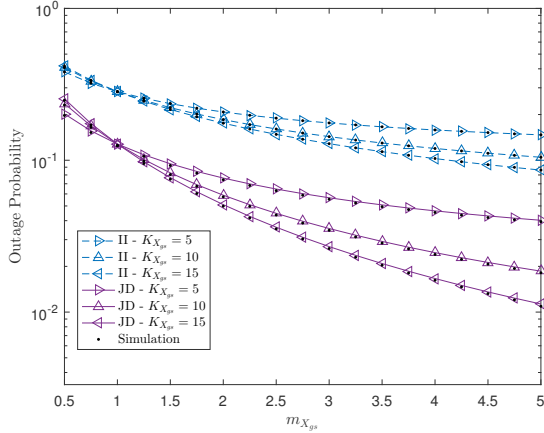


Fig. 5.11: Impact of shadowing and Rician K factors on outage probability at UAV-2 for $\Omega_X = 5\text{dB}$, $\alpha_{g,2} = 1$, $\alpha_{1,2} = 0.5$, $K_{Y_1} = 10$, $m_{Y_1} = 10$.

From Fig. 5.10, outage probability trends observed for the II detector in [52, Fig. 4] are also seen in Fig. 5.10. Specifically, it is seen in Fig. 5.10 that the II detector attained lower outage probability than the HD-UCS at low SNR regimes. The same is also observed when the HD-UCS is not experiencing the effects of shadowing, i.e., HD-UCS over Rician fading channels. However, at high SNR regimes, the II detector is observed to be interference-limited due to the error floor observed in Fig. 5.10.

For the joint detector, the attained outage probability is lower than that of HD-UCS when shadowing is considered. When shadowing is not experienced at the HD-UCS, the joint detector achieves lower outage probability for $\Omega_X < 7\text{dB}$. In addition, the superiority of the joint detector over the II detector is highlighted. Therefore, the HBD-UCS shows superior reliability over HD-UCS. The joint detector clearly outperforms the II detector in terms of reliability. Thus, the former is more suitable for multi-UAV networks with high QoS requirements.

Observation 5.5.2.4 *Severe shadowing with strong LOS component has less effect on the joint detector than on the II detector.*

In Fig. 5.11, the same observations made in Fig. 5.8 are noted. Thus, severe shadowing on the desired link ($h_{g,2}$) with large Rician K factor diminishes the reliability of the II and joint detectors. However, the effect is less extensive for the joint detector than the

II detector since outage probability of the former is lower than the latter. As such, the superiority of the joint detector over the II detector is highlighted in severe shadowing environments, e.g., urban environments.

5.6 Chapter Summary

An HBD-UCS, consisting of HD UAVs and FD GSs, is investigated as an alternative to address spectrum scarcity in UAV communications. To effectively model the underlying communication channels, Rician shadowed fading is assumed on all links to account for shadowing introduced in urban environments. To this end, an innovative mathematical framework is presented to obtain alternative closed-form representations related to both the Rician shadowed fading and the Rician fading models. Closed-form outage probability expressions for the II and the joint detectors are then obtained from the derived expressions. An extensive outage probability analysis of the HBD-UCS was conducted under various inter-UAV interference and shadowing scenarios over Rician shadowed fading channels. At the GS, the impact of shadowing on the desired link and the SI link was demonstrated. Specifically, at the GS, shadowing on the desired link impacts the outage probability considerably. On the other hand, shadowing on the SI link has negligible impact on GS outage probability. Additionally, it is also demonstrated the GS operates with lower outage probability in FD mode than in HD mode. At UAV-2, it was shown that the joint detector attains lower outage probability than the II detector and the HD-UCS. The robustness of the joint detector under severe shadowing on the desired link was also demonstrated. Thus, the superior reliability and robustness of the joint detectors makes it an ideal candidate for multi-UAV networks operating in congested urban environments.

It is also important to note that the analysis in this chapter, as well as the preceding chapters, focused on the specific case of two UAVs in the HBD-UCS. To this end, the performance of the HBD-UCS is analyzed in the next chapter for arbitrary number of UAVs deployed in an HBD multi-UAV network.

Chapter 6

Towards Hybrid-Duplex Multi-UAV Networks

6.1 Introduction

While HBD systems have thus far been investigated to address spectrum scarcity in both manned aerial vehicle and UAV communications [17,18], the analysis seen in the preceding chapters have focused on the specific case of single uplink and downlink nodes in the network. To account for any arbitrary number of uplink and downlink nodes, stochastic geometry tools need to be employed. One such stochastic geometry tool is the PPP, which is commonly used for terrestrial networks. While PPPs have been extensively used to model the spatial locations of base stations and user equipments in cellular networks, a PPP effectively covers an infinite region [112]. Furthermore, the number of nodes modeled at each instance of a PPP is not fixed. In contrast, UAV networks are more likely to be deployed over a small region with fixed numbers of deployed UAVs [112,113].

In light of the above discussions, the BPP model is more suitable to model the spatial locations of UAVs in multi-UAV networks [112,113]. Compared to PPPs, the BPP model allows for the area of the considered region, i.e., area of the cell, to be defined. Also, in contrast to PPPs, BPPs enable the number of deployed nodes, i.e., UAVs, at every realization to be fixed, while ensuring that the spatial locations of the nodes are uniformly distributed. With these considerations in mind, this chapter investigates the performance of a multi-UAV network with HBD-UCS under a stochastic geometry framework. In particular, system models from prior chapters are extended in this chapter

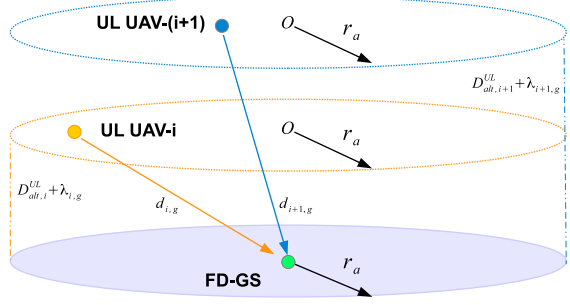


Fig. 6.1: An illustration of the UL UAV spatial locations. The spatial location of DL UAV-1 is described in the same fashion.

to incorporate the BPP model for large-scale UAV deployments.¹

6.2 System Model

We consider an HBD-UCS with N_{UL} HD UL UAVs and one HD DL UAV communicating with a FD-GS in a suburban environment. In particular, the FD-GS receives uplink data from the N_{UL} UL UAVs while simultaneously transmitting downlink data to the DL UAV. Furthermore, inter-UAV interference between the UL and DL UAVs is unavoidable due to the nature of HBD transmissions [17, 18]. Thus, a SIC detector is considered at the DL UAV, with SI mitigation assumed at the FD-GS in this chapter. To account for the spatial deployment of UAVs, a BPP assumption is considered [112, 113], with $D_{alt,i}^{UL}$ denoting the altitude of UL UAV- i and $D_{alt,1}^{DL}$ denoting the altitude of the DL UAV. Rician fading channels are also assumed to appropriately model the propagation characteristics of the suburban environment in UAV communications [8]. Finally, the effect of Doppler shift is assumed to be compensated in this chapter [17, 18].

Let the spatial location of the UAVs be uniformly distributed in a disc with radius r_a , angle $[0, 2\pi)$, and origin O above the FD-GS [112]. By letting the FD-GS be located on the ground at origin O , we define the Euclidean distance (in km) between UL UAV- i and the FD-GS as $d_{i,g} = \sqrt{D_{i,g}^2 + (D_{alt,i}^{UL} + \lambda_{i,g})^2}$, where $D_{i,g}$ denotes the Euclidean distance between the projection of UL UAV- i onto the ground plane and the FD-GS. Similarly, let the

¹The work in this chapter has been published in [20].

Euclidean distance between the FD-GS and DL UAV be $d_{g,1} = \sqrt{D_{g,1}^2 + (D_{alt,1}^{DL} + \lambda_{g,1})^2}$, where $D_{g,1}$ denotes the Euclidean distance between the projection of the DL UAV onto the ground plane and the FD-GS. The variable λ_x , $x \in \{(i, g), (g, 1)\}$ denotes a minimum distance between the UAVs and the FD-GS such that $0 < \lambda_x < r_a$, $D_{alt,i}^{UL} \leq D_{alt,i+1}^{UL}$ and $\lambda_{i,g} < \lambda_{i+1,g}$, are satisfied to enable the SIC-based detection process at the FD-GS. Finally, we define the Euclidean distance between the UL and DL UAVs, i.e., inter-UAV distance, as $d_{i,1}$.

As the spatial locations of the UAVs follow a BPP, the PDF $f_{d_x}(w)$ of d_x is defined as [112, eq. (3)] $f_{d_x}(w) = \frac{2w}{r_a^2}$ where $x \in \{(i, g), (g, 1)\}$, $D_{alt} + \lambda_x \leq w \leq \sqrt{(D_{alt} + \lambda_x)^2 + r_a^2}$, and $D_{alt} \in \{D_{alt,i}^{UL}, D_{alt,1}^{DL}\}$.

For the inter-UAV distance ($d_{i,1}$), the conditional PDF $f_{d_{i,1}}(w|d_{g,1})$ is given as [112, eq. (2)]:

$$f_{d_{i,1}}(w|d_{g,1}) = \begin{cases} \frac{2w}{r_a^2}, & \lambda_{i,1} \leq w \leq w_{m,1} \\ \frac{2w}{\pi r_a^2} \arccos \left(\frac{w^2 + d_{g,1}^2 - (r_a^2 + \lambda_{i,1}^2)}{2d_{g,1}\sqrt{w^2 - \lambda_{i,1}^2}} \right), & w_{m,1} < w \leq w_{p,1} \end{cases} \quad (6.1)$$

where $w_{m,1} = \sqrt{(r_a - d_{g,1})^2 + (\lambda_{i,1})^2}$, $w_{p,1} = \sqrt{(r_a + d_{g,1})^2 + (\lambda_{i,1})^2}$, and $0 < \lambda_{i,1} < w_{m,1}$ is the minimum distance between UL UAV- i and the DL UAV.

At the FD-GS, only residual SI is considered, with the SI channel modeled as a Rician fading channel to account for SI mitigation [17, 18]. Let x_{gs} and x_i be the respective transmitted signals from the FD-GS and UL UAV- i . Then, the SOI and the SI signal at the FD-GS are x_i and $x_{si} = x_{gs}$, respectively. Also, let $h_{i,g}$ denote the channel between UL UAV- i and GS, and h_{si} be the SI channel gain. The resultant received signal at GS can thus be written as [21]:

$$y_{gs} = \sum_{i=1}^{N_{UL}} \sqrt{\frac{P_i}{d_{i,g}^n}} h_{i,g} x_i + \sqrt{P_{si}} |\tilde{h}_{si}| x_{si} + \sqrt{P_{si}} |h_{si}| \gamma_\phi w_\phi + w_g, \quad (6.2)$$

where n is the pathloss exponent, P_i is the transmit power of UL UAV- i , P_{si} is the power of the SI, \tilde{h}_{si} is the error of the imperfect SI channel gain estimate, defined as $\tilde{h}_{si} = h_{si} - \hat{h}_{si}$, \hat{h}_{si} is the imperfect estimation of the SI channel gain, w_g is the AWGN

Table 6.1: Summary of Important Notations

Notations	Description
Ω_X	Average received power
$\alpha_{i,j}, i \in \{g, 1\}, j \in \{g, 2\}, i \neq j$	Strength of interference between i and j
ϵ	SI channel estimation error at the FD-enabled GS
γ_ϕ^2	Strength of phase noise at the FD- enabled GS oscillator
σ_g^2	Strength of AWGN at the FD-enabled GS
σ_2^2	Strength of AWGN at the UAV-2
r_a	Radius of the the disc
$d_{i,1}$	Euclidean distance between UL UAV- i and the DL UAV
$d_{i,g}$	Euclidean distance between UL UAV- i and the FD-GS
$D_{alt,i}^{UL}$	Altitude of UL UAV- i
$D_{alt,1}^{DL}$	Altitude of the DL UAV
$\lambda_x, x \in \{(i, g), (g, 1)\}$	Minimum distance between the UAVs and the FD-GS

with zero-mean and variance σ_g^2 , and w_ϕ is the Gaussian distributed phase noise with zero-mean and unit variance scaled by the strength of the phase noise γ_ϕ^2 [21].²

To model the worst case residual SI, the channel estimation error (\tilde{h}_{si}) is modeled as a circularly symmetric zero-mean complex Gaussian random variable RV with variance ϵ [17, 18]. Also, the total amount of SI suppression is $\frac{1}{\epsilon\sigma_g^2}$ [17]. Finally, as $D_{alt,i}^{UL} \leq D_{alt,i+1}^{UL}$ and $\lambda_{i,g} < \lambda_{i+1,g}$, the SIC-based detection order begins from UL UAV- i at the FD-GS, i.e., closest UL UAV, while treating the remaining $N_{UL} - i$ UL UAVs as interference.

At the DL UAV, the received signal can be written as:

$$y_{DL} = \sqrt{\frac{P_g}{d_{g,i}^n}} h_{g,1} x_{gs} + \sum_{j=1}^{N_{UL}} \sqrt{\frac{P_j}{d_{j,1}^n}} h_{j,1} x_j + w_1, \quad (6.3)$$

where P_g is the transmit power of the GS, $h_{g,1}$ is the channel between the FD-GS and the DL UAV, $h_{j,1}$ is the channel between UL UAV- j and the DL UAV, and w_1 is the AWGN at the DL UAV with zero-mean and variance σ_1^2 . As inter-UAV interference (x_i) is present at the DL UAV, we consider an imperfect SIC detector which removes inter-UAV interference first before detecting the SOI (x_{gs}). A summary of important notations is given in Table 6.1.

6.3 Outage Probability

In this section, outage probability expressions of the UL and DL UAVs are presented for the HBD-UCS. The outage probability expression for HD-UCS is also presented for

²The phase noise term γ_ϕ reflects the jitter effect in oscillators due to hardware imperfections [21]

benchmark comparison. Let R_i^j and R_{gs}^j for $j \in \{HBD, HD\}$ be the transmission rates of the UL UAV- i and GS, respectively. For a fair comparison between the HBD-UCS and HD-UCS, we let $R_i^{HBD} = \frac{1}{2N_{UL}}R_i^{HD}$ and $R_{gs}^{HBD} = \frac{1}{2}R_{gs}^{HD}$ for uplink and downlink transmissions, respectively.

6.3.1 Hybrid-Duplex Outage Probability

For a SINR of $\frac{X_i d_i^{-n}}{1 + \sum_{j=i+1}^N X_j d_j^{-n}}$ with N interferers, where $X_i, 0 \leq i \leq N$ is a non-centered Chi-squared distributed random variable RV with Rician K factor K_i , and d_l^{-n} denotes the distance of transmitting node l , the outage probability is presented in the following Lemma.

Lemma 6.1 *The outage probability $Pr(O)$ for the outage event O at an arbitrary receiver is:*

$$\begin{aligned} Pr(O) &\approx \sum_{q=0}^{K_{tr}} \sum_{l_1+\dots+l_{N-q+1}=q+1} \alpha(q, \bar{P}_i, K_i, \gamma) \binom{l_1 + \dots + l_{N-q+1}}{l_1, \dots, l_{N-q+1}} \\ &\quad \times \int_{-\infty}^{\infty} w_i^{n(q+1)} f_{d_i}(w_i) \left(\prod_{j=1}^{N-i} E\{X_j^{l_j}\} \int_{-\infty}^{\infty} w_j^{-nl_j} f_{d_j}(w_j) dw_j \right) dw_i, \end{aligned} \quad (6.4)$$

where $O = \left\{ X_i, X_j : R \geq \log_2 \left(1 + \frac{X_i d_i^{-n}}{1 + \sum_{j=i+1}^N X_j d_j^{-n}} \right) \right\}$, R is the transmission rate, K_{tr} is the truncation order, $\alpha(q, \bar{P}_i, K_i, \gamma) = (-1)^q \exp(-K_i) \frac{L_q^{(i)}(K_i)}{(1+q)!} \left(\frac{(1+K_i)}{\bar{P}_i} \gamma \right)^{q+1}$ is the CDF expansion of the RV X_i , \bar{P}_i is the variance of X_i , γ is the threshold, $L_q^{(0)}(\bullet)$ is the q -th degree, zero-order Laguerre polynomials [17, 18], and $E\{\bullet\}$ is the statistical expectation. Also, $E\{X_j^{l_j}\} = \Gamma(1 + l_j) \left[\frac{\bar{P}_j}{1+K_j} \right]^{l_j} {}_1F_1(-l_j, 1; -K_j)$ is the l_j^{th} moment of X_j [17, eq. (7)] with ${}_1F_1(\bullet)$ representing the confluent Hypergeometric function [17].

Proof: The proof is provided in Appendix D.1.

From Lemma 6.1, the outage probability expressions of the UL and DL UAVs can be obtained.

6.3.1.1 Uplink UAV- i

Let $X_{i,g} = P_{i,g}|h_{i,g}|^2$ be the instantaneous received power of the SOI from UL UAV- i at the FD-GS, where $P_{i,g} = \frac{P_i}{\sigma_g^2}$. Also, let $Y_{si,1} = P_{si}\gamma_\phi^2|h_{si}|^2$ and $Y_{si,2} = P_{si}\epsilon|\tilde{h}_{si}|^2$ be the

instantaneous received power of the residual SI components, where $P_{si} = P_{i,g}$. The symbols $X_{i,g}$ and $Y_{si,1}$ are non-centered Chi-squared distributed RVs with respective Rician K factors $K_{i,g}$ and $K_{si,1}$ while $Y_{si,2}$ is an exponentially distributed RV. Defining the outage event of UL UAV- i as $\mathcal{O}_{UL,i}^{HBD} = \left\{ h_{i,g}, h_{si} : R_i^{HBD} \geq \log_2 \left(1 + \frac{X_{i,g} d_{i,g}^{-n}}{\sum_{j=i+1}^{N_{UL}} X_{j,g} d_{j,g}^{-n} + Y_{si,1} + Y_{si,2} + 1} \right) \right\}$, with threshold $\gamma_{gs}^{HBD} = 2^{R_i^{HBD}} - 1$, the outage probability $Pr(\mathcal{O}_{UL,i}^{HBD})$ of UL UAV- i is presented in the following theorem:

Theorem 6.1 *The outage probability at UL UAV- i is*

$$Pr(\mathcal{O}_{UL,i}^{HBD}) \approx \sum_{q=0}^{K_{tr}} \sum_{l_1+\dots+l_{N_{UL}-i+3}=q+1} \alpha(q, P_{i,g}, K_{i,g}, \gamma_{gs}^{HBD}) \Delta(D_{alt,i}^{UL}, \lambda_{i,g}, q) \\ \times \binom{l_1 + \dots + l_{N_{UL}-i+3}}{l_1, \dots, l_{N_{UL}-i+3}} E\{Y_{si,1}^{l_1}\} E\{Y_{si,2}^{l_2}\} \prod_{j=1}^{N_{UL}-i} E\{X_{j,g}^{l_j}\} \bar{\Delta}(D_{alt,j}^{UL}, \lambda_{j,g}, l_j), \quad (6.5)$$

where $n \neq 2$, $\Delta(D_{alt,i}^{UL}, \lambda_{i,g}, q) = \frac{2}{[n(q+1)+2]r_a^2} \left([(D_{alt,i}^{UL} + \lambda_{i,g})^2 + r_a^2]^{\frac{n(q+1)+2}{2}} - [(D_{alt,i}^{UL} + \lambda_{i,g})^2]^{\frac{n(q+1)+2}{2}} \right)$, and $\bar{\Delta}(D_{alt,j}^{UL}, \lambda_{j,g}, l_j) = \frac{2}{[2-nl_j]r_a^2} \left([(D_{alt,j}^{UL} + \lambda_{j,g})^2 + r_a^2]^{\frac{2-nl_j}{2}} - [(D_{alt,j}^{UL} + \lambda_{j,g})^2]^{\frac{2-nl_j}{2}} \right)$.

Proof: Applying Lemma 6.1 and integrating the resulting expression over the PDFs $f_{d_{i,g}}(w_i)$ and $f_{d_{j,g}}(w_j)$ yields Theorem 6.1.

As $2-nl_j$ is present in the denominator of $\bar{\Delta}(D_{alt,j}^{UL}, \lambda_{j,g}, l_j)$, Theorem 6.1 is valid only when $n \neq 2$. However, it must be noted that selecting $n \approx 2$, e.g., $n = 2 + 10^{-6}$, enables Theorem 6.1 to be applied for outage probability analysis involving free space path loss scenarios.³ ⁴

6.3.1.2 Downlink UAV

At the DL UAV, let $X_{g,1} = P_{g,1}|h_{g,1}|^2$ be the instantaneous received power of the SOI from the GS at the DL UAV, where $P_{g,1} = \frac{P_g}{\sigma_1^2}$. Also, let $X_{j,1} = P_{j,1}\beta_{j,1}|h_{j,1}|^2$ be the instantaneous received powers of the inter-UAV interference from UL UAV- j due to

³Selecting $n \approx 2$, e.g., $n = 2 + 10^{-6}$, allows $\bar{\Delta}(D_{alt,j}^{UL}, \lambda_{j,g}, l_j)$ to be evaluated for free space path loss scenarios while avoiding a zero in the denominator.

⁴To analytically ascertain the accuracy of the new power series expressions in this chapter, one will need to conduct a truncation analysis. Work in this direction is left as an open research challenge which can be addressed in future studies.

HBD transmissions, where $P_{j,1} = \frac{P_j}{\sigma_1^2}$, and $0 \leq \beta_{j,1} \leq 1$ denotes the strength of the residual interference due to imperfect SIC. The symbols $X_{g,1}$ and $X_{j,1}$ are non-centered Chi-squared distributed RVs with respective Rician K factors $K_{g,1}$ and $K_{j,1}$. Defining the outage event at the DL UAV as $O_{DL}^{HBD} = \left\{ h_{g,1}, h_{j,1} : R_{gs}^{HBD} \geq \log_2 \left(1 + \frac{X_{g,1} d_{g,1}^{-n}}{\sum_{j=1}^{N_{UL}} X_{j,1} d_{j,1}^{-n} + 1} \right) \right\}$, the outage probability expression for the DL UAV is presented in the following theorem.

Theorem 6.2 *The HBD outage probability at the DL UAV is*

$$\begin{aligned} Pr(O_{DL}^{HBD}) &\approx \sum_{q=0}^{K_{tr}} \sum_{l_1+\dots+l_{N_{UL}+1}=q+1} \alpha(q, P_{g,1}, K_{g,1}, \gamma_{DL}^{HBD}) \binom{l_1 + \dots + l_{N_{UL}-i+3}}{l_1, \dots, l_{N_{UL}-i+3}} \\ &\quad \times \int_{L_1}^{L_2} \frac{2w_{g,1}^{n(q+1)+1}}{r_a^2} \left(\prod_{j=1}^{N_{UL}} E\{X_{j,1}^{l_j}\} \Xi_{j,1}(w_{g,1}, l_j) \right) dw_{g,1}, \end{aligned} \quad (6.6)$$

where $L_1 = D_{alt,1}^{DL} + \lambda_{g,1}$, $L_2 = \sqrt{(D_{alt,1}^{DL} + \lambda_{g,1})^2 + r_a^2}$, $\gamma_{DL}^{HBD} = 2^{R_{gs}^{HBD}} - 1$, and $\Xi_{j,1}(w_{g,1}, l_j) = \frac{2[(w_{m,1})^{2-nl_j} - \lambda_{j,1}^{2-nl_j}]}{r_a^2[2-nl_j]} + \int_{w_{m,1}}^{w_{p,1}} \frac{2w_{j,1}}{\pi r_a^2} \arccos \left(\frac{w_{j,1}^2 + w_{g,1}^2 - (r_a^2 + \lambda_{j,1}^2)}{2w_{g,1}\sqrt{w_{j,1}^2 - \lambda_{j,1}^2}} \right) dw_{j,1}$.

Proof: Theorem 6.2 is proven using the same approach in Theorem 6.1.

6.3.2 Half-Duplex Outage Probability

We compare the HBD-UCS with HD-UCS as a benchmark scheme. For the HD-UCS, an outage is declared for UL UAV- i when $R_i^{HD} \geq \log_2 (1 + X_{i,g} d_{i,g}^{-n})$. Similarly, an outage is declared for the DL UAV when $R_{gs}^{HD} \geq \log_2 (1 + X_{g,1} d_{g,1}^{-n})$. Thus, the HD-UCS outage events for UL UAV- i and the DL UAV are defined as $O_{UL,i}^{HD} = \{h_{i,g} : R_i^{HD} \geq \log_2 (1 + X_{i,g} d_{i,g}^{-n})\}$ and $O_{DL}^{HD} = \{h_{g,1} : R_{gs}^{HD} \geq \log_2 (1 + X_{g,1} d_{g,1}^{-n})\}$, respectively. Following the same approach presented in Appendix D.1, the HD-UCS outage probability expressions for UL UAV- i and the DL UAV are:

$$Pr(O_{UL,i}^{HD}) \approx \sum_{q=0}^{K_{tr}} \alpha(q, P_{i,g}, K_{i,g}, \gamma_{gs}^{HD}) \Delta(D_{alt,i}^{UL}, \lambda_{i,g}, q), \quad (6.7)$$

$$Pr(O_{DL}^{HD}) \approx \sum_{q=0}^{K_{tr}} \alpha(q, P_{g,1}, K_{g,1}, \gamma_{DL}^{HD}) \Delta(D_{alt,1}^{DL}, \lambda_{g,1}, q), \quad (6.8)$$

where $\gamma_{gs}^{HD} = 2^{R_1^{HD}} - 1$ and $\gamma_{DL}^{HD} = 2^{R_{gs}^{HD}} - 1$.

6.4 Numerical Results

The outage probability of the HBD-UCS is analyzed in this section for Rician K factors of 10 dB [8, Table V], $0 \text{ dB} \leq P_t \leq 30 \text{ dB}$, $P_{i,g} = P_{g,1} = P_{j,1} = P_t$, $\sigma_g^2 = \sigma_1^2 = -131 \text{ dBm}$ [159], $R_x^{HD} = 0.1 \text{ b/s/Hz}$, $i \in \{i, gs\}$, $\gamma_\phi^2 = -140 \text{ dBm}$, $\epsilon = 0.01$ [17], $r_a = 4 \text{ km}$, $n \approx 2$ [8, Table III], $N_{UL} = 3$, $\lambda_{1,g} = 1.3$, $\lambda_{2,g} = 1.4$, $\lambda_{3,g} = 1.5$, $\beta_{j,1} = 0.5^2$, and Monte Carlo simulations using 10^5 samples.

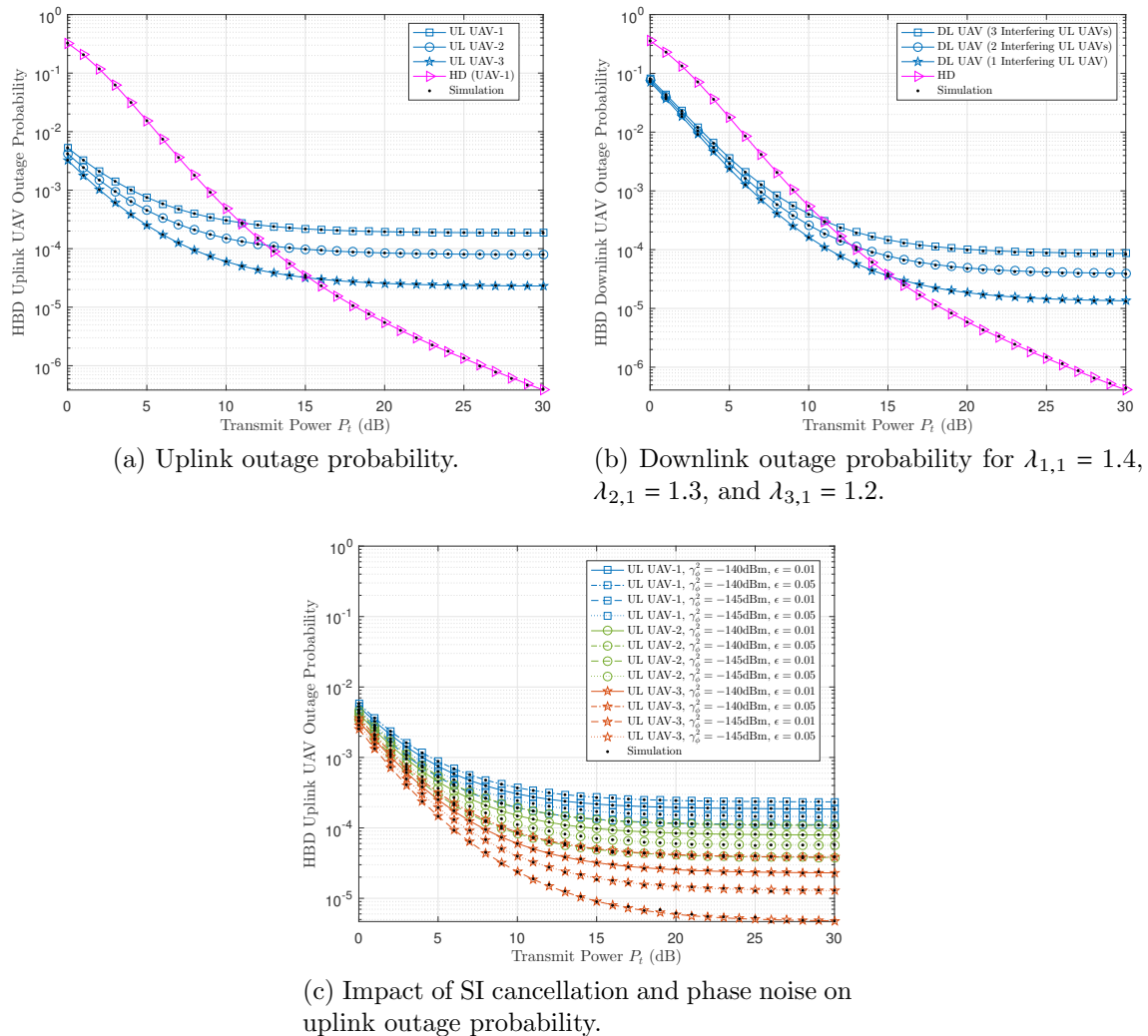


Fig. 6.2: Outage probability of the HBD-UCS.

Observation 6.4.1 *With effective SI mitigation, the HBD-UCS achieves lower outage*

probability at low P_t regimes than the HD-UCS and is able to fulfill *PER* requirements for CNPC links in LTE networks.

The outage probability of the HBD-UCS is compared against the HD-UCS for both UL and DL transmissions in Fig. 6.2. At low P_t regimes, the HBD-UCS outperforms the HD-UCS in terms of UL and DL outage probability. In particular, the HBD-UCS is able to fulfill *PER* requirements for UAV control links over Long Term Evolution (LTE) networks, i.e., $PER < 10^{-3}$ [187].⁵ Additionally, for UL transmissions, recall that the FD-GS detects UL UAV- i by treating the remaining $N_{UL} - i$ UL UAVs as interference. As such, UL UAV-1 is seen to exhibit higher outage probability than UL UAV-2 and UAV-3, with similar observations also noted for the subsequent UL UAVs. It is also seen that, depending on the number of interfering UL UAVs, the DL UAV can also attain lower DL outage probability than the HD-UCS at moderate P_t regimes, e.g., $N_{UL} \in \{2, 3\}$.

At high P_t regimes, the HD-UCS attains lower outage probability than the HBD-UCS for both UL and DL outage probability. For UL transmissions, error floors are observed since the detection process at the FD-GS becomes interference-limited due to interference from the remaining $N_{UL} - i$ UL UAVs. Similarly, for DL transmissions, error floors are observed due to the DL UAV becoming interference-limited as a result of residual SIC interference. Thus, it is shown that the HBD-UCS is well suited for multi-UAV networks since UAV communications operate at low P_t regimes.^{6,7} The impact of SI cancellation and phase noise on uplink outage probability is seen in Fig. 6.2c. It is observed that an increase in either γ_ϕ^2 or ϵ causes the outage probability of the UL UAVs to increase. Furthermore, an increasing γ_ϕ^2 causes higher outage probability than an increasing ϵ due to higher residual SI at the FD-GS. Thus, the reliability of UL UAV transmissions in an HBD-UCS hinges on having effective SI mitigation architectures with low phase noise FD transceivers at the GS.

⁵Outage probability can be used to represent *PER* if the transmitted signals span over one fading block [17].

⁶It is worth noting that UAVs largely operate at low P_t regimes due to size, weight, and power restrictions. For instance, $29\text{dBm} \leq P_t \leq 40\text{dBm}$ was noted in [159], while in [188], cellular-to-UAV links were evaluated for $P_t = 20\text{dBm}$. The values found in [159, 188] translates into $-10\text{dB} \leq P_t \leq 10\text{dB}$.

⁷Outage probability can be further reduced when the transmit power and trajectory of the UAVs are optimized iteratively. For transmit power optimization, one should consider the spatial location of the UAVs and the trajectory. For trajectory optimization, both the spiral and oval trajectory processes should be considered to maintain a uniform distribution under the BPP model [189].

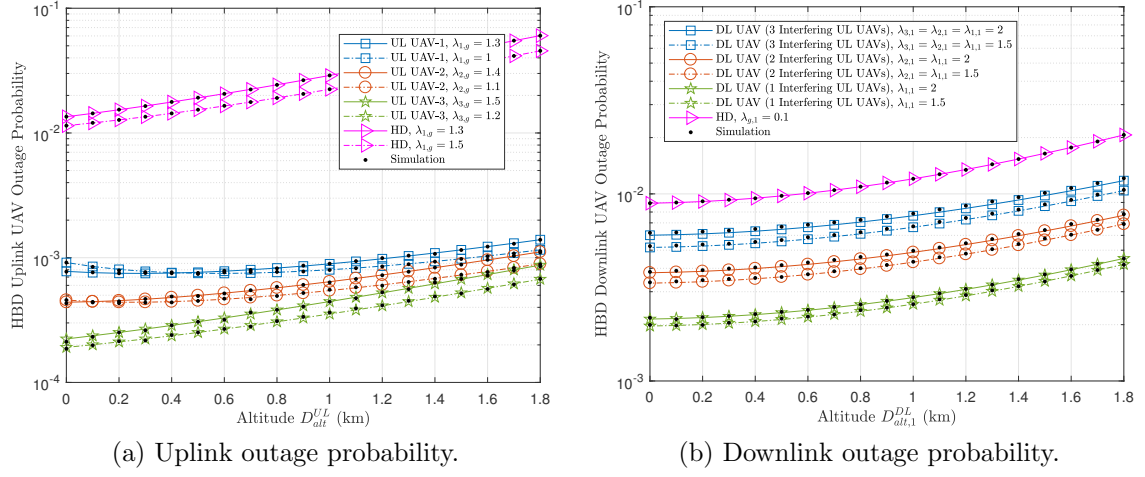


Fig. 6.3: Impact of height and minimum distance on the outage probability of the HBD-UCS at $P_t = 5$ dB, $\beta = 1$, $\lambda_{g,1} = 0.1$, and $D_{alt}^{UL} = D_{alt,i}^{UL}$.

Observation 6.4.2 *Increasing the altitude of the UAVs leads to higher outage probability for the HBD-UCS.*

In Fig. 6.3, the impact of height and minimum distance on the outage probability of the HBD-UCS is analyzed. For UL transmissions, a lower outage probability is attained when $0 \leq D_{alt}^{UL} \leq 1$ and when $\lambda_{i,g}$ is reduced, since weaker UL interference is experienced. However, when $D_{alt}^{UL} > 1$, outage probability increases due to a weaker SOI. Similarly, increasing $\lambda_{i,g}$ leads to higher outage probability as the SOI is further weakened. For DL transmissions, increasing $D_{alt,1}^{DL}$ leads to higher outage probability for the HBD-UCS and HD-UCS due to a weaker SOI. It is also observed that increasing $\lambda_{i,1}$ reduces outage probability since inter-UAV interference is weakened. Therefore, as seen in Fig. 6.3, one may have to consider other approaches if support for UAVs deployed at high altitudes is required. Nonetheless, Fig. 6.2 and Fig. 6.3 have demonstrated that the multi-UAV network with HBD-UCS is able to support more UAVs concurrently on the same spectrum while attaining a lower outage probability than the HD-UCS.

6.5 Chapter Summary

In this chapter, the outage probability analysis of a multi-UAV network with HBD-UCS is investigated within a stochastic geometry framework. It is demonstrated that at low

transmit power regimes, the HBD-UCS achieves lower outage probability than the HD-UCS for both uplink and downlink transmissions. It is also shown that the HBD-UCS can support uplink and downlink transmissions that are more reliable than the HD-UCS, when the UAV operating altitude is increased. Thus, we demonstrate that the HBD-UCS is able to concurrently support more UAVs while achieving a higher reliability than the HD-UCS.

To enable a greater number of deployed UAVs in multi-UAV networks with ease of deployment, one can consider tapping on existing cellular infrastructure to support multi-UAV communications. In this spirit, NOMA-aided multi-UAV communications is examined in the next chapter for FD heterogeneous networks.

Chapter 7

NOMA-Aided Multi-UAV Communications in Full-Duplex Heterogeneous Networks

7.1 Introduction

Apart from FD-based HBD-UCSs, one can also consider power-domain NOMA as a means to further improve spectrum efficiency in UAV communications. The concept of NOMA hinges on the fact that nodes in NOMA-aided systems are multiplexed in the power-domain to share the same spectrum. In contrast, conventional orthogonal multiple access schemes employ orthogonal allocation of time-frequency resource blocks for each node in the network. Thus, compared to orthogonal multiple access systems, NOMA-aided systems are capable of achieving higher spectrum utilization. When adopted for multi-UAV communications, superposition coding is employed to enforce unequal power allocation for all UAVs and GSs. Thereafter, the desired messages are recovered at the receivers via SIC when the interference is stronger than the desired message [87, 124, 126, 134, 135, 190, 191]. For receivers experiencing weak interference, the desired message is simply detected by treating interference as noise [124, 190].¹

Already, NOMA has been investigated as a means to improve spectrum efficiency in heterogeneous networks (HetNets) for cellular communications [136, 193] and UAV communications [194]. Although promising, the orthogonal allocation of time-frequency

¹The work in this chapter is derived from [192], which has been submitted for publication.

resources is still necessary as power-domain multiplexing is only employed during UL or DL transmissions [101, 195].

To further address spectrum scarcity, one can consider integrating NOMA-aided multi-UAV communications into FD HetNets, i.e., FD-HetNets, comprising FD-capable GSs (FD-GSs) and HD macro base stations (MBSs). In particular, implementing NOMA-aided multi-UAV communications in FD-HetNets enable UL UAVs and DL UAVs, equipped with conventional HD transceivers, to simultaneously operate on the same spectrum thanks to the operation of FD-GSs. As compared to conventional NOMA-aided HD-HetNets, where all nodes operate in HD mode, higher spectrum efficiency can be attained via NOMA-aided FD-HetNets. However, such FD-based systems are also impaired by residual SI due to carrier phase noise and imperfect SI channel estimation [21], and interference from UL UAVs [18, 19, 101].

7.1.1 Related Literature

Despite being limited by residual SI and UL interference, NOMA-aided FD-HetNets have started receiving interest in the literature as a potential solution to address spectrum scarcity. For instance, a power control technique was proposed in [196] for interference management in a NOMA-aided FD-HetNet, with similar works on NOMA-aided HD-HetNets [136, 193] noted. For UAV communications in FD-HetNets and HD-HetNets, there exists limited studies in the literature. To illustrate, resource allocation and UAV placement in HD-HetNets were investigated in [194] and [197], respectively, while [198] and [199] analyzed the placement of aerial BSs for FD-HetNets. From the above studies, an analysis of NOMA-aided multi-UAV communications in FD-HetNets is, to the best of our knowledge, unavailable in the literature. Although there exists some works on NOMA-aided FD-HetNets and NOMA-aided HD-HetNets in cellular networks, the conclusions from those studies may not be readily applied for multi-UAV communications due to differences in operating environments and deployment constraints between cellular and multi-UAV systems.

One such difference is the channel model for both cellular and UAV communications. In cellular communications, Rayleigh fading [195] and Nakagami- m fading [200, 201] are commonly assumed. However, apart from UAV communications taking place over

Rayleigh fading [202, 203] and Nakagami- m fading [112], other types of fading can also be encountered. For instance, transmissions over Rician fading channels have been noted for UAV-to-GS links [8, 18, 19, 46, 47, 101, 204, 205] and UAV-to-UAV links [18, 19, 55].

Another difference stems from the spatial distribution of nodes in cellular and UAV communications. As discussed earlier, the application of UAVs in future wireless networks has garnered intense interest in deploying UAV-aided wireless connectivity via aerial BSs or relays. Hence, the spatial location and mobility of the UAVs need to be accounted for before any accurate performance evaluation. To accomplish such a feat, one can employ the useful tools of stochastic geometry for multi-UAV networks. A common technique seen in the literature involves modeling the spatial location of UEs as a PPP. However, it has since been shown in [112] that the PPP model is unsuitable for multi-UAV networks, as the number of deployed UAVs is usually fixed. Such an instance can be illustrated when UAVs function as aerial BSs in a given region [112, 113]. In such scenarios, the homogeneous BPP can be used to provide an accurate modeling of the UAV spatial locations [112, 113]. In spite of several studies that have analyzed multi-UAV networks using the BPP model, e.g., [112, 113, 189], similar studies involving NOMA-aided multi-UAV communications in FD-HetNets are lacking in the literature.

Based on the above discussions, an ergodic capacity analysis of NOMA-aided multi-UAV communications in a FD-HetNet is conducted in this chapter. By considering Rician fading channels and the BPP model for UAV spatial location modeling, we demonstrate the feasibility and advantages of NOMA-aided multi-UAV communications in FD-HetNets in a realistic setting.

7.2 System Model

Consider a FD-HetNet supporting NOMA-aided multi-UAV communications in a suburban environment (Fig. 7.1). The FD-HetNet comprises N_U HD single-antenna UL UAVs, N_D HD single-antenna DL UAVs, one HD single-antenna MBS, and a FD-GS. The FD-GS is assumed to be operating with one antenna each for signal transmission and reception. It is also assumed that the FD-GS receives uplink data from the N_U UL UAVs and MBS-to-GS data from the MBS while concurrently transmitting DL data to the N_D DL UAVs

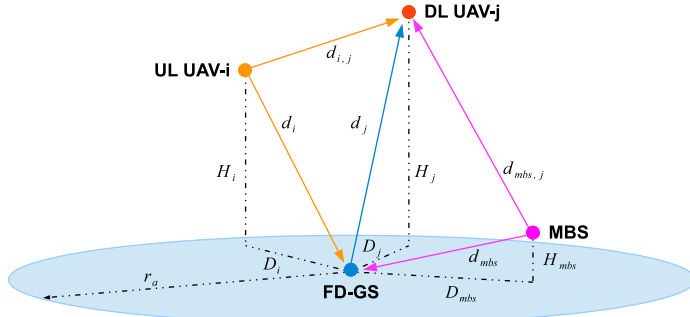


Fig. 7.1: The FD-HetNet for NOMA-aided multi-UAV communications is illustrated here. The FD-GS in the FD-HetNet enables HD uplink and downlink UAVs and the HD MBS to concurrently share the same spectrum for NOMA transmissions. Through the BPP, it is assumed that the spatial locations of the deployed UAVs and the MBS follow a uniform distribution around a disc, with origin O at the FD-GS and radius r_a .

on the same spectrum through power-domain NOMA.² Due to FD transmissions at the GS, the DL UAVs experience interference from the MBS and UL UAVs [17, 18], as well as MUI from other DL UAVs [101]. In this regard, the DL UAVs are assumed to be equipped with imperfect SIC detectors. For the FD-GS, SI mitigation is assumed and only residual SI is considered to account for FD transceiver impairments [17, 18, 20, 21]. Finally, it is assumed that the suburban UAV channel undergoes Rician fading [8], with compensated Doppler shift assumed in this chapter [17, 18]. Rician fading is also assumed for the SI channel at the FD-GS to account for SI mitigation [17, 18, 20]. A summary of important notations is given in Table 7.1.

7.2.1 Distance Distribution of the UAVs and MBS

Inspired by the studies in [20, 112, 113], the spatial locations of the UL UAVs, DL UAVs and the MBS are assumed to follow a BPP. Let the UL UAVs and DL UAVs be indexed by $1 \leq i \leq N_U$ and $1 \leq j \leq N_D$, respectively. Then, we denote $H_i = H_{\min} + \omega \frac{i}{N_U}$ and $H_j = H_{\min} + \omega \left[1 + \frac{j}{N_D}\right]$ as the respective altitudes (km) of UL UAV- i and DL UAV- j , where $\omega > 0$ indicates the altitude separation factor between the UL and DL UAVs, H_{\min} denotes a minimum altitude such that $0 < H_{mbs} < H_{\min}$, and H_{mbs} is the height of the MBS antenna.

²It is worth noting that such a system model has been studied in [198] and [199] in the context of aerial BSs.

Based on the BPP assumption, let the spatial location of the UL UAVs, DL UAVs, and MBS be uniformly distributed around a disc with origin O at the FD-GS, radius r_a , and angle $[0, 2\pi)$ [20, 112]. The Euclidean distances (km) from the FD-GS to the MBS, UL UAV- i , and DL UAV- j are denoted as d_{mbs} , d_i , and d_j , respectively. For $x \in \{i, j, mbs\}$, the Euclidean distance d_x is defined as $d_x = \sqrt{D_x^2 + H_x^2}$, where D_x is the Euclidean distance between the projection of node- x onto the ground plane and the FD-GS. Finally, the inter-UAV distance between UL UAV- i and DL UAV- j is defined as $d_{i,j}$ while the distance between the MBS and DL UAV- j is denoted as $d_{mbs,j}$.

The PDF of d_x is given as [112, eq. (3)]:

$$f_{d_x}(w_x) = \frac{2w_x}{r_a^2}, \quad (7.1)$$

where $x \in \{i, j, mbs\}$, $L_{m,x} \leq w_x \leq L_{p,x}$, $L_{m,x} = H_x$, and $L_{p,x} = \sqrt{H_x + r_a^2}$.

For the inter-UAV distance ($d_{i,j}$) and the distance between the MBS and DL UAV- j ($d_{mbs,j}$), the conditional PDF $f_{d_{x,j}}(w|d_j)$, $x \in \{i, mbs\}$ is defined as [112, eq. (2)], [20, eq. (1)]:

$$f_{d_{x,j}}(w|d_j) = \begin{cases} \frac{2w}{r_a^2}, & H_{x,j} \leq w \leq L_{q,x} \\ \frac{2w}{\pi r_a^2} \arccos \left(\frac{w^2 + d_j^2 - (r_a^2 + H_{x,j}^2)}{2d_j \sqrt{w^2 - H_{x,j}^2}} \right), & L_{q,x} < w \leq L_{r,x} \end{cases} \quad (7.2)$$

where $L_{q,x} = \sqrt{(r_a - d_j)^2 + H_{x,j}^2}$, $L_{r,x} = \sqrt{(r_a + d_j)^2 + H_{x,j}^2}$, $H_{i,j} = H_j - H_i$ is the separation altitude between UL UAV- i and DL UAV- j , and $H_{mbs,j} = H_j - H_{mbs}$ is the altitude between the MBS and DL UAV- j .

Through the PDFs, $f_{d_x}(w)$ and $f_{d_{x,j}}(w|d_j)$, a performance analysis of NOMA-aided multi-UAV communications in the FD-HetNet can be obtained with the spatial locations of the UAVs and MBS taken into consideration.

7.2.2 Instantaneous SINR at the FD-GS

To detect the messages transmitted by both the MBS and UL UAVs at the FD-GS, an SIC detection process is employed.³ In particular, the FD-GS performs SIC to detect

³By extension, it is assumed that the FD-GS has prior knowledge of the locations of the MBS and all UAVs. For the latter, such information can be obtained from flight plans approved by relevant authorities.

and remove the MBS SOI from the received composite signal. The FD-GS then detects the SOI from the UL UAVs, starting with UL UAV-1, in the presence of MUI [87, 124, 126, 134, 135]. The SIC detection process is repeated until the SOIs of all the remaining UL UAVs are detected.

Let X_{mbs} , X_i , and $Y_{si,1}$ be non-centered Chi-squared distributed RVs with respective Rician K factors K_{mbs} , K_i , and $K_{si,1}$. Also, let $Y_{si,2}$ be an exponentially distributed RV. Then, the instantaneous SINR to detect the SOI of the MBS at the FD-GS ($SINR_{mbs}^{FD}$) is:

$$SINR_{mbs}^{FD} = \frac{\rho d_{mbs}^{-n} X_{mbs}}{1 + \rho \sum_{i=1}^{N_U} d_i^{-n} X_i + \rho_{si} Y_{si,1} + \rho_{si} Y_{si,2}}, \quad (7.3)$$

where n is the pathloss exponent, $\rho \propto \frac{P_t}{G\sigma^2}$ is the normalized transmit power [17], P_t is the transmit power, $G = \left(\frac{4\pi \cdot 10^9}{3 \cdot 10^8} f_c\right)^2$, f_c is the carrier frequency (MHz), $\sigma^2 = -174 + 10 \log_{10}(B_W)$ is the strength of the AWGN in dBm [206], B_W is the bandwidth (Hz), $\rho_{si} = P_{si}/\sigma^2$ is the normalized power of the SI, $P_{si} = P_t$ denotes the received power of the SI, $X_{mbs} = |h_{mbs}|^2$, $X_i = |h_i|^2$, h_{mbs} is the channel between the FD-GS and the MBS, and h_i is the channel between the FD-GS and UL UAV- i . Also, $Y_{si,1} = \epsilon |\tilde{h}_{si}|^2$ and $Y_{si,2} = \gamma_\phi^2 |h_{si}|^2$, where $\tilde{h}_{si} = h_{si} - \hat{h}_{si}$ is the error of the imperfect SI channel gain estimate, \hat{h}_{si} is the imperfect estimation of the SI channel gain, and γ_ϕ^2 is the strength of the Gaussian distributed phase noise [21].⁴ The SI channel estimation error (\tilde{h}_{si}) is modeled as a circularly symmetric zero-mean complex Gaussian RV with variance ϵ to account for the worst case residual SI, [17, 18, 81]. In this way, the total amount of SI suppression to bring the residual SI signal below the noise floor (σ^2) is calculated as $1/(\epsilon\sigma^2)$ [17].

Similarly, the instantaneous SINR to detect the SOI of the UL UAVs at the FD-GS ($SINR_i^{FD}$) is:

$$SINR_i^{FD} = \frac{\rho d_i^{-n} X_i}{1 + \sum_{k=i+1}^{N_U} \rho d_k^{-n} Y_k + \rho_{si} Y_{si,1} + \rho_{si} Y_{si,2}}, \quad (7.4)$$

where $Y_k = |h_k|^2$ is a non-centered Chi-squared distributed RV with Rician K factor K_k , and h_k is the channel between the FD-GS and the remaining UL UAVs.

⁴The phase noise term γ_ϕ reflects the jitter effect in oscillators due to hardware imperfections [21].

Table 7.1: Summary of Important Notations

Notations	Description
$1 \leq i \leq N_U$	Index of UL UAV- i
$1 \leq j \leq N_D$	Index of DL UAV- j
$H_{min}; \omega$	Minimum UAV altitude; Altitude separation factor
$H_i; H_j$	Altitude of UL UAV- i ; Altitude of DL UAV- j
H_{mbs}	MBS antenna height
$H_{i,j}$	Altitude between UL UAV- i and DL UAV- j
$H_{mbs,j}$	Altitude between the MBS and DL UAV- j
d_{mbs}	Euclidean distance between the FD-GS and the MBS
d_i	Euclidean distance between the FD-GS and UL UAV- i
d_j	Euclidean distance between the FD-GS and DL UAV- j
$d_{mbs,j}$	Euclidean distance between the MBS and DL UAV- j
$d_{i,j}$	Euclidean distance between UL UAV- i and DL UAV- j
$P_t; \rho$	Transmit power; Normalized transmit power
$P_{si}; \rho_{si}$	Received power of the SI; Normalized SI power
σ^2	Strength of AWGN
ϵ	SI channel estimation error at the FD-GS
γ_ϕ^2	Strength of phase noise at the FD-GS oscillator
$\beta_{mbs,j}$	Residual interference from the MBS at DL UAV- j
$\beta_{i,j}$	Residual interference from UL UAV- i at DL UAV- j
α_j	NOMA power allocation factor for DL UAV- j

7.2.3 Instantaneous SINR at Downlink UAV- j

At DL UAV- j , an SIC detector is employed to detect the SOI transmitted by the FD-GS. In particular, the SIC detector at DL UAV- j detects the SOI in the presence of MUI from the other DL UAVs, as well as interference from both the UL UAVs and MBS.⁵

Let X_j , $Y_{mbs,j}$, and $Y_{i,j}$ be non-centered Chi-squared distributed random variables RVs with respective Rician K factors K_i , $K_{mbs,j}$, and $K_{i,j}$. Then, the instantaneous SINR $(SINR_j^{FD})$ at DL UAV- j is:

$$SINR_j^{FD} = \frac{\rho \alpha_j d_j^{-n} X_j}{1 + \rho d_{mbs,j}^{-n} Y_{mbs,j} + \rho d_j^{-n} X_j \sum_{k=1}^{j-1} \alpha_k + \rho \sum_{i=1}^{N_U} d_{i,j}^{-n} Y_{i,j}}, \quad (7.5)$$

where $X_j = |h_j|^2$, $Y_{mbs,j} = \beta_{mbs,j} |h_{mbs,j}|^2$, $Y_{i,j} = \beta_{i,j} |h_{i,j}|^2$, h_j is the channel between the FD-GS and DL UAV- j , $h_{mbs,j}$ is the channel between the MBS and DL UAV- j , $h_{i,j}$ is the channel between UL UAV- i and DL UAV- j , and α_j is the power allocation factor for DL UAV- j such that $\sum_{j=1}^{N_D} \alpha_j = 1$. Also, $0 \leq \beta_{x,j} \leq 1, x \in \{mbs, i\}$ is the strength of the residual interference after SIC [83, 126, 137, 207].

⁵Similar to the FD-GS, it is assumed that all DL UAVs have prior knowledge of the locations of the FD-GS, MBS and surrounding UAVs.

As the DL UAVs are deployed at different altitudes, i.e., $H_j < H_{j+1}$, the power allocation factor α_j can be heuristically defined based on the altitudes of the N_D DL UAVs to ensure fairness. In particular, the power allocation factor α_j can be defined as:

$$\alpha_j = \frac{H_j}{\sum_{k=1}^{N_U} H_k}, \quad (7.6)$$

so that DL UAVs that are further away from the FD-GS are assigned higher transmit powers [136], i.e., $\alpha_j < \alpha_{j+1}$. In this way, DL UAV- j recovers the SOI by performing SIC to remove MUI from DL UAV- m for $m > j$, while ignoring MUI from DL UAV- k for $k < j$ [124, 135].

7.3 Ergodic Capacity Derivations

In this section, ergodic capacity expressions are presented for NOMA-aided multi-UAV communications in the FD-HetNet. The UL and DL ergodic capacity expressions for NOMA-aided multi-UAV communications in a HD-HetNet are also presented as a benchmark.

The ergodic capacity expressions presented in this section are derived based on the work in [208, Lemma 1], where a technique was proposed that enables the ergodic capacity calculation of instantaneous SINRs with both uncorrelated and correlated RVs. The present approach extends this method to evaluate the ergodic capacities of multi-UAV communications in FD-HetNets and HD-HetNets within a stochastic geometry framework.

7.3.1 Ergodic Capacity of the MBS in the NOMA-Aided FD-HetNet

The MBS ergodic capacity is defined as $C_{mbs}^{FD} = E \left\{ \ln \left(1 + SINR_{mbs}^{FD} \right) \right\}$, where $E\{\bullet\}$ denotes the statistical expectation operator. To evaluate C_{mbs}^{FD} , one has to employ calculations involving $(2N_U + 4)$ -fold numerical integrations to average the PDFs of the associated RVs in $SINR_{mbs}^{FD}$. To avoid such highly intensive computations, one can instead invoke the method proposed in [208] that enables a simple evaluation of ergodic capacity.

In the next theorem, we present an exact expression for C_{mbs}^{FD} obtained using the technique in [208].

Theorem 7.1 *The ergodic capacity of the MBS in the FD-HetNet is:*

$$\begin{aligned} C_{mbs}^{FD} = & \int_{L_{m,mbs}}^{L_{p,mbs}} \int_0^\infty \frac{\exp(-z)}{z} \left(1 - M_{X_{mbs}}(z\rho w_{mbs}^{-n}) \right) \\ & \times \left(\prod_{i=1}^{N_U} \tau_i(z\rho) \right) M_{Y_{si,1}}(z\rho s_i) M_{Y_{si,2}}(z\rho s_i) f_{d_{mbs}}(w_{mbs}) dz dw_{mbs}, \end{aligned} \quad (7.7)$$

where $M_X(z)$ is the moment generating function (MGF) of the non-centered Chi-squared distributed RV X , with Rician K factor K_X , which is given as [89, Table. I]:

$$M_X(z) = \frac{1 + K_X}{1 + K_X + z} \exp\left(\frac{-K_X z}{1 + K_X + z}\right), \quad (7.8)$$

and the function $\tau_i(z\rho)$ is defined as:

$$\tau_i(z\rho) = \int_{L_{m,i}}^{L_{p,i}} M_{X_i}(z\rho w_i^{-n}) f_{d_i}(w_i) dw_i, \quad (7.9)$$

which averages the MGF $M_{Y_i}(z\rho w_i^{-n})$ of interfering UL UAV- i with the PDF $f_{d_i}(w_i)$.

Proof: The proof is provided in Appendix E.1.

The expression in (7.7) enables C_{mbs}^{FD} to be evaluated at finite P_t , i.e., ρ , regimes, in the presence of receiver noise and interference, using $(N_U + 2)$ -fold numerical integration. In contrast, a direct evaluation of C_{mbs}^{FD} will require $(2N_U + 4)$ -fold numerical integrations.

From (7.7), it is noted that C_{mbs}^{FD} is largely limited by the number of interfering UL UAVs (N_U) and the strength of the residual SI, i.e., ϵ and γ_ϕ^2 . Thus, the ergodic capacity of the MBS at asymptotic P_t regimes, i.e., $C_{mbs,\infty}^{FD}$, can be obtained from (7.7) as shown in the following corollary.

Corollary 7.1 *The asymptotic ergodic capacity of the MBS in the FD-HetNet is:*

$$\begin{aligned} C_{mbs,\infty}^{FD} = & \int_{L_{m,mbs}}^{L_{p,mbs}} \int_0^\infty \frac{1}{z} \left(1 - M_{X_{mbs}}(z w_{mbs}^{-n}) \right) \left(\prod_{i=1}^{N_U} \tau_i(z) \right) \\ & \times M_{Y_{si,1}}(z) M_{Y_{si,2}}(z) f_{d_{mbs}}(w_{mbs}) dz dw_{mbs}. \end{aligned} \quad (7.10)$$

Proof: At asymptotic P_t regimes, $SINR_{mbs}^{FD}$ in (7.3) reduces to the following instantaneous signal-to-interference ratio (SIR), i.e., SIR_{mbs}^{FD} :

$$SIR_{mbs}^{FD} = \frac{d_{mbs}^{-n} X_{mbs}}{\sum_{i=1}^{N_U} d_i^{-n} X_i + Y_{si,1} + Y_{si,2}}. \quad (7.11)$$

Then, evaluating $C_{mbs,\infty}^{FD} = E\left\{\ln\left(1 + SIR_{mbs}^{FD}\right)\right\}$ using the same steps in Appendix E.1 yields (7.10). This completes the proof.

From (7.10), the impact of interference from the UL UAVs can be analyzed within a stochastic geometry framework. Similar to (7.7), (7.10) is also influenced by the residual SI at the FD-GS and the number of interfering UL UAVs. Furthermore, scenarios where the detection of the SOI from the MBS is interference-limited can now be identified using (7.10).

7.3.2 Ergodic Capacity of UL UAV- i in the NOMA-Aided FD-HetNet

The ergodic capacity for UL UAV- i is defined as $C_i^{FD} = E\left\{\ln\left(1 + SINR_i^{FD}\right)\right\}$. As a direct evaluation of C_i^{FD} requires $(2N_U - 2i + 4)$ -fold numerical integrations, we present an exact expression for C_i^{FD} based on the technique in [208] in the next theorem.

Theorem 7.2 *The ergodic capacity of UL UAV- i in the FD-HetNet is:*

$$\begin{aligned} C_i^{FD} = & \int_{L_{m,i}}^{L_{p,i}} \int_0^\infty \frac{\exp(-z)}{z} \left(1 - M_{X_i}(z\rho w_i^{-n})\right) \\ & \times \left(\prod_{k=i+1}^{N_U} \tau_k(z\rho)\right) M_{Y_{si,1}}(z\rho s_i) M_{Y_{si,2}}(z\rho s_i) f_{d_i}(w_i) dz dw_i. \end{aligned} \quad (7.12)$$

Proof: Applying the same technique in Appendix E.1 yields (7.12), which completes the proof.

Similar to (7.7), (7.12) enables the ergodic capacity of UL UAV- i to be evaluated at finite P_t regimes in the presence of receiver noise and interference. Furthermore, (7.12) is simpler to compute, requiring $(N_U - i + 2)$ -fold numerical integrations compared to $(2N_U - 2i + 4)$ -fold numerical integrations using direct evaluation.

From (7.12), C_i^{FD} is limited by both the remaining number of interfering UL UAVs (B_U) and also the strength of residual SI, i.e., ϵ and γ_ϕ^2 . However, as $i \rightarrow N_U$, (7.12) becomes SI-limited due to a diminishing number of interfering UL UAVs. As P_t increases, the asymptotic ergodic capacity of UL UAV- i , i.e., $C_{i,\infty}^{FD}$, can be obtained from (7.12) as shown in the next corollary.

Corollary 7.2 *The asymptotic ergodic capacity of UL UAV- i in the FD-HetNet is:*

$$\begin{aligned} C_{i,\infty}^{FD} = & \int_{L_{m,i}}^{L_{p,i}} \int_0^\infty \frac{1}{z} \left(1 - M_{X_i}(zw_i^{-n}) \right) \left(\prod_{k=i+1}^{N_U} \tau_k(z) \right) \\ & \times M_{Y_{si,1}}(z) M_{Y_{si,2}}(z) f_{d_i}(w_i) dz dw_i. \end{aligned} \quad (7.13)$$

Proof: As P_t increases, $SINR_i^{FD}$ in (7.4) simplifies into the following instantaneous SIR (SIR_i^{FD}) expression:

$$SIR_i^{FD} = \frac{d_i^{-n} X_i}{\sum_{k=i+1}^{N_U} d_k^{-n} Y_k + Y_{si,1} + Y_{si,2}}, \quad (7.14)$$

Then, (7.13) is obtained by evaluating $C_{i,\infty}^{FD} = E \left\{ \ln \left(1 + SIR_i^{FD} \right) \right\}$ using the same steps in Appendix E.1. This completes the proof.

It can be seen from (7.13) that, apart from residual SI at the FD-GS, interference from the remaining $N_U - i$ UL UAVs can significantly affect the asymptotic ergodic capacity of UL UAV- i when N_U is large. Therefore, (7.13) can be used to identify a suitable value of N_U when asymptotic ergodic capacity requirements must be satisfied for all UL UAVs.

7.3.3 Ergodic Capacity of DL UAV- j in the NOMA-Aided FD-HetNet

The ergodic capacity of DL UAV- j is defined as $C_j^{FD} = E \left\{ \ln \left(1 + SINR_j^{FD} \right) \right\}$, which requires $(2+2N_U+2j)$ -fold numerical integrations in direct computations. In the following theorem, we invoke the approach in [208] to present an exact expression for C_i^{FD} .

Theorem 7.3 *The ergodic capacity of DL UAV- j in the FD-HetNet is:*

$$\begin{aligned} C_j^{FD} = & \int_{L_{m,j}}^{L_{p,j}} \int_0^\infty \frac{\exp(-z)}{z} \left[M_{X_j} \left(z\rho w_j^{-n} \sum_{k=1}^{j-1} \alpha_k \right) - M_{X_j} \left(z\rho w_j^{-n} \sum_{k=1}^j \alpha_k \right) \right] \\ & \times \mu_{mbs,j}(z\rho) \left(\prod_{i=1}^{N_U} \mu_{i,j}(z\rho) \right) f_{d_j}(w_j) dz dw_j, \end{aligned} \quad (7.15)$$

where the function $\mu_{x,j}(z\rho), x \in \{mbs, i\}$ is defined as:

$$\begin{aligned} \mu_{x,j}(z\rho) = & \int_{H_{x,j}}^{L_{q,x}} M_{Y_{x,j}}(z\rho w_{x,j}^{-n}) f_{d_{x,j}}(w_{x,j}|w_j) dw_{x,j} \\ & + \int_{L_{q,x}}^{L_{r,x}} M_{Y_{x,j}}(z\rho w_{x,j}^{-n}) f_{d_{x,j}}(w_{x,j}|w_j) dw_{x,j}, \end{aligned} \quad (7.16)$$

which averages the MGFs of the interfering MBS and UL UAVs ,i.e., $M_{Y_{mbs,j}}(z\rho w_{mbs,j}^{-n})$ and $M_{Y_{i,j}}(z\rho w_{i,j}^{-n})$, over the respective distance PDFs, i.e., $f_{d_{mbs,j}}(w_{mbs,j}|w_j)$ and $f_{d_{i,j}}(w_{i,j}|w_j)$.

Proof: The proof is given in Appendix E.2.

The expression in (7.15) enables a simpler evaluation of the ergodic capacity for DL UAV- j at finite P_t regimes by using $(3 + N_U)$ -fold numerical integrations. Also, (7.15) shows that C_j^{FD} is limited by the number of interfering UL UAVs (N_U) and the strength of the residual interference ($\beta_{x,j}, x \in \{mbs, i\}$). The height of DL UAV- j also influences the strength of the SOI in C_j^{FD} due to the term $M_{X_j}(z\rho w_j^{-n} \sum_{k=1}^{j-1} \alpha_k) - M_{X_j}(z\rho w_j^{-n} \sum_{k=1}^j \alpha_k)$ in (7.15). To see this, recall that the power allocation of DL UAV- j (α_j) is determined based on altitude (H_j). Thus, DL UAVs at lower altitudes can remove more MUI than the other DL UAVs at higher altitude, as embodied by $M_{X_j}(z\rho w_j^{-n} \sum_{k=1}^{j-1} \alpha_k) - M_{X_j}(z\rho w_j^{-n} \sum_{k=1}^j \alpha_k)$.

From (7.15), it is useful to note that under effective SIC, i.e., $\beta_{x,j} \rightarrow 0, x \in \{mbs, i\}$, the impact of interference on C_j^{FD} in (7.15) is negligible for DL UAV-1. However, for $j > 1$ and $N_D > 1$, C_j^{FD} is limited by interference from the remaining $j - 1$ DL UAVs as $P_t \rightarrow \infty$. Under such circumstances, the asymptotic ergodic capacity of DL UAV- j ($C_{j,\infty}^{FD}$), can be obtained from (7.15) as shown in the next corollary.

Corollary 7.3 *The asymptotic ergodic capacity of DL UAV- j , for $j > 1$ and $N_D > 1$, in the FD-HetNet is:*

$$C_{j,\infty}^{FD} = \int_{L_{m,j}}^{L_{p,j}} \int_0^\infty \frac{\exp(-z)}{z} \left[M_{X_j}\left(zw_j^{-n} \sum_{k=1}^{j-1} \alpha_k\right) - M_{X_j}\left(zw_j^{-n} \sum_{k=1}^j \alpha_k\right) \right] f_{d_j}(w_j) dz dw_j, \quad (7.17)$$

Proof: When $\beta_{x,j} \rightarrow 0, x \in \{mbs, i\}$, $j > 1$, $N_D > 1$ and $P_t \rightarrow \infty$, $SINR_j^{FD}$ in (7.5) can be simplified into the following instantaneous SIR (SIR_j^{FD}) expression:

$$SIR_j^{FD} = \frac{\alpha_j d_j^{-n} X_j}{d_j^{-n} X_j \sum_{k=1}^{j-1} \alpha_k} \quad (7.18)$$

Next, (7.17) is obtained by evaluating $C_{j,\infty}^{FD} = E\left\{ \ln\left(1 + SIR_j^{FD}\right) \right\}$ using the same steps in Appendix E.2. This completes the proof.

The expression in (7.17) indicates that the quality of NOMA-aided transmissions in the FD-HetNet depends on the quality of the imperfect SIC and strength of the interference from the MBS and UL UAVs. As such, (7.17) can be used to study tradeoffs between supporting more UL UAVs on the same spectrum and meeting ergodic capacity requirements.

7.3.4 Ergodic Capacity of the NOMA-aided HD-HetNet

In NOMA-aided HD-HetNets, SI is not present as the GS operates in HD mode. As such, the instantaneous SINRs of the MBS ($SINR_{mbs}^{HD}$), UL UAVs ($SINR_i^{HD}$), and DL UAVs ($SINR_j^{HD}$) are defined as $SINR_{mbs}^{HD} = \frac{\rho d_{mbs}^{-n} X_{mbs}}{1+\rho \sum_{i=1}^{N_U} d_i^{-n} X_i}$, $SINR_i^{HD} = \frac{\rho d_i^{-n} X_i}{1+\sum_{k=i+1}^{N_U} \rho d_k^{-n} Y_k}$, and $SINR_j^{HD} = \frac{\rho \alpha_j d_j^{-n} X_j}{1+\rho d_j^{-n} X_j \sum_{k=1}^{j-1} \alpha_k}$, respectively.

Then, the ergodic capacity of the MBS, UL UAV- i , and DL UAV- j as respectively defined as $C_{mbs}^{HD} = E\left\{\frac{1}{2} \ln\left(1 + SINR_{mbs}^{HD}\right)\right\}$, $C_i^{HD} = E\left\{\frac{1}{2} \ln\left(1 + SINR_i^{HD}\right)\right\}$, and $C_j^{HD} = E\left\{\frac{1}{2} \ln\left(1 + SINR_j^{HD}\right)\right\}$. In the following theorem, exact expressions are presented for C_{mbs}^{HD} , C_i^{HD} , and C_j^{HD} .

Theorem 7.4 *The ergodic capacity of the MBS, UL UAV- i , and DL UAV- j in the HD-HetNet are given in (7.19), (7.20), and (7.21), respectively.*

$$C_{mbs}^{HD} = \frac{1}{2} \int_{L_{m,mbs}}^{L_{p,mbs}} \int_0^\infty \frac{\exp(-z)}{z} \left(1 - M_{X_{mbs}}(z\rho w_{mbs}^{-n})\right) \left(\prod_{i=1}^{N_U} \tau_i(z\rho)\right) \times f_{d_{mbs}}(w_{mbs}) dz dw_{mbs}, \quad (7.19)$$

$$C_i^{HD} = \frac{1}{2} \int_{L_{m,i}}^{L_{p,i}} \int_0^\infty \frac{\exp(-z)}{z} \left(1 - M_{X_i}(z\rho w_i^{-n})\right) \left(\prod_{k=i+1}^{N_U} \tau_k(z\rho)\right) f_{d_i}(w_i) dz dw_i, \quad (7.20)$$

$$C_j^{HD} = \frac{1}{2} \int_{L_{m,j}}^{L_{p,j}} \int_0^\infty \frac{\exp(-z)}{z} \left[M_{X_j}\left(z\rho w_j^{-n} \sum_{k=1}^{j-1} \alpha_k\right) - M_{X_j}\left(z\rho w_j^{-n} \sum_{k=1}^j \alpha_k\right)\right] \times f_{d_j}(w_j) dz dw_j. \quad (7.21)$$

Proof: The expressions for (7.19) and (7.20) are obtained using the same steps in Appendix E.1 while (7.21) is obtained using the same method in Appendix E.2. This completes the proof.

From Theorem 7.4, the ergodic capacity of the MBS and UL UAV- i , $1 \leq i \leq N_U - 1$ are interference-limited at high P_t regimes due to the presence of interference from other UL UAVs. Likewise, the ergodic capacity of DL UAV- j when $j > 1$ is also interference-limited at high P_t regimes due to MUI from the DL UAVs. To this end, we present the asymptotic ergodic capacity of the MBS ($C_{mbs,\infty}^{HD}$), UL UAV- i ($C_{i,\infty}^{HD}$), and DL UAV- j ($C_{j,\infty}^{HD}$) using (7.19), (7.20), and (7.21), respectively, as shown in the following corollary.

Corollary 7.4 *The asymptotic ergodic capacity of the MBS, UL UAV- i , and DL UAV- j in the HD-HetNet are given in (7.22), (7.23), and (7.24), respectively, for $i \leq N_U - 1$ and $j > 1$.*

$$C_{mbs,\infty}^{HD} = \frac{1}{2} \int_{L_{m,mbs}}^{L_{p,mbs}} \int_0^{\infty} \frac{1}{z} \left(1 - M_{X_{mbs}}(zw_{mbs}^{-n}) \right) \left(\prod_{i=1}^{N_U} \tau_i(z) \right) \times f_{d_{mbs}}(w_{mbs}) dz dw_{mbs}, \quad (7.22)$$

$$C_{i,\infty}^{HD} = \frac{1}{2} \int_{L_{m,i}}^{L_{p,i}} \int_0^{\infty} \frac{1}{z} \left(1 - M_{X_i}(zw_i^{-n}) \right) \left(\prod_{k=i+1}^{N_U} \tau_k(z) \right) f_{d_i}(w_i) dz dw_i, \quad (7.23)$$

$$C_{j,\infty}^{HD} = \frac{1}{2} \int_{L_{m,j}}^{L_{p,j}} \int_0^{\infty} \frac{\exp(-z)}{z} \left[M_{X_j}\left(zw_j^{-n} \sum_{k=1}^{j-1} \alpha_k\right) - M_{X_j}\left(zw_j^{-n} \sum_{k=1}^j \alpha_k\right) \right] \times f_{d_j}(w_j) dz dw_j. \quad (7.24)$$

Proof: The expressions in (7.22), (7.23), and (7.24) are obtained through the same techniques seen in Corollaries 7.1, 7.2, and 7.3, respectively. This completes the proof.

Unlike in FD-HetNets, UL and DL transmissions in HD-HetNets cannot concurrently occur on the same spectrum as separate spectrum bands or timeslots, i.e., time-frequency resource blocks, are required. To account for the orthogonality of time-frequency resource blocks in HD-HetNets, a factor of $\frac{1}{2}$ is introduced in (7.22), (7.23) and (7.24). Doing so enables a fair comparison between HD-HetNets and FD-HetNets.

7.3.5 Ergodic Capacity Gains of NOMA-aided FD-HetNets over HD-HetNets

Although HD-HetNets inherently experience less interference than FD-HetNets, a much higher throughput can still be achieved by the latter. In particular, ergodic capacity gains can be achieved FD-HetNets with effective interference management and also through the higher number of UAVs that can be concurrently supported on the same spectrum.

To this end, quantifying the ergodic capacity gain of NOMA-aided multi-UAV communications in FD-HetNets over HD-HetNets is of practical significance for system designers. Let the ergodic capacity gain of the MBS, UL UAV- i , and DL UAV- j be defined as $\Delta_{mbs} = C_{mbs}^{FD} - C_{mbs}^{HD}$, $\Delta_i = C_i^{FD} - C_i^{HD}$, and $\Delta_j = C_j^{FD} - C_j^{HD}$, respectively. Then, from Theorems 7.1, 7.2, 7.3, and 7.4, we present exact expressions for $\Delta_x, x \in \{mbs, i, j\}$ in the next corollary.

Corollary 7.5 *The ergodic capacity gains of the MBS, UL UAV- i , and DL UAV- j in the FD-HetNet over the HD-HetNet are given in (7.25), (7.26), and (7.27), respectively.*

$$\begin{aligned} \Delta_{mbs} &= \int_{L_{m,mbs}}^{L_{p,mbs}} \int_0^\infty \frac{\exp(-z)}{z} \left(1 - M_{X_{mbs}}(z\rho w_{mbs}^{-n}) \right) \\ &\quad \times \left(\prod_{i=1}^{N_U} \tau_i(z\rho) \right) \left(M_{Y_{si,1}}(z\rho_{si}) M_{Y_{si,2}}(z\rho_{si}) - \frac{1}{2} \right) f_{d_{mbs}}(w_{mbs}) dz dw_{mbs}, \end{aligned} \quad (7.25)$$

$$\begin{aligned} \Delta_i &= \int_{L_{m,i}}^{L_{p,i}} \int_0^\infty \frac{\exp(-z)}{z} \left(1 - M_{X_i}(z\rho w_i^{-n}) \right) \\ &\quad \times \left(\prod_{k=i+1}^{N_U} \tau_k(z\rho) \right) \left(M_{Y_{si,1}}(z\rho_{si}) M_{Y_{si,2}}(z\rho_{si}) - \frac{1}{2} \right) f_{d_i}(w_i) dz dw_{im}, \end{aligned} \quad (7.26)$$

$$\begin{aligned} \Delta_j &= \int_{L_{m,j}}^{L_{p,j}} \int_0^\infty \frac{\exp(-z)}{z} \left[M_{X_j}\left(z\rho w_j^{-n} \sum_{k=1}^{j-1} \alpha_k\right) - M_{X_j}\left(z\rho w_j^{-n} \sum_{k=1}^j \alpha_k\right) \right] \\ &\quad \times \left(\mu_{mbs,j}(z\rho) \left(\prod_{i=1}^{N_U} \mu_{i,j}(z\rho) \right) - \frac{1}{2} \right) f_{d_j}(w_j) dz dw_j. \end{aligned} \quad (7.27)$$

Proof: The proof is provided in Appendix E.3.

The ergodic capacity gain expressions given in (7.25), (7.26), and (7.27) can be used to determine scenarios where the FD-HetNet is able to achieve higher ergodic capacity than the HD-HetNet. In particular, $\Delta_x < 0, x \in \{mbs, i, j\}$ indicates that node x in the FD-HetNet achieves lower ergodic capacity than the HD-HetNet. Similarly, $\Delta_x > 0, x \in \{mbs, i, j\}$ indicates that node x achieves a higher ergodic capacity in the FD-HetNet than the HD-HetNet.

It is also worth emphasizing that $\Delta_x, x \in \{mbs, i, j\}$ can be used to provide system design guidelines. For instance, Δ_{mbs} and Δ_i can be negative due to the term $M_{Y_{si,1}}(z\rho_{si}) M_{Y_{si,2}}(z\rho_{si}) - \frac{1}{2}$ in (7.25) and (7.26), respectively. To illustrate this, it can be seen that increasing SI channel estimation errors (ϵ), i.e., reducing SI cancellation, or phase noise (γ_ϕ^2) leads to $M_{Y_{si,1}}(z\rho_{si}) M_{Y_{si,2}}(z\rho_{si}) \rightarrow 0$. Likewise, Δ_j can also be negative due to the term $\mu_{mbs,j}(z\rho) [\prod_{i=1}^{N_U} \mu_{i,j}(z\rho)] - \frac{1}{2}$ in (7.27). Specifically, it is noted that $\mu_{mbs,j}(z\rho) [\prod_{i=1}^{N_U} \mu_{i,j}(z\rho)] \rightarrow 0$ as residual interference ($\beta_{x,j}, x \in \{mbs, i\}$) increases. Therefore, the expressions given in (7.25), (7.26), and (7.27) can be used to identify crucial system parameters, e.g., transmit power (P_t), SI channel estimation error (ϵ) or

Table 7.2: Simulation Parameters

Parameter	Value
Number of UAVs	$N_U \in \{3, 4, 5, 6\}, N_D \in \{3, 4, 5, 6\}$ [113, 187]
Rician K Factors	10 dB [8, Table V]
Transmit Power	$0 \text{ dBm} \leq P_t \leq 30 \text{ dBm}$ [187]
Carrier Frequency	$f_c = 2 \text{ GHz}$ [187]
Bandwidth	$B_W = 20 \text{ MHz}$ [187]
Phase Noise	$\gamma_\phi^2 \in \{-130 \text{ dBm}, -140 \text{ dBm}\}$ [17, 18, 20]
SI Channel Estimation Error	$\epsilon \in \{0.5, 0.1, 0.01\}$ [17, 18, 20]
Radius	$r_a = 10 \text{ km}$ [206]
MBS Antenna Height	$H_{mbs} = 0.03 \text{ km}$ [187]
Minimum UAV Altitude	$H_{min} \in \{0.1, 1\} \text{ km}$ [187]
Altitude Separation Factor	$\omega \in \{0.1, 1\}$
Residual Interference	$\beta_{mbs,j}, \beta_{i,j} \in \{0, (0.04)^3, (0.07)^3\}$ [126]
Pathloss Exponent	$n = 2$ [8, Table III], [204]

bandwidth (B_W), that enables the FD-HetNet an advantageous ergodic capacity gain over HD-HetNets while meeting operational constraints.

7.4 Numerical Results

Numerical results pertaining to the ergodic capacity and ergodic sum capacity of NOMA-aided multi-UAV communications in the FD-HetNet and HD-HetNet are presented in this section. For the FD-HetNet and HD-HetNet, the ergodic sum capacity is defined as $C_{sum}^{FD} = C_{mbs}^{FD} + \sum_{i=1}^{N_U} C_i^{FD} + \sum_{j=1}^{N_D} C_j^{FD}$ and $C_{sum}^{HD} = C_{mbs}^{HD} + \sum_{i=1}^{N_U} C_i^{HD} + \sum_{j=1}^{N_D} C_j^{HD}$, respectively. Likewise, ergodic sum capacity gain for UL and DL transmissions are defined as $\Delta_{UL} = \Delta_{mbs} + \sum_{i=1}^{N_U} \Delta_i$ and $\Delta_{DL} = \sum_{j=1}^{N_D} \Delta_j$, respectively. We also present Monte Carlo simulation results conducted with 10^5 samples, using simulation parameters that are provided in Table 7.2.

7.4.1 Ergodic Capacity at the FD-GS and DL UAVs

Observation 7.4.1.1 *The MBS, UL UAVs, and DL UAVs deployed in the FD-HetNet attain higher ergodic capacity than the HD-HetNet.*

The ergodic capacity at the FD-GS is plotted in Fig. 7.2a for the MBS (C_{mbs}^{FD}) and UL UAV- i (C_i^{FD}). Likewise, the ergodic capacity at the DL UAVs (C_j^{FD}) is plotted in Fig. 7.2b. As a benchmark, the ergodic capacities of the MBS (C_{mbs}^{HD}), UL UAV- i (C_i^{HD}), and DL UAV- j (C_j^{HD}) are plotted for the NOMA-aided HD-HetNet.

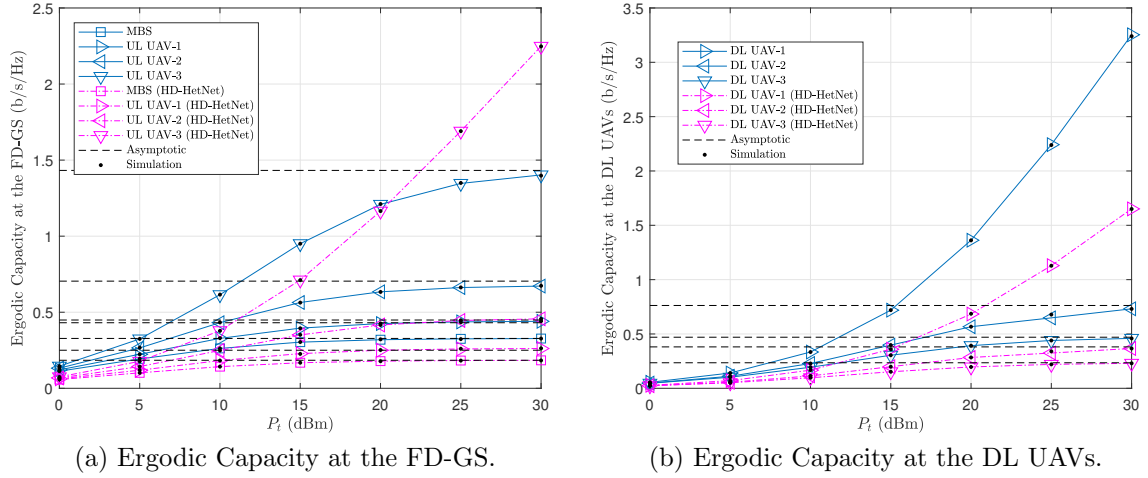


Fig. 7.2: Ergodic capacity comparison at the FD-GS and DL UAVs in the NOMA-aided FD-HetNet for $N_U = N_D = 3$, $H_{min} = 0.1$ km, $\omega = 0.1$, $\gamma_\phi^2 = -130$ dBm, $\epsilon = 0.01$, and $\beta_{mbs,j} = \beta_{i,j} = (0.04)^3$.

Despite the FD-GS experiencing residual SI and MUI from the UL UAVs, it is observed from Fig. 7.2a that $C_{mbs}^{FD} > C_{mbs}^{HD}$ and $C_i^{FD} > C_i^{HD}, i \in \{1, 2\}$ for $0 \text{ dBm} \leq P_t \leq 30 \text{ dBm}$. Moreover, Corollaries 7.1 and 7.2 are confirmed, since $C_{mbs}^{FD} \approx C_{mbs,\infty}^{FD}$ and $C_i^{FD} \approx C_{i,\infty}^{FD}$ at high P_t regimes. For the case of UL UAV-3, strong residual SI at the FD-GS is experienced at high P_t regimes, leading to $C_3^{FD} < C_3^{HD}$.

In Fig. 7.2b, it is observed that $C_j^{FD} > C_j^{HD}$ for $0 \text{ dBm} \leq P_t \leq 30 \text{ dBm}$. Furthermore, at high P_t regimes, Corollary 7.3 is confirmed since $C_j^{FD} \approx C_{j,\infty}^{FD}, j \in \{2, 3\}$. Specifically, it is observed that $C_j^{FD}, j \in \{2, 3\}$ begins to plateau. Such a trend is due to the fact that the instantaneous SINR at DL UAV- j , $j \in \{2, 3\}$, i.e., $SINR_j^{FD}$ becomes largely limited by MUI from the preceding $j - 1$ DL UAVs, which cannot be canceled due to the nature of the SIC ordering.

From Fig. 7.2, it is demonstrated that having the GS operate in FD mode, i.e., FD-HetNet, enables higher ergodic capacity over the HD-GS to be attained for the MBS, UL UAVs, and DL UAVs.

7.4.2 Impact of Height on Ergodic Sum Capacity

Observation 7.4.2.1 *The FD-HetNet attain higher ergodic sum capacity than the HD-HetNet when the altitude of the UAVs is increased.*

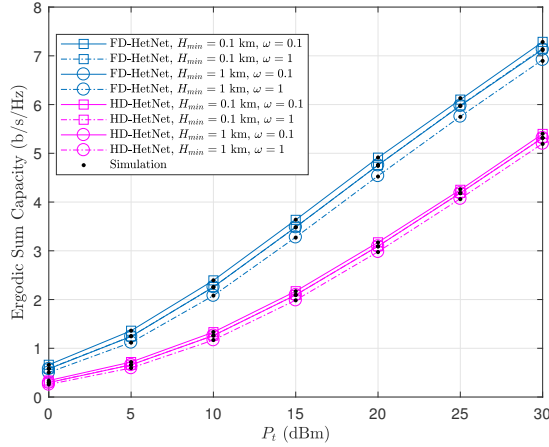


Fig. 7.3: Impact of height on the ergodic sum capacity of the NOMA-aided FD-HetNet and HD-HetNet for $N_U = N_D = 3$, $\gamma_\phi^2 = -130$ dBm, $\epsilon = 0.01$, and $\beta_{mbs,j} = \beta_{i,j} = (0.04)^3$.

Fig. 7.3 shows the impact of height on the ergodic sum capacity for the FD-HetNet and HD-HetNet. It can be seen that the ergodic sum capacity of the FD-HetNet (C_{sum}^{FD}) and HD-HetNet (C_{sum}^{HD}) exhibit similar trends, with $C_{sum}^{FD} > C_{sum}^{HD}$ for $0 \text{ dBm} \leq P_t \leq 30 \text{ dBm}$. When the minimum UAV altitude (H_{min}) is low and the altitude separation factor (ω) is small, a higher $C_{sum}^x, x \in \{FD, HD\}$ is observed. Correspondingly, it is seen that a higher H_{min} and larger ω leads to a lower $C_{sum}^x, x \in \{FD, HD\}$.

To see the reasons behind such a trend, it is important to note that increasing H_{min} causes the UL and DL UAVs to be operating at a higher altitude. In turn, the SOIs of UL UAV- i and the GS become weaker at the receiving GS and DL UAV- j , respectively. Similarly, increasing ω results in a larger separating altitude among all UAVs, i.e., higher operating altitude for all UAVs, leading to weaker MUI at the FD-GS and the DL UAVs. However, a larger ω also leads to a weaker SOI at the receiving GS and DL UAVs.

When SIC detection is employed at the GS and DL UAV- j , MUI from the UAVs can be effectively managed. Hence, both the FD-HetNet and HD-HetNet are able to have the UL and DL UAVs operate at a lower H_{min} and smaller ω while achieving higher $C_{sum}^x, x \in \{FD, HD\}$, leading to the trend in Fig. 7.3.

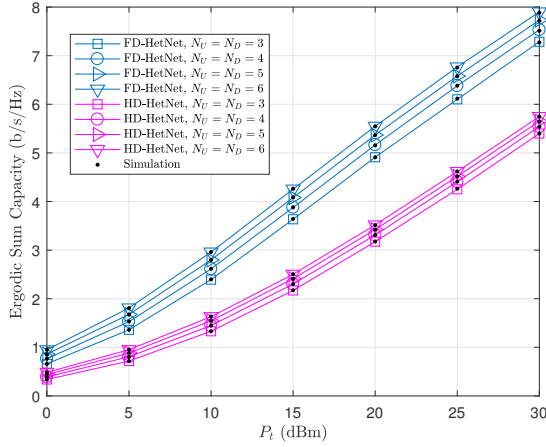


Fig. 7.4: Impact of the number of deployed UAVs on the ergodic sum capacity of the NOMA-aided FD-HetNet and HD-HetNet for $H_{min} = 0.1$ km, $\omega = 0.1$, $\gamma_\phi^2 = -130$ dBm, $\epsilon = 0.01$, and $\beta_{mbs,j} = \beta_{i,j} = (0.04)^3$.

7.4.3 Impact of the Number of Deployed UAVs on Ergodic Sum Capacity

Observation 7.4.3.1 *Effective SIC at the GS and DL UAVs enables the FD-HetNet to attain higher ergodic capacity over the HD-HetNet.*

The impact of the number of deployed UAVs on the ergodic sum capacity for the FD-HetNet and HD-HetNet is plotted in Fig. 7.4. As SIC detectors are employed at the GS and DL UAVs, MUI from the UAVs can be effectively mitigated in the FD-HetNet and HD-HetNet. As a consequence, more UL and DL UAVs can be supported. Thus, increasing N_U and N_D leads to higher ergodic sum capacity ($C_{sum}^x, x \in \{FD, HD\}$) for both FD-HetNet and HD-HetNet, as observed in Fig. 7.4.

It is also useful to note that in HD-HetNets, the MBS and UL UAVs communicate on time-frequency resource blocks that are orthogonal to those allocated for DL UAVs. In contrast, the FD-GS enables the MBS, UL UAVs and DL UAVs to communicate over the same time-frequency resource block. As a result, increasing N_U and N_D leads to a higher increase in C_{sum}^{FD} than in C_{sum}^{HD} , which in turn leads to $C_{sum}^{FD} > C_{sum}^{HD}$ for $0 \text{ dBm} \leq P_t \leq 30 \text{ dBm}$.

Therefore, Fig. 7.4 highlights the potential for FD-HetNets to address spectrum scarcity in UAV communications.

7.4.4 Impact of SI Cancellation, Phase Noise, and Residual Interference on Ergodic Sum Capacity

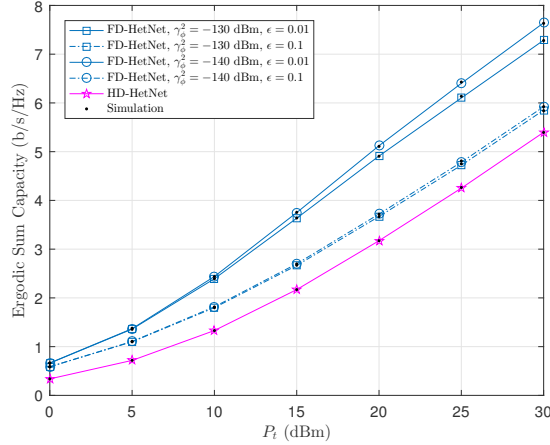


Fig. 7.5: Impact of SI cancellation and phase noise on the ergodic sum capacity of the NOMA-aided FD-HetNet for $N_U = N_D = 3$, $H_{min} = 0.1$ km, $\omega = 0.1$, and $\beta_{mbs,j} = \beta_{i,j} = (0.04)^3$.

Observation 7.4.4.1 *The benefits of the considered FD-HetNet require SI cancellation of at least 137 dB. Such levels of SI cancellation have been reported in the literature.*

The impact of SI cancellation (ϵ) and phase noise (γ_ϕ^2) on the FD-HetNet ergodic sum capacity (C_{sum}^{FD}) is shown in Fig. 7.5. To begin, it is useful to recall that SI cancellation is computed as $1/(\epsilon\sigma^2)$ [17, 81]. Thus, increasing $\epsilon = 0.01$ to $\epsilon=0.1$ also increases the SI channel estimation error while leading to a lower level of SI cancellation at the FD-GS. Consequently, the resultant instantaneous SINR of the MBS ($SINR_{mbs}^{FD}$) and UL UAV-*i* ($SINR_i^{FD}$) at the FD-GS becomes limited by residual SI. Similarly, increasing γ_ϕ^2 also causes the strength of the residual SI to increase. However, as $\gamma_\phi^2 < \sigma^2$, changes in ϵ have more significant impact on the FD-GS as the residual SI may be above the noise floor. Thus, as seen in Fig. 7.5, decreasing ϵ , i.e., increasing SI cancellation, elicits a higher C_{sum}^{FD} than reducing γ_ϕ^2 .

Fig. 7.6 shows the impact of SI cancellation, phase noise, and residual interference ($\beta_{x,j}, x \in \{mbs, i\}$) on the ergodic capacity gain for UL and DL transmissions, i.e., Δ_{UL} and Δ_{DL} . As explained earlier, increasing ϵ leads to a more drastic drop in Δ_{UL} than

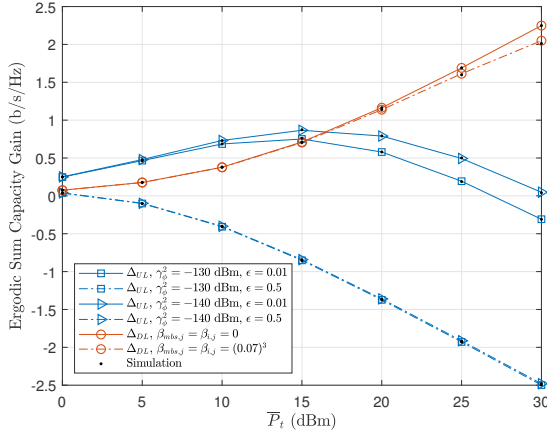


Fig. 7.6: Impact of SI cancellation, phase noise, and residual interference on the ergodic sum capacity gain of the NOMA-aided FD-HetNet for $N_U = N_D = 3$, $H_{min} = 0.1$ km, and $\omega = 0.1$.

increasing γ_ϕ^2 , as seen in Fig. 7.6. Furthermore, a slight increase in $\beta_{mbs,j}$ and $\beta_{i,j}$ also leads to a drop in Δ_{DL} as the DL UAVs become limited by residual interference at high P_t regimes. Therefore, Corollary 7.5 is confirmed in Fig. 7.6.

It is worth emphasizing that the analysis in this chapter assumes SI cancellation levels of 137 dB ($\epsilon = 0.5$) to 154 dB ($\epsilon = 0.01$). Such SI cancellation levels have been reported in [209], where SI cancellation beyond 150 dB was noted. Therefore, Fig. 7.5 and Fig. 7.6 highlights the feasibility of achieving practical FD-HetNets for NOMA-aided multi-UAV communications.

7.5 Chapter Summary

NOMA-aided multi-UAV communications in FD-HetNets is proposed in this chapter as a pragmatic and attractive solution to address spectrum scarcity in UAV communications. Through an analysis of the ergodic capacity within a BPP-based stochastic geometry framework, it is shown that higher ergodic capacities are attained by the MBS and UAVs in the FD-HetNet. In addition, the FD-HetNet allows more UAVs to be at lower altitudes while achieving a higher ergodic sum capacity and ergodic capacity gains over HD-HetNets. Finally, it is demonstrated that NOMA-aided multi-UAV communications in FD-HetNets achieve higher ergodic sum capacity over HD-HetNets despite weaker

SI suppression and stronger phase noise. Hence, the feasibility of addressing spectrum scarcity in UAV communications is highlighted.

Thus far, the performance analysis of multi-UAV networks has focused on the specific case of single-antenna UAVs and GSs. However, multi-antenna transmitters and receivers are more commonly used in practice to improve the diversity gain of wireless systems. One drawback of such multi-antenna transceivers stems from the fact that the communications channel may become correlated due to insufficient antenna spacing. To this end, the performance of a NOMA-aided multi-UAV network over correlated fading channels is studied in the next chapter.

Chapter 8

NOMA-aided UAV Communications over Bivariate Rician Shadowed Fading Channels

8.1 Introduction

As one of the key enabling technologies being considered for future wireless systems, a NOMA-aided UCS was studied in Chapter 7 where it was evaluated against OMA-based UCSs. Yet, the analytical framework in Chapter 7 assumed only single-antenna UAVs and GSs. In practice, multi-antenna transceivers at the GSs and UAVs are more attractive as it enables greater diversity gain for NOMA-aided UCSs. However, channel correlation at the multi-antenna receivers of the UAVs, e.g., dual-antenna receivers, can be a major challenge.¹

For instance, when dual-antenna systems are considered, UAV communications over correlated, i.e., bivariate, fading channels can occur due to insufficient antenna separation, the heading of the UAVs, UAV elevation angle, and the received signal's angle of arrival [174, 211–213]. In the literature, multivariate and bivariate fading models have been investigated in diversity combining systems, e.g., in [214–216], and multi-antenna UAV communication systems [174, 212, 213, 217], to model the spatial correlation at the reception antennas. In this aspect, a bivariate Rician shadowed fading channel model was proposed in [211] using a power series approach, with performance analysis of downlink NOMA-aided UCS also conducted. Nonetheless, investigations into the performance of

¹The work in this chapter is derived from [210], which has been submitted for publication.

NOMA-aided dual-antenna UCSs over bivariate Rician shadowed fading channels remain an open problem.

Separately, it is noted that existing NOMA-related studies have largely focused on outage probability as key performance metric. To further complement the analysis, one can also analyze the finite SNR diversity gain of NOMA-aided systems. In the literature, finite SNR diversity gain has been used to evaluate the outage performance of wireless systems, e.g., in [17, 18, 105, 106]. In particular, finite SNR diversity gain is a measure of the outage probability slope at particular SNR levels [105]. Through the analysis of finite SNR diversity gain, the outage probability behaviors that are only observable at non-asymptotic SNR regimes, i.e., finite SNR regimes, are revealed. Such finite SNR analysis are particularly useful in providing an accurate picture of a system’s outage performance, since most wireless systems typically operate at low-to-moderate SNR ranges [17]. For instance, the SNR needed to achieve a particular rate of error decay, through turbo codes or low-density parity-check codes, can be estimated via finite SNR analysis [106]. Finite SNR analysis can also be used to determine the upper and lower limits of bit error rate performance [107, 109], and also to determine scenarios that can lead to a wireless system becoming interference-limited [17, 18]. Yet, despite gaining research interest in recent years, e.g., [17, 18, 108, 111], only a few NOMA-related studies, e.g., [191, 218], have quantified the asymptotic diversity gain of NOMA-aided networks. Thus, to the best of our knowledge, the analysis of finite SNR diversity gain in NOMA-aided networks remains an open research problem.

With the above discussions in mind, the viability of NOMA-aided UCSs operating in realistic operating environments, e.g., bivariate Rician shadowed fading channels, with constraints, e.g., low SNR regimes, has not received much attention, despite several NOMA-related studies for UAV communications, e.g., [201–203]. To this end, a comprehensive performance analysis of a NOMA-aided UCS, comprising dual-antenna UAVs with selection combining, communicating over bivariate Rician shadowed fading channels is conducted in this chapter.

8.2 System Model

Consider a NOMA-aided UCS operating in a suburban environment, comprising one single-antenna GS and N_D downlink UAVs equipped with two receive antennas (Fig.

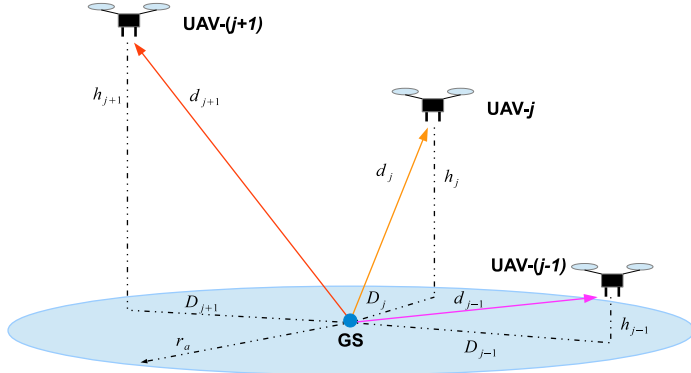


Fig. 8.1: An illustration of the NOMA-aided UCS operating in a suburban environment. The GS employs downlink NOMA to transmit data to the UAVs equipped with two reception antennas. At the UAVs, selection combining is employed to recover the transmitted data from the GS.

8.1). The GS in the NOMA-aided UCS employs downlink NOMA to transmit data, while selection combining is employed as the reception strategy at the N_D downlink UAVs. However, due to insufficient spacing between the receive antennas at the UAVs and the relative position of the UAVs to the GS, the downlink NOMA transmissions are assumed to occur over correlated fading channels. Separately, based on studies in [112] and [113], a BPP model is employed in the present work to account for the spatial locations of the UAVs. It is also assumed that the UAVs are operating at a minimum altitude of h_{min} [112, 113], with compensated Doppler shifts [18]. Lastly, as a suburban setting is considered in this work, the bivariate Rician shadowed fading model is assumed for the UAV channels to account for the correlation between the receive antennas at the downlink UAVs.² A summary of important notations is also given in Table 8.1.

8.2.1 Distribution of UAV Spatial Locations

Let the spatial location of the UAVs follow a uniform distribution in a disc centered at origin O above the GS with radius r_a and angle $[0, 2\pi)$. Then, the Euclidean distance (km) between downlink UAV- j and the GS is $d_j = \sqrt{D_j^2 + h_j^2}$, where $1 \leq j \leq N_D$ is the

²It is worth noting that the analytical approach in this paper is also extensible to multi-antenna selection combining receivers.

index of downlink UAV- j , D_j is the projected Euclidean distance on the ground plane between the GS and downlink UAV- j , $h_j = h_{min} + \omega \frac{j}{N_D}$ is the altitude of downlink UAV- j , $\omega > 0$ is the altitude separation factor between the DL UAVs.

As the spatial location of downlink UAV- j follows a uniform distribution, the PDF $f_{d_j}(w)$ of d_j is given as [112, eq. (3)], [20]:

$$f_{d_j}(w) = \frac{2w}{r_a^2}, \quad (8.1)$$

where $L_{m,j} \leq w \leq L_{p,j}$, $L_{m,j} = h_j$, and $L_{p,j} = \sqrt{h_j^2 + r_a^2}$. Through the PDF $f_{d_j}(w)$, a performance analysis of correlated downlink NOMA transmissions can now be conducted with the spatial distribution of the UAVs taken into consideration.

8.2.2 Instantaneous SINR at Downlink UAV- j

Following downlink NOMA transmission principles, the GS uses superposition coding to transmit the SOI to all downlink UAVs. Specifically, an SIC detector is employed at downlink UAV- j to detect the SOI in the presence of MUI from the SOIs of the other downlink UAVs. Let $R_{j,l}$ be the instantaneous channel envelope of the l th receive antenna at downlink UAV- j for $l \in \{1, 2\}$, where $R_{j,l}$ follows a bivariate Rician shadowed distribution. Then, the instantaneous SINR of the l th receive antenna at downlink UAV- j ($SINR_{j,l}$) is:

$$SINR_{j,l} = \frac{P_r a_j d_j^{-L} |R_{j,l}|^2}{1 + P_r d_j^{-L} |R_{j,l}|^2 \sum_{i=1}^{j-1} a_i} \quad (8.2)$$

where $P_r \propto \frac{P_t}{P_L \eta}$ is the normalized average received power [17], P_t is the transmit power of the GS, $P_L = (\frac{4\pi \cdot 10^9}{3 \cdot 10^8} f_c)^2$, L is the pathloss exponent, $\eta = -174 + 10 \log_{10}(B_W)$ is the strength of the AWGN in dBm [206], f_c is the carrier frequency (MHz), B_W is the bandwidth (Hz), and a_j is the power allocation factor for DL UAV- j such that $\sum_{j=1}^{N_D} a_j = 1$.

It is useful to recall that the downlink UAVs operate at different altitudes, i.e., $H_j < H_{j+1}$. As such, the power allocation factor a_j is heuristically defined based on the altitudes of the N_D downlink UAVs to ensure fairness. Specifically, we let $a_j = \frac{H_j}{\sum_{k=1}^{N_D} H_k}$ in

Table 8.1: Summary of Important Notations

Notations	Description
$1 \leq j \leq N_D$	Index of DL UAV- j
$h_{min}; \omega$	Minimum UAV altitude; Altitude separation factor
h_j	Altitude of DL UAV- j
d_j	Euclidean distance between the GS and DL UAV- j
P_r	Normalized average received power
a_j	Power allocation factor for DL UAV- j
ρ	Cross correlation factor
m	Shaping parameter, denotes shadowing severity
σ^2	Varinace of bivariate Rician shadowed random variable

order to assign higher transmit powers to UAVs operating far away from the GS [136], i.e., $a_j < a_{j+1}$. Doing so allows downlink UAV- j to recover the SOI by performing SIC to remove MUI from downlink UAV- m for $m > j$, while ignoring MUI from DL UAV- k for $k < j$ [124, 135].

8.3 Bivariate Rician Shadowed Fading Model

In UAV communications, correlation of the UAV channels can occur due to insufficient spacing between the UAV's receive antenna, the heading of the UAV, and the position of the UAV relative to the GS [174, 211–213]. As such, we introduce the bivariate Rician shadowed fading model in this section as the basis to model the correlated UAV channels.

To begin, a pair of bivariate Rician shadowed distributed random variables RVs, H_1 and H_2 , is modeled as [216]:

$$H_k = \sigma\sqrt{1-\rho}X_k + \sigma\sqrt{\rho}X_0 + Z, \quad (8.3)$$

where $X_k, k \in \{0, 1, 2\}$ are Gaussian RVs with zero mean and variance $\frac{1}{2}$, $0 \leq \rho \leq 1$ is the cross correlation coefficient, $E\{(\sigma\sqrt{1-\rho}X_k + \sigma\sqrt{\rho}X_0)^2\} = \sigma^2$ [216], and $E\{\bullet\}$ is the statistical expectation operator. Finally, the RV Z follows a Nakagami- m distribution with shaping parameter $m \geq 0.5$ and $E\{|Z|^2\} = \Omega_N$.

8.3.1 Derivation of the Joint PDF and Joint CDF

Defining $R_k = |H_k|$, we note that the RV R_k follows a bivariate Rician shadowed distribution with $E\{R_k^2\} = \sigma^2(1 + K)$ and Rician factor $K = \frac{\Omega_N}{\sigma^2}$. From [216, eq. (4)], the joint

PDF $f_{R_1, R_2}(r_1, r_2)$ of R_k is:

$$\begin{aligned} f_{R_1, R_2}(r_1, r_2) &= \frac{8(\frac{m\rho}{m\rho+K})^m}{\sigma^6\rho(1-\rho)^2} r_1 r_2 \exp\left(-\frac{r_1^2 + r_2^2}{\sigma^2(1-\rho)}\right) \\ &\times \int_0^\infty x \exp\left(\frac{-(1+\rho)}{\sigma^2\rho(1-\rho)}x^2\right) I_0\left(\frac{2r_1 x}{\sigma^2(1-\rho)}\right) I_0\left(\frac{2r_2 x}{\sigma^2(1-\rho)}\right) \\ &\quad \times {}_1F_1\left(m, 1; \frac{K}{\sigma^2\rho(\rho m + K)}x^2\right) dx, \end{aligned} \quad (8.4)$$

where $I_0(\bullet)$ is the modified Bessel function of the first kind with zero order [219, eq. (9.6.10)] and ${}_1F_1(\bullet)$ is the confluent Hypergeometric function [49].

The joint PDF expression in (8.4) may require the use of complicated numerical methods when evaluating commonly used performance metrics, e.g., outage probability. We present an alternative closed-form expression for $f_{R_1, R_2}(r_1, r_2)$ in the following Lemma:

Lemma 8.1 *The closed-form expression for $f_{R_1, R_2}(r_1, r_2)$ can be expressed as the following power series:*

$$f_{R_1, R_2}(r_1, r_2) \approx \sum_{k=0}^{K_{tr,1}} \sum_{i=0}^k \sum_{n=0}^i \alpha(k, i, n) r_1^{2n+1} r_2^{2(i-n)+1} \exp\left(-\frac{r_1^2 + r_2^2}{\sigma^2(1-\rho)}\right), \quad (8.5)$$

where

$$\alpha(k, i, n) = \frac{8(m)_{k-i} \left(\frac{K}{\sigma^2\rho(\rho m + K)}\right)^{k-i} \left(\frac{m\rho}{m\rho+K}\right)^m k!}{\Gamma^2(n+1)\Gamma^2(i-n+1)[\sigma^2(1-\rho)]^{2i} (1)_{k-i}(k-i)! \sigma^6 \rho (1-\rho)^2 \cdot 2 \left(\frac{1+\rho}{\sigma^2\rho(1-\rho)}\right)^{k+1}},$$

$K_{tr,j}, j \in \{1, 2\}$ is the truncation order, and $(a)_k = \frac{\Gamma(a+k)}{\Gamma(a)}$ is the Pochhammer symbol [219, eq. (6.1.22)].

Proof: The proof is provided in Appendix F.1

As the subsequent analysis in the rest of this chapter are based on the power series expression in (8.5), it is crucial to show that (8.5) is convergent. In the next Corollary, we show that the alternative closed-form expression for $f_{R_1, R_2}(r_1, r_2)$ in (8.5) is convergent.

Corollary 8.1 *The closed-form expression for $f_{R_1, R_2}(r_1, r_2)$ in (8.5) has a convergence radius of ∞ .*

Proof: The proof is given in Appendix F.2.

As a result of Corollary 8.1, term-wise integration and differentiation can be performed on the power series expression in (8.5) [49, 171]. Therefore, the closed-form joint CDF $F_{R_1, R_2}(\gamma_1, \gamma_2)$ can also be obtained from (8.5) as shown in the following Lemma:

Lemma 8.2 *The closed-form expressions for $F_{R_1, R_2}(\gamma_1, \gamma_2)$ can be expressed as:*

$$F_{R_1, R_2}(\gamma_1, \gamma_2) \approx \sum_{k=0}^{K_{tr,1}} \sum_{i=0}^k \sum_{n=0}^i \sum_{l=0}^{K_{tr,2}} \sum_{q=0}^l \alpha(k, i, n) G(l, n, i, q) (\gamma_1)^{2(q+n+1)} (\gamma_2)^{2(l-q+i-n+1)}, \quad (8.6)$$

$$\text{where } G(l, n, i, q) = \frac{(-1)^l \binom{l}{q}}{[\sigma^2(1-\rho)]^l l! 4(q+n+1)(l-q+i-n+1)}.$$

Proof: The proof is provided in Appendix F.3.

Compared to the expression of $F_{R_1, R_2}(\gamma_1, \gamma_2)$ given in [216, eq. (23)], (8.6) demonstrates that $F_{R_1, R_2}(\gamma_1, \gamma_2)$ can be evaluated in closed-form. Furthermore, (8.6) is presented in a desirable form, as term-wise integration and differentiation can be conducted using the presented power series expression. As it will be shown, (8.6) enables the tractable derivation of the NOMA-aided UCS outage probability and diversity gain under the BPP model, which may not be possible using [216, eq. (23)].

8.3.2 Truncation Analysis of the Joint PDF and Joint CDF

It is worth noting that Corollary 8.1 is evaluated by applying the D'Alembert test on k , i , and n in (8.5). Since the D'Alembert test indicates a convergence radius of ∞ , the same technique can also be extended to determine the truncation error (\mathcal{T}_ϵ) of the joint PDF $f_{R_1, R_2}(r_1, r_2)$ in (8.5). In particular, \mathcal{T}_ϵ can be defined as [220, eq. (92)]:

$$\begin{aligned} \mathcal{T}_\epsilon &= \sum_{k=K_{tr,1}+1}^{\infty} \sum_{i=0}^{K_{tr,1}} \sum_{n=0}^i \alpha(k, i, n) \\ &\quad \times r_1^{2n+1} r_2^{2(i-n)+1} \exp\left(-\frac{r_1^2 + r_2^2}{\sigma^2(1-\rho)}\right). \end{aligned} \quad (8.7)$$

From (8.7), we present an upper bound of the truncation error ($\mathcal{T}_{\epsilon,upper}$) for the joint PDF $f_{R_1, R_2}(r_1, r_2)$ in (8.5) in the next Lemma:

Lemma 8.3 *For a sufficiently large truncation order ($K_{tr,1}$), the upper bound of the truncation error in (8.5) is:*

$$\begin{aligned} \mathcal{T}_{\epsilon,upper} &= \sum_{i=0}^{K_{tr,1}} \sum_{n=0}^i \frac{\alpha(K_{tr,1}, i, n)}{1 - \Delta(K_{tr,1})} \\ &\quad \times r_1^{2n+1} r_2^{2(i-n)+1} \exp\left(-\frac{r_1^2 + r_2^2}{\sigma^2(1-\rho)}\right), \end{aligned} \quad (8.8)$$

where $\Delta(k) = \left(\frac{K}{\sigma^2\rho(\rho m+K)}\right)\frac{1}{k}$.

Proof: The proof is provided in Appendix F.4

The expression in (8.8) is useful in determining the necessary value of $K_{tr,1}$ that satisfies $\mathcal{T}_{\epsilon,upper} < \epsilon$, where ϵ is an error threshold value, for varying values of the Rician K factor, m , σ , and ρ . From (8.8), the behavior of $\mathcal{T}_{\epsilon,upper}$ with respect to the Rician K factor, m , σ , and ρ is given in the following Corollaries:

Corollary 8.2 *Increasing m , σ , or ρ leads to a smaller $\mathcal{T}_{\epsilon,upper}$.*

Proof: From (8.8), it is noted that m , σ , and ρ are in the denominator of $\Delta(k)$. Therefore, $\Delta(k) \rightarrow 0$ when m , σ , or ρ is increased. This completes the proof.

Corollary 8.3 *As the Rician K factor increases, a sufficiently large $K_{tr,1}$ is needed in order to reduce $\mathcal{T}_{\epsilon,upper}$.*

Proof: From (8.8), it is seen that $\lim_{k \rightarrow \infty} \Delta(k) = \frac{1}{k} \lim_{k \rightarrow \infty} \frac{K}{\sigma^2\rho(\rho m+K)} = \frac{1}{k}$. Therefore, as the Rician K factor increases, $\Delta(k) \rightarrow 0$ only when $K_{tr,1}$ is sufficiently large. This completes the proof.

The impact of the Rician K factor, m , σ , and ρ on $\mathcal{T}_{\epsilon,upper}$ is established in Corollaries 8.2 and 8.3. For instance, smaller $K_{tr,1}$ can be used when (8.5) is used to model a bivariate Rayleigh shadowed fading environment, i.e., Rician K factor is zero. Furthermore, Corollaries 8.2 and 8.3 can also be used to provide an indication of the necessary $K_{tr,1}$ for varying values of the Rician K factor, m , σ , and ρ .

The approach in Lemma 8.3 and Corollaries 8.2 and 8.3 can also be used to analyze the truncation error (e) of the joint CDF $F_{R_1,R_2}(\gamma_1, \gamma_2)$ in (8.6). Specifically, e can be

defined as [220, eq. (82)]:

$$\begin{aligned} e &= \sum_{k=0}^{K_{tr}} \sum_{i=0}^k \sum_{n=0}^i \sum_{l=K_{tr}+1}^{\infty} \sum_{q=0}^l \mu(k, l) + \sum_{k=K_{tr}+1}^{\infty} \sum_{i=0}^k \sum_{n=0}^i \sum_{l=0}^{K_{tr}} \sum_{q=0}^l \mu(k, l) \\ &\quad + \sum_{k=K_{tr}+1}^{\infty} \sum_{i=0}^k \sum_{n=0}^i \sum_{l=k}^{\infty} \sum_{q=0}^l \mu(k, l) + \sum_{l=K_{tr}+1}^{\infty} \sum_{q=0}^l \sum_{k=l}^{\infty} \sum_{i=0}^k \sum_{n=0}^i \mu(k, l), \end{aligned} \quad (8.9)$$

where $K_{tr,1} = K_{tr,2} = K_{tr}$ and $\mu(k, l) = \alpha(k, i, n)G(l, n, i, q)(\gamma_1)^{2(q+n+1)}(\gamma_2)^{2(l-q+i-n+1)}$. From (8.9), the upper bound of the truncation error (e_{upper}) for the joint CDF $F_{R_1, R_2}(\gamma_1, \gamma_2)$ in (8.6) is presented in the next Lemma:

Lemma 8.4 *For a sufficiently large truncation order (K_{tr}), the upper bound of the truncation error in (8.6) is:*

$$\begin{aligned} e_{upper} &= \sum_{k=0}^{K_{tr}} \sum_{i=0}^k \sum_{n=0}^i \sum_{q=0}^{K_{tr}+1} \frac{\mu(k, K_{tr}+1)}{1 - \Theta_1(k, K_{tr}+1)} + \sum_{i=0}^{K_{tr}} \sum_{n=0}^i \sum_{l=0}^{K_{tr}} \sum_{q=0}^l \frac{\mu(K_{tr}, l)}{1 - \Theta_2(K_{tr})} \\ &\quad + \sum_{k=K_{tr}+1}^{\infty} \sum_{i=0}^k \sum_{n=0}^i \sum_{q=0}^{K_{tr}+1} \frac{\mu(k, K_{tr}+1)}{1 - \Theta_1(k, K_{tr}+1)} + \sum_{q=0}^{K_{tr}+1} \sum_{i=0}^{K_{tr}} \sum_{n=0}^i \frac{\mu(K_{tr}, K_{tr}+1)}{1 - \Theta_2(K_{tr})}, \end{aligned} \quad (8.10)$$

where $\Theta_1(k, l) = \frac{(-1)(\gamma_2)^{2(l+1)}(l-q+i-n+1)}{\sigma^2(1-\rho)l^2(l-q+i-n+2)}$ and $\Theta_2(k) = \Delta(k) = \left(\frac{K}{\sigma^2\rho(\rho m+K)}\right)^{\frac{1}{k}}$.

Proof: The proof is provided in Appendix F.5

Similar to (8.8), the upper bound in (8.4) can be used to identify the necessary value of K_{tr} such that $e_{upper} < \epsilon$, where ϵ is an error threshold value, for varying values of the Rician K factor, m , σ , ρ , and γ_2 . From (8.10), the behavior of e_{upper} with respect to ρ and γ_2 is given in the following Corollary:

Corollary 8.4 *Increasing ρ or decreasing γ_2 leads to a smaller e_{upper} .*

Proof: From (8.10), it is noted that ρ is in the denominator of $\Theta_1(k, l)$. Likewise, γ_2 is in the numerator of $\Theta_1(k, l)$. Therefore, $\Theta_1(k, l) \rightarrow 0$ when ρ is increased or when γ_2 is decreased. This completes the proof.

The impact of ρ and γ_2 on e_{upper} is established in Corollary 8.4. Hence, one can now use Corollary 8.4 to decide on the choice of K_{tr} to obtain $e_{upper} < \epsilon$ based on ρ and γ_2 . It should also be noted that Corollaries 8.2 and 8.3 are also applicable to (8.10).

8.4 Outage Probability Derivations

In this section, the downlink NOMA outage probability expression for downlink UAV- j employing selection combining is presented. The OMA outage probability expression for downlink UAV- j is also provided as a benchmark. Let the transmission rate of the GS be defined as \mathcal{R}^x , where $x \in \{NOMA, OMA\}$. For a fair comparison between NOMA and OMA, we let $\mathcal{R}^{NOMA} = \frac{1}{N_D} \mathcal{R}^{OMA}$.

8.4.1 Downlink NOMA Outage Probability

At downlink UAV- j , let the selection combining NOMA outage event (\mathcal{O}_j^{NOMA}) be defined as:

$$\mathcal{O}_j^{NOMA} = \left\{ R_{j,l}, d_j : \max(R_{j,1}, R_{j,2}) < \gamma_j^{NOMA} \sqrt{\frac{d_j^L}{P_r}} \right\}, \quad (8.11)$$

where $\gamma_j^{NOMA} = \sqrt{\frac{2^{\mathcal{R}^{NOMA}} - 1}{a_j - \left(\sum_{i=1}^{j-1} a_i\right) \left(2^{\mathcal{R}^{NOMA}} - 1\right)}}$ is the NOMA threshold such that $R^{NOMA} < \log_2 \left(1 + \frac{a_j}{\sum_{i=1}^{j-1} a_i}\right)$. Then, the closed-form downlink NOMA outage probability expression for UAV- j is presented in the following Theorem.

Theorem 8.1 *The NOMA outage probability at downlink UAV- j is:*

$$Pr(\mathcal{O}_j^{NOMA}) \approx \sum_{k=0}^{K_{tr,1}} \sum_{i=0}^k \sum_{n=0}^i \sum_{l=0}^{K_{tr,2}} \sum_{q=0}^l \alpha(k, i, n) G(l, n, i, q) \Xi_j(l, i) \left[\frac{(\gamma_j^{NOMA})^2}{P_r} \right]^{2+l+i}, \quad (8.12)$$

$$\text{where } \Xi_j(l, i) = \frac{2 \left[(L_{p,j})^{L(2+l+i)+2} - (L_{m,j})^{L(2+l+i)+2} \right]}{r_a^2 [L(2+l+i)+2]}.$$

Proof: The proof is provided in Appendix F.6.

In Theorem 8.1, the effects of correlation, shadowing, and the Rician K factors on the SOIs at the UAVs are mostly captured in the functions $\alpha(k, i, n)$ and $G(l, n, i, q)$. Similarly, the effects of the GS transmission rate and NOMA power allocation factor on outage probability are reflected in γ_j^{NOMA} , while the function $\Xi_j(l, i)$ in Theorem 8.1 captures the stochastic geometry behavior of the UAV spatial locations. Thus, using Theorem 8.1, the reliability of downlink NOMA can be analyzed within the BPP model for UCSSs.

It is also worth emphasizing that the normalized average received power (P_r) appears in the denominator of (8.12). As it will be shown subsequently, (8.12) indicates the absence of an outage probability error floor in $\Pr(O_j^{NOMA})$ for downlink NOMA over correlated Rician shadowed fading channels.

8.4.2 Downlink OMA Outage Probability

As compared to NOMA, the GS transmits data to the downlink UAVs over separate time-frequency resources in OMA transmission schemes. Let the instantaneous SNR of the l th receive antenna at downlink UAV- j be $SNR_{j,l} = P_r d_j^{-L} |R_{j,l}|^2$. Also, let the selection combining OMA outage event (O_j^{OMA}) be defined as:

$$O_j^{OMA} = \left\{ R_{j,l}, d_j : \max(R_{j,1}, R_{j,2}) < \gamma_j^{OMA} \sqrt{\frac{d_j^L}{P_r}} \right\}, \quad (8.13)$$

where $\gamma_j^{OMA} = \sqrt{2^{\mathcal{R}^{OMA}} - 1}$ is the OMA threshold. Then, the closed-form OMA outage probability expression for UAV- j is given in the next Theorem.

Theorem 8.2 *The OMA outage probability at downlink UAV- j is:*

$$\Pr(O_j^{OMA}) \approx \sum_{k=0}^{K_{tr,1}} \sum_{i=0}^k \sum_{n=0}^i \sum_{l=0}^{K_{tr,2}} \sum_{q=0}^l \alpha(k, i, n) G(l, n, i, q) \Xi_j(l, i) \left[\frac{(\gamma_j^{OMA})^2}{P_r} \right]^{2+l+i} \quad (8.14)$$

Proof: The expression in (8.14) is obtained using the same approach in Appendix F.6.

Although one can also invoke [216, eq. (48)] to evaluate $\Pr(O_j^{OMA})$, tractable analytical expressions may not be possible once the BPP model is considered. In contrast, we demonstrate in (8.14) that evaluating $\Pr(O_j^{OMA})$ within the BPP model can be achieved in a straightforward fashion using Lemma 8.2.

8.5 Finite SNR Diversity Gain Derivations

The finite SNR diversity gain expressions for downlink NOMA and uplink NOMA are presented in this section. We also present finite SNR diversity gain expressions for OMA in this section.

The finite SNR diversity gain d_f of a given system quantifies the decay of outage probability at low to moderate SNR regimes [105, 106]. In particular, the finite SNR diversity gain is defined as [106, eq. (5)]:

$$d_f = \frac{-P_r}{Pr(O)} \frac{\partial}{\partial P_r} Pr(O), \quad (8.15)$$

where O and $Pr(O)$ are the considered outage event and outage probability, respectively. From [105] and [108], one obtains the asymptotic diversity gain, defined in [107], by evaluating (8.15) at high SNR regimes. In this spirit, finite SNR analysis is employed to investigate the impact of MUI in downlink NOMA for UAV communications.

8.5.1 Downlink NOMA Finite SNR Diversity Gain

Let the downlink NOMA finite SNR diversity gain at UAV- j be $d_{f,j}^{NOMA}$. Then, the closed-form expression for $d_{f,j}^{NOMA}$ is presented in the following Proposition.

Proposition 8.1 *The downlink NOMA finite SNR diversity gain at UAV- j is:*

$$d_{f,j}^{NOMA} \approx \frac{-P_r}{Pr(O_j^{NOMA})} \sum_{k=0}^{K_{tr,1}} \sum_{i=0}^k \sum_{n=0}^i \sum_{l=0}^{K_{tr,2}} \sum_{q=0}^l \alpha(k, i, n) \\ \times G(l, n, i, q) \Xi_j(l, i) \frac{(\gamma_j^{NOMA})^{2(2+l+i)} (-2 - l - i)}{(P_r)^{3+l+i}}. \quad (8.16)$$

Proof: Equation (8.16) can be obtained from (8.12) by applying (8.15). It should be noted that the differentiation conducted as a result of deriving (8.16) is valid due to Corollary 8.1 [49, 171].

As (8.12) is presented in a desirable form, i.e., as a power series, one can obtain a closed-form expression of $d_{f,j}^{NOMA}$ in (8.16), which may not be tractable using the expression in [216, eq. (48)]. Furthermore, the expression in (8.16) quantifies the NOMA outage probability decay of downlink UAV- j as a function of P_r . Thus, a larger $d_{f,j}^{NOMA}$ indicates a steeper drop in $Pr(O_j^{NOMA})$ as P_r varies.

Using Proposition 8.1, one also arrives at the asymptotic NOMA diversity gain for downlink UAV- j in the following Corollary.

Corollary 8.5 *At asymptotic SNR regimes, NOMA achieves full diversity gain at downlink UAV- j , i.e., $d_{f,j}^{NOMA} = 2$.*

Proof: The proof is provided in Appendix F.7.

Corollary 8.5 shows that the NOMA-aided UCS is not interference-limited when employing downlink NOMA, despite the presence of MUI from the SOIs of other downlink UAVs. Furthermore, $d_{f,j}^{NOMA}$ is not affected by ρ at high P_t regimes.

8.5.2 Downlink OMA Finite SNR Diversity Gain

Let the downlink OMA finite SNR diversity gain at UAV- j be $d_{f,j}^{OMA}$. Then, the closed-form expression for $d_{f,j}^{OMA}$ is presented in the following Proposition.

Proposition 8.2 *The downlink OMA finite SNR diversity gain at UAV- j is:*

$$d_{f,j}^{OMA} \approx \frac{-P_r}{Pr(O_j^{OMA})} \sum_{k=0}^{K_{tr,1}} \sum_{i=0}^k \sum_{n=0}^i \sum_{l=0}^{K_{tr,2}} \sum_{q=0}^l \alpha(k, i, n) \\ \times G(l, n, i, q) \Xi_j(l, i) \frac{(\gamma_j^{OMA})^{2(2+l+i)} (-2 - l - i)}{(P_r)^{3+l+i}}. \quad (8.17)$$

Proof: The closed-form expression in (8.17) is obtained using the same approach in Appendix F.7.

Similar to Proposition 8.1, one obtains the asymptotic OMA diversity gain for downlink UAV- j using Proposition 8.2 as shown in the following Corollary.

Corollary 8.6 *At asymptotic SNR regimes, OMA achieves full diversity gain at downlink UAV- j , i.e., $d_{f,j}^{OMA} = 2$.*

Proof: Corollary 8.6 is proven in the same manner as Corollary 8.5.

Using Proposition 8.2, the finite SNR diversity gain of OMA transmissions at downlink UAV- j with selection combining can now be analyzed over correlated Rician shadowed fading channels.

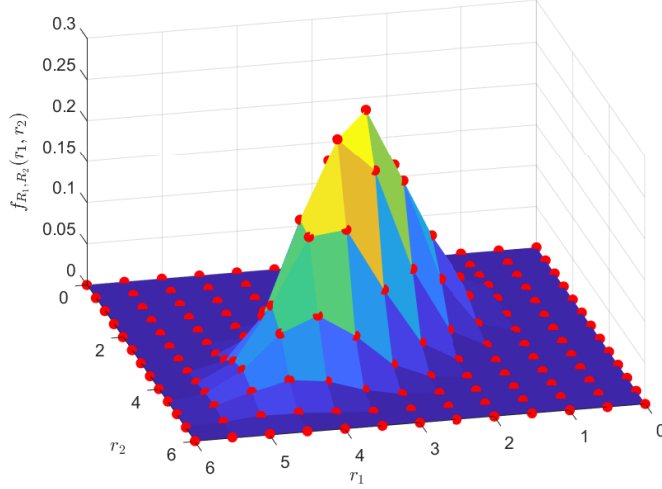


Fig. 8.2: Joint PDF comparison between the exact expression in (8.4) (denoted in red markers) and the closed-form expression in (8.5) for $m = 10$, $K_{tr,1} = 150$, and Rician K factor of 10 dB.

8.6 Numerical Results

Numerical and simulation results pertaining to both NOMA-aided and OMA-based UCSs are presented in this section. Monte Carlo simulations were also conducted with 10^6 samples, based on simulation parameters provided in Table 8.2 (unless otherwise stated). For the rest of the section, we present observations and discussions pertaining to the performance analysis of the NOMA-aided UCS.

8.6.1 Joint PDF Validation and Truncation Analysis

Fig. 8.2 shows a comparison between the closed-form joint PDF expression in (8.5) and the exact expression in [216, eq. (4)]. Evidently, (8.5) is validated as it is shown to be in very close agreement with [216, eq. (4)]. Furthermore, as $m \rightarrow \infty$, the closed-form expression in (8.5) can be used to model a bivariate Rician fading PDF.

The impact of the Rician K factor, m , σ , and ρ on the upper bound of the truncation error ($\mathcal{T}_{\epsilon,upper}$) is shown in Fig. 8.3. Likewise, the impact of ρ and γ on the upper bound of the truncation error (e_{upper}) is plotted in Fig. 8.4. In particular, it is seen in Fig. 8.3 and Fig. 8.4 that Lemmas 8.3 and 8.4 are validated, since $\mathcal{T}_\epsilon < \mathcal{T}_{\epsilon,upper}$ and $e < e_{upper}$

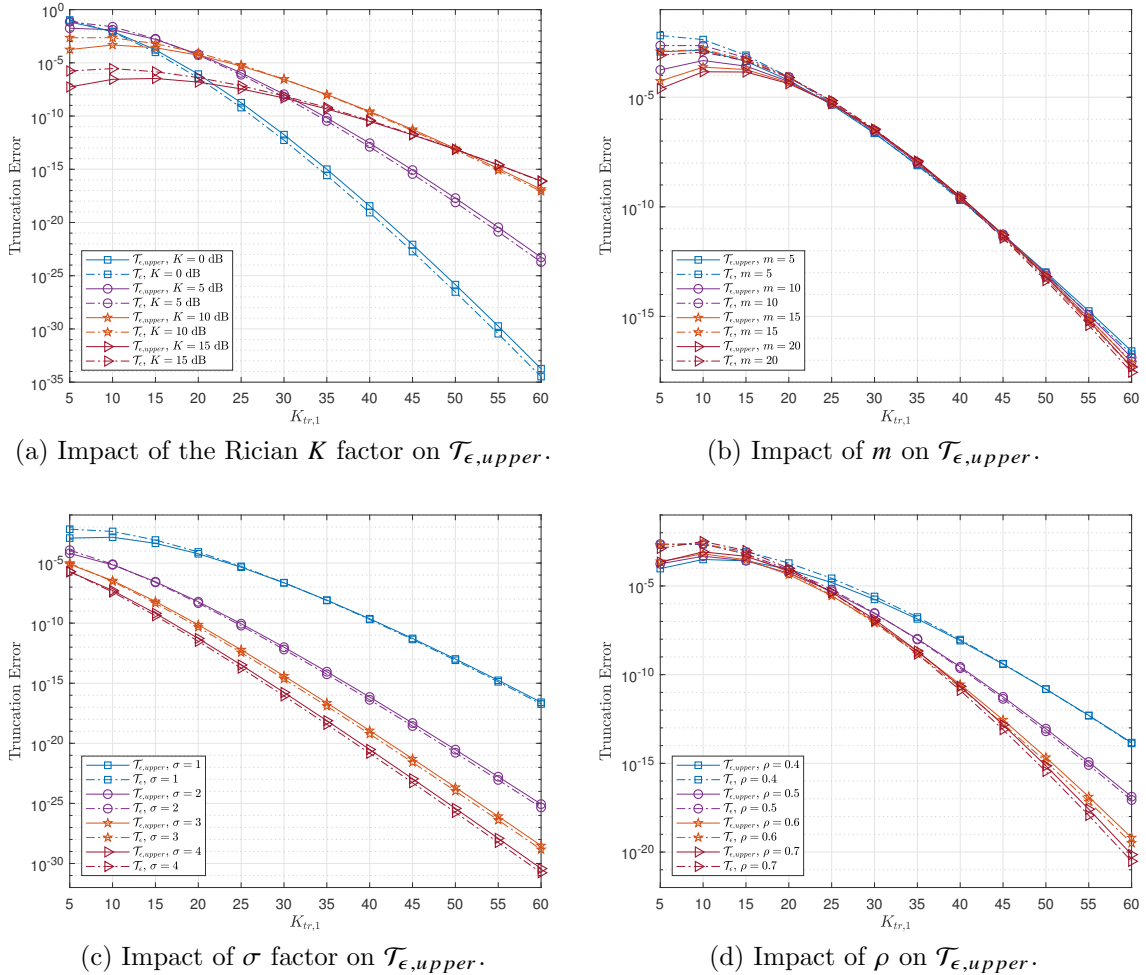


Fig. 8.3: Impact of the Rician K factor, m , σ , and ρ on $\mathcal{T}_{\epsilon,upper}$ for $r_1 = r_2 = 1$ and Rician K factor of 10 dB.

when $K_{tr,1}$ and K_{tr} are sufficiently large. Also, Fig. 8.3 shows a small $K_{tr,1}$ leads to an insufficient number of terms to achieve convergence in the power series expressions, e.g., (8.5), (8.7), and (8.8). Thus, it can also be observed in Fig. 8.3 that $\mathcal{T}_\epsilon > \mathcal{T}_{\epsilon,upper}$ at the lower range of $K_{tr,1}$. From Fig. 8.3a, it is seen that a larger $K_{tr,1}$ is needed to reduce $\mathcal{T}_{\epsilon,upper}$ as the Rician K factor increases. It is also observed in Fig. 8.3b, Fig. 8.3c, and Fig. 8.3d that an increase in m , σ , and ρ leads to a decrease in $\mathcal{T}_{\epsilon,upper}$. Similarly, Fig. 8.4 shows that an increase in ρ or decrease in γ leads to a decrease in e_{upper} . Therefore, Corollaries 8.2, 8.3, and 8.4 are validated.

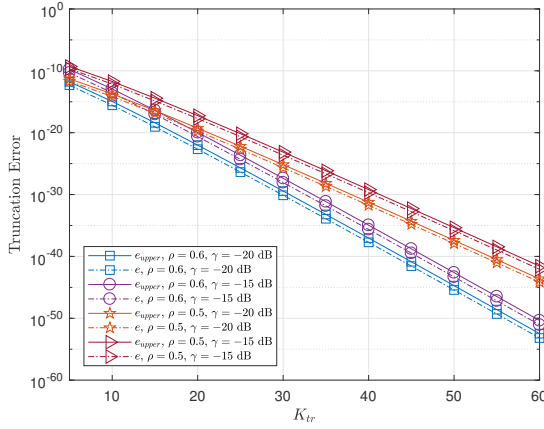


Fig. 8.4: Impact of ρ and γ on e_{upper} for $\gamma_1 = \gamma_2 = -10$ dB and Rician K factor of 7 dB.

Table 8.2: Simulation Parameters

Parameter(s)	Value(s)
Number of Downlink UAVs	$N_D = 3$ [113, 187]
Rician K Factors	7 dB [8, Table V] for $\sigma = 1$
Shaping Parameter	$m = 5$
Transmit Power	$0 \leq P_t \leq 30$ (dBm) [187]
Path Loss Exponent	$L = 2$ [8, Table III], [204]
Cross Correlation Coefficient	$\rho = 0.5$
Carrier Frequency	$f_c = 2$ GHz [187]
Bandwidth	$B_W = 10$ MHz [187]
Transmission rate	$\mathcal{R}^{OMA} = 0.1$ b/s/Hz
Radius	$r_a = 10$ km [206]
Minimum UAV Altitude	$h_{min} = 0.1$ km [187]
Altitude Separation Factor	$\omega = 0.1$
Truncation Order	$K_{tr,1} = 30, K_{tr,2} = 40$

8.6.2 Outage Probability and Finite SNR Diversity Gain Analysis

Observation 8.6.2.1 The NOMA-aided UCS can simultaneously support more downlink UAVs on the same spectrum than an OMA-based UCS while achieving almost similar reliability.

Observation 8.6.2.2 Smaller cross correlation corresponds to higher reliability for both NOMA and OMA transmissions.

The impact of the minimum altitude (h_{min}) on the NOMA outage probability of downlink UAV- j ($Pr(O_j^{NOMA})$) is plotted in Fig. 8.5 for $1 \leq j \leq N_D$.

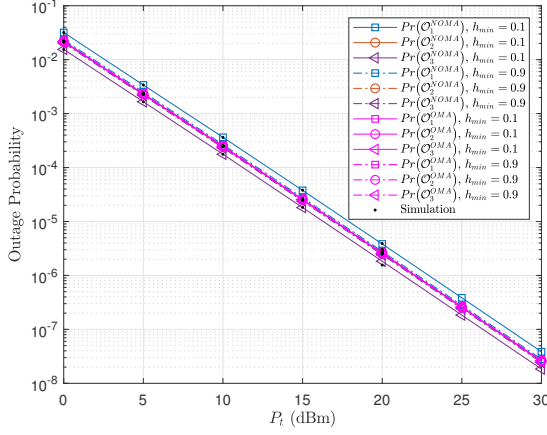


Fig. 8.5: Impact of minimum altitude h_{min} on NOMA outage probability.

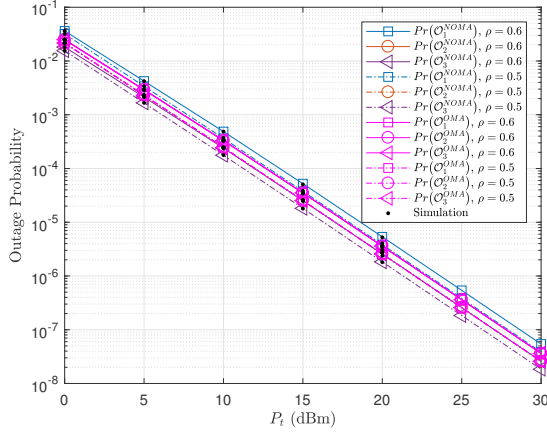


Fig. 8.6: Impact of cross correlation coefficient ρ on NOMA outage probability.

It is observed that $Pr(O_j^{NOMA})$ is not limited by MUI, despite interference from the SOIs of other downlink UAVs. It is also seen that $Pr(O_{j-1}^{NOMA}) > Pr(O_j^{NOMA}) > Pr(O_{j+1}^{NOMA})$ at low h_{min} . Such an occurrence is due to the power allocation factor (a_j), which is larger for downlink UAVs operating at higher altitudes (h_j). Specifically, when h_{min} is low, the difference between a_j and a_{j+1} is larger, leading to lower NOMA outage probability for downlink UAVs at higher altitudes. As h_{min} is increased, the difference between a_j and a_{j+1} diminishes due to the altitude separation factor (ω). Thus, the downlink UAVs exhibit very similar NOMA outage probabilities for $h_{min} = 0.9$. When compared against the OMA-based UCS, it is evident that the NOMA-aided UCS achieve

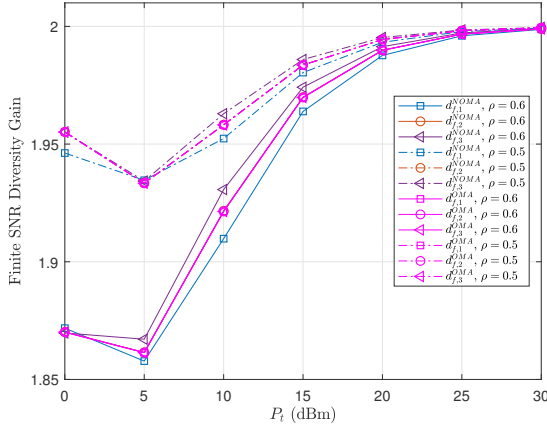


Fig. 8.7: Impact of cross correlation coefficient ρ on NOMA finite SNR diversity gain.

similar outage probability particularly at high h_{min} . Therefore, the NOMA-aided UCS is able to achieve similar reliability to an OMA-based UCS while simultaneously supporting a greater number of downlink UAVs.

The impact of the cross correlation coefficient (ρ) on the NOMA outage probability of downlink UAV- j , i.e., $Pr(O_j^{NOMA})$, is plotted in Fig. 8.6 for $1 \leq j \leq N_D$. It is seen that an increase in ρ corresponds to an increase in $Pr(O_j^{NOMA})$ and $Pr(O_j^{OMA})$. Such a behavior is due to the decrease in diversity gain, i.e., $d_{f,j}^{NOMA}$ and $d_{f,j}^{OMA}$, as cross correlation (ρ) increases [216].

A clearer picture of the outage probability decay behavior is seen in Fig. 8.7, where $d_{f,j}^{NOMA}$ and $d_{f,j}^{OMA}$ is plotted for $1 \leq j \leq N_D$. Specifically, similar trends are also observed in Fig. 8.7 at low P_t regimes, with both NOMA and OMA transmissions experiencing lower $d_{f,j}^{NOMA}$ and $d_{f,j}^{OMA}$, respectively, as ρ is increased. However, at high P_t regimes, it is observed that the impact of ρ diminishes since both $d_{f,j}^{NOMA} \rightarrow 2$ and $d_{f,j}^{OMA} \rightarrow 2$ as P_t increases. Such an observation is due to the fact that ρ only affects the coding gain of selection combining techniques [221]. In particular, the coding gain of both NOMA and OMA transmissions increases as P_t increases at low P_t regimes. As a result, a lower $d_{f,j}^{NOMA}$ and $d_{f,j}^{OMA}$ is experienced when ρ is increased. However, at high P_t regimes, the increase in the coding gain becomes negligible. Hence, $d_{f,j}^{NOMA} = d_{f,j}^{OMA} = 2$ for $\rho \in \{0.5, 0.6\}$, which validate Corollaries 8.5 and 8.6. Therefore, it is demonstrated that a low cross correlation is required in order to achieve a lower outage probability for the

NOMA-aided UCS. Additionally, the coding gain of selection combining for both NOMA and OMA transmissions becomes stagnant at high P_t regimes.

8.7 Chapter Summary

To address spectrum scarcity in UAV communications, a NOMA-aided UCS with dual-antenna downlink UAVs employing selection combining is investigated in this chapter. Through new closed-form expressions for the joint PDF and joint CDF, new expressions pertaining to the outage probability and finite SNR diversity gain of the NOMA-aided UCS are presented. It is shown that more downlink UAVs can be supported on the same spectrum with the NOMA-aided UCS, with an outage probability that is similar to OMA-based UCSs. Furthermore, the effect of cross correlation is analyzed, where it is shown that lower correlation leads to lower outage probability in the NOMA-aided UCS. Also, it is demonstrated that correlation only reduces the diversity gain of NOMA-aided and OMA-based UCSs at low SNR regimes. Therefore, NOMA-aided UCSs are an attractive alternative over OMA-based schemes in future wireless systems.

Chapter 9

Conclusions and Future Directions

9.1 Conclusions

Hybrid-duplex communications is proposed as a viable step towards enhancing spectrum efficiency for MAV and UAV networks in various realistic environments. Through new analytical frameworks, HBD communications in networks with single or an arbitrary number of uplink and downlink nodes are shown to achieve significantly better performance over HD systems at low SNR regimes.

Beginning with the case of single uplink and downlink nodes in HBD-ACSSs and HBD-UCSSs, closed-form outage probability, finite SNR diversity gain and finite SNR DMT expressions are obtained for the II, SIC and joint detectors in Rician fading environments. At low SNR regimes, HBD systems are shown to achieve lower outage probability and higher diversity gain than HD systems. Suitable interference scenarios for the II, SIC and joint detectors are also identified. At asymptotic SNR regimes, it is shown that the SIC detector attains zero diversity gain. It is also demonstrated that the diversity gain of the joint detector is not affected by the data rate of the interfering signal under sufficiently strong interference. In contrast, it is established that the data rate of the interference must be lower than the data rate of the desired signal in order for the SIC detector to achieve non-zero diversity gain.

Apart from Rician fading environments, aeronautical communications can also occur over environments where fading and shadowing are jointly present. In this aspect, the outage probabilities of UAV networks with single uplink and downlink UAVs are analyzed for Rician shadowed fading channels. Through new analytical frameworks based on a

power series approach, closed-form expressions for the PDF, CDF, fractional moment, and outage probability are obtained under the Rician shadowed fading model. Extensive analysis shows that the impact of shadowing on the SI channel is negligible at the FD-GS. It is also demonstrated that severe shadowing on the desired link of the FD-GS causes higher outage probability, despite SI mitigation measures. At the downlink UAV, it is seen that the joint detector is more robust to shadowing than the II detector.

Analytical frameworks are also proposed for multi-UAV networks with an arbitrary number of uplink and downlink UAVs. Specifically, a BPP-based outage probability analysis framework is proposed for multi-UAV networks with an arbitrary number of uplink UAVs. When compared against HD-UCSs, it is observed that multi-UAV networks employing HBD-UCSs can concurrently support a greater number of uplink UAVs with lower outage probability.

NOMA-aided multi-UAV networks are also investigated as a means to further enhance spectrum efficiency in HBD-based UAV communications. Through the introduction of a BPP-based analytical framework, the ergodic capacity of multi-UAV NOMA-aided FD-HetNets is analyzed over Rician fading channels. It is shown that a higher ergodic capacity is achieved with FD-HetNets than HD-HetNets, with FD-HetNets able to simultaneously support more UAVs on the same spectrum at lower altitudes. In the presence of weak SI suppression and strong oscillator phase noise at the FD-GS, FD-HetNets are still able to achieve higher ergodic sum capacity than HD-HetNets.

As NOMA-aided UAV communications over correlated channels are a possibility when considering multi-antenna transceivers, the performance of NOMA transmissions over correlated Rician shadowed fading channels is investigated for UAVs employing dual-diversity selection combining. Using a bivariate Rician shadowed fading model, the joint PDF, joint CDF, outage probability and finite SNR diversity gain of the NOMA-aided UCS is obtained in closed-form. Performance analysis of the NOMA-aided UCS reveals that a greater number of UAVs can simultaneously share the same spectrum while achieving an outage probability that is comparable to that of OMA-based UCSs. It is also demonstrated that cross correlation only affects the diversity gain of both NOMA and OMA transmissions at low SNR regimes.

Therefore, the analysis conducted in this thesis demonstrates the feasibility of addressing spectrum scarcity in aeronautical communications through HBD systems.

9.2 Future Directions

9.2.1 Impact of UAV Flight Velocity

One unique characteristic of UAV communications is the associated flight velocity of UAVs due to mobility. By considering the impact of UAV flight velocity in UAV channel models, a greater understanding of Doppler effects in UAV communications can be obtained. While some works in the literature have ignored UAV flight velocity, e.g., in [4], the present research and other UAV-related studies have assumed that Doppler can be compensated, e.g., in [44] and [48].

From the remaining studies that have considered UAV flight velocity in UAV channel models, a few approaches towards modeling velocity can be seen. In [50, 51], and [55], the authors assumed that the UAVs are flying at constant velocities in the UAV channel models. However, such an assumption may not always be valid as UAVs in the same airspace can vary flight velocities in response to air traffic or operational requirements. Another approach is to model flight velocity as a RV, as was done in [63] where the UAV flight velocity relative to a ground receiver is modeled as a Gaussian RV. Future works can consider extending the approach in [63] to obtain PDF expressions of Doppler PDF expressions for UAV channel models.

9.2.2 FD Transceivers for UAV Communications

In HBD UAV communications, the spectrum efficiency of UAV communications is improved by enabling uplink and downlink UAVs, equipped with HD transceivers, to concurrently operate on the same spectrum, as shown in [18]. To further improve spectrum efficiency, UAVs can be equipped with FD transceivers instead of HD transceivers. Already, research interest in this direction has been seen in recent works, e.g., [16, 222, 223].

From a system model perspective, there is little difference in the FD transceiver modeling for UAVs and GSs. For instance, the SI-related terms in (4.1) can be introduced in (4.4) to model UAV-2 as a FD-capable node in the HBD-UCS. However, in practice, FD transceivers equipped on UAVs must comply with regulatory requirements. For instance, UAVs must adhere to weight restrictions stipulated by the Civil Aviation Authority of Singapore (CAAS) unless it is operating under special permits [224]. In this context, the

feasibility of having FD transceivers on UAVs that satisfy a small and light form factor requirement remains to be seen.

Tradeoffs between cost and performance is another challenge in realizing FD transceivers on UAVs. In particular, achieving high levels of SI mitigation in FD transceivers requires high-quality oscillators [74]. Similarly, it has been shown in [70] that using cheaper and less components leads to considerable nonlinearities in FD transceivers. Evidently, sacrificing performance to reduce the cost of FD transceivers equipped on UAVs may not enable an HBD-UCS to meet UAV communication requirements, e.g., in terms of reliability. As such, the characterization of FD transceiver design limitations in terms of cost and design considerations is an open research problem, which must be addressed before FD-enabled UAVs can be realized.

9.2.3 Feasibility of Interference Forwarding in HBD UAV Communications

The concept of interference forwarding (IF), as an interference management strategy, involves interference being forwarded by a relay node to a destination node for the purpose of interference cancellation [22, 85]. In particular, the destination node experiences stronger interference due to IF from the relay. As such, SIC is undertaken at the destination node to recover the SOI.

As an interference management strategy, IF enables improved performance at receivers experiencing moderate interference [22]. Thus, IF is an attractive alternative to the computationally expensive JD approach in moderate interference scenarios, where interference is neither strong nor weak. In the literature, IF has been studied for both HD or FD relays. In the former, i.e., HD relays, IF occurs over more than one time slot [22, 200]. In contrast, IF with FD relays enables the concurrent reception and transmission of signals on the same spectrum [85, 126]. Therefore, when compared to HD relays, improved spectrum utilization is realizable with FD relays. In this context, IF is a pragmatic interference management technique for HBD UAV communications. When adopted for the HBD-UCS in Fig. 2.7, the FD-enabled GS, or an additional FD-enabled UAV, can act as a relay to perform IF to UAV-2 that is equipped with a SIC detector.

Although the performance of the HBD-UCS can be improved through IF when moderate interference is experienced at UAV-2, the feasibility of IF for practical HBD UAV communications is an open research problem. For instance, IF for scenarios involving a small number of nodes has been well investigated, e.g., [85, 126, 200]. However, considering the ubiquitous nature of UAV communications, supporting a considerable number of deployed UAVs is a must for any practical multi-UAV network with HBD communications. In this aspect, the scalability of IF to support a large number of UAVs in an HBD-UCS is currently unknown, with a feasibility study of implementing IF for HBD UAV communications lacking in the existing literature. The outcome of such a feasibility study can, for example, be used to determine the ideal number of FD-enabled GSs or UAVs functioning as relays, and the expected processing delays, for a given number of deployed UAVs. Another outcome of the feasibility study involves quantifying the outage probability and finite SNR diversity gain of IF in HBD UAV communications, which can be compared against the II, SIC, and JD approaches. Such details will, in due time, come in handy for system designers when considering the various available strategies for inter-UAV interference management.

9.2.4 SIC-based Detection Complexity and Error Propagation in Power-Domain NOMA

The signal models and the resultant SINR expressions in Chapter 7 and Chapter 8 enables an arbitrary number of uplink UAVs (N_U) and downlink UAVs (N_D) to be considered in the multi-UAV HBD-UCS. Yet, when N_U or N_D is large, the SIC detection process can become complex [124, 125].

For instance, the FD-enabled GS and downlink UAVs perform SIC-based detection in the presence of MUI and inter-UAV interference from uplink UAVs. In order for the SIC-based detection process to be effective, it is necessary that CSI knowledge is made known to the FD-enabled GS and downlink UAVs. Although one can assume that full CSI is available, such an assumption is unrealistic in practice. Instead, a more prudent approach can be to assume that only partial CSI is available at the FD-enabled GS and the downlink UAVs. One possible approach to model partial CSI is to employ the technique in [81], where channel estimation error is assumed to follow a Gaussian distribution.

However, it is important to note that the technique in [81] only reflects the accuracy of the partial CSI acquisition process and not the complexity of partial CSI acquisition. In particular, acquiring the CSI of all UAVs in the multi-UAV HBD-UCS when N_U or N_D is large can increase the complexity of the CSI acquisition process especially when mobility is considered. Thus, accounting for both the accuracy and complexity of partial CSI acquisition in the context of HBD UAV communications is an open research problem.

Apart from SIC-based detection complexity, error propagation is another issue faced in power-domain NOMA for a multi-UAV HBD-UCS when N_U or N_D is increased [124, 125]. Specifically, for the SIC-based detection at the FD-enabled GS and downlink UAVs, detection errors in the early stage of SIC detection hinders the detection process of the subsequent stages as interference may not be adequately removed. The issue of error propagation during SIC is further compounded when partial CSI is assumed, since channel estimation errors can contribute to residual interference after SIC [125]. In [83, 126, 137, 138], the authors accounted for residual interference after SIC by introducing a residual interference power coefficient. Likewise, $\beta_{x,j}, x \in \{mbs, i\}$ was introduced in Chapter 7 to account for imperfect SIC at the downlink UAVs, where $\beta_{x,j} = 0$ denotes perfect cancellation and $\beta_{x,j} = 1$ denotes no cancellation [126]. The variable β can also be used to represent the accuracy of the CSI acquisition process [83]. Thus, by introducing a residual interference power coefficient, e.g., β , the impact of channel estimation errors on the residual SIC interference can be analyzed. However, it is noted that this approach does not account for error propagation through each SIC stage and instead assumes some level of residual interference at the end of the SIC detection process. Thus, modeling the error propagation for each SIC stage through a comprehensive mathematical framework in power-domain NOMA remains an open research problem.

9.2.5 User Pairing in Power-Domain NOMA

Thus far, the signal models and resultant SINR expressions in Chapter 7 and Chapter 8 are based on the assumption that the uplink and downlink UAVs are assumed to be grouped, i.e., paired, based on distance. Specifically, the motivation behind such an assumption is due to the conjecture that a shorter distance provides stronger channel gains when the average CSI is considered [126]. However, in practice, the grouping of all

UAVs must first be made known to the FD-enabled GS and downlink UAVs to enable the SIC-based detection process to be carried out. Such a problem is known as user pairing in NOMA-related literature.

In this regard, there exists some studies on user pairing in power-domain NOMA, e.g., [138–141]. In [139], users are uniformly distributed in a disc that is divided into two regions. Then, by assuming a distance-based pairing strategy, users in the inner region of the disc are paired with users in the outer region of the disc. Then, the authors studied the impact of power allocation and signal alignment for the distance-based pairing strategy. In [140], the impact of power allocation for a pairing strategy based on channel gain was studied. Specifically, the authors paired a user with weak instantaneous channel gain with a user that has strong instantaneous channel gain before analyzing fixed and dynamic power allocation strategies. Similarly, a user pairing strategy based on instantaneous channel gain was employed in [141], where a matching algorithm that optimizes user pairing and transmit power allocation was proposed. The authors in [138] investigated two strategies for user pairing based on instantaneous channel gain. The first strategy involves randomly choosing two users. Then, the user with the stronger instantaneous channel gain, i.e., strong user, employs SIC-based detection while the other weaker user employs II detection. The second scheme involves comparing the instantaneous channel gains against a pair of threshold variables, T_1 and T_2 , that satisfy $T_2 \leq T_1$. Then, the user with instantaneous channel gain above T_1 is designated as the strong user while the other user is designated as the weaker user only if the instantaneous channel gain is below T_2 .

It is apparent that user pairing strategies based on instantaneous channel gains have been widely investigated. In particular, it is intuitive that user pairing based on instantaneous channel gains can yield better performance in power-domain NOMA transmissions. However, in a multi-UAV HBD-UCS, such approaches may require high overhead costs due to the need for frequent CSI acquisition and UAV scheduling. To avoid these issues, one can consider a distance-based pairing strategy for HBD UAV communications. Such distance-based pairing strategies may be useful in a multi-UAV HBD-UCS when prior knowledge of the UAV trajectories are available. Interestingly, the effectiveness of a distance-based pairing strategy, when compared against instantaneous channel gain-based user pairing, has not been widely studied. Thus, the tradeoffs between both

distance-based and channel gain-based user pairing remains an open research challenge for power-domain NOMA in multi-UAV HBD-UCSs.

Appendices

Appendix A

Mathematical Proofs in Chapter 3

A.1 Proof of Outage Probability with SIC detector at AS-2

Let X_{gs} be the average received power of the SOI with non-centered chi-squared PDF $f_{X_{gs}}(x) = \frac{K_{X_{gs}}+1}{\Omega_X \alpha_{g,2}} \exp\left(-K_{X_{gs}} - \frac{K_{X_{gs}}+1}{\Omega_X \alpha_{g,2}}x\right) I_0\left(2\sqrt{\frac{K_{X_{gs}}(K_{X_{gs}}+1)}{\Omega_X \alpha_{g,2}}}x\right)$, where $I_0(\cdot)$ is the modified

Bessel function of the first kind with zero order [49, Eq. (8.445)]. Similarly, let Y_1 be the average received power of the interfering signal with non-centered chi-squared PDF $f_{Y_1}(y) = \frac{K_{Y_1}+1}{\Omega_X \alpha_{1,2}} \exp\left(-K_{Y_1} - \frac{K_{Y_1}+1}{\Omega_X \alpha_{1,2}}y\right) I_0\left(2\sqrt{\frac{K_{Y_1}(K_{Y_1}+1)}{\Omega_X \alpha_{1,2}}}y\right)$.

The closed-form SIC outage probability at AS-2 is equivalent to computing the sum of the areas of outage regions P_1 and P_2 , i.e., $\Pr(O_2^{HBD(SIC)}) = P_1 + P_2$. Let the outage regions be defined as $P_1 = \Pr\left\{Y_1 < \gamma_{th,gs}^{HBD}(1 + X_{gs})\right\}$ and $P_2 = \Pr\left\{Y_1 \geq \gamma_{th,2}^{HBD}(1 + X_{gs}), X_{gs} < \gamma_{th,2}^{HBD}\right\}$. The expression for P_1 can be rewritten as [45]:

$$\begin{aligned} P_1 &= \int_0^\infty \int_0^{\gamma_{th,gs}^{HBD}(1+X_{gs})} f_{Y_1}(y) f_{X_{gs}}(x) dy dx \\ &= \sum_{q \geq 0} \sum_{l=0}^{q+1} \alpha(q, \Omega_X \alpha_{1,2}, K_{Y_1}, \gamma_{th,gs}^{HBD}) \binom{q+1}{l} E\{X_{gs}^l\}, \end{aligned} \quad (\text{A.1})$$

where $E\{\cdot\}$ represents the expectation function. The expression for P_2 can be expressed

as:

$$\begin{aligned}
 P_2 &= \int_0^{\gamma_{th,2}^{HBD}} \int_{\gamma_{th,gs}^{HBD}(1+X_{gs})}^{\infty} f_{Y_1}(y) f_{X_{gs}}(x) dy dx \\
 &= \int_0^{\gamma_{th,2}^{HBD}} Q_1 \left(\sqrt{2K_{Y_1}}, \sqrt{\frac{2(K_{Y_1} + 1)\gamma_{th,gs}^{HBD}(1+x)}{\Omega_X \alpha_{1,2}}} \right) f_{X_{gs}}(x) dx. \quad (\text{A.2})
 \end{aligned}$$

From [157], $f_{X_{gs}}(x) = \sum_{j \geq 0} \alpha(j, \Omega_X \alpha_{g,2}, K_{X_{gs}}, 1)x^j$. Thus, (A.2) can be rewritten as:

$$\begin{aligned}
 P_2 &= 1 - Q_1 \left(\sqrt{2K_{X_{gs}}}, \sqrt{\frac{2(K_{X_{gs}} + 1)\gamma_{th,2}^{HBD}}{\Omega_X \alpha_{g,2}}} \right) \\
 &\quad - \int_0^{\gamma_{th,2}^{HBD}} \left(\sum_{j \geq 0} \alpha(j, \Omega_X \alpha_{g,2}, K_{X_{gs}}, 1)x^j \right) \\
 &\quad \times \left(\sum_{n \geq 0} \alpha(n, \Omega_X \alpha_{1,2}, K_{Y_1}, \gamma_{th,gs}^{HBD}) \sum_{i=0}^{n+1} \binom{n+1}{i} x^i \right) dx. \quad (\text{A.3})
 \end{aligned}$$

Let $c(n) = \alpha(n, \Omega_X \alpha_{1,2}, K_{Y_1}, \gamma_{th,gs}^{HBD}) \sum_{i=0}^{n+1} \binom{n+1}{i} x^i$ and $d(j) = \alpha(j, \Omega_X \alpha_{g,2}, K_{X_{gs}}, 1)x^j$, then the integral in (A.3) can be written as [157, 225]:

$$\begin{aligned}
 &\int_0^{\gamma_{th,2}^{HBD}} \left(\sum_{n \geq 0} c(n) \right) \left(\sum_{j \geq 0} d(j) \right) dx \\
 &= \int_0^{\gamma_{th,2}^{HBD}} \sum_{n \geq 0} \sum_{i=0}^n c(i) d(n-i) dx \\
 &= \sum_{n \geq 0} \sum_{i=0}^n \alpha(i, \Omega_X \alpha_{1,2}, K_{Y_1}, \gamma_{th,gs}^{HBD}) \alpha(n-i, \Omega_X \alpha_{g,2}, K_{X_{gs}}, 1) \sum_{j=0}^{i+1} \binom{i+1}{j} \int_0^{\gamma_{th,2}^{HBD}} x^{j+n-i} dx \\
 &= \sum_{n \geq 0} \sum_{i=0}^n \sum_{j=0}^{i+1} \alpha(i, \Omega_X \alpha_{1,2}, K_{Y_1}, \gamma_{th,gs}^{HBD}) \alpha(n-i, \Omega_X \alpha_{g,2}, K_{X_{gs}}, 1) \binom{i+1}{j} \frac{(\gamma_{th,2}^{HBD})^{j+n-i+1}}{j+n-i+1}. \quad (\text{A.4})
 \end{aligned}$$

Combining (A.1) and (A.4), the expression in (3.9) can be obtained.

In (A.2), $Q_1 \left(\sqrt{2K_{Y_1}}, \sqrt{\frac{2(K_{Y_1}+1)\gamma_{th,gs}^{HBD}(1+x)}{\Omega_X \alpha_{1,2}}} \right) = 1 - \sum_{n \geq 0} \alpha(n, \Omega_X \alpha_{1,2}, K_{Y_1}, \gamma_{th,gs}^{HBD})(1+x)^{n+1}$ if $\frac{K_{Y_1}+1}{\Omega_X \alpha_{1,2}}(\gamma_{th,gs}^{HBD})(1+x) \geq 0$ [157]. In addition, the PDF $f_{X_{gs}}(x)$ can be expressed as a convergent power series if $\frac{K_{X_{gs}}+1}{\Omega_X \alpha_{g,2}}x \geq 0$ [157]. Assuming the power series in (A.3) is convergent, the resultant product of the power series in (A.4) will also be convergent

[225]. Similarly in (A.1), the power series is convergent if $\gamma_{th,gs}^{HBD} \leq \frac{(\Omega_X \alpha_{1,2})/(1+K_{Y_1})}{2(\Omega_X \alpha_{g,2})/(1+K_{X_{gs}})}$ [45]. Therefore, the closed-form expression in (3.9) holds if the power series in (A.1) and (A.4) are convergent. This completes the proof.

A.2 Proof of Asymptotic Diversity Gain at the FD-enabled GS

From (3.6) and (3.19), $(\Omega_X)^{l_1+l_2-q-1} < 1$ when $l_1+l_2+l_3 \leq q$. Thus, $\lim_{\Omega_X \rightarrow \infty} (\Omega_X)^{l_1+l_2-q-1} = 0$, $l_1 + l_2 + l_3 \leq q$. Therefore, only $l_1 + l_2 + l_3 = q + 1$ needs to be considered, which consequently leads to the numerator in (3.19) to be zero, i.e., $l_1 + l_2 - q - 1 = 0$. This completes the proof.

A.3 Proof of Asymptotic Diversity Gain for the II and SIC detectors at AS-2

To evaluate $\lim_{\Omega_X \rightarrow \infty} d_{f,2}^{HBD(II)}$, the approach seen in (3.20) can be used. Starting with the denominator of $d_{f,2}^{HBD(II)}$, $(\Omega_X)^{l-q-1} < 1$ when $l \leq q$. Thus, $\lim_{\Omega_X \rightarrow \infty} (\Omega_X)^{l-q-1} = 0$ when $l \leq q$. In the numerator, $(l - q - 1)(\Omega_X)^{l-q-2} = 0$ when $l = q + 1$. Similarly, to evaluate $\lim_{\Omega_X \rightarrow \infty} d_{f,2}^{HBD(SIC)}$, we first begin with the denominator of $d_{f,2}^{HBD(SIC)}$. Specifically, $\lim_{\Omega_X \rightarrow \infty} (\Omega_X)^{l-q-1} = 0$ when $l \leq q$ and $(\Omega_X)^{l-q-1} = 1$ when $l = q + 1$. For $(\Omega_X)^{-m-1}$, $\lim_{\Omega_X \rightarrow \infty} (\Omega_X)^{-m-1} = 0$ for $m \geq 0$ and for $(\Omega_X)^{-n-2}$, $\lim_{\Omega_X \rightarrow \infty} (\Omega_X)^{-n-2} = 0$ for $n \geq 0$. In the numerator, $(l - q - 1)(\Omega_X)^{l-q-2} = 0$ when $l = q + 1$. Additionally, $\lim_{\Omega_X \rightarrow \infty} (\Omega_X)^{-m-2} = 0$ when $m \geq 0$ and $\lim_{\Omega_X \rightarrow \infty} (\Omega_X)^{-n-3} = 0$ when $n \geq 0$. This completes the proof.

A.4 Proof of Asymptotic Diversity Gain at the GS and AS-2 in the HD-ACS

At GS, the asymptotic behavior of $d_{f,gs}^{HD}$ can be easily evaluated after some simplifications as shown below:

$$\lim_{\Omega_X \rightarrow \infty} d_{f,gs}^{HD} = \lim_{\Omega_X \rightarrow \infty} \frac{-\sum_{m \geq 0} \alpha(m, 1, K_{X_1}, \gamma_{th,gs}^{HD})(-m - 1)(\Omega_X)^{-m}}{\sum_{m \geq 0} \alpha(m, 1, K_{X_1}, \gamma_{th,gs}^{HD})(\Omega_X)^{-m}}. \quad (\text{A.5})$$

From (A.5), It can be seen that $\lim_{\Omega_X \rightarrow \infty} (\Omega_X)^{-m} = 1$ when $m = 0$, and $\lim_{\Omega_X \rightarrow \infty} (\Omega_X)^{-m} = 0$ when $m > 0$. Thus, when evaluating (A.5), only $m = 0$ needs to be considered. The asymptotic behavior of $d_{f,2}^{HD}$ can also be proven using the same approach. This completes the proof.

Appendix B

Mathematical Proofs in Chapter 4

B.1 Proof of Outage Probability with Joint Detector at UAV-2

Let the non-centered Chi-squared PDF of the instantaneous received SOI power (X_{gs}) be $f_{X_{gs}}(x) = \frac{K_{X_{gs}}+1}{\Omega_X \alpha_{g,2}} \exp\left(-K_{X_{gs}} - \frac{(K_{X_{gs}}+1)}{\Omega_X \alpha_{g,2}} x\right) I_0\left(2\sqrt{\frac{K_{X_{gs}}(K_{X_{gs}}+1)}{\Omega_X \alpha_{g,2}}} x\right)$, where $I_0(\cdot)$ is the modified Bessel function of the first kind with zero order [49]. Likewise, let $f_{Y_1}(y) = \frac{K_{Y_1}+1}{\Omega_X \alpha_{1,2}} \exp\left(-K_{Y_1} - \frac{(K_{Y_1}+1)}{\Omega_X \alpha_{1,2}} y\right) I_0\left(2\sqrt{\frac{K_{Y_1}(K_{Y_1}+1)}{\Omega_X \alpha_{1,2}}} y\right)$ be the PDF of the instantaneous received interfering signal power (Y_1). Let $Pr(O_{JD}^1)$ and $Pr(O_{JD}^2)$ be outage regions, where O_{JD}^1 and O_{JD}^2 are defined in (4.6) and (4.7), respectively. Then, the closed-form outage expression for the joint detector is evaluated as follows [153, eq. (17)]:

$$Pr(O_2^{HBD(JD)}) = \int_0^{\gamma_{th,2}^{HBD}} f_{X_{gs}}(x) dx + \int_{\gamma_{th,2}^{HBD}}^{b_1} \int_{\frac{x}{\gamma_{th,2}^{HBD}}-1}^{b_2-x} f_{Y_1}(y) f_{X_{gs}}(x) dy dx. \quad (\text{B.1})$$

The first term on the RHS of (B.1) is easily evaluated to be [45, Table I]:

$$\int_0^{\gamma_{th,2}^{HBD}} f_{X_{gs}}(x) dx = 1 - Q_1\left(\sqrt{2K_{X_{gs}}}, \sqrt{\frac{2(K_{X_{gs}}+1)\gamma_{th,2}^{HBD}}{\Omega_X \alpha_{g,2}}}\right), \quad (\text{B.2})$$

which is valid for all $\frac{K_{Y_1}+1}{\Omega_X \alpha_{1,2}} \gamma_{th,2}^{HBD} \geq 0$ [157]. To evaluate the second term on the RHS of (B.1), we first express the PDF of the instantaneous received SOI power ($f_{X_{gs}}(x)$) into a

power series as follows [157, eq. (5)]:

$$f_{X_{gs}}(x) \approx \sum_{q=0}^{K_{tr}} (-1)^q \exp(-K_{X_{gs}}) \frac{L_q^{(0)}(K_{X_{gs}})}{q!} \left(\frac{1+K_{X_{gs}}}{\Omega_X \alpha_{g,2}} \right)^{q+1} x^q \approx \sum_{q=0}^{K_{tr}} \hat{d}(q). \quad (\text{B.3})$$

Likewise, the PDF of the instantaneous received interfering signal power ($f_{Y_1}(y)$) becomes [157, eq. (5)]:

$$f_{Y_1}(y) \approx \sum_{n=0}^{K_{tr}} (-1)^n \exp(-K_{Y_1}) \frac{L_n^{(0)}(K_{Y_1})}{n!} \left(\frac{1+K_{Y_1}}{\Omega_X \alpha_{1,2}} \right)^{n+1} y^n. \quad (\text{B.4})$$

Let $c(n) = \sum_{k=0}^{n+1} \bar{\alpha}(n, \Omega_X \alpha_{1,2}, K_{Y_1}, 1) \binom{n+1}{k} (-1)^{n+1} [(-b_2)^{n+1-k} - (-\gamma_{th,2}^{HBD})^{-k}] x^k$. Then, the second term on the RHS of (B.1) becomes [157, 225]:

$$\begin{aligned} & \int_{\gamma_{th,2}^{HBD}}^{b_1} \int_{\frac{x}{\gamma_{th,2}^{HBD}}-1}^{b_2-x} f_{Y_1}(y) f_{X_{gs}}(x) dy dx \\ & \approx \int_{\gamma_{th,2}^{HBD}}^{b_1} f_{X_{gs}}(x) \left[\sum_{n=0}^{K_{tr}} \sum_{k=0}^{n+1} \bar{\alpha}(n, \Omega_X \alpha_{1,2}, K_{Y_1}, 1) \binom{n+1}{k} \right. \\ & \quad \left. \times (-1)^{n+1} [(-b_2)^{n+1-k} - (-\gamma_{th,2}^{HBD})^{-k}] x^k \right] dx \end{aligned} \quad (\text{B.5})$$

$$\approx \int_{\gamma_{th,2}^{HBD}}^{b_1} \left(\sum_{n=0}^{K_{tr}} c(n) \right) \left(\sum_{q=0}^{K_{tr}} \hat{d}(q) \right) dx \quad (\text{B.6})$$

$$\approx \int_{\gamma_{th,2}^{HBD}}^{b_1} \sum_{n=0}^{K_{tr}} \sum_{i=0}^n c(i) \hat{d}(n-i) dx \quad (\text{B.7})$$

$$\begin{aligned} & \approx \sum_{n=0}^{K_{tr}} \sum_{i=0}^n \sum_{j=0}^{i+1} \bar{\alpha}(i, \Omega_X \alpha_{1,2}, K_{Y_1}, 1) \\ & \quad \times \bar{\alpha}(n-i, \Omega_X \alpha_{g,2}, K_{X_{gs}}, 1) \binom{i+1}{j} (-1)^{i+1} \\ & \quad \times G_1(i, j, b_2, \gamma_{th,2}^{HBD}) \frac{G_2(j+n-i+1, b_1, \gamma_{th,2}^{HBD})}{j+n-i+1}, \end{aligned} \quad (\text{B.8})$$

where $G_1(i, j, b_2, \gamma_{th,2}^{HBD})$ and $G_2(j+n-i+1, b_1, \gamma_{th,2}^{HBD})$ are defined in (4.9). It should be pointed out that (B.5) is obtained by interchanging the order of summation and integration, which is valid for $\gamma_{th,2}^{HBD} \leq x \leq b_2$ [157], and (B.7) is a result of the Cauchy product [171] in (B.6). Also, $\sum_{q \geq 0} \hat{d}(q)$ in (B.6) is valid for $K_{X_{gs}} \geq 0$ [157]. Combining (B.2) and (B.8) yields the closed-form outage probability expression for $Pr(O_2^{HBD(JD)})$ in (4.9). This completes the proof.

B.2 Proof of Convergence Radius for (4.9)

We begin by noting that (B.6) is convergent if $\sum_{n \geq 0} c(n)$ and $\sum_{q \geq 0} \widehat{d}(q)$ are absolutely convergent [157,171]. Starting with $\sum_{n \geq 0} c(n)$, we note that the PDF of the instantaneous received interfering signal power ($f_{Y_1}(y)$) can be expressed into a power series, as given in (B.4). Also, the term-wise integration of a convergent power series is only valid within the convergence radius [49]. Therefore, it is of importance to verify the convergence of (B.4). Let $|L_n^{(0)}(K_{Y_1})| \leq \exp\left(\frac{K_{Y_1}}{2}\right)$ [157] and $n! = n\Gamma(n)$ [45,49], where $\Gamma(\cdot)$ is the Gamma function. Then, (B.4) becomes:

$$f_{Y_1}(y) = \sum_{n \geq 0} (-1)^n \frac{\exp(-K_{Y_1}/2)}{n\Gamma(n)} \left(\frac{1+K_{Y_1}}{\Omega_X \alpha_{1,2}}\right)^{n+1} y^n = \sum_{n \geq 0} f(n). \quad (\text{B.9})$$

Employing the D'Alembert test, we get:

$$\lim_{n \rightarrow \infty} \frac{|f(n+1)|}{|f(n)|} = \lim_{n \rightarrow \infty} \frac{1}{n} \left(\frac{1+K_{Y_1}}{\Omega_X \alpha_{1,2}}\right) y = 0. \quad (\text{B.10})$$

Therefore, (B.9) has a convergence radius of ∞ , i.e., absolutely convergent, and accordingly, $\sum_{n \geq 0} c(n)$ is also absolutely convergent. The absolute convergence of $\sum_{q \geq 0} \widehat{d}(q)$ is proven in the same manner. Thus, (B.6) and (B.8), are also absolutely convergent. This completes the proof.

Appendix C

Mathematical Proofs in Chapter 5

C.1 Proof for the PDF of $|h|^2$ in (5.9)

To begin, we note that the confluent hypergeometric function ${}_1F_1(\bullet)$ is expressed as [226]:

$${}_1F_1(a; b; z) = \sum_{k \geq 0} \frac{(a)_k z^k}{(b)_k k!}, \quad (\text{C.1})$$

where $(a)_k = \frac{\Gamma(a+k)}{\Gamma(a)}$ is the Pochhammer symbol [177].

Since $\frac{(a)_{k+1}}{(a)_k} = a + n$ [227], and applying the identity in [45, eq. (25)] yields $\Gamma(k+a) \approx k^a \Gamma(k)$ when $k \rightarrow \infty$, then:

$${}_1F_1(a; 1; z) = \sum_{k \geq 0} f(k), \quad (\text{C.2})$$

where $f(k) = \frac{(a)_k}{\Gamma^2(k+1)} z^k$. The absolute convergence of $\sum_{k \geq 0} f(k)$ is easily proven via the D'Alembert test:

$$\lim_{k \rightarrow \infty} \frac{f(k+1)}{f(k)} = \lim_{k \rightarrow \infty} \frac{(a+k)z}{k^2} = 0. \quad (\text{C.3})$$

From the Cauchy product theorem [157, 171], (5.7) can be expressed in truncated form, thus yielding (5.9):

$$\begin{aligned} f_h(x) &= \left(\sum_{n \geq 0} c(n) \right) \left(\sum_{i \geq 0} d(i) \right) \\ &\approx \sum_{n=0}^{K_{tr}} \sum_{i=0}^n \frac{m^m (1+K)}{\Omega (K+m)^m} \frac{(m)_i}{\Gamma^2(i+1)} \left(\frac{K(1+K)}{(K+m)\Omega} \right)^i \left(\frac{-(1+K)}{\Omega} \right)^{n-i} \frac{x^n}{(n-i)!}, \end{aligned} \quad (\text{C.4})$$

where $c(n) = \frac{m^m (1+K)}{\Omega (K+m)^m} \frac{(m)_n}{\Gamma^2(n+1)} \left(\frac{K(1+K)}{(K+m)\Omega} \right)^n x^n$, and $d(i) = \left(\frac{-(1+K)}{\Omega} \right)^i \frac{x^i}{i!}$. Thus, combining (C.4) with (5.8) yields (5.9) which completes the proof.

C.2 Proof of $\widehat{a}(n, \Omega, K, \gamma)$ in (5.12)

To evaluate the function $\bar{a}(n, \Omega, K, m, \gamma)$ for $m \rightarrow \infty$, we first note that the asymptotic expression of $\Gamma[m + n]$, given in [45, eq. (25)], is $\Gamma[m + n] \approx m^n \Gamma[m]$, which yields $(m)_i \approx m^i$. Thereafter, substituting $(m)_i \approx m^i$ into (5.8) yields the following expression:

$$\bar{a}(n, \Omega, K, m, \gamma) \approx \sum_{i=0}^n (-1)^{n-i} \left(\frac{m}{K+m} \right)^m \frac{K^i}{\Gamma^2(i+1)} \left(\frac{m}{K+m} \right)^i \left(\frac{1+K}{\Omega} \right)^{n+1} \frac{\gamma^{n+1}}{(n-i)!(n+1)}. \quad (\text{C.5})$$

Invoking the product rule for limits, $\lim_{m \rightarrow \infty} \bar{a}(n, \Omega, K, m, \gamma)$ can be evaluated separately:

$$\lim_{m \rightarrow \infty} \left(\frac{m}{K+m} \right)^i = \exp \left(i \lim_{m \rightarrow \infty} \ln \left(\frac{m}{K+m} \right) \right) = 1. \quad (\text{C.6})$$

$$\lim_{m \rightarrow \infty} \left(\frac{m}{K+m} \right)^m = \exp \left(\frac{\lim_{m \rightarrow \infty} \ln \left(\frac{m}{K+m} \right)}{\lim_{m \rightarrow \infty} \frac{1}{m}} \right) = \exp(-K). \quad (\text{C.7})$$

Combining (C.6) and (C.7) into (C.5) yields:

$$\begin{aligned} \widehat{a}(n, \Omega, K, \gamma) &= \lim_{m \rightarrow \infty} \bar{a}(n, \Omega, K, m, \gamma) \\ &= \sum_{i=0}^n \frac{(-1)^{n-i} K^i}{\Gamma^2(i+1)} \exp(-K) \left(\frac{1+K}{\Omega} \right)^{n+1} \frac{\gamma^{n+1}}{(n-i)!(n+1)}. \end{aligned} \quad (\text{C.8})$$

This completes the proof.

C.3 Proof for the l^{th} Moment of $|h'|^2$ in (5.15)

To obtain the l^{th} moment of $|h'|^2$, i.e., $E\{|h'|^2\}^l$, from (5.11), the transformation formula ${}_2F_1(a, b; c; z) = (1-z)^{c-a-b} {}_2F_1(c-a, c-b; c; z)$ [49] is invoked upon (5.11) to yield:

$$E\{|h'|^2\}^l = \left(\frac{\Omega}{1+K} \right)^l \Gamma(1+l) \left(\frac{m}{K+m} \right)^{m-1-l} \left(1 + \frac{K}{m} \right)^{m-1-l} {}_2F_1\left(m, -l; 1; \frac{-K}{m}\right). \quad (\text{C.9})$$

Thereafter, $E\{|h'|^2\}^l$ is obtained by evaluating $\lim_{m \rightarrow \infty} E\{|h'|^2\}^l$ with the product rule for limits:

$$\lim_{m \rightarrow \infty} \left(1 + \frac{K}{m} \right)^{m-1-l} = \exp \left(\frac{\lim_{m \rightarrow \infty} \ln \left(1 + \frac{K}{m} \right)}{\lim_{m \rightarrow \infty} \frac{1}{m-1-l}} \right) = \exp(K). \quad (\text{C.10})$$

$$\lim_{m \rightarrow \infty} \left(\frac{m}{K+m} \right)^{m-1-l} = \exp \left(\frac{\lim_{m \rightarrow \infty} \ln \left(\frac{m}{K+m} \right)}{\lim_{m \rightarrow \infty} \frac{1}{m-1-l}} \right) = \exp(-K). \quad (\text{C.11})$$

Additionally, using the asymptotic expression $\Gamma[m + n] \approx m^n \Gamma[m]$ [45, eq. (25)], yields:

$${}_2F_1\left(m, -l; 1; \frac{-K}{m}\right) \approx \sum_{n \geq 0} \frac{(-l)_n}{n!(1)_n} (-K)^n. \quad (\text{C.12})$$

Therefore, combining (C.10), (C.11), and (C.12) into (C.9) leads to (5.15), which completes the proof.

C.4 Proof of Convergence for (5.16)

It is useful to note that (5.16) can be expanded as:

$$\begin{aligned} Pr(O_{gs}^{HBD}) &\approx \sum_{n=0}^{K_{tr}} \sum_{i=0}^n \sum_{l_1+l_2+l_3=n+1} (-1)^{n-i} \left(\frac{m_{X_1}}{K_{X_1} + m_{X_1}} \right)^{m_{X_1}} \frac{(m_{X_1})_i}{\Gamma^2(i+1)} \left(\frac{K_{X_1}}{K_{X_1} + m_{X_1}} \right)^i \\ &\quad \times \left(\frac{1+K_{X_1}}{\Omega_X} \right)^{n+1} \frac{(\gamma_{th,gs}^{HBD})^{n+1}}{(n-i)!(n+1)} \frac{(l_1+l_2+l_3)!}{l_1! \cdot l_2! \cdot l_3!} E\{Y_{si,1}^{l_1}\} E\{Y_{si,2}^{l_2}\} \\ &\approx \sum_{n=0}^{K_{tr}} \sum_{i=0}^n \sum_{l_1+l_2+l_3=n+1} \Xi(n, i, l_1, l_2, l_3). \end{aligned} \quad (\text{C.13})$$

Taking the D'Alembert test, it is easily shown that:

$$\lim_{n \rightarrow \infty} \frac{|\Xi(n+1, i, l_1, l_2, l_3)|}{|\Xi(n, i, l_1, l_2, l_3)|} \stackrel{(a)}{=} \lim_{n \rightarrow \infty} \left(\frac{1+K_{X_1}}{\Omega_X} \right) \left(\frac{n+1}{n+2} \right) \left(\frac{\gamma_{th,gs}^{HBD}}{n} \right) = 0, \quad (\text{C.14})$$

where (a) is obtained using the identity $\Gamma[m + n] \approx m^n \Gamma[m]$ [45, eq. (25)]. Therefore, (5.16) is absolutely convergent. This completes the proof.

C.5 Proof of Outage Probability at the GS over Rician Shadowed Fading and Rician Fading channels

We begin by first proving (5.21). Starting from (5.16), the outage probability expression can be written as:

$$\begin{aligned} Pr(O_{gs}^{HBD}) &\approx \sum_{n=0}^{K_{tr}} \sum_{l_1+l_2+l_3=n+1} \bar{a}(n, 1, K_{X_1}, m_{X_1}, \gamma_{th,gs}^{HBD}) \\ &\quad \times \frac{(n+1)!}{l_1! \cdot l_2! \cdot l_3!} M\{Y_{si,1}^{l_1}\} M\{Y_{si,2}^{l_2}\} (\Omega_X)^{l_1+l_2-n-1}. \end{aligned} \quad (\text{C.15})$$

To obtain the asymptotic outage probability at the GS, one will need to evaluate (C.15) as $\Omega_X \rightarrow \infty$. However, it is useful to note that $\lim_{\Omega_X \rightarrow \infty} (\Omega_X)^{l_1+l_2-n-1} = 0$ when $l_1+l_2 < n+1$, i.e., $l_3 > 0$. On the other hand, $\lim_{\Omega_X \rightarrow \infty} (\Omega_X)^{l_1+l_2-n-1} = 1$ when $l_1+l_2 = n+1$, i.e., $l_3 = 0$. Thus, evaluating (C.15) for multinomial index $l_1 + l_2 = n + 1$ yields the asymptotic outage probability expression in (5.21). The same technique is also used to obtain (5.22). This completes the proof.

C.6 Proof of Outage Probability for the Joint Detector at UAV-2 over Rician shadowed fading channels

C.6.1 Outage Probability Derivation

Before evaluating the closed-form outage probability expression for the joint detector ($Pr(O_2^{HBD(JD)})$), it is useful to first obtain the PDFs of X_{gs} and Y_1 . From (5.9), the PDFs of X_{gs} and Y_1 are given in (C.16) and (C.17), respectively:

$$f_{X_{gs}}(x) \approx \sum_{n=0}^{K_{tr}} \bar{a}(n, \Omega_X \alpha_{g,2}, K_{X_{gs}}, m_{X_{gs}}, 1)(n+1)x^n. \quad (C.16)$$

$$f_{Y_1}(y) \approx \sum_{n=0}^{K_{tr}} \bar{a}(n, \Omega_X \alpha_{1,2}, K_{Y_1}, m_{Y_1}, 1)(n+1)y^n. \quad (C.17)$$

Then, $Pr(O_2^{HBD(JD)})$ is obtained from [153, eq. (17)] as:

$$\begin{aligned} Pr(O_2^{HBD(JD)}) &= Pr\{O_{JD}^1\} + Pr\{O_{JD}^2\} \\ &= F_{X_{gs}}(\gamma_{th,2}^{HBD}) + \int_{\gamma_{th,2}^{HBD}}^{b_1} f_{X_{gs}}(x) \left[F_{Y_1}(b_2 - x) - F_{Y_1}\left(\frac{x}{\gamma_{th,2}^{HBD}} - 1\right) \right] dx, \end{aligned} \quad (C.18)$$

where O_{JD}^1 and O_{JD}^2 are defined in (5.28) and (5.29), respectively, and both b_1 and b_2 are defined in (5.30). The functions $F_{X_{gs}}(\bullet)$ and $F_{Y_1}(\bullet)$ are the CDFs of X_{gs} and Y_1 , respectively, obtainable from (5.10). To simplify the integral on the RHS of (C.18), we note that $(b_2 - x)^{n+1} - \left(\frac{x}{\gamma_{th,2}^{HBD}} - 1\right)^{n+1} = (-1)^{n+1} \sum_{k=0}^{n+1} \binom{n+1}{k} [(-b_2)^{n+1-k} - (-\gamma_{th,2}^{HBD})^{-k}]x^k$, and thus:

$$\begin{aligned} F_{Y_1}(b_2 - x) - F_{Y_1}\left(\frac{x}{\gamma_{th,2}^{HBD}} - 1\right) &\approx \sum_{n=0}^{K_{tr}} \sum_{k=0}^{n+1} \bar{a}(n, \Omega_X \alpha_{1,2}, K_{Y_1}, m_{Y_1}, 1) \binom{n+1}{k} \\ &\quad \times [(-b_2)^{n+1-k} - (-\gamma_{th,2}^{HBD})^{-k}]x^k. \end{aligned} \quad (C.19)$$

Let $c(n)$ and $d(n)$ be defined as:

$$c(n) = \sum_{k=0}^{n+1} \bar{a}(n, \Omega_X \alpha_{1,2}, K_{Y_1}, m_{Y_1}, 1) \binom{n+1}{k} [(-b_2)^{n+1-k} - (-\gamma_{th,2}^{HBD})^{-k}] x^k, \quad (\text{C.20})$$

$$d(n) = \bar{a}(n, \Omega_X \alpha_{g,2}, K_{X_{gs}}, m_{X_{gs}}, 1) (n+1) x^n. \quad (\text{C.21})$$

Then, applying the Cauchy product theorem onto the integral in (C.18) yields [157, 171]:

$$\begin{aligned} & \int_{\gamma_{th,2}^{HBD}}^{b_1} f_{X_{gs}}(x) \left[F_{Y_1}\left(b_2 - x\right) - F_{Y_1}\left(\frac{x}{\gamma_{th,2}^{HBD}} - 1\right) \right] dx \\ & \approx \int_{\gamma_{th,2}^{HBD}}^{b_1} \left(\sum_{n=0}^{K_{tr}} c(n) \right) \left(\sum_{q=0}^{K_{tr}} d(q) \right) dx \\ & \approx \int_{\gamma_{th,2}^{HBD}}^{b_1} \sum_{n=0}^{K_{tr}} \sum_{q=0}^n c(q) d(n-q) dx \end{aligned} \quad (\text{C.22})$$

$$\begin{aligned} & \approx \sum_{n=0}^{K_{tr}} \sum_{q=0}^n \sum_{k=0}^{q+1} \bar{a}(q, \Omega_X \alpha_{1,2}, K_{Y_1}, m_{Y_1}, 1) \bar{a}(n-q, \Omega_X \alpha_{g,2}, K_{X_{gs}}, m_{X_{gs}}, 1) \\ & \quad \times (n+1) \binom{q+1}{k} (-1)^{q+1} G_1(q, k, b_2, \gamma_{th,2}^{HBD}) \frac{G_2(k+n-q, b_1, \gamma_{th,2}^{HBD})}{k+n-q+1}, \end{aligned} \quad (\text{C.23})$$

where $G_1(q, k, b_2, \gamma_{th,2}^{HBD})$ and $G_2(k+n-q+1, b_1, \gamma_{th,2}^{HBD})$ are defined in (5.30). It should be pointed out that (C.23) is obtained by interchanging the summation and integration in (C.22), i.e., term-wise integration [49], which is valid for $\gamma_{th,2}^{HBD} \leq x \leq b_1$. Substituting (C.23) into (C.18) yields the closed-form outage probability expression for $Pr(O_2^{HBD(JD)})$ in (5.30) which completes the proof.

C.6.2 Convergence of (5.30)

We start by expanding the joint detector outage probability expression in (5.30) as:

$$\begin{aligned}
 Pr(O_2^{HBD(JD)}) &\approx \sum_{n=0}^{K_{tr}} \sum_{i=0}^n (-1)^{n-i} \left(\frac{m_{X_{gs}}}{K_{X_{gs}} + m_{X_{gs}}} \right)^{m_{X_{gs}}} \frac{(m_{X_{gs}})_i}{\Gamma^2(i+1)} \\
 &\quad \times \left(\frac{K_{X_{gs}}}{K_{X_{gs}} + m_{X_{gs}}} \right)^i \left(\frac{1 + K_{X_{gs}}}{\Omega_X \alpha_{g,2}} \right)^{n+1} \frac{(\gamma_{th,2}^{HBD})^{n+1}}{(n-i)!(n+1)} \\
 &+ \sum_{n=0}^{K_{tr}} \sum_{q=0}^n \sum_{k=0}^{q+1} \sum_{s=0}^q \sum_{z=0}^{n-q} \left(\frac{m_{Y_1}}{K_{Y_1} + m_{Y_1}} \right)^{m_{Y_1}} \frac{(m_{Y_1})_s}{\Gamma^2(s+1)} \left(\frac{K_{Y_1}}{K_{Y_1} + m_{Y_1}} \right)^s \\
 &\quad \times \left(\frac{1 + K_{Y_1}}{\Omega_X \alpha_{1,2}} \right)^{q+1} \frac{(-1)^{q-s}}{(q-s)!(q+1)} \left(\frac{m_{X_{gs}}}{K_{X_{gs}} + m_{X_{gs}}} \right)^{m_{X_{gs}}} \frac{(m_{X_{gs}})_z}{\Gamma^2(z+1)} \\
 &\quad \times \left(\frac{K_{X_{gs}}}{K_{X_{gs}} + m_{X_{gs}}} \right)^z \left(\frac{1 + K_{X_{gs}}}{\Omega_X \alpha_{g,2}} \right)^{n-q+1} \frac{(-1)^{n-q-z}(n+1)\binom{q+1}{k}(-1)^{q+1}}{(n-q-z)!(n-q+1)} \\
 &\quad \times G_1(q, k, b_2, \gamma_{th,2}^{HBD}) \frac{G_2(k+n-q+1, b_1, \gamma_{th,2}^{HBD})}{k+n-q+1} \\
 &\approx \sum_{n=0}^{K_{tr}} \sum_{i=0}^n \Theta(n, i) + \sum_{n=0}^{K_{tr}} \sum_{q=0}^n \sum_{k=0}^{q+1} \sum_{s=0}^q \sum_{z=0}^{n-q} \Delta(n, q, k, s, z). \tag{C.24}
 \end{aligned}$$

For the first term in (C.24), applying the D'Alembert test yields:

$$\lim_{n \rightarrow \infty} \frac{|\Theta(n+1, i)|}{|\Theta(n, i)|} \stackrel{(a)}{=} \lim_{n \rightarrow \infty} \gamma_{th,2}^{HBD} \left(\frac{1 + K_{X_{gs}}}{\Omega_X \alpha_{g,2}} \right) \left(\frac{n+1}{n+2} \right) \left(\frac{1}{n} \right) = 0, \tag{C.25}$$

where (a) results from the identity $\Gamma[m+n] \approx m^n \Gamma[m]$ [45, eq. (25)]. Therefore, the first term in (C.24) is absolutely convergent.

For the second term in (C.24), applying the D'Alembert test yields:

$$\begin{aligned}
 \lim_{n \rightarrow \infty} \frac{|\Delta(n+1, q, k, s, z)|}{|\Delta(n, q, k, s, z)|} &\stackrel{(a)}{=} \lim_{n \rightarrow \infty} \frac{(n-q+1)(n+2)(k+n-q+1)}{(n-q+2)(n+1)(k+n-q+2)} \left(\frac{1}{n} \right) \\
 &\quad \times \frac{G_2(k+n-q+2, b_1, \gamma_{th,2}^{HBD})}{G_2(k+n-q+1, b_1, \gamma_{th,2}^{HBD})} \\
 &\stackrel{(b)}{=} \lim_{n \rightarrow \infty} \frac{(n-q+1)(n+2)(k+n-q+1)}{(n-q+2)(n+1)(k+n-q+2)} \left(\frac{\gamma_{th,2}^{HBD} 2^{R_1^{HBD}}}{n} \right) = 0, \tag{C.26}
 \end{aligned}$$

where (a) is due to the identity $\Gamma[m+n] \approx m^n \Gamma[m]$ [45, eq. (25)], and (b) is due to the

fact that:

$$\begin{aligned} \lim_{n \rightarrow \infty} \frac{G_2(k+n-q+2, b_1, \gamma_{th,2}^{HBD})}{G_2(k+n-q+1, b_1, \gamma_{th,2}^{HBD})} &= \lim_{n \rightarrow \infty} \frac{(\gamma_{th,2}^{HBD})^{k+n-q+2} [(2^{R_1^{HBD}})^{k+n-q+2} - 1]}{(\gamma_{th,2}^{HBD})^{k+n-q+1} [(2^{R_1^{HBD}})^{k+n-q+1} - 1]} \\ &= \gamma_{th,2}^{HBD} 2^{R_1^{HBD}}. \end{aligned} \quad (\text{C.27})$$

As such, (C.26) shows that the second term in (C.24) is absolutely convergent. Therefore, (5.30) is also absolutely convergent. This completes the proof.

C.7 Proof of Outage Probability Error Floor for the Joint Detector at UAV-2 over Rician Shadowed Fading and Rician Fading channels

Starting with the case of the joint detector over Rician shadowed fading channels, the outage probability expression from (5.30) can be expressed as:

$$\begin{aligned} Pr(O_2^{HBD(JD)}) &\approx \sum_{n=0}^{K_{tr}} \bar{a}(n, \alpha_{g,2}, K_{X_{gs}}, m_{X_{gs}}, \gamma_{th,2}^{HBD})(\Omega_X)^{-n-1} \\ &+ \sum_{n=0}^{K_{tr}} \sum_{q=0}^n \sum_{k=0}^{q+1} \bar{a}(q, \alpha_{1,2}, K_{Y_1}, m_{Y_1}, 1) \bar{a}(n-q, \alpha_{g,2}, K_{X_{gs}}, m_{X_{gs}}, 1)(n+1) \\ &\times \binom{q+1}{k} (-1)^{q+1} G_1(q, k, b_2, \gamma_{th,2}^{HBD}) \frac{G_2(k+n-q, b_1, \gamma_{th,2}^{HBD})}{k+n-q+1} (\Omega_X)^{-n-2}. \end{aligned} \quad (\text{C.28})$$

From (C.28), it can be seen that $\lim_{\Omega_X \rightarrow \infty} Pr(O_2^{HBD(JD)}) = 0$, since $\lim_{\Omega_X \rightarrow \infty} (\Omega_X)^{-n-1} = 0$ and $\lim_{\Omega_X \rightarrow \infty} (\Omega_X)^{-n-2} = 0$. As such, the joint detector achieves zero outage probability at asymptotic SNR regimes. For the case of the joint detector over Rician fading channels, repeating the above steps also yield zero outage probability at asymptotic SNR regimes. This completes the proof.

Appendix D

Mathematical Proofs in Chapter 6

D.1 Proof of Outage Probability for the Outage Event O at an Arbitrary Receiver

From [17, eq. (6)], the conditional outage probability $Pr(O|d_i, d_j)$ at receiver i is:

$$Pr(O|d_i, d_j) \approx \sum_{q=0}^{K_{tr}} \sum_{l_1+\dots+l_{N-i+1}=q+1} \alpha(q, \bar{P}_i d_i^{-n}, K_i, \gamma) \binom{l_1 + \dots + l_{N-i+1}}{l_1, \dots, l_{N-i+1}} \prod_{j=1}^{N-i} E\{(X_j d_j^{-n})^{l_j}\}. \quad (\text{D.1})$$

Thereafter, averaging $Pr(O|d_i, d_j)$ over the respective distributions of d_i and d_j yields Lemma 6.1. This completes the proof.

Appendix E

Mathematical Proofs in Chapter 7

E.1 Proof of Ergodic Capacity at the MBS in the FD-HetNet

From [208, eq. (5)], the instantaneous ergodic capacity of the MBS in the FD-HetNet can be written as:

$$\begin{aligned} \ln \left(1 + SINR_{mbs}^{FD} \right) &= \int_0^{\infty} \frac{\exp(-z)}{z} \left[1 - \exp \left(-z\rho d_{mbs}^{-n} X_{mbs} \right) \right] \\ &\quad \times \exp \left(-z \left(\rho \sum_{i=1}^{N_U} d_i^{-n} X_i + \rho_{si} Y_{si,1} + \rho_{si} Y_{si,2} \right) \right) dz. \end{aligned} \quad (\text{E.1})$$

Thereafter, the ergodic capacity C_{mbs}^{FD} conditioned on d_{mbs} and d_i can be given as:

$$\begin{aligned} E \left\{ \ln \left(1 + SINR_{mbs}^{FD} \right) \middle| d_{mbs}, d_i \right\} &= \int_0^{\infty} \frac{\exp(-z)}{z} \left(1 - M_{X_{mbs}} \left(z\rho d_{mbs}^{-n} \right) \right) \\ &\quad \times \left(\prod_{i=1}^{N_U} M_{X_i} \left(z\rho d_i^{-n} \right) \right) M_{Y_{si,1}} \left(z\rho_{si} \right) M_{Y_{si,2}} \left(z\rho_{si} \right) dz \end{aligned} \quad (\text{E.2})$$

Averaging (E.2) over the PDFs of d_{mbs} and d_i yields (7.7). This completes the proof.

E.2 Proof of Ergodic Capacity at DL UAV- j in the FD-HetNet

From (7.5), $SINR_j^{FD}$ comprises uncorrelated RVs, i.e., $Y_{i,j}$ and $Y_{mbs,j}$, and a correlated RV X_j . Using [208, eq. (5)], the instantaneous ergodic capacity of DL UAV- j in the

FD-HetNet is:

$$\begin{aligned} \ln \left(1 + SINR_j^{FD} \right) &= \int_0^\infty \frac{\exp(-z)}{z} \left[\exp \left(-z \frac{\rho}{d_j^n} X_j \sum_{k=1}^{j-1} \alpha_k \right) - \exp \left(-z \frac{\rho}{d_j^n} X_j \sum_{k=1}^j \alpha_k \right) \right] \\ &\quad \times \exp \left(-z \rho \left[d_{mbs,j}^{-n} Y_{mbs,j} + \sum_{i=1}^{N_U} d_{i,j}^{-n} Y_{i,j} \right] \right) dz, \end{aligned} \quad (\text{E.3})$$

From (E.3), the ergodic capacity C_j^{FD} conditioned on d_j , $d_{i,j}$, and $d_{mbs,j}$ is:

$$\begin{aligned} E \left\{ \ln \left(1 + SINR_j^{FD} \right) \middle| d_j, d_{i,j}, d_{mbs,j} \right\} &= \int_0^\infty \frac{\exp(-z)}{z} \left[M_{X_j} \left(z \frac{\rho}{d_j^n} \sum_{k=1}^{j-1} \alpha_k \right) - M_{X_j} \left(z \frac{\rho}{d_j^n} \sum_{k=1}^j \alpha_k \right) \right] \\ &\quad \times M_{Y_{mbs,j}} \left(z \rho d_{mbs,j}^{-n} \right) \left(\prod_{i=1}^{N_U} M_{Y_{i,j}} \left(z \rho d_{i,j}^{-n} \right) \right) dz, \end{aligned} \quad (\text{E.4})$$

Subsequently, averaging (E.4) over the PDFs of d_j , $d_{i,j}$, and $d_{mbs,j}$ yields:

$$\begin{aligned} E \left\{ \ln \left(1 + SINR_j^{FD} \right) \right\} &= \int_{L_{m,j}}^{L_{p,j}} \int_0^\infty \frac{\exp(-z)}{z} \left[M_{X_j} \left(z \frac{\rho}{w_j^n} \sum_{k=1}^{j-1} \alpha_k \right) - M_{X_j} \left(z \frac{\rho}{w_j^n} \sum_{k=1}^j \alpha_k \right) \right] \\ &\quad \times \left(\int_{H_{mbs,j}}^{L_{q,mbs}} M_{Y_{mbs,j}} \left(z \rho w_{mbs,j}^{-n} \right) f_{d_{mbs,j}}(w_{mbs,j}|w_j) dw_{mbs,j} \right. \\ &\quad \left. + \int_{L_{q,mbs}}^{L_{r,mbs}} M_{Y_{mbs,j}} \left(z \rho w_{mbs,j}^{-n} \right) f_{d_{mbs,j}}(w_{mbs,j}|w_j) dw_{mbs,j} \right) \\ &\quad \times \left(\prod_{i=1}^{N_U} \left[\int_{H_{i,j}}^{L_{q,i}} M_{Y_{i,j}} \left(z \rho w_{i,j}^{-n} \right) f_{d_{i,j}}(w_{i,j}|w_j) dw_{i,j} \right. \right. \\ &\quad \left. \left. + \int_{L_{q,i}}^{L_{r,i}} M_{Y_{i,j}} \left(z \rho w_{i,j}^{-n} \right) f_{d_{i,j}}(w_{i,j}|w_j) dw_{i,j} \right] \right) f_{d_j}(w_j) dz dw_j. \end{aligned} \quad (\text{E.5})$$

Thereafter, (7.15) is obtained after simplifying (E.5). This completes the proof.

E.3 Proof of Ergodic Capacity Gain at the MBS, UL UAV-*i*, and DL UAV-*j* in the FD-HetNet over the HD-HetNet

Starting with Δ_{mbs} , the exact expression can be written in terms of C_{mbs}^{FD} in (7.7) and C_{mbs}^{HD} in (7.19) as:

$$\begin{aligned}\Delta_{mbs} &= C_{mbs}^{FD} - C_{mbs}^{HD} \\ &= \int_{L_{m,mbs}}^{L_{p,mbs}} \int_0^\infty \frac{\exp(-z)}{z} \left(1 - M_{X_{mbs}}(z\rho w_{mbs}^{-n}) \right) \\ &\quad \times \left(\prod_{i=1}^{N_U} \tau_i(z\rho) \right) M_{Y_{si,1}}(z\rho s_i) M_{Y_{si,2}}(z\rho s_i) f_{d_{mbs}}(w_{mbs}) dz dw_{mbs} \\ &\quad - \frac{1}{2} \int_{L_{m,mbs}}^{L_{p,mbs}} \int_0^\infty \frac{\exp(-z)}{z} \left(1 - M_{X_{mbs}}(z\rho w_{mbs}^{-n}) \right) \\ &\quad \times \left(\prod_{i=1}^{N_U} \tau_i(z\rho) \right) f_{d_{mbs}}(w_{mbs}) dz dw_{mbs}. \end{aligned} \tag{E.6}$$

Thereafter, (7.25) is obtained after some algebraic simplification. The exact expressions for Δ_i and Δ_j are also obtained in the same manner. This completes the proof.

Appendix F

Mathematical Proofs in Chapter 8

F.1 Proof for the Bivariate Rician Shadowed Joint PDF in (8.5)

We first begin by noting that $I_0\left(\frac{2r_i x}{\sigma^2(1-\rho)}\right)$ for $i = 1, 2$ in (8.4) can be represented as the following power series [219, eq. (9.6.10)]:

$$I_0\left(\frac{2r_i x}{\sigma^2(1-\rho)}\right) = \sum_{n=0}^{\infty} \frac{(1/4)^n}{n! \Gamma(n+1)} \left(\frac{2r_i x}{\sigma^2(1-\rho)}\right)^{2n} = \sum_{n=0}^{\infty} C_i(n). \quad (\text{F.1})$$

Then, using the Cauchy product theorem [49, eq. (0.316)], $\prod_{i=1}^2 I_0\left(\frac{2r_i x}{\sigma^2(1-\rho)}\right)$ in (8.4) becomes:

$$\prod_{i=1}^2 I_0\left(\frac{2r_i x}{\sigma^2(1-\rho)}\right) \approx \sum_{k=0}^{\infty} \sum_{n=0}^k C_1(n) C_2(k-n) \approx \sum_{k=0}^{K_{tr,1}} A(k), \quad (\text{F.2})$$

where $A(k) = \sum_{n=0}^k \frac{(1/4)^k (2r_1)^{2n} (2r_2)^{2(k-n)}}{\Gamma^2(n+1) \Gamma^2(k-n+1) [\sigma^2(1-\rho)]^{2k}} x^{2k}$.

Next, ${}_1F_1\left(m, 1; \frac{K}{\sigma^2 \rho (\rho m + K)} x^2\right)$ in (8.4) is also expressed as the following power series [219, eq. (13.1.2)]:

$${}_1F_1\left(m, 1; \frac{K}{\sigma^2 \rho (\rho m + K)} x^2\right) \approx \sum_{i=0}^{\infty} B(i), \quad (\text{F.3})$$

where $B(i) = \frac{(m)_i}{i!(1)_i} \left(\frac{K}{\sigma^2 \rho (m \rho + K)}\right)^i x^{2i}$.

Using (F.2) and (F.3), along with the Cauchy product theorem [49, eq. (0.316)], the

expression $\prod_{i=1}^2 I_0\left(\frac{2r_i x}{\sigma^2(1-\rho)}\right) {}_1F_1\left(m, 1; \frac{K}{\sigma^2\rho(\rho m+K)}x^2\right)$ in (8.4) can be expressed as:

$$\begin{aligned}
 & \prod_{i=1}^2 I_0\left(\frac{2r_i x}{\sigma^2(1-\rho)}\right) {}_1F_1\left(m, 1; \frac{K}{\sigma^2\rho(\rho m+K)}x^2\right) \\
 & \approx \sum_{k=0}^{K_{tr,1}} \sum_{i=0}^k A(i)B(k-i) \\
 & \approx \sum_{k=0}^{K_{tr,1}} \sum_{i=0}^k \sum_{n=0}^i \frac{\left(\frac{1}{4}\right)^i (2r_1)^{2n} (2r_2)^{2(i-n)}}{\Gamma^2(n+1)\Gamma^2(i-n+1)[\sigma^2(1-\rho)]^{2i}(1)_{k-i}} \\
 & \quad \times \frac{(m_{k-i})}{(k-i)!} \left(\frac{K}{\sigma^2\rho(\rho m+K)}\right)^{k-i} x^{2k}. \tag{F.4}
 \end{aligned}$$

Substituting (F.4) into (8.4) and utilizing the fact that $\int_0^\infty x^{2k+1} \exp\left(\frac{-(1-\rho)}{\sigma^2\rho(1-\rho)}x^2\right) dx = \frac{k!}{2} \left(\frac{1-\rho}{\sigma^2\rho(1-\rho)}\right)^{-(k+1)}$ [49, eq. (3.461.3)], one obtains the expression in (8.5). This completes the proof.

F.2 Proof of Convergence Radius for (8.5)

To show that (8.5) is convergent, the D'Alembert test is invoked to show that

$$\lim_{n \rightarrow \infty} \frac{|\alpha(k,i,n+1)r_1^{2(n+1)+1}r_2^{2(i-n-1)+1}|}{|\alpha(k,i,n)r_1^{2n+1}r_2^{2(i-n)+1}|} = 0, \lim_{i \rightarrow \infty} \frac{|\alpha(k,i+1,n)r_2^{2(i-n+1)+1}|}{|\alpha(k,i,n)r_2^{2(i-n)+1}|} = 0, \text{ and } \lim_{k \rightarrow \infty} \frac{|\alpha(k+1,i,n)|}{|\alpha(k,i,n)|} = 0.$$

Starting with $\lim_{n \rightarrow \infty} \frac{|\alpha(k,i,n+1)r_1^{2(n+1)+1}r_2^{2(i-n-1)+1}|}{|\alpha(k,i,n)r_1^{2n+1}r_2^{2(i-n)+1}|}$, the limit can be evaluated as:

$$\lim_{n \rightarrow \infty} \frac{|\alpha(k,i,n+1)r_1^{2(n+1)+1}r_2^{2(i-n-1)+1}|}{|\alpha(k,i,n)r_1^{2n+1}r_2^{2(i-n)+1}|} \stackrel{(a)}{=} \lim_{n \rightarrow \infty} \frac{r_1}{r_2^2} \left(\frac{n\Gamma(n)i^{1-n}\Gamma(i)}{n^2\Gamma(n)i^{-n}\Gamma(i)} \right)^2 = \lim_{n \rightarrow \infty} \frac{r_1}{r_2^2} \left(\frac{i}{n} \right)^2 = 0 \tag{F.5}$$

where (a) is obtained using the asymptotic identity $\Gamma[m+n] \approx m^n\Gamma[m]$ in [45, eq. (25)].

For $\lim_{i \rightarrow \infty} \frac{|\alpha(k, i+1, n) r_2^{2(i-n+1)+1}|}{|\alpha(k, i, n) r_2^{2(i-n)+1}|}$, the limit is evaluated as:

$$\begin{aligned}
 \lim_{i \rightarrow \infty} \frac{|\alpha(k, i+1, n) r_2^{2(i-n+1)+1}|}{|\alpha(k, i, n) r_2^{2(i-n)+1}|} &\stackrel{(a)}{=} \lim_{i \rightarrow \infty} r_2^2 \left(\frac{\Gamma(k-i-1+m) \left(\frac{K}{\sigma^2 \rho (\rho m + K)} \right)^{k-i-1}}{\Gamma^2(i-n+2) [\sigma^2(1-\rho)]^{2i+2} \Gamma^2(k-i)} \right) \\
 &\quad \times \left(\frac{\Gamma^2(i-n+1) [\sigma^2(1-\rho)]^{2i} \Gamma^2(k-i+1)}{\Gamma(k-i+m) \left(\frac{K}{\sigma^2 \rho (\rho m + K)} \right)^{k-i}} \right) \\
 &\stackrel{(b)}{=} \lim_{i \rightarrow \infty} r_2^2 \left(\frac{k^{m-i-1} \Gamma(k) \left(\frac{K}{\sigma^2 \rho (\rho m + K)} \right)^{k-i-1}}{i^{2-n} \Gamma(i) [\sigma^2(1-\rho)]^{2i+2} k^{-2i} \Gamma^2(k)} \right) \\
 &\quad \times \left(\frac{i^{1-n} \Gamma(i) [\sigma^2(1-\rho)]^{2i} k^{-2i+2} \Gamma^2(k)}{k^{m-i} \Gamma(k) \left(\frac{K}{\sigma^2 \rho (\rho m + K)} \right)^{k-i}} \right) \\
 &= \lim_{i \rightarrow \infty} \frac{r_2^2 k}{\left(\frac{K}{\sigma^2 \rho (\rho m + K)} \right) i} = 0,
 \end{aligned} \tag{F.6}$$

where (a) is due to $(a)_k = \frac{\Gamma(a+k)}{\Gamma(a)}$ [219, eq. (6.1.22)] and $(k-i)! = \Gamma(k-i+1)$, and (b) is obtained using the asymptotic identity $\Gamma[m+n] \approx m^n \Gamma[m]$ in [45, eq. (25)].

Finally, for $\lim_{k \rightarrow \infty} \frac{|\alpha(k+1, i, n)|}{|\alpha(k, i, n)|}$, the limit is evaluated as:

$$\begin{aligned}
 \lim_{k \rightarrow \infty} \frac{|\alpha(k+1, i, n)|}{|\alpha(k, i, n)|} &\stackrel{(a)}{=} \lim_{k \rightarrow \infty} \left(\frac{\Gamma(k-i+1+m) \left(\frac{K}{\sigma^2 \rho (\rho m + K)} \right)^{k+1-i}}{\Gamma^2(k-i+2)} \right) \\
 &\quad \times \left(\frac{\Gamma^2(k-i+1)}{\Gamma(k-i+m) \left(\frac{K}{\sigma^2 \rho (\rho m + K)} \right)^{k-i}} \right) \\
 &\stackrel{(b)}{=} \lim_{k \rightarrow \infty} \left(\frac{K}{\sigma^2 \rho (\rho m + K)} \right) \left(\frac{k^{m+1-i} \Gamma(k)}{[k^{2-i} \Gamma(k)]^2} \right) \left(\frac{[k^{1-i} \Gamma(k)]^2}{k^{m-i} \Gamma(k)} \right) \\
 &= \lim_{k \rightarrow \infty} \left(\frac{K}{\sigma^2 \rho (\rho m + K)} \right) \frac{1}{k} = 0,
 \end{aligned} \tag{F.7}$$

where (a) is due to $(a)_k = \frac{\Gamma(a+k)}{\Gamma(a)}$ [219, eq. (6.1.22)] and $(k-i)! = \Gamma(k-i+1)$, and (b) is obtained using the asymptotic identity $\Gamma[m+n] \approx m^n \Gamma[m]$ in [45, eq. (25)].

Thus, from (F.5), (F.6), and (F.7), the expression in (8.5) has a convergence radius of ∞ . Therefore, (8.5) is shown to be convergent. This completes the proof.

F.3 Proof for the Bivariate Rician Shadowed Joint CDF in (8.6)

We begin by noting that $\exp(x) \approx \sum_{l=0}^{K_{tr,2}} \frac{x^l}{l!}$ [49, eq. (1.211.1)]. Then, the joint CDF $F_{R_1,R_2}(\gamma_1, \gamma_2)$ can be obtained from (8.5) as follows:

$$\begin{aligned} F_{R_1,R_2}(\gamma_1, \gamma_2) &\stackrel{(a)}{=} \int_0^{\gamma_2} \int_0^{\gamma_1} \sum_{k=0}^{K_{tr,1}} \sum_{i=0}^k \sum_{n=0}^i \sum_{l=0}^{K_{tr,2}} \sum_{q=0}^l \alpha(k, i, n) \\ &\quad \times \frac{(-1)^l \binom{l}{q}}{l! [\sigma^2(1-\rho)]^l} (r_1)^{2(q+n)+1} (r_2)^{2(l-q+i-n)+1} dr_1 dr_2 \\ &\stackrel{(b)}{=} \sum_{k=0}^{K_{tr,1}} \sum_{i=0}^k \sum_{n=0}^i \sum_{l=0}^{K_{tr,2}} \sum_{q=0}^l \alpha(k, i, n) \\ &\quad \times \frac{(-1)^l \binom{l}{q}}{l! [\sigma^2(1-\rho)]^l 4(q+n+1)(l-q+i-n+1)} \\ &\quad \times (\gamma_1)^{2(q+n+1)} (\gamma_2)^{2(l-q+i-n+1)} \end{aligned} \quad (\text{F.8})$$

where (a) is obtained by applying the identities in [49, eq. (1.211.1)] and [49, eq. (1.111)], and (b) is obtained through term-wise integration [49, 171]. This completes the proof.

F.4 Proof for the Upper Bound of the Truncation Error in (8.5)

The upper bound of the truncation error is obtained using the same approach in [220]. From the expression in (8.7), taking the ratio between terms ($\Delta(k)$) as k increases yields:

$$\Delta(k) = \frac{|\alpha(k+1, i, n)|}{|\alpha(k, i, n)|} \stackrel{(a)}{=} \left(\frac{K}{\sigma^2 \rho (\rho m + K)} \right) \frac{1}{k} = 0, \quad (\text{F.9})$$

where (a) is obtained from (F.7). Since $\Delta(k)$ monotonically decreases as $k \rightarrow \infty$, (8.7) becomes upper bounded by $\Delta(K_{tr,1})$ as shown [220, eq. (92)]:

$$\begin{aligned} \mathcal{T}_\epsilon &\leq \sum_{i=0}^{K_{tr,1}} \sum_{n=0}^i \frac{\alpha(K_{tr,1}, i, n)}{1 - \Delta(K_{tr,1})} \\ &\quad \times r_1^{2n+1} r_2^{2(i-n)+1} \exp \left(- \frac{r_1^2 + r_2^2}{\sigma^2(1-\rho)} \right) \\ &\leq \mathcal{T}_{\epsilon,upper}. \end{aligned} \quad (\text{F.10})$$

This completes the proof.

F.5 Proof for the Upper Bound of the Truncation Error in (8.6)

The upper bound of the truncation error e is obtained using the same approach in [220]. From (8.9), e can be rewritten as:

$$\begin{aligned} e &= e_1 + e_2 + e_3 + e_4, \\ \text{where } e_1 &= \sum_{k=0}^{K_{tr}} \sum_{i=0}^k \sum_{n=0}^i \sum_{l=K_{tr}+1}^{\infty} \sum_{q=0}^l \mu(k, l), \\ e_2 &= \sum_{k=K_{tr}+1}^{\infty} \sum_{i=0}^k \sum_{n=0}^i \sum_{l=0}^{K_{tr}} \sum_{q=0}^l \mu(k, l), \\ e_3 &= \sum_{k=K_{tr}+1}^{\infty} \sum_{i=0}^k \sum_{n=0}^i \sum_{l=k}^{\infty} \sum_{q=0}^l \mu(k, l), \\ e_4 &= \sum_{l=K_{tr}+1}^{\infty} \sum_{q=0}^l \sum_{k=l}^{\infty} \sum_{i=0}^k \sum_{n=0}^i \mu(k, l). \end{aligned} \quad (\text{F.11})$$

Starting with e_1 , taking the ratio between terms $(\Theta_1(k, l))$ as l increases yields:

$$\begin{aligned} \Theta_1(k, l) &= \frac{\mu(k, l+1)}{\mu(k, l)} \\ &\stackrel{(a)}{=} \frac{(-1)(\gamma_2)^2(l+1)(l-q+i-n+1)}{\sigma^2(1-\rho)l^2(l-q+i-n+2)} = 0, \end{aligned} \quad (\text{F.12})$$

where (a) is obtained through algebraic simplifications after applying the identities $\Gamma[m+n] \approx m^n \Gamma[m]$ [45, eq. (25)] and $\binom{x}{y} = \frac{\Gamma(x+1)}{\Gamma(y+1)\Gamma(x-y+1)}$ [219, eq. (3.1.2)]. Thereafter, e_1 is upper bounded as [220, eq. (89)]:

$$e_1 \leq \sum_{k=0}^{K_{tr}} \sum_{i=0}^k \sum_{n=0}^i \sum_{q=0}^{K_{tr}+1} \frac{\mu(k, K_{tr}+1)}{1 - \Theta_1(k, K_{tr}+1)}. \quad (\text{F.13})$$

For e_2 , taking the ratio between terms $(\Theta_2(k))$ as k increases yields:

$$\Theta_2(k) = \frac{\mu(k+1, l)}{\mu(k, l)} = \Delta(k) = 0,$$

where $\Delta(k)$ is given in (F.9). Then, e_2 can be upper bounded as [220, eq. (92)]:

$$e_2 \leq \sum_{i=0}^{K_{tr}} \sum_{n=0}^i \sum_{l=0}^{K_{tr}} \sum_{q=0}^l \frac{\mu(K_{tr}, l)}{1 - \Theta_2(K_{tr})}. \quad (\text{F.14})$$

For e_3 and e_4 , the upper bound can be respectively obtained from [220, eq. (93)] and [220, eq. (102)] as:

$$e_3 \leq \sum_{k=K_{tr}+1}^{\infty} \sum_{i=0}^k \sum_{n=0}^i \sum_{q=0}^{K_{tr}+1} \frac{\mu(k, K_{tr}+1)}{1 - \Theta_1(k, K_{tr}+1)}, \quad (\text{F.15})$$

$$e_4 \leq \sum_{q=0}^{K_{tr}+1} \sum_{i=0}^{K_{tr}} \sum_{n=0}^i \frac{\mu(K_{tr}, K_{tr}+1)}{1 - \Theta_2(K_{tr})}. \quad (\text{F.16})$$

Then, combining (F.13), (F.14), (F.15), and (F.16) into (F.11) yields the upper bound in (8.10). This completes the proof.

F.6 Proof of Outage Probability for NOMA at Downlink UAV- j

From the selection combining NOMA outage event at downlink UAV- j (O_j^{NOMA}), the NOMA outage probability ($Pr(O_j^{NOMA})$) can be obtained from the closed-form expression of $F_{R_1, R_2}(\gamma_1, \gamma_2)$ in Lemma 8.2 as follows:

$$\begin{aligned} Pr(O_j^{NOMA}) &= Pr\left(\max(R_{j,1}, R_{j,2}) < \gamma_j^{NOMA} \sqrt{\frac{d_j^L}{P_r}}\right) \\ &= \int_{L_{m,j}}^{L_{p,j}} F_{R_{j,1}, R_{j,2}}\left(\gamma_j^{NOMA} \sqrt{\frac{w^L}{P_r}}, \gamma_j^{NOMA} \sqrt{\frac{w^L}{P_r}}\right) f_{d_j}(w) dw \\ &\approx \int_{L_{m,j}}^{L_{p,j}} \sum_{k=0}^{K_{tr,1}} \sum_{i=0}^k \sum_{n=0}^i \sum_{l=0}^{K_{tr,2}} \sum_{q=0}^l \alpha(k, i, n) G(l, n, i, q) \\ &\quad \times \left[\frac{(\gamma_j^{NOMA})^2}{P_r}\right]^{l+i+2} \left(\frac{2}{r_a^2}\right) w^{L(l+i+2)+1} dw \end{aligned} \quad (\text{F.17})$$

From (F.17), (8.12) is obtained by interchanging the order of integration and summation [49, 171]. This completes the proof.

F.7 Proof of Asymptotic Diversity Gain for NOMA at Downlink UAV- j

After some algebraic simplifications, (8.16) can be expressed as:

$$d_{f,j}^{NOMA} \approx \left(\sum_{k=0}^{K_{tr,1}} \sum_{i=0}^k \sum_{n=0}^{i} \sum_{l=0}^{K_{tr,2}} \sum_{q=0}^l \alpha(k, i, n) G(l, n, i, q) \Xi_j(l, i) (\gamma_j^{NOMA})^{2(2+l+i)} (2 + l + i) (P_r)^{-l-i} \right) \\ \left/ \left(\sum_{k=0}^{K_{tr,1}} \sum_{i=0}^k \sum_{n=0}^{i} \sum_{l=0}^{K_{tr,2}} \sum_{q=0}^l \alpha(k, i, n) G(l, n, i, q) \Xi_j(l, i) (\gamma_j^{NOMA})^{2(2+l+i)} (P_r)^{-l-i} \right) \right. \quad (F.18)$$

Next, it is straightforward to see that:

$$\lim_{P_r \rightarrow \infty} (P_r)^{-l-i} = \begin{cases} 1, & \text{for } l = 0, i = 0 \\ 0, & \text{for } l > 0, i > 0 \end{cases} \quad (F.19)$$

Therefore, only $l = i = 0$ needs to be considered when evaluating $d_{f,j}^{NOMA}$ at asymptotic SNR regimes. Thus, after further algebraic simplifications, (F.18) reduces to $d_{f,j}^{NOMA} = 2$. This completes the proof.

References

- [1] A. Yadav, G. I. Tsiropoulos, and O. A. Dobre, "Full-duplex communications: performance in ultradense mm-wave small-cell wireless networks," *IEEE Veh. Technol. Mag.*, vol. 13, no. 2, pp. 40–47, June 2018.
- [2] M. Mozaffari, W. Saad, M. Bennis, and M. Debbah, "Wireless communication using unmanned aerial vehicles (uavs): Optimal transport theory for hover time optimization," *IEEE Trans. Wireless Commun.*, vol. 16, no. 12, pp. 8052–8066, Dec 2017.
- [3] T. Andre, K. A. Hummel, A. P. Schoellig, E. Yanmaz, M. Asadpour, C. Bettstetter, P. Grippa, H. Hellwagner, S. Sand, and S. Zhang, "Application-driven design of aerial communication networks," *IEEE Commun. Mag.*, vol. 52, no. 5, pp. 129–137, May 2014.
- [4] M. M. Azari, F. Rosas, K.-C. Chen, and S. Pollin, "Ultra reliable uav communication using altitude and cooperation diversity," *IEEE Trans. Commun.*, vol. 66, no. 1, pp. 330–344, 2018.
- [5] L. Xiao, X. Lu, D. Xu, Y. Tang, L. Wang, and W. Zhuang, "Uav relay in vanets against smart jamming with reinforcement learning," *IEEE Trans. Veh. Technol.*, vol. 67, no. 5, pp. 4087–4097, May 2018.
- [6] L. Xiao, C. Xie, M. Min, and W. Zhuang, "User-centric view of unmanned aerial vehicle transmission against smart attacks," *IEEE Trans. Veh. Technol.*, vol. 67, no. 4, pp. 3420–3430, April 2018.
- [7] J. Wang, C. Jiang, Z. Han, Y. Ren, R. G. Maunder, and L. Hanzo, "Taking drones to the next level: Cooperative distributed unmanned-aerial-vehicular networks for small and mini drones," *IEEE Veh. Technol. Mag.*, vol. 12, no. 3, pp. 73–82, Sept. 2017.
- [8] D. W. Matolak and R. Sun, "Air-ground channel characterization for unmanned aircraft systems - part iii: The suburban and near-urban environments," *IEEE Trans. Veh. Technol.*, vol. 66, no. 8, pp. 6607–6618, Aug. 2017.
- [9] Federal Communications Commission. FCC Online Table of Frequency Allocations. Accessed on 23-11-2019. [Online]. Available: <https://transition.fcc.gov/oet/spectrum/table/fccitable.pdf>
- [10] Infocomm Media Development Authority, Singapore. Operation of unmanned aircraft systems (uas). Accessed on 23-11-2019. [Online]. Available: <https://www.imda.gov.sg/regulations-and-licensing-listing/spectrum-management-and-coordination/frequency-allocation-and-assignment/operation-of-unmanned-aircraft-systems-uas>
- [11] ——. Singapore Spectrum Allocation Chart. Accessed on 23-11-2019. [Online]. Available: <https://www.imda.gov.sg/-/media/imda/files/regulation-licensing-and-consultations/frameworks-and-policies/spectrum-management-and-coordination/spectrumchart.pdf?la=en>
- [12] ——. Spectrum management handbook. Accessed on 23-11-2019. [Online]. Available: <https://www.imda.gov.sg/-/media/imda/files/regulation-licensing-and-consultations/frameworks-and-policies/spectrum-management-and-coordination/spectrummgmthb.pdf?la=en>
- [13] Eurocontrol. (2013) Challenges of growth 2013 summary report. Accessed on 23-11-2019. [Online]. Available: <https://www.eurocontrol.int/sites/default/files/content/documents/official-documents/reports/201307-challenges-of-growth-summary-report.pdf>
- [14] N. Neji, R. De Lacerda, A. Azoulay, T. Letertre, and O. Outtier, "Survey on the future aeronautical communication system and its development for continental communications," *IEEE Trans. Veh. Technol.*, vol. 62, no. 1, pp. 182–191, 2013.

REFERENCES

- [15] A. Barba and F. Battisti, "Sesar and sandra: A co-operative approach for future aeronautical communications," 2011, accessed on 23-11-2019. [Online]. Available: <https://doi.org/10.5772/28975>
- [16] L. Zhang and N. Ansari, "A Framework for 5G Networks with In-Band Full-Duplex Enabled Drone-Mounted Base-Stations," *IEEE Wireless Commun.*, vol. 26, no. 5, pp. 121–127, 2019.
- [17] T. Z. H. Ernest, A. S. Madhukumar, R. P. Sirigina, and A. K. Krishna, "Outage Analysis and Finite SNR Diversity-Multiplexing Tradeoff of Hybrid-Duplex Systems for Aeronautical Communications," *IEEE Trans. Wireless Commun.*, vol. 18, no. 4, pp. 2299–2313, April 2019.
- [18] ———, "A Hybrid-Duplex System with Joint Detection for Interference-Limited UAV Communications," *IEEE Trans. Veh. Technol.*, vol. 68, no. 1, pp. 335–348, January 2019.
- [19] ———, "A Power Series Approach for Hybrid-Duplex UAV Communication Systems under Rician Shadowed Fading," *IEEE Access*, vol. 7, pp. 76 949–76 966, June 2019.
- [20] ———, "Hybrid-Duplex Communications for Multi-UAV Networks: An Outage Probability Analysis," *IEEE Commun. Lett.*, vol. 23, no. 10, pp. 1831–1835, October 2019.
- [21] A. Sahai, G. Patel, C. Dick, and A. Sabharwal, "On the impact of phase noise on active cancelation in wireless full-duplex," *IEEE Trans. Veh. Technol.*, vol. 62, no. 9, pp. 4494–4510, Nov. 2013.
- [22] R. P. Sirigina and A. Madhukumar, "On the symbol error rate and diversity gain region of the relay-assisted z-channel," *IEEE Trans. Wireless Commun.*, vol. 15, no. 3, pp. 1965–1978, March 2016.
- [23] H. Hellaoui, O. Bekkouche, M. Bagaa, and T. Taleb, "Aerial Control System for Spectrum Efficiency in UAV-to-Cellular Communications," *IEEE Commun. Mag.*, vol. 56, no. 10, pp. 108–113, October 2018.
- [24] U. Epple and M. Schnell, "Overview of legacy systems in l-band and its influence on the future aeronautical communication system ldacs1," *IEEE Aerospace and Electronic Systems Magazine*, vol. 29, no. 2, pp. 31–37, 2014.
- [25] J. Zhang, S. Chen, R. G. Maunder, R. Zhang, and L. Hanzo, "Adaptive coding and modulation for large-scale antenna array-based aeronautical communications in the presence of co-channel interference," *IEEE Trans. Wireless Commun.*, vol. 17, no. 2, pp. 1343–1357, 2017.
- [26] R. A. J. Castillo, R. Grünheid, G. Bauch, F. Wolff, and S. von der Heide, "Communication Analysis Between an Airborne Mobile User and a Terrestrial Mobile Network," *IEEE Trans. Veh. Technol.*, vol. 67, no. 4, pp. 3457–3465, April 2018.
- [27] X. Cao, P. Yang, M. Alzenad, X. Xi, D. Wu, and H. Yanikomeroglu, "Airborne communication networks: A survey," *IEEE J. Sel. Areas Commun.*, vol. 36, no. 9, pp. 1907–1926, 2018.
- [28] N. H. Motlagh, T. Taleb, and O. Arouk, "Low-altitude unmanned aerial vehicles-based internet of things services: Comprehensive survey and future perspectives," *IEEE Internet Things J.*, vol. 3, no. 6, pp. 899–922, Dec. 2016.
- [29] A. Fotouhi, H. Qiang, M. Ding, M. Hassan, L. G. Giordano, A. Garcia-Rodriguez, and J. Yuan, "Survey on UAV cellular communications: Practical aspects, standardization advancements, regulation, and security challenges," *IEEE Commun. Surveys Tut.*, 2019.
- [30] T. Z. H. Ernest, A. S. Madhukumar, R. P. Sirigina, and A. K. Krishna, "Addressing Spectrum Efficiency Through Hybrid-Duplex UAV Communications: Challenges and Opportunities," *Submitted to Elsevier Veh. Commun. for publication*, 2019.
- [31] G. Bartoli, R. Fantacci, and D. Marabissi, "Aeromacs: A new perspective for mobile airport communications and services," *IEEE Wireless Commun.*, vol. 20, no. 6, pp. 44–50, December 2013.
- [32] L. Gupta, R. Jain, and G. Vaszkun, "Survey of important issues in UAV communication networks," *IEEE Commun. Surveys Tut.*, vol. 18, no. 2, pp. 1123–1152, 2015.
- [33] S. Hayat, E. Yanmaz, and R. Muzaffar, "Survey on unmanned aerial vehicle networks for civil applications: A communications viewpoint," *IEEE Commun. Surveys Tut.*, vol. 18, no. 4, pp. 2624–2661, 2016.
- [34] J. Liu, Y. Shi, Z. M. Fadlullah, and N. Kato, "Space-air-ground integrated network: A survey," *IEEE Commun. Surveys Tut.*, vol. 20, no. 4, pp. 2714–2741, 2018.

REFERENCES

- [35] M. Mozaffari, W. Saad, M. Bennis, Y.-H. Nam, and M. Debbah, "A tutorial on UAVs for wireless networks: Applications, challenges, and open problems," *IEEE Commun. Surveys Tut.*, vol. 21, no. 3, pp. 2334–2360, 2019.
- [36] B. Li, Z. Fei, and Y. Zhang, "UAV communications for 5G and beyond: Recent advances and future trends," *IEEE Internet Things J.*, vol. 6, no. 2, pp. 2241–2263, April 2018.
- [37] A. A. Khuwaja, Y. Chen, N. Zhao, M.-S. Alouini, and P. Dobbins, "A survey of channel modeling for UAV communications," *IEEE Commun. Surveys Tut.*, vol. 20, no. 4, pp. 2804–2821, 2018.
- [38] W. Khawaja, I. Guvenc, D. W. Matolak, U.-C. Fiebig, and N. Schneckenberger, "A survey of air-to-ground propagation channel modeling for unmanned aerial vehicles," *IEEE Commun. Surveys Tut.*, vol. 21, no. 3, pp. 2361–2391, 2019.
- [39] R. J. Kerczewski and J. H. Griner, "Control and non-payload communications links for integrated unmanned aircraft operations," 2012, accessed on 23-11-2019. [Online]. Available: <https://ntrs.nasa.gov/search.jsp?R=20120016398>
- [40] D. W. Matolak, "Air-ground channels & models: Comprehensive review and considerations for unmanned aircraft systems," in *Proc. IEEE Aerosp. Conf.* IEEE, Big Sky, MT, USA, 2012, pp. 1–17.
- [41] E. Haas, "Aeronautical channel modeling," *IEEE Trans. Veh. Technol.*, vol. 51, no. 2, pp. 254–264, 2002.
- [42] A. Hayajneh, S. Zaidi, D. C. McLernon, M. Di Renzo, and M. Ghogho, "Performance analysis of uav enabled disaster recovery networks: A stochastic geometric framework based on cluster processes," *IEEE Access*, vol. 6, pp. 26 215–26 230, 2018.
- [43] J. Li and Y. Han, "Optimal resource allocation for packet delay minimization in multi-layer uav networks," *IEEE Commun. Lett.*, vol. 21, no. 3, pp. 580–583, 2017.
- [44] J. Lyu, Y. Zeng, and R. Zhang, "Spectrum sharing and cyclical multiple access in uav-aided cellular offloading," in *Proc. IEEE Global Commun. Conf. (GLOBECOM)*, Singapore, 2017, pp. 1–6.
- [45] N. B. Rached, A. Kammoun, M.-S. Alouini, and R. Tempone, "A unified moment-based approach for the evaluation of the outage probability with noise and interference," *IEEE Trans. Wireless Commun.*, vol. 16, no. 2, pp. 1012–1023, Feb. 2017.
- [46] D. W. Matolak and R. Sun, "Air-ground channel characterization for unmanned aircraft systems—part i: Methods, measurements, and models for over-water settings," *IEEE Trans. Veh. Technol.*, vol. 66, no. 1, pp. 26–44, 2017.
- [47] R. Sun and D. W. Matolak, "Air-ground channel characterization for unmanned aircraft systems part ii: Hilly and mountainous settings," *IEEE Trans. Veh. Technol.*, vol. 66, no. 3, pp. 1913–1925, March 2017.
- [48] Y. Zeng, R. Zhang, and T. J. Lim, "Wireless communications with unmanned aerial vehicles: opportunities and challenges," *IEEE Communications Magazine*, vol. 54, no. 5, pp. 36–42, 2016.
- [49] I. S. Gradshteyn and I. M. Ryzhik, *Table of integrals, series, and products*. Academic press, 2014.
- [50] P. K. Sharma and D. I. Kim, "Uav-enabled downlink wireless system with non-orthogonal multiple access," in *Globecom Workshops (GC Wkshps), 2017 IEEE*, 2017, pp. 1–6.
- [51] F. Ono, H. Ochiai, and R. Miura, "A wireless relay network based on unmanned aircraft system with rate optimization," *IEEE Trans. Wireless Commun.*, vol. 15, no. 11, pp. 7699–7708, 2016.
- [52] T. Z. H. Ernest, A. S. Madhukumar, R. P. Sirigina, and A. K. Krishna, "Hybrid-Duplex Systems for UAV Communications under Rician Shadowed Fading," in *Proc. IEEE 88th Veh. Technol. Conf. (VTC Fall)*, Chicago, IL, USA, 2018, pp. 1–5.
- [53] M. M. Azari, H. Sallouha, A. Chiumento, S. Rajendran, E. Vinogradov, and S. Pollin, "Key technologies and system trade-offs for detection and localization of amateur drones," *IEEE Commun. Mag.*, vol. 56, no. 1, pp. 51–57, 2018.
- [54] N. Goddemeier and C. Wietfeld, "Investigation of air-to-air channel characteristics and a uav specific extension to the rice model," in *Proc. IEEE Globecom Workshops (GC Wkshps)*, San Diego, CA, USA, 2015, pp. 1–5.
- [55] X. Yuan, Z. Feng, W. Xu, W. Ni, J. A. Zhang, Z. Wei, and R. P. Liu, "Capacity analysis of uav communications: Cases of random trajectories," *IEEE Trans. Veh. Technol.*, vol. 67, no. 8, pp. 7564–7576, August 2018.

REFERENCES

- [56] ITU-R, “P.1410 : Propagation data and prediction methods required for the design of terrestrial broadband radio access systems operating in a frequency range from 3 to 60 ghz,” Tech. Rep., 2013, accessed on 23-11-2019. [Online]. Available: <https://www.itu.int/rec/R-REC-P.1410/en>
- [57] S. Chandrasekharan, K. Gomez, A. Al-Hourani, S. Kandeepan, T. Rasheed, L. Goratti, L. Reynaud, D. Grace, I. Bucaille, T. Wirth *et al.*, “Designing and implementing future aerial communication networks,” *IEEE Commun. Mag.*, vol. 54, no. 5, pp. 26–34, 2016.
- [58] Q. Feng, J. McGeehan, E. K. Tameh, and A. R. Nix, “Path loss models for air-to-ground radio channels in urban environments,” in *in Proc. IEEE 63rd Veh. Technol. Conf (VTC Spring)*, vol. 6. IEEE, Melbourne, Vic., Australia, 2006, pp. 2901–2905.
- [59] A. Al-Hourani, S. Kandeepan, and S. Lardner, “Optimal lap altitude for maximum coverage,” *IEEE Wireless Commun. Lett.*, vol. 3, no. 6, pp. 569–572, Dec. 2014.
- [60] Y. Wan, K. Namuduri, Y. Zhou, and S. Fu, “A smooth-turn mobility model for airborne networks,” *IEEE Trans. Veh. Technol.*, vol. 62, no. 7, pp. 3359–3370, 2013.
- [61] A. Al-Hourani and K. Gomez, “Modeling cellular-to-uav path-loss for suburban environments,” *IEEE Wireless Commun. Lett.*, vol. 7, no. 1, pp. 82–85, Feb. 2018.
- [62] R. Amorim, H. Nguyen, P. Mogensen, I. Z. Kovács, J. Wigard, and T. B. Sørensen, “Radio channel modeling for uav communication over cellular networks,” *IEEE Wireless Commun. Lett.*, vol. 6, no. 4, pp. 514–517, Aug. 2017.
- [63] A. Pokkunuru, Q. Zhang, and P. Wang, “Capacity analysis of aerial small cells,” in *Proc. 2017 IEEE Int. Conf. Commun. (ICC)*. IEEE, Paris, France, 2017, pp. 1–7.
- [64] H. Sallouha, M. M. Azari, A. Chiumento, and S. Pollin, “Aerial Anchors Positioning for Reliable RSS-Based Outdoor Localization in Urban Environments,” *IEEE Wireless Commun. Lett.*, vol. 7, no. 3, pp. 376–379, 2017.
- [65] E. Everett, A. Sahai, and A. Sabharwal, “Passive self-interference suppression for full-duplex infrastructure nodes,” *IEEE Trans. Wireless Commun.*, vol. 13, no. 2, pp. 680–694, 2014.
- [66] M. Jain, J. I. Choi, T. Kim, D. Bharadia, S. Seth, K. Srinivasan, P. Levis, S. Katti, and P. Sinha, “Practical, real-time, full duplex wireless,” in *Proceedings of the 17th annual international conference on Mobile computing and networking*. ACM, 2011, pp. 301–312.
- [67] D. Korpi, J. Tamminen, M. Turunen, T. Huusari, Y.-S. Choi, L. Anttila, S. Talwar, and M. Valkama, “Full-duplex mobile device: Pushing the limits,” *IEEE Commun. Mag.*, vol. 54, no. 9, pp. 80–87, 2016.
- [68] M. S. Amjad, H. Nawaz, K. Özsoy, Ö. Gürbüz, and I. Tekin, “A low-complexity full-duplex radio implementation with a single antenna,” *IEEE Trans. Veh. Technol.*, vol. 67, no. 3, pp. 2206–2218, 2018.
- [69] E. Ahmed, A. M. Eltawil, and A. Sabharwal, “Rate gain region and design tradeoffs for full-duplex wireless communications,” *IEEE Trans. Wireless Commun.*, vol. 12, no. 7, pp. 3556–3565, 2013.
- [70] V. Syrjälä, K. Yamamoto, and M. Valkama, “Analysis and design specifications for full-duplex radio transceivers under rf oscillator phase noise with arbitrary spectral shape,” *IEEE Trans. Veh. Technol.*, vol. 65, no. 8, pp. 6782–6788, 2016.
- [71] M. Bernhardt, F. Gregorio, J. Cousseau, and T. Riihonen, “Self-interference cancelation through advanced sampling,” *IEEE Trans. Signal Process.*, vol. 66, no. 7, pp. 1721–1733, 2018.
- [72] Rice Univ., Houston, TX, USA. WARP project. Accessed on 23-11-2019. [Online]. Available: <http://warp.rice.edu>
- [73] Agilent Technologies. E4438C ESG Vector Signal Generator. Accessed on 23-11-2019. [Online]. Available: <https://literature.cdn.keysight.com/litweb/pdf/5988-4039EN.pdf>
- [74] D. Korpi, T. Riihonen, V. Syrjälä, L. Anttila, M. Valkama, and R. Wichman, “Full-duplex transceiver system calculations: Analysis of ADC and linearity challenges,” *IEEE Trans. Wireless Commun.*, vol. 13, no. 7, pp. 3821–3836, July 2014.
- [75] E. Ahmed and A. M. Eltawil, “All-digital self-interference cancellation technique for full-duplex systems,” *IEEE Trans. Wireless Commun.*, vol. 14, no. 7, pp. 3519–3532, 2015.

REFERENCES

- [76] R. Li, A. Masmoudi, and T. Le-Ngoc, "Self-interference cancellation with nonlinearity and phase-noise suppression in full-duplex systems," *IEEE Trans. Veh. Technol.*, vol. 67, no. 3, pp. 2118–2129, 2018.
- [77] N. V. Shende, Ö. Gürbüz, and E. Erkip, "Half-duplex or full-duplex communications: Degrees of freedom analysis under self-interference," *IEEE Trans. Wireless Commun.*, vol. 17, no. 2, pp. 1081–1093, 2018.
- [78] D. Hwang, S. S. Nam, and J. Yang, "Multi-antenna beamforming techniques in full-duplex and self-energy recycling systems: Opportunities and challenges," *IEEE Commun. Mag.*, vol. 55, no. 10, pp. 160–167, 2017.
- [79] B. K. Chalise, H. A. Suraweera, G. Zheng, and G. K. Karagiannidis, "Beamforming optimization for full-duplex wireless-powered mimo systems," *IEEE Trans. Commun.*, vol. 65, no. 9, pp. 3750–3764, 2017.
- [80] M. Mohammadi, B. K. Chalise, A. Hakimi, Z. Mobini, H. A. Suraweera, and Z. Ding, "Beamforming design and power allocation for full-duplex non-orthogonal multiple access cognitive relaying," *IEEE Trans. Commun.*, vol. 66, no. 12, pp. 5952–5965, 2018.
- [81] N. Zlatanov, E. Sippel, V. Jamali, and R. Schober, "Capacity of the gaussian two-hop full-duplex relay channel with residual self-interference," *IEEE Trans. Commun.*, vol. 65, no. 3, pp. 1005–1021, March 2017.
- [82] V. Syrjala, M. Valkama, L. Anttila, T. Riihonen, and D. Korpi, "Analysis of oscillator phase-noise effects on self-interference cancellation in full-duplex ofdm radio transceivers," *IEEE Trans. Wireless Commun.*, vol. 13, no. 6, pp. 2977–2990, 2014.
- [83] Y. Wang, Q. Cui, M. Haenggi, and Z. Tan, "On the SIR meta distribution for Poisson networks with interference cancellation," *IEEE Wireless Commun. Lett.*, vol. 7, no. 1, pp. 26–29, February 2018.
- [84] R. H. Etkin, N. David, and H. Wang, "Gaussian interference channel capacity to within one bit," *IEEE Trans. Inf. Theory*, vol. 54, no. 12, pp. 5534–5562, December 2008.
- [85] R. P. Sirigina and A. Madhukumar, "Full-duplex decode-and-forward relay-assisted interference management: A diversity gain region perspective," *IEEE Trans. Commun.*, vol. 64, no. 1, pp. 141–152, January 2016.
- [86] P. S. Bithas and A. A. Rontogiannis, "Mobile communication systems in the presence of fading/shadowing, noise and interference," *IEEE Trans. Commun.*, vol. 63, no. 3, pp. 724–737, March 2015.
- [87] S. P. Weber, J. G. Andrews, X. Yang, and G. De Veciana, "Transmission capacity of wireless ad hoc networks with successive interference cancellation," *IEEE Trans. Inf. Theory*, vol. 53, no. 8, pp. 2799–2814, Aug. 2007.
- [88] L. Qu, J. He, and C. Assi, "Understanding the benefits of successive interference cancellation in multi-rate multi-hop wireless networks," *IEEE Trans. Commun.*, vol. 62, no. 7, pp. 2465–2477, July 2014.
- [89] M. O. Hasna, M.-S. Alouini, A. Bastami, and E. S. Ebbini, "Performance analysis of cellular mobile systems with successive co-channel interference cancellation," *IEEE Trans. Wireless Commun.*, vol. 2, no. 1, pp. 29–40, January 2003.
- [90] Z. Zhang, Z. Ma, M. Xiao, Z. Ding, and P. Fan, "Full-duplex device-to-device-aided cooperative nonorthogonal multiple access," *IEEE Trans. Veh. Technol.*, vol. 66, no. 5, pp. 4467–4471, May 2017.
- [91] A. Abdi, H. A. Barger, and M. Kaveh, "A simple alternative to the lognormal model of shadow fading in terrestrial and satellite channels," in *Proc. IEEE 54th Veh. Technol. Conf. (VTC Fall)*, vol. 4, Atlantic City, NJ, USA, 2001, pp. 2058–2062.
- [92] S. S. Bidokhti and V. M. Prabhakaran, "Is non-unique decoding necessary?" *IEEE Trans. Inf. Theory*, vol. 60, no. 5, pp. 2594–2610, May 2014.
- [93] W. Nam, D. Bai, J. Lee, and I. Kang, "Advanced interference management for 5g cellular networks," *IEEE Commun. Mag.*, vol. 52, no. 5, pp. 52–60, May 2014.
- [94] G. Zhou, W. Xu, and G. Bauch, "Is mac joint decoding optimal for interference channels?" in *Proc. Veh. Technol. Conf. (VTC Spring)*, Glasgow, UK, 2015, pp. 1–5.
- [95] B. Bandemer, A. El Gamal, and Y.-H. Kim, "Simultaneous nonunique decoding is rate-optimal," in *Communication, Control, and Computing (Allerton), 2012 50th Annual Allerton Conference on*. IEEE, Monticello, IL, USA, 2012, pp. 9–16.

REFERENCES

- [96] Y.-b. Kim, M. G. Kang, and W. Choi, “On-off switched interference alignment for diversity multiplexing tradeoff improvement in the 2-user x-network with two antennas,” *IEEE Trans. Wireless Commun.*, vol. 18, no. 1, pp. 546–558, January 2019.
- [97] X. Lin, M. Tao, Y. Xu, and R. Wang, “Outage probability and finite-snr diversity–multiplexing tradeoff for two-way relay fading channels,” *IEEE Trans. Veh. Technol.*, vol. 62, no. 7, pp. 3123–3136, September 2013.
- [98] Y.-D. Yao and A. U. Sheikh, “Investigations into cochannel interference in microcellular mobile radio systems,” *IEEE Trans. Veh. Technol.*, vol. 41, no. 2, pp. 114–123, 1992.
- [99] T. Z. H. Ernest, R. P. Sirigina, A. K. Krishna, and A. S. Madhukumar, “On the Performance Analysis of Hybrid-Duplex Systems for Aeronautical Communications,” in *Proc. IEEE 87th Veh. Technol. Conf. (VTC Spring)*, Porto, Portugal, 2018, pp. 1–5.
- [100] T. Z. H. Ernest, A. S. Madhukumar, R. P. Sirigina, and A. K. Krishna, “Hybrid-Duplex based Control and Non-Payload Communication Systems for UAVs: An Outage Analysis,” in *Proc. IEEE/AIAA 37th Digit. Avionics Syst. Conf.*, London, UK, 2018.
- [101] ———, “An Outage Probability Analysis of Full-Duplex NOMA in UAV Communications,” in *Proc. IEEE Wireless Commun. Netw. Conf. (WCNC)*, Marrakech, Morocco, 2019, pp. 1–5.
- [102] J. M. Romero-Jerez and A. J. Goldsmith, “Receive antenna array strategies in fading and interference: an outage probability comparison,” *IEEE Trans. Wireless Commun.*, vol. 7, no. 3, pp. 920–932, 2008.
- [103] T. Elkourdi and O. Simeone, “Femtocell as a relay: An outage analysis,” *IEEE Trans. Wireless Commun.*, vol. 10, no. 12, pp. 4204–4213, December 2011.
- [104] J.-H. Wui and D. Kim, “Outage probability and power allocation for collaborative relaying of multiple-access primary users by secondary user with partial/full channel knowledge,” *IEEE Trans. Veh. Technol.*, vol. 65, no. 11, pp. 9098–9111, November 2016.
- [105] W.-Y. Shin, S.-Y. Chung, and Y. H. Lee, “Diversity–multiplexing tradeoff and outage performance for rician mimo channels,” *IEEE Trans. Inf. Theory*, vol. 54, no. 3, pp. 1186–1196, 2008.
- [106] R. Narasimhan, “Finite-snr diversity–multiplexing tradeoff for correlated rayleigh and rician mimo channels,” *IEEE Trans. Inf. Theory*, vol. 52, no. 9, pp. 3965–3979, 2006.
- [107] L. Zheng and D. N. C. Tse, “Diversity and multiplexing: A fundamental tradeoff in multiple-antenna channels,” *IEEE Trans. Inf. Theory*, vol. 49, no. 5, pp. 1073–1096, 2003.
- [108] A. R. Heidarpour, G. K. Kurt, and M. Uysal, “Finite-snr diversity-multiplexing tradeoff for network coded cooperative ofdma systems,” *IEEE Trans. Wireless Commun.*, vol. 16, no. 3, pp. 1385–1396, 2017.
- [109] R. U. Nabar, H. Bolcskei, and A. J. Paulraj, “Diversity and outage performance in space-time block coded ricean mimo channels,” *IEEE Trans. Wireless Commun.*, vol. 4, no. 5, pp. 2519–2532, 2005.
- [110] L. Wang, Y. Cai, and W. Yang, “On the finite-snr dmt of two-way af relaying with imperfect csi,” *IEEE Wireless Commun. Lett.*, vol. 1, no. 3, pp. 161–164, 2012.
- [111] K. Yang, H. Cui, L. Song, and Y. Li, “Efficient full-duplex relaying with joint antenna-relay selection and self-interference suppression,” *IEEE Trans. Wireless Commun.*, vol. 14, no. 7, pp. 3991–4005, 2015.
- [112] V. V. Chetlur and H. S. Dhillon, “Downlink coverage analysis for a finite 3-d wireless network of unmanned aerial vehicles,” *IEEE Trans. Commun.*, vol. 65, no. 10, pp. 4543–4558, 2017.
- [113] X. Wang, H. Zhang, Y. Tian, and V. C. Leung, “Modeling and analysis of aerial base station-assisted cellular networks in finite areas under los and nlos propagation,” *IEEE Trans. Wireless Commun.*, vol. 17, no. 10, pp. 6985–7000, October 2018.
- [114] L. Wang, F. Tian, T. Svensson, D. Feng, M. Song, and S. Li, “Exploiting full duplex for device-to-device communications in heterogeneous networks,” *IEEE Commun. Mag.*, vol. 53, no. 5, pp. 146–152, May 2015.
- [115] H. Ju and R. Zhang, “Optimal resource allocation in full-duplex wireless-powered communication network,” *IEEE Trans. Commun.*, vol. 62, no. 10, pp. 3528–3540, October 2014.

REFERENCES

- [116] X. Kang, C. K. Ho, and S. Sun, "Full-duplex wireless-powered communication network with energy causality," *IEEE Trans. Wireless Commun.*, vol. 14, no. 10, pp. 5539–5551, October 2015.
- [117] G. Yang, D. Yuan, Y.-C. Liang, R. Zhang, and V. C. Leung, "Optimal resource allocation in full-duplex ambient backscatter communication networks for wireless-powered IoT," *IEEE Internet Things J.*, vol. 6, no. 2, pp. 2612–2625, April 2019.
- [118] S. Shao, D. Liu, K. Deng, Z. Pan, and Y. Tang, "Analysis of carrier utilization in full-duplex cellular networks by dividing the co-channel interference region," *IEEE Commun. Lett.*, vol. 18, no. 6, pp. 1043–1046, 2014.
- [119] C. Nam, C. Joo, and S. Bahk, "Joint subcarrier assignment and power allocation in full-duplex OFDMA networks," *IEEE Trans. Wireless Commun.*, vol. 14, no. 6, pp. 3108–3119, June 2015.
- [120] B. Di, S. Bayat, L. Song, Y. Li, and Z. Han, "Joint user pairing, subchannel, and power allocation in full-duplex multi-user OFDMA networks," *IEEE Trans. Wireless Commun.*, vol. 15, no. 12, pp. 8260–8272, December 2016.
- [121] X. Zhang, T.-H. Chang, Y.-F. Liu, C. Shen, and G. Zhu, "Max-min fairness user scheduling and power allocation in full-duplex OFDMA systems," *IEEE Trans. Wireless Commun.*, vol. 18, no. 6, pp. 3078–3092, June 2019.
- [122] G. Chen, Y. Gong, P. Xiao, and J. A. Chambers, "Physical layer network security in the full-duplex relay system," *IEEE Trans. Inf. Forensics Security*, vol. 10, no. 3, pp. 574–583, March 2015.
- [123] Q. Gao, G. Chen, L. Liao, and Y. Hua, "Full-duplex cooperative transmission scheduling in fast-fading MIMO relaying wireless networks," in *Proc. 2014 Int. Conf. Comput. Netw. Commun. (ICNC)*. IEEE, Honolulu, HI, USA, 2014, pp. 771–775.
- [124] S. R. Islam, N. Avazov, O. A. Dobre, and K.-S. Kwak, "Power-domain non-orthogonal multiple access (NOMA) in 5G systems: Potentials and challenges," *IEEE Commun. Surveys Tut.*, vol. 19, no. 2, pp. 721–742, 2017.
- [125] L. Dai, B. Wang, Z. Ding, Z. Wang, S. Chen, and L. Hanzo, "A survey of non-orthogonal multiple access for 5G," *IEEE Communications Surveys & Tutorials*, vol. 20, no. 3, pp. 2294–2323, 2018.
- [126] M. F. Kader, S. Y. Shin, and V. C. Leung, "Full-duplex non-orthogonal multiple access in cooperative relay sharing for 5g systems," *IEEE Trans. Veh. Technol.*, vol. 67, no. 7, pp. 5831–5840, July 2018.
- [127] R. Hoshyar, F. P. Wathan, and R. Tafazolli, "Novel low-density signature for synchronous cdma systems over awgn channel," *IEEE Trans. Signal Process.*, vol. 56, no. 4, pp. 1616–1626, 2008.
- [128] R. Razavi, R. Hoshyar, M. A. Imran, and Y. Wang, "Information theoretic analysis of LDS scheme," *IEEE Commun. Lett.*, vol. 15, no. 8, pp. 798–800, 2011.
- [129] R. Hoshyar, R. Razavi, and M. Al-Imari, "LDS-OFDM an efficient multiple access technique," in *Proc. 2010 IEEE 71st Veh. Technol. Conf. (VTC Spring)*. IEEE, Taipei, Taiwan, 2010, pp. 1–5.
- [130] M. Al-Imari, P. Xiao, M. A. Imran, and R. Tafazolli, "Uplink non-orthogonal multiple access for 5G wireless networks," in *Proc. 2014 11th Int. Symp. Wireless Commun. Syst. (ISWCS)*. IEEE, Barcelona, Spain, 2014, pp. 781–785.
- [131] H. Nikopour and H. Baligh, "Sparse code multiple access," in *Proc. IEEE 24th Annu. Int. Symp. PIMRC*. IEEE, London, UK, 2013, pp. 332–336.
- [132] H. Mu, Z. Ma, M. Alhaji, P. Fan, and D. Chen, "A fixed low complexity message pass algorithm detector for up-link SCMA system," *IEEE Wireless Commun. Lett.*, vol. 4, no. 6, pp. 585–588, 2015.
- [133] Y. Du, B. Dong, Z. Chen, J. Fang, and X. Wang, "A fast convergence multiuser detection scheme for uplink SCMA systems," *IEEE Wireless Commun. Lett.*, vol. 5, no. 4, pp. 388–391, 2016.
- [134] J. Cui, Z. Ding, and P. Fan, "A novel power allocation scheme under outage constraints in noma systems," *IEEE Signal Process. Lett.*, vol. 23, no. 9, pp. 1226–1230, September 2016.
- [135] M. Salehi, H. Tabassum, and E. Hossain, "Meta Distribution of SIR in Large-Scale Uplink and Downlink NOMA Networks," *IEEE Trans. Commun.*, vol. 67, no. 4, pp. 3009–3025, April 2019.

REFERENCES

- [136] C.-H. Liu and D.-C. Liang, "Heterogeneous networks with power-domain NOMA: coverage, throughput, and power allocation analysis," *IEEE Trans. Wireless Commun.*, vol. 17, no. 5, pp. 3524–3539, May 2018.
- [137] M. F. Kader and S. Y. Shin, "Coordinated direct and relay transmission using uplink NOMA," *IEEE Wireless Commun. Lett.*, vol. 7, no. 3, pp. 400–403, June 2018.
- [138] Z. Zhang, H. Sun, and R. Q. Hu, "Downlink and uplink non-orthogonal multiple access in a dense wireless network," *IEEE J. Sel. Areas Commun.*, vol. 35, no. 12, pp. 2771–2784, December 2017.
- [139] Z. Ding, R. Schober, and H. V. Poor, "A general MIMO framework for NOMA downlink and uplink transmission based on signal alignment," *IEEE Trans. Wireless Commun.*, vol. 15, no. 6, pp. 4438–4454, June 2016.
- [140] Z. Ding, P. Fan, and H. V. Poor, "Impact of user pairing on 5G nonorthogonal multiple-access downlink transmissions," *IEEE Trans. Veh. Technol.*, vol. 65, no. 8, pp. 6010–6023, August 2016.
- [141] W. Liang, Z. Ding, Y. Li, and L. Song, "User pairing for downlink non-orthogonal multiple access networks using matching algorithm," *IEEE Trans. Commun.*, vol. 65, no. 12, pp. 5319–5332, December 2017.
- [142] L. Xiao, Y. Li, C. Dai, H. Dai, and H. V. Poor, "Reinforcement learning-based NOMA power allocation in the presence of smart jamming," *IEEE Trans. Veh. Technol.*, vol. 67, no. 4, pp. 3377–3389, April 2017.
- [143] M. Kim, N.-I. Kim, W. Lee, and D.-H. Cho, "Deep learning-aided SCMA," *IEEE Commun. Lett.*, vol. 22, no. 4, pp. 720–723, April 2018.
- [144] ICAO, "Icao long-term traffic forecasts," 2016, accessed on 23-11-2019. [Online]. Available: <https://www.icao.int/Meetings/aviationdataseminar/Documents/ICAO-Long-Term-Traffic-Forecasts-July-2016.pdf>
- [145] T. Z. H. Ernest, A. K. Krishna, A. S. Madhukumar, and R. P. Sirigina, "On the efficiency improvements to aeronautical waveforms and integrated modular avionics systems," in *Proc. IEEE/AIAA 35th Digit. Avionics Syst. Conf.*, Sacramento, CA, USA, 2016, pp. 1–8.
- [146] S. Li, R. D. Murch, and V. K. Lau, "Linear transceiver design for full-duplex multi-user mimo system," in *Proc. IEEE Int. Conf. Commun. (ICC)*, Sydney, NSW, Australia, 2014, pp. 4921–4926.
- [147] M. Mohammadi, H. A. Suraweera, Y. Cao, I. Krikidis, and C. Tellambura, "Full-duplex radio for uplink/downlink wireless access with spatially random nodes," *IEEE Trans. Commun.*, vol. 63, no. 12, pp. 5250–5266, Dec. 2015.
- [148] Y. Jang, K. Min, S. Park, and S. Choi, "Spatial resource utilization to maximize uplink spectral efficiency in full-duplex massive MIMO," in *Proc. IEEE Int. Conf. Commun. (ICC)*, London, UK, 2015, pp. 1583–1588.
- [149] A. C. Cirik, S. Biswas, O. Taghizadeh, and T. Ratnarajah, "Robust transceiver design in full-duplex MIMO cognitive radios," *IEEE Trans. Veh. Technol.*, vol. 67, no. 2, pp. 1313–1330, Feb. 2018.
- [150] H. Lee, S. Eom, J. Park, and I. Lee, "UAV-Aided Secure Communications With Cooperative Jamming," *IEEE Trans. Veh. Technol.*, October 2018.
- [151] H. Jamal and D. W. Matolak, "Fbmc and l-dacs performance for future air-to-ground communication systems," *IEEE Transactions on Vehicular Technology*, vol. 66, no. 6, pp. 5043–5055, 2017.
- [152] A. Goldsmith, *Wireless Communications*. Cambridge University Press, Cambridge, UK, 2005.
- [153] R. Narasimhan, "Individual outage rate regions for fading multiple access channels," in *Proc. 2007 ISIT*. IEEE, Nice, France, 2007, pp. 1571–1575.
- [154] T. Kwon, S. Lim, S. Choi, and D. Hong, "Optimal duplex mode for df relay in terms of the outage probability," *IEEE Trans. Veh. Technol.*, vol. 59, no. 7, pp. 3628–3634, 2010.
- [155] T. K. Baranwal, D. S. Michalopoulos, and R. Schober, "Outage analysis of multihop full duplex relaying," *IEEE Commun. Lett.*, vol. 17, no. 1, pp. 63–66, 2013.
- [156] P. C. Sofotasios, M. K. Fikadu, S. Muhaidat, Q. Cui, G. K. Karagiannidis, and M. Valkama, "Full-duplex regenerative relaying and energy-efficiency optimization over generalized asymmetric fading channels," *IEEE Trans. Wireless Commun.*, vol. 16, no. 5, pp. 3232–3251, May 2017.

REFERENCES

- [157] S. András, A. Baricz, and Y. Sun, “The generalized marcum q-function: an orthogonal polynomial approach,” *Acta Universitatis Sapientiae Mathematica*, vol. 3, no. 1, pp. 60–76, 2011.
- [158] M. K. Simon and M.-S. Alouini, *Digital communication over fading channels*. John Wiley & Sons, NJ, USA, 2005, vol. 95.
- [159] ITU, “Itu-r report m.2233, examples of technical characteristics for unmanned aircraft control and nonpayload communications links,” Tech. Rep., 2011, accessed on 23-11-2019. [Online]. Available: <http://www.itu.int/pub/R-REP-M.2233-2011>
- [160] D. Stacey, *Aeronautical radio communication systems and networks*. John Wiley & Sons, UK, 2008.
- [161] S. Gligorevic, U. Epple, and M. Schnell, “The LDACS1 physical layer design,” in *Future Aeronautical Communications*. InTech, 2011.
- [162] Civil Aviation Authority of Singapore, “Manual of Standards - Air Traffic Services,” Tech. Rep., 2014, accessed on 23-11-2019. [Online]. Available: https://www.caas.gov.sg/docs/default-source/pdf/manual_of_standards_air_traffic_services_v2-35403dfbb3903666590f0ff000087c682.pdf
- [163] L. G. Ordóñez, D. P. Palomar, and J. R. Fonollosa, “Array gain in the DMT framework for MIMO channels,” *IEEE Trans. Inf. Theory*, vol. 58, no. 7, pp. 4577–4593, July 2012.
- [164] V. S. Annapureddy and V. V. Veeravalli, “Gaussian interference networks: Sum capacity in the low-interference regime and new outer bounds on the capacity region,” *IEEE Trans. Inf. Theory*, vol. 55, no. 7, pp. 3032–3050, July 2009.
- [165] D. Zahavi and R. Dabora, “On cooperation and interference in the weak interference regime,” *IEEE Trans. Inf. Theory*, vol. 63, no. 6, pp. 3894–3922, June 2017.
- [166] I. Shubhi and Y. Sanada, “Joint turbo decoding for overloaded mimo-ofdm systems,” *IEEE Trans. Veh. Technol.*, vol. 66, no. 1, pp. 433–442, Jan. 2017.
- [167] S. Sharifi, A. K. Tanc, and T. M. Duman, “LDPC code design for the two-user Gaussian multiple access channel,” *IEEE Trans. Wireless Commun.*, vol. 15, no. 4, pp. 2833–2844, 2016.
- [168] S. Karmakar and M. K. Varanasi, “The generalized multiplexing gain region of the slow fading mimo interference channel and its achievability with limited feedback,” in *Information Theory Proceedings (ISIT), 2012 IEEE International Symposium on*. IEEE, Cambridge, MA, USA, 2012, pp. 3135–3139.
- [169] J. Blomer and N. Jindal, “Transmission capacity of wireless ad hoc networks: Successive interference cancellation vs. joint detection,” in *Proc. IEEE Int. Conf. Commun. (ICC)*. IEEE, Dresden, Germany, 2009, pp. 1–5.
- [170] A. Bennatan, S. Shamai, and A. R. Calderbank, “Soft-decoding-based strategies for relay and interference channels: Analysis and achievable rates using ldpc codes,” *IEEE Trans. Inf. Theory*, vol. 60, no. 4, pp. 1977–2009, April 2014.
- [171] H. Amann, J. Escher, S. Levy, and M. Cargo, *Analysis I*. Springer, Germany, 2005, vol. 3.
- [172] D. W. Matolak and R. Sun, “Unmanned aircraft systems: Air-ground channel characterization for future applications,” *IEEE Veh. Technol. Mag.*, vol. 10, no. 2, pp. 79–85, June 2015.
- [173] L. Zeng, X. Cheng, C.-X. Wang, and X. Yin, “A 3d geometry-based stochastic channel model for uav-mimo channels,” in *Proc. IEEE Wireless Commun. Netw. Conf. (WCNC)*. IEEE, San Francisco, CA, USA, 2017, pp. 1–5.
- [174] K. Jin, X. Cheng, X. Ge, and X. Yin, “Three dimensional modeling and space-time correlation for uav channels,” in *Proc. IEEE 85th Veh. Technol. Conf. (VTC Spring)*. IEEE, Sydney, Australia, 2017, pp. 1–5.
- [175] H. Jiang, Z. Zhang, and G. Gui, “Three-dimensional non-stationary wideband geometry-based uav channel model for a2g communication environments,” *IEEE Access*, vol. 7, pp. 26 116–26 122, January 2019.
- [176] H. Jiang, Z. Zhang, L. Wu, and J. Dang, “Three-dimensional geometry-based uav-mimo channel modeling for a2g communication environments,” *IEEE Commun. Lett.*, vol. 22, no. 7, pp. 1438–1441, July 2018.

REFERENCES

- [177] Y. J. Chun, S. L. Cotton, H. S. Dhillon, F. J. Lopez-Martinez, J. F. Paris, and S. K. Yoo, “A comprehensive analysis of 5g heterogeneous cellular systems operating over $\kappa - \mu$ shadowed fading channels,” *IEEE Trans. Wireless Commun.*, vol. 16, no. 11, pp. 6995–7010, Nov. 2017.
- [178] J. F. Paris, “Statistical characterization of $\kappa - \mu$ shadowed fading,” *IEEE Trans. Veh. Technol.*, vol. 63, no. 2, pp. 518–526, Feb. 2014.
- [179] J. Zhang, X. Chen, K. P. Peppas, X. Li, and Y. Liu, “On high-order capacity statistics of spectrum aggregation systems over $\kappa - \mu$ and $\kappa - \mu$ shadowed fading channels,” *IEEE Trans. Commun.*, vol. 65, no. 2, pp. 935–944, Feb. 2017.
- [180] X. Li, J. Li, L. Li, J. Jin, J. Zhang, and D. Zhang, “Effective rate of miso systems over $\kappa - \mu$ shadowed fading channels,” *IEEE Access*, vol. 5, pp. 10 605–10 611, June 2017.
- [181] S. Kumar, “Approximate outage probability and capacity for $\kappa - \mu$ shadowed fading,” *IEEE Wireless Commun. Lett.*, vol. 4, no. 3, pp. 301–304, June 2015.
- [182] N. H. Motlagh, M. Bagaa, and T. Taleb, “UAV selection for a UAV-Based integrative IoT platform,” in *Proc. IEEE Global Commun. Conf.(GLOBECOM)*. IEEE, Washington, DC, USA, 2016, pp. 1–6.
- [183] A. Abdi, W. C. Lau, M.-S. Alouini, and M. Kaveh, “A new simple model for land mobile satellite channels: first-and second-order statistics,” *IEEE Trans. Wireless Commun.*, vol. 2, no. 3, pp. 519–528, May 2003.
- [184] X. Yue, Y. Liu, S. Kang, A. Nallanathan, and Z. Ding, “Exploiting full/half-duplex user relaying in noma systems,” *IEEE Trans. Commun.*, vol. 66, no. 2, pp. 560–575, 2018.
- [185] C. Yao, L. Song, and Y. Li, “X-duplex radios: Flexible switching between full-duplex and half-duplex,” *IEEE Wireless Commun. Lett.*, vol. 7, no. 1, pp. 94–97, Feb. 2018.
- [186] S. Kumar and S. Kalyani, “Outage probability and rate for $\kappa - \mu$ shadowed fading in interference limited scenario,” *IEEE Trans. Wireless Commun.*, vol. 16, no. 12, pp. 8289–8304, Dec. 2017.
- [187] 3GPP, “TR36.77 Study on Enhanced LTE Support for Aerial Vehicles,” Tech. Rep., 2017, accessed on 23-11-2019. [Online]. Available: <https://portal.3gpp.org/desktopmodules/Specifications/SpecificationDetails.aspx?specificationId=3231>
- [188] Y. Zeng, J. Lyu, and R. Zhang, “Cellular-connected uav: Potential, challenges and promising technologies,” *IEEE Wireless Commun.*, vol. 26, no. 1, pp. 120–127, 2018.
- [189] S. Enayati, H. Saeedi, H. Pishro-Nik, and H. Yanikomeroglu, “Moving aerial base station networks: Stochastic geometry analysis and design perspective,” *IEEE Trans. Wireless Commun.*, vol. 18, no. 6, pp. 2977–2988, 2019.
- [190] Y. Liu, Z. Qin, Y. Cai, Y. Gao, G. Y. Li, and A. Nallanathan, “UAV communications based on non-orthogonal multiple access,” *IEEE Wireless Commun.*, vol. 26, no. 1, pp. 52–57, 2019.
- [191] Z. Yang, Z. Ding, P. Fan, and N. Al-Dahir, “A general power allocation scheme to guarantee quality of service in downlink and uplink NOMA systems,” *IEEE Trans. Wireless Commun.*, vol. 15, no. 11, pp. 7244–7257, November 2016.
- [192] T. Z. H. Ernest, A. S. Madhukumar, R. P. Sirigina, and A. K. Krishna, “NOMA-Aided Multi-UAV Communications in Full-Duplex Heterogeneous Networks,” *Submitted to IEEE Trans. Commun. for publication*, 2019.
- [193] M. Moltafet, P. Azmi, N. Mokari, M. R. Javan, and A. Mokdad, “Optimal and fair energy efficient resource allocation for energy harvesting-enabled-PD-NOMA-based HetNets,” *IEEE Trans. Wireless Commun.*, vol. 17, no. 3, pp. 2054–2067, March 2018.
- [194] M. Liu, J. Yang, and G. Gui, “DSF-NOMA: UAV-assisted emergency communication technology in a heterogeneous Internet of Things,” *IEEE Internet Things J.*, vol. 6, no. 3, pp. 5508–5519, June 2019.
- [195] Z. Ding, P. Fan, and H. V. Poor, “On the coexistence between full-duplex and NOMA,” *IEEE Wireless Commun. Lett.*, vol. 7, no. 5, pp. 692–695, Oct. 2018.
- [196] L. Lei, E. Lagunas, S. Chatzinotas, and B. Ottersten, “Noma aided interference management for full-duplex self-backhauling hetnets,” *IEEE Commun. Lett.*, vol. 22, no. 8, pp. 1696–1699, August 2018.

REFERENCES

- [197] V. Sharma, R. Sabatini, and S. Ramasamy, “Uavs assisted delay optimization in heterogeneous wireless networks,” *IEEE Commun. Lett.*, vol. 20, no. 12, pp. 2526–2529, December 2016.
- [198] L. Zhang, Q. Fan, and N. Ansari, “3-d drone-base-station placement with in-band full-duplex communications,” *IEEE Commun. Lett.*, vol. 22, no. 9, pp. 1902–1905, September 2018.
- [199] L. Zhang and N. Ansari, “On the number and 3-D placement of in-band full-duplex enabled drone-mounted base-stations,” *IEEE Wireless Commun. Lett.*, vol. 8, no. 1, pp. 221–224, February 2018.
- [200] T. M. C. Chu and H.-J. Zepernick, “Performance of a non-orthogonal multiple access system with full-duplex relaying,” *IEEE Commun. Lett.*, vol. 22, no. 10, pp. 2084–2087, October 2018.
- [201] T. Hou, Y. Liu, Z. Song, X. Sun, and Y. Chen, “Multiple Antenna Aided NOMA in UAV Networks: A Stochastic Geometry Approach,” *IEEE Trans. Commun.*, vol. 67, no. 2, pp. 1031–1044, 2018.
- [202] N. Zhao, X. Pang, Z. Li, Y. Chen, F. Li, Z. Ding, and M.-S. Alouini, “Joint Trajectory and Precoding Optimization for UAV-Assisted NOMA Networks,” *IEEE Trans. Commun.*, vol. 67, no. 5, pp. 3723–3735, May 2019.
- [203] W. Mei and R. Zhang, “Uplink cooperative NOMA for cellular-connected UAV,” *IEEE J. Sel. Topics Signal Process.*, vol. 13, no. 3, pp. 644–656, June 2019.
- [204] A. A. Nasir, H. D. Tuan, T. Q. Duong, and H. V. Poor, “UAV-enabled communication using NOMA,” *IEEE Trans. Commun.*, vol. 67, no. 7, pp. 5126–5138, July 2019.
- [205] T. M. Nguyen, W. Ajib, and C. Assi, “A novel cooperative NOMA for designing UAV-assisted wireless backhaul networks,” *IEEE J. Sel. Areas Commun.*, vol. 36, no. 11, pp. 2497–2507, November 2018.
- [206] T. Hou, Y. Liu, Z. Song, X. Sun, and Y. Chen, “Exploiting NOMA for UAV Communications in Large-Scale Cellular Networks,” *IEEE Trans. Commun.*, vol. 67, no. 10, pp. 6897–6911, October 2019.
- [207] G. Im and J. H. Lee, “Outage probability for cooperative noma systems with imperfect sic in cognitive radio networks,” *IEEE Commun. Lett.*, vol. 23, no. 4, pp. 692–695, April 2019.
- [208] K. A. Hamdi, “A useful lemma for capacity analysis of fading interference channels,” *IEEE Trans. Commun.*, vol. 58, no. 2, pp. 411–416, February 2010.
- [209] Y.-S. Choi and H. Shirani-Mehr, “Simultaneous transmission and reception: Algorithm, design and system level performance,” *IEEE Trans. Wireless Commun.*, vol. 12, no. 12, pp. 5992–6010, 2013.
- [210] T. Z. H. Ernest, A. S. Madhukumar, R. P. Sirigina, and A. K. Krishna, “NOMA-aided UAV Communications over Correlated Rician Shadowed Fading Channels,” *Submitted to IEEE. Trans. Signal Process. for publication*, 2019.
- [211] ———, “Downlink NOMA in Multi-UAV Networks over Bivariate Rician Shadowed Fading Channels,” in *Proc. IEEE 90th Veh. Technol. Conf. (VTC-Fall)*, Honolulu, HI, USA, 2019.
- [212] F. Jiang and A. L. Swindlehurst, “Dynamic uav relay positioning for the ground-to-air uplink,” in *2010 IEEE Globecom Workshops*. IEEE, Miami, FL, USA, 2010, pp. 1766–1770.
- [213] ———, “Optimization of uav heading for the ground-to-air uplink,” *IEEE J. Sel. Areas Commun.*, vol. 30, no. 5, pp. 993–1005, 2012.
- [214] N. C. Beaulieu and K. T. Hemachandra, “Novel representations for the bivariate rician distribution,” *IEEE Trans. Commun.*, vol. 59, no. 11, pp. 2951–2954, 2011.
- [215] ———, “Novel simple representations for gaussian class multivariate distributions with generalized correlation,” *IEEE Trans. Inf. Theory*, vol. 57, no. 12, pp. 8072–8083, 2011.
- [216] J. López-Fernández, J. F. Paris, and E. Martos-Naya, “Bivariate rician shadowed fading model,” *IEEE Trans. Veh. Technol.*, vol. 67, no. 1, pp. 378–384, 2018.
- [217] P. Zhan, K. Yu, and A. L. Swindlehurst, “Wireless relay communications with unmanned aerial vehicles: Performance and optimization,” *IEEE Trans. Aerosp. Electron. Syst.*, vol. 47, no. 3, pp. 2068–2085, 2011.

REFERENCES

- [218] T. Hou, X. Sun, and Z. Song, "Outage performance for non-orthogonal multiple access with fixed power allocation over nakagami-m fading channels," *IEEE Commun. Lett.*, vol. 22, no. 4, pp. 744–747, April 2018.
- [219] M. Abramowitz and I. Stegun, "Handbook of mathematical functions with formulas, graphs, and mathematical tables (applied mathematics series 55)," *National Bureau of Standards, Washington, DC, USA*, 1964.
- [220] N. O'Donoughue and J. M. Moura, "On the product of independent complex gaussians," *IEEE Trans. Signal Process.*, vol. 60, no. 3, pp. 1050–1063, March 2011.
- [221] A. H. A. El-Malek, F. S. Al-Qahtani, T. Q. Duong, S. A. Zummo, and H. Alnuweiri, "MIMO cognitive relay networks with correlated antennas over Rayleigh fading channels," *IEEE Trans. Veh. Technol.*, vol. 65, no. 7, pp. 5349–5363, July 2015.
- [222] H. Wang, J. Wang, G. Ding, J. Chen, Y. Li, and Z. Han, "Spectrum sharing planning for full-duplex UAV relaying systems with underlaid D2D communications," *IEEE J. Sel. Areas in Commun.*, vol. 36, no. 9, pp. 1986–1999, September 2018.
- [223] Q. Song, F.-C. Zheng, Y. Zeng, and J. Zhang, "Joint beamforming and power allocation for UAV-enabled full-duplex relay," *IEEE Trans. Veh. Technol.*, vol. 68, no. 2, pp. 1657–1671, February 2019.
- [224] Civil Aviation Authority of Singapore. Unmanned aircraft systems. Accessed on 23-11-2019. [Online]. Available: <https://www.caas.gov.sg/public-passengers/unmanned-aircraft-systems>
- [225] A. Bartoszewicz and S. Glab, "Algebrability of conditionally convergent series with cauchy product," *Journal of Mathematical Analysis and Applications*, vol. 385, no. 2, pp. 693–697, 2012.
- [226] S. Parthasarathy and R. K. Ganti, "Coverage analysis in downlink poisson cellular network with $\kappa - \mu$ shadowed fading," *IEEE Wireless Commun. Lett.*, vol. 6, no. 1, pp. 10–13, Feb. 2017.
- [227] G. Boros and V. Moll, *Irresistible Integrals. : Symbolics, Analysis and Experiments in the Evaluation of Integrals*. Cambridge University Press, Cambridge, UK, 2004.